Strojniški vestnik

Journal of Mechanical Engineering

Strojniški vestnik – Journal of Mechanical Engineering (SV-JME)

Contents

Strojniški vestnik
Journal of Mechanical Engineering

ON THE COVER

Offshore wind turbine repair robots can be affected by wind and blade angles, making it hard to keep grinding pressure steady. To fix this, a new pneumatic device and smart controller were developed to keep a constant force during repairs. The controller uses advanced algorithms to handle disturbances like wind, tilt, and equipment limitations. Tests showed that this system is faster and more accurate than traditional methods, with better control and fewer errors. This makes robot repairs safer and more reliable, even in tough offshore conditions.
Image Courtesy: iStock.com

Design and Evaluation of a Passive Compliance Control Method of an Offshore Wind Turbine Blade Grinding Robot

Xinrong Liu ✉ – Hao Li – Yu Fang – Diqing Fan

Shanghai University of Engineering Science, School of Mechanical and Automotive Engineering, China
✉ lxr4849@126.com

Abstract   Robots that repair offshore wind turbine blades are susceptible to interference from different factors such as external wind, which can lead to damage to the blades by the robot during the grinding process. Therefore, the robot needs to keep the grinding contact force constant in the complex operating environment. In this study, a constant force control device that is based on a pneumatic system is designed to address this problem, and a controller that is based on an improved Active Disturbance Rejection Control (ADRC) algorithm was proposed to control this device. Based on the analysis of the mechanism of the constant force control device and according to the relative order of the system, a second-order ADRC is designed. The controller utilizes a tracking differentiator (TD) to filter the input signal, an extended state observer (ESO) to estimate the total perturbation in the system, and a nonlinear state error feedback control law (NLSEF) for compensation. In order to solve the problems of electric proportional valve dead-zone characteristics, unknown interference during high altitude operation, tilt angle changes during grinding, dead-zone compensation, and gravity compensation algorithms were incorporated into the controller. Finally, the experimental platform is built to carry out experiments under various working conditions. The experimental results show that the controller improves the system regulation time by 59%, with an overshoot close to zero, when compared with the traditional proportional-integral-derivative (PID) algorithm. Also, both the absolute value of the maximum error and the mean square value of the error have been reduced to a large extent. As a result, the controller has a better force control accuracy and dynamic tracking performance, strong interference rejection capability and adaptability, and provides a theoretical basis for practical engineering applications.

Keywords   improved active disturbance rejection control, gravity compensation, dead-zone compensation, offshore wind turbine blade, pneumatic loading system

Highlights
▪ Design and mathematical model of a pneumatic constant force control device are presented.
▪ A controller based on an improved ADRC algorithm is proposed.
▪ Dead-band compensation and gravity compensation algorithms are added to the controller.
▪ The improved ADRC has better responsiveness, control accuracy, and immunity to interference.

1 INTRODUCTION

With the massive consumption of fossil fuels, the problems of environmental degradation, climate warming, and the energy crisis have become more serious [1]. As well, offshore wind energy, as one of the very promising renewable and clean energy sources, can alleviate the energy pressure to a great extent [2,3]. The global offshore wind capacity has grown rapidly over the last decade [4]. China's installed offshore wind capacity was 35.6 GW by the end of 2023. The increase in installed offshore wind capacity means that some of the installed wind turbines are ageing and so maintenance of the wind turbine equipment is very important [5]. The first maintenance of the blades should be carried out after the offshore wind turbine has been dynamically commissioned and has been in normal operation for 7 to 10 days, and then every 6 months. Offshore wind turbine blades, are key components of the wind turbine system, and are at the heart of wind turbine equipment repair [6], with repair costs accounting for 20 % to 25 % of the total average cost [7]. This includes losses due to downtime for maintenance and labor costs. Currently, offshore wind turbine blade surface repair primarily relies on manual labor with the following problems: first, the high-risk factor of overhead operation, high labor intensity, a grinding process where there is great noise and a significant amount of dust, and long-term work in this environment tends to lead to earlier suffering

from occupational diseases. Second, the blade grinding quality is not stable, with an artificial grinding blade that has uneven quality. Third, blade maintenance incurs higher costs, and fourth, low efficiency. In order to solve the problems of manual repair, the use of robots instead of manually repairing the wind turbine blades is a good solution [8,9]. In comparison to manual repair of an offshore wind turbine blade, robotic repair has the advantages of high safety and efficiency [10].

If a robot is utilized in the blade polishing process, where the end of the polishing tool and blade contact generates the contact force, that contact force is too small and leads to a blade polishing quality that cannot meet the requirements. It should be noted that if the contact force is too large, an overcutting phenomenon damage to the surface of the blade will appear. Therefore, the size of the sanding force directly determines the quality of the processed workpiece, and how to maintain a constant sanding contact force has become a key issue to be solved by robot grinding. Current robotic constant force control methods include active compliance control and passive compliance control [11].

The essence of active compliance control is that the robot feeds back on the contact force signal and adopts a corresponding active control strategy to keep the contact force constant by adjusting the position, speed, and acceleration of the robot end, thus realizing the force compliance control of the grinding process. Guo et al. [12]

and Lakshminarayanan et al. [13] propose an adaptive variable, impedance active, compliance constant force control method, and an iterative learning controller based on impedance control. Zhang et al. [14] proposed a force-position anti-disturbance control strategy based on fuzzy proportional-integral-derivative (PID) control. Zhang et al. [15] proposed a constant force control based on active disturbance rejection control theory. However, when encountering unknown wind disturbances in blade grinding for offshore wind turbines, it is difficult to maintain the control accuracy regardless of whether impedance control or force-position hybrid control is adopted.

In order to cope with the problem of external disturbances, the researchers developed a force control end-effector [16-24], which achieves contact force control by means of passive compliance control. Wei and Xu [16] proposed the always symmetric structure to avoid the vibration caused by an eccentric force. Zhang et al. [17] utilized the second bending mode of fixed-guided compliant beams to design the compliance constant force mechanism. Chen et al. [18] and Xu et al. [19] designed a magnetic vibration absorber and integrated them into a smart end-effector for force control. Li et al. [20] and Mohammad et al. [21] use servo motors and a voice coil actuator, respectively, to design the end-effector to realize the control of the grinding contact force, but the force control is difficult. Liang et al. [22] and Huang et al. [23] used a low friction air cylinder to design the end-effector and used a PID algorithm to control it. Even though this compliance is better, the control accuracy is lower.

In order to solve the force control accuracy to improve the disturbance rejection capability, this study developed an end-effector using a low-friction cylinder. Also, an improved ADRC algorithm combining dead-zone compensation algorithm and a gravity compensation algorithm is proposed as the controller of this device, according to the principle of ADRC [24-26]. The algorithm not only solves the problems of the dead zone characteristics of the electric proportional valve and the change of the tilt angle during the grinding process, but also effectively copes with the problem of the unknown wind interference during high-altitude operation. Finally, the authors conclude that through experimental verification the adjustment of system time is less, the maximum deviation is lower, and the tracking error is smaller under the improved ADRC algorithm. Therefore, it can be surmised that compared to the PID algorithm, the improved ADRC has better dynamic response performance, force control accuracy, and anti-interference ability.

2 METHODS AND MATERIALS

The robot is lifted by the lifting mechanism to the vicinity of the blade, then guided by a traction rope where the robot adheres to the blade by a bottom vacuum suction cup, and after that it can begin the repair work on the blade. Fig. 1 shows the schematic diagram of robotic grinding, where the robot grinds the area to be repaired by guiding the end-effector.

2.1 Composition and Working Theory of an End-effector

The schematic diagram of the end-effector is shown in Fig. 2, and its main parts are: an air compressor, a pneumatic filter and regulator (F.R.), a 5-way 2-position pneumatic solenoid valve, an electrical proportional valve, a pneumatic cylinder, an inclination sensor, a force sensor, a STM32, a host computer, etc. The end-effector collects the grinding contact force through the force sensor, and the improved ADRC algorithm controls the opening of the electric proportional valve according to the pressure feedback value so as to achieve the expansion and contraction of the cylinder, and to ultimately achieve control of the grinding contact force.
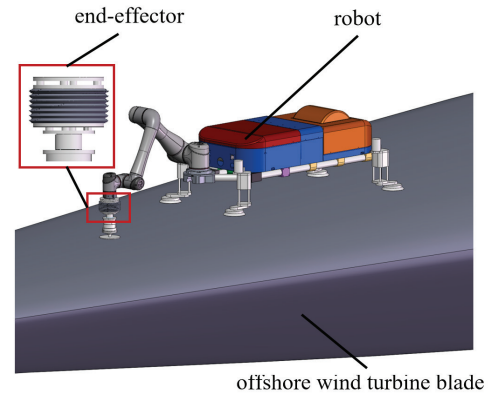
Fig. 1. Schematic Diagram of Robot Grinding

2.2 Modelling of the End-effector

From the composition and working theory of the end-effector, it can be seen that the end-effector is mainly composed of an electrical proportional valve, a cylinder, connecting air tubes, and force feedback in four parts. These four parts need to be modelled next.

2.2.1 Modelling of the Electrical Proportional Valve

The flow rate through the valve port of an electrical proportional valve is related to the flow area of the valve port and the magnitude of the inlet and outlet pressures. Approximating the gas flow at the valve port as a one-dimensional isentropic flow of an ideal gas, with the SANVILLE gas flow formula, the following formula is derived:

$$q = C_q A_q p_0 \sqrt{\frac{2}{RT}} \varphi\left(\frac{P_1}{p_0}\right) = C_q w x_v p_0 \sqrt{\frac{2}{RT}} \varphi\left(\frac{P_1}{p_0}\right). \tag{1}$$
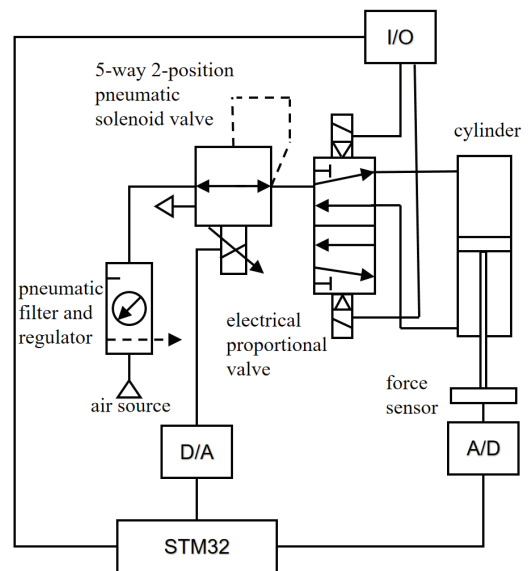
Fig. 2. Schematic diagram of the end-effector

$$\varphi\left(\frac{P_1}{p_0}\right) = \begin{cases} \left(\frac{2}{k+1}\right)^{1/(k-1)} \sqrt{\frac{k}{k+1}}, & 0 \le \frac{P_1}{P_0} \le C_t \\ \sqrt{\frac{k}{k-1}\left(\left(\frac{P_1}{P_0}\right)^{2/k} - \left(\frac{P_1}{P_0}\right)^{(k+1)/k}\right)}, & C_t \le \frac{P_1}{P_0} \le 1 \end{cases}, \tag{2}$$

$$C_t = \left(\frac{2}{k+1}\right)^{\frac{k}{k-1}}, \tag{3}$$

q is the mass flow rates into the electrical proportional valve; C_q is the flow coefficient; A_q is the orifice open area of the electrical proportional valve; w is the electrical proportional valve opening area gradient; x_v is the electrical proportional valve spool displacement; p_0 is the electrical proportional valve inlet pressure; p_1 is the electrical proportional valve outlet pressure; R is the universal gas constant; T is the absolute temperature; C_t is the critical pressure ratio; k is the isentropic constant; and k is taken to be 1.4, [27].

Electrical proportional valves are electrically driven spools to achieve continuous control of the flow rate. When the supply port pressure and the temperature inside the valve is unchanged, the electrical proportional valve spool displacement and the input voltage can be equated into a proportional link, the following formula is derived:

$$x_v = e_v u_v, \tag{4}$$

where e_v is the electrical proportional valve flow gain and u_v is the control voltage.

2.2.2 Modelling of the Cylinder

The gas flows out of the electric proportional valve and into the cylinder, according to the law of conservation of energy:

$$\begin{cases} q_{ma} = \dfrac{dm_a}{dt} = \dfrac{d(\rho V_a)}{dt}, \\ q_{mb} = \dfrac{dm_b}{dt} = \dfrac{d(\rho V_b)}{dt}, \end{cases} \tag{5}$$

where q_{ma} is the inflow cylinder gas mass flow rate; q_{mb} is the outflow cylinder gas mass flow rate; m_a is the inflow cylinder gas mass; m_b is the outflow cylinder gas mass; V_a is the rod end volume; and V_b is the rear end volume.

Assume that the gas is an ideal gas and satisfies the formula:

$$P_d = \rho R T, \tag{6}$$

where P_d is the gas pressure in the cylinder; ρ is the gas density in the cylinder, and T is the gas temperature in the cylinder.

Assuming that the spool pushes the cylinder downward, the cylinder displacement is x; and the cylinder stroke is l. From Eq. (6), it follows that:

$$\begin{cases} q_{ma} = P_a \dot{x}\dfrac{A_a}{RT} + \dot{P}_a\dfrac{(l/2+x)}{kRT} \\ q_{mb} = -P_b \dot{x}\dfrac{A_b}{RT} + \dot{P}_b\dfrac{(l/2-x)}{kRT}, \end{cases} \tag{7}$$

where k is the adiabatic index, $k=1.4$; A_a is the contact area of the without rod chamber of the cylinder; and A_b is the contact area of the with rod chamber.

2.2.3 Modelling of the Pneumatic Hose

The gas flow from the electric proportional valve passes through a pneumatic hose of length L and enters the chamber of the cylinder without a rod. The gas flow in the tube is equal to the outlet flow of the proportional valve. According to Anderson's theory, Eq. (8) is derived:

$$q = K_1(P_1 - P_2), \tag{8}$$

$$K_1 = \frac{\rho_v D^2}{32\mu}\frac{A}{L}, \tag{9}$$

where q is the gas mass flow rate of the g pneumatic hose; P_1 is the inlet pressure of the pneumatic hose; P_2 is the outlet pressure of the pneumatic hose; ρ_v is the average density of the system gas; D is the

inner diameter of the gas pipe; μ is the viscosity coefficient of the system gas; and A is the cross-sectional area of the pneumatic hose. From Eqs. (1), (7) and (8), it follows that:

$$\begin{cases} \dot{P}_a = \dfrac{-kP_a \dot{x}A_a}{(l/2+x)} + \dfrac{kRTC_qWx_vP_0H_0\varphi(P_a/(P_1-q/K_1))}{(l/2+x)} \\ \dot{P}_b = \dfrac{kP_b \dot{x}A_b}{(l/2-x)} - \dfrac{kRTC_qWx_vP_0H_0\varphi(P_b/(P_1-q/K_1))}{(l/2-x)}. \end{cases} \tag{10}$$

2.2.4 Modelling of the Force Sensor

The force sensor belongs to the resistive type sensors, and is considered as an equivalent proportional element, from which Eq. (11) is derived:

$$u = K_u F, \tag{11}$$

u is the output voltage; K_u is the voltage gain; and F is the detection pressure.

Since the force transducer has a good linear relationship, it is linearized and the following formula is derived.

$$F = K_m x, \tag{12}$$

K_m is the pressure gain; x is the output signal.

2.2.5 End-effector Force Balance Analysis

The end-effector force sketch is shown in Fig. 3. According to Newton's second theorem, without considering the effect of cylinder friction, and the cylinder piston force, the balance equation is:

$$P_a A_a - P_b A_b = m\ddot{s} + B\dot{s} + F_n, \tag{13}$$

where A_a is the contact area of the rear end of the pneumatic cylinder and A_b is the contact area of the rod end; P_a is the rear end of the cylinder pressure; P_b is the rod end pressure; m is the cylinder piston and load total mass; $\dot{s}$ is the cylinder piston moving speed; $\ddot{s}$ is the cylinder piston moving acceleration; B is the damping coefficient; F_n is the end-effector grinding contact force.
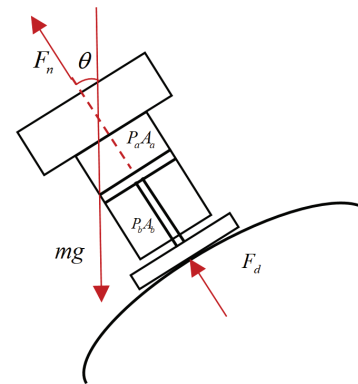
Fig. 3. Schematic diagram of the end-effector

When the robot performs grinding work, the spatial attitude changes in real time, and the grinding contact force collected by the force sensor has a large error due to the gravity effect of the end-effector. Therefore, it is necessary to design a gravity compensator to eliminate the gravity influence of the end-effector along the force control direction. The force analysis of the end-effector is shown in Fig. 3, where mg is the gravity of the end-effector, F_d is the force measured by the force sensor, and θ is the angle between the gravity and the force measured by the force sensor. Therefore, the actual output force F_n is:

$$F_n = F_d + mg\cos\theta. \tag{14}$$

When the end-effector is in contact with the blade, the axial force is F_n, the resulting displacement is y, and the equivalent stiffness model coefficient is K_e, the following formula is derived:

$$F_n = K_e y. \tag{15}$$

From Eqs. (13-15), it follows that:

$$P_a A_a - P_b A_b = M\ddot{s} + B\dot{s} + K_e y. \tag{16}$$

To facilitate the analysis and design of the controller, from Eqs. (1-16). If we define the state variable $F = x_1$, $\dot{F} = x_2$, $P_a = x_3$, $P_b = x_4$, $x_v = u$, then the system state space equation set is obtained as:

$$\begin{cases} \dot{x}_1 = x_2 \\ \dot{x}_2 = K_n(A_a x_3 - A_b x_4 - B\dot{s} - K_e y) \\ \dot{x}_3 = \dfrac{-kP_a \dot{x} A_a}{(l/2+x)} + \dfrac{kRTC_q Wx_v P_0 H_0 \varphi(P_a/(P_1 - q/K_1))}{(l/2+x)}, \\ \dot{x}_4 = \dfrac{kP_b \dot{x} A_b}{(l/2-x)} - \dfrac{kRTC_q Wx_v P_0 H_0 \varphi(P_b/(P_1 - q/K_1))}{(l/2-x)} \\ y = x_1 \end{cases} \tag{17}$$

3 IMPROVED ADRC CONTROLLER DESIGN

If we take Eq. (17), the end-effector model described as a 3rd order system, then according to the method of active disturbance rejection controller order selection [28], the relative order of the system is taken to be 2, the 3rd order is regarded as a perturbation, and the second-order nonlinear active disturbance rejection controller is designed and Eq. (17) is rewritten as:

$$\ddot{F} = \underbrace{f\left(\dot{F}, P_a, P_b, w, t\right)}_{w(.)} + bu, \tag{18}$$

where $w(.)$ is a nonlinear function of the "total disturbance" of the end-effector, including the unmodelled portion, higher-order nonlinearities, and control gain estimation errors, and b is the control gain estimate.
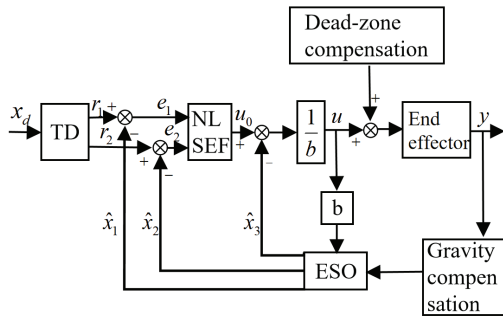
Fig. 4. End-effector controller

The improved ADRC controller consists of a tracking differentiator, a nonlinear state error feedback control law, an extended state observer, gravity compensation, dead-zone compensation of five parts, as shown in Fig. 4.

3.1 The Tracking Differentiator

The tracking differentiator is used to smooth the desired force and reduce the overshoot caused by excessive error. According to Han [28], the tracking differentiator (TD) is as follows:

$$\begin{cases} \dot{r}_1 = r_2 \\ \dot{r}_2 = fhan\left(r_1 - x_d, r_2, R, h\right) \end{cases}, \tag{19}$$

where x_d is the desired force loading input signal; r_1 is the tracked value of the input signal x_d, and r_2 is the differential of the input signal x_d. The $fhan(z_1, z_2, R, h)$ function is as follows:

$$\begin{cases} d = Rh^2, a_0 = hz_2, y = z_1 + a_0 \\ a_1 = \sqrt{d(d + 8|y|)} \\ a_2 = a_0 + sign(y)(a_1 - d)/2 \\ s_y = [sign(y + d) - sign(y - d)]/2 \\ a = (a_0 + y - a_2)s_y + a_2 \\ s_a = [sign(a + d) - sign(a - d)]/2 \\ fhan = -R[a/d - sign(a)]s_a - r_0 sign(a) \end{cases}, \tag{20}$$

where z_1 and z_2 are the state quantities of the $fhan$; R and h are the control parameters of the $fhan$. R depends on the smoothing processing speed and the system capacity; the larger the value of R, the stronger the ability to track the input signal. The value of r is usually not infinite, and so it needs to be adjusted according to the actual situation. Additionally, h is the step size.

3.2 Extended State Observer

The extended state observer is used to estimate the total perturbation of the system in real time and is the central aspect of the active disturbance rejection control algorithm. The extended state observer (ESO) derives a state estimate $\hat{x}_1$, $\hat{x}_2$ of the desired signal and an estimate of the total disturbance $\hat{x}_3$ from the total disturbance $w(.)$, output signals y and $\dot{y}$. The ESO design is as follows:

$$\begin{cases} e_0 = \hat{x}_1 - y \\ \dot{\hat{x}}_1 = \hat{x}_2 + \beta_1 e_0 \\ \dot{\hat{x}}_2 = \hat{x}_3 - \beta_2 fal(e_0, \alpha_1, h) + bu \\ \dot{\hat{x}}_3 = -\beta_3 fal(e_0, \alpha_2, h) \end{cases}, \tag{21}$$

β_1, β_2, β_3, α_1, α_2, h is the parameter of ESO and the $fal()$ expression is as follows:

$$fal(e_0, \alpha, h) = \begin{cases} e_0/h^{(1-\alpha)}, |e_0| \leq h \\ sign(e_0) \cdot |e_0|^\alpha, |e_0| \geq h \end{cases}, \tag{22}$$

3.3 The Nonlinear State Error Feedback Control Law

The nonlinear state error feedback (NLSEF) is a nonlinear control combination used instead of the linear combination of the conventional PID controller. Combining the observations of ESO with the output of TD, the combination NLSEF is as follows:

$$\begin{cases} e_1 = r_1 - \hat{x}_1 \\ e_2 = r_2 - \hat{x}_2 \\ u_0 = k_p \cdot fal(e_1, \alpha_1, h) + k_d \cdot fal(e_2, \alpha_2, h) \end{cases}, \tag{23}$$

where k_p and k_d are the NLSEF nonlinear combination coefficients, respectively. In order to reduce the model uncertainty and the effect of external perturbations, $\hat{x}_3$ is compensated to the control quantity with the compensation equation:

$$u = \frac{u_0 - \hat{x}_3}{b}. \tag{24}$$

3.4 The Dead-zone Compensator

The dead-zone compensation is an algorithm to make the spool of the electrical proportional valve jump out of the neutral dead-zone quickly and enter the control zone. The dead-zone model parameters

are obtained by experimental identification methods to achieve pre-compensation for a wide range of dead-zones. The dead band compensator is designed as follows:

$$u_f = \begin{cases} u + u_3, 0 < u \\ u + u_4, u \leq 0 \end{cases}, \quad (25)$$

where u_f dead-zone compensation after the control amount; u_3 for the experimentally measured electrical proportional valve inlet minimum operating voltage; u_4 for the experimentally measured electrical proportional valve maximum operating voltage.

4 RESULTS AND DISCUSSION

When repairing offshore wind turbine blades, the external environment is very complex, and at the same time there will be wind and other disturbances in the high-altitude air to increase the difficulty of the whole grinding operation. The robot controls the end position in the sanding process while using the end-effector to correct the end contact force, so as to realize the decomposition of force control and position control in the grinding process. This makes it possible to complete offshore wind turbine blade grinding even when the entire grinding process is disturbed by the external environment. In order to verify the application of the improved ADRC algorithm in the real working environment, an experimental rig was built and simulated offshore wind turbine blade grinding experiments were carried out. The robot model is Elibot ec66 with a working radius of 914 mm and a repeat positioning accuracy of ±0.02 mm. Both algorithms use image processing and vision-guided path-planning-based methods. The test bench is shown in Fig. 5, and the main components and parameters of the experiment are shown in Table 1.
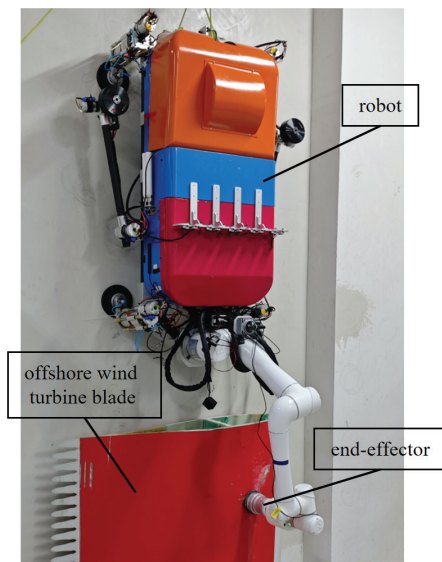
Fig. 5. Laboratory bench

Table 1. Key Components and Parameters

Component	Parameters
Air source	Outlet pressure: 1.0 MPa
F.R.	Set pressure: 0.9 MPa
Electrical proportional valve	Max. pressure: 0.9 MPa; Sensitivity: 0.2 %
Pneumatic cylinder	Stroke: 20 mm
Inclination sensor	Angular range: ±90°, Repeatability: 0.5°
Force sensor	Capacity: 0 N - 100 N; Sensitivity: 0.1 %

4.1 Dead-zone Compensation Experiment

Firstly, it is verified whether the improved ADRC algorithm is able to compensate for the dead-zone effectively. Since the effect of the dead-zone is mainly manifested during commutation, a sinusoidal signal is used as the input signal. In the formula, where the input signal is $F = 60 + 10\sin(1.257t)$, the amplitude is 20 N, and the force tracking curve and force tracking error curve are shown in Fig. 6. As can be seen in Fig. 6, the input signal can be tracked well with the dead-zone compensation algorithm; whereas without the dead zone compensation algorithm there is a hysteresis that leads to a large error. Therefore, this algorithm enables the controller to cross the dead-zone quickly and improves the dynamic performance of the system.
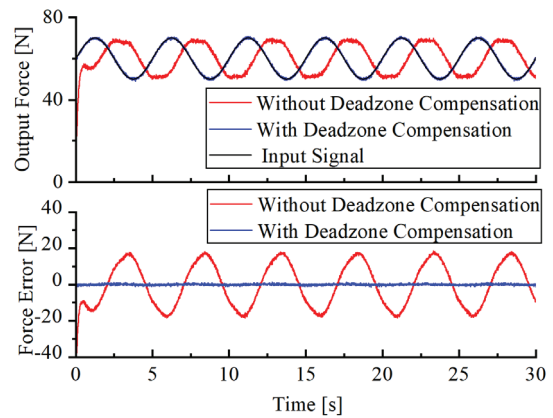
Fig. 6. Dead-zone compensation experiment

4.2 Gravity Compensation Experiment

When the end-effector is tilted, the grinding contact force is varied by the gravity of the device. This experiment, in order to verify the compensation effect of the gravity compensation algorithm, sets the desired force to 60 N, the grinding inclination angle is 0° to 90°, and the output force change curve is shown in Fig. 7. Without the gravity compensation algorithm, the output force error increases with the inclination angle, reaching a maximum of 18.7 N, while with the gravity compensation algorithm, the output force is smooth, and the maximum error is 2.3 N.
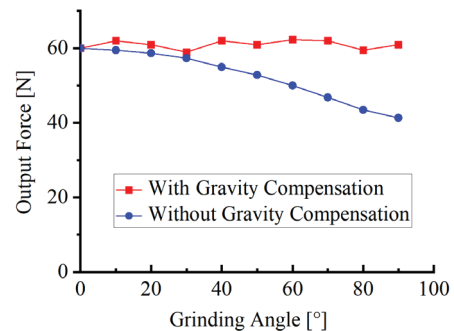
Fig. 7. Gravity compensation experiment

4.3 Constant Force Loading Experiment

The constant force loading experiment can test the transient response performance of the system. The desired force is set to $F = 60$ N according to the real grinding situation. The output force response curve and force tracking error curve are shown in Fig. 8. The system regulation time of the PID control is 1.83 s, with a maximum

overshoot of 10.93 %; while the system regulation time of the improved ADRC control is 0.75 s, with an overshoot close to zero. Therefore, the improved ADRC exhibits better transient response performance than PID control in the control system.
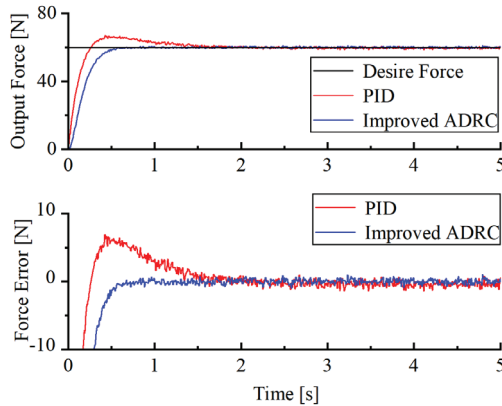
Fig. 8. Constant force loading experiment

4.4 Sinusoidal Force Loading Experiment

Sinusoidal loading experiments can test the dynamic performance of the whole system. The desired force is set to $F = 60 + 10\sin(1.257t)$ in the experiment. The output force response curve and force tracking error curve are shown in Fig. 9. The maximum force tracking error is 5.2 N for PID control and 1.3 N for improved ADRC control. It can be obtained that the improved ADRC algorithm exhibits a smaller force tracking error, a smoother trend, and higher quality of control than PID control.
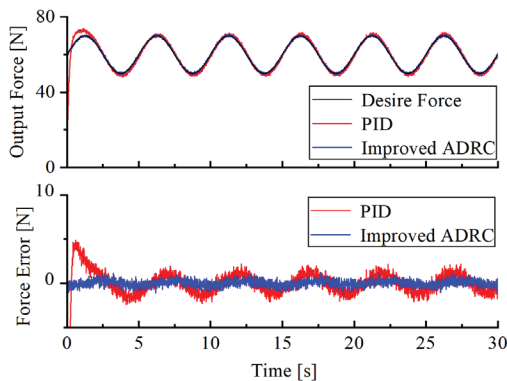
Fig. 9. Sinusoidal force loading experiment

4.5 Triangular Force Loading Experiment

Triangular force loading experiments can test the responsiveness of the system to sudden changes in the input signal. The triangular force signal has a period of 5, an amplitude of 20, and an initial value of 50. The output force response curve and force tracking error curve are shown in Fig. 10. It can be seen in the output force response curve and force tracking error curve that the PID control has some hysteresis when the force signal changes suddenly. Compared to the PID algorithm, the improved ADRC algorithm has a faster response and less force tracking error.

4.6 Trapezoidal Force Loading Experiment

Trapezoidal force loading can further test the fast performance and sudden change response performance of the controller, and the output force response curve and force tracking error curve are shown in

Fig. 11. When the direction of the loading signal changes abruptly, the control effect of the improved ADRC algorithm is significantly better than that of the PID algorithm, showing better anti-interference ability and stronger robustness.
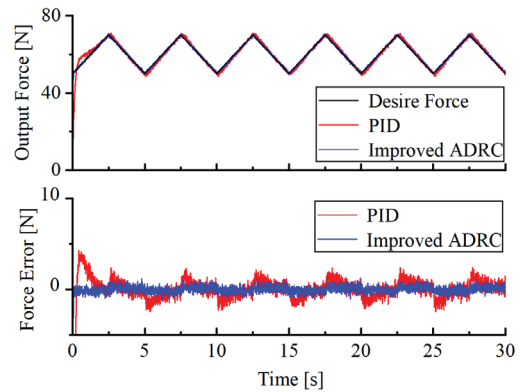
Fig. 10. Triangular force loading experiment
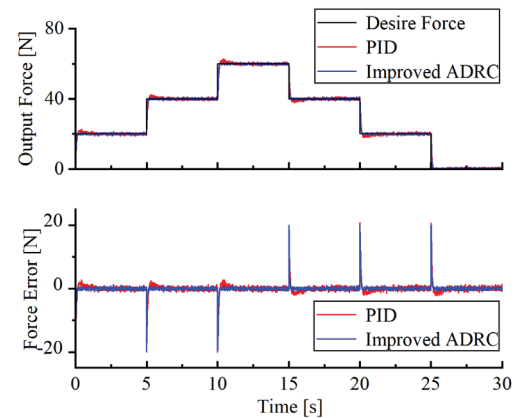
Fig. 11. Trapezoidal force loading experiment

4.7 Constant Force Loading Interference Experiment

In order to further verify the anti-disturbance performance of the improved ADRC algorithm, this experiment simulates the effects of the unknown wind disturbance and the deformation of the suction cup of the robot base at the high altitude. In the constant force loading process of two different algorithms, two different directions of disturbance forces are added. The output force response curves and force tracking error curves are shown in Fig. 12. From Fig. 12, it can be concluded that the improved ADRC algorithm is much stronger than the PID algorithm in the case of adding the same disturbance.
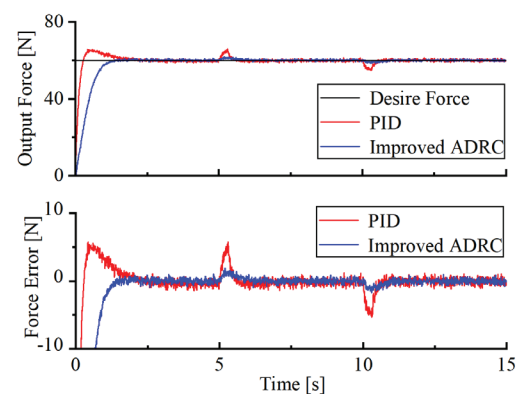
Fig. 12. Constant force loading interference experiment

Table 2. Performance indices

Control method	Performance indices	Constant loading	Sinusoidal loading	Triangular loading	Trapezoidal loading	Constant loading interference
PID	M_e	6.56	4.89	4.29	20.73	5.74
	μ_e	4.27	1.32	0.92	3.05	2.14
ADRC	M_e	0.52	1.24	1.14	20.16	1.89
	μ_e	0.12	0.13	0.13	2.59	0.26

4.8 Constant Force Loading Interference Experiment

In order to better quantitatively compare the two control algorithms, two sets of data, the absolute value of the maximum error M_e and the mean-square value of the error μ_e, are introduced for further illustration:

$$M_e = \max_{i=1,2,\ldots,N}\left\{\left|e(i)\right|\right\}, \tag{26}$$

$$\mu_e = \frac{1}{N}\sum_{i=1}^{N}\left[e(i)\right]^2. \tag{27}$$

The results are shown in Table 2. Comparing the performance indicators from the Table 2, it can be seen that the absolute value of the maximum error and the mean square value of the error of the improved ADRC algorithm in several force loading experiments are smaller than that of the PID control. From this, the improved ADRC algorithm is superior to the PID control algorithm in terms of system regulation time, dynamic response ability, and anti-interference ability, which prove the effectiveness of the algorithm in the control of the contact force of end grinding of a high altitude wind turbine blade grinding robot.

5 CONCLUSIONS

In this paper, an end-effector based on passive flexible control is designed for the problems of unknown wind interference and deformation of suction cups at the robot base when the robot is grinding high-altitude wind turbine blades. The device is fixed at one end of the robot end while the other end fixes the grinding tool, effectively controlling the grinding contact force.

The end-effector adopts a pneumatic control system. Several problems such as electrical proportional valve dead-zone, attitude transformation, and external interference appear. In this paper, by establishing a mathematical model of the control system and analyzing the influence of system parameters and dead-zone characteristics on force control accuracy, an improved third-order ADRC controller with dead-zone compensation and gravity compensation is designed. It not only solves the problems of system lag caused by dead zone and attitude transformation affecting the contact force, but also improves the anti-interference ability of the control system.

Finally, seven sets of experiments are conducted to make a comprehensive comparison of the control algorithms. It can be concluded that the improved ADRC algorithm is more stable, faster, and more accurate than the PID algorithm in terms of the robustness of the control system and the anti-interference ability.

References

[1] Liu, L., Wu, M., Mao, Y., Zheng, L., Xue, M., Bing, L., et al. Offshore Wind Energy Potential in Shandong Sea of China Revealed by ERA5 Reanalysis Data and Remote Sensing. *J Clean Prod* 464 142745 (2024) **DOI:10.1016/j.jclepro.2024.142745**

[2] Sun, Y., Ai, H., Li, Y., Wang, R., Ma, R. Data-driven Large-Scale Spatial Planning Framework For Determining Size And Location Of Offshore Wind Energy Development: A Case Study of China. *Appl Energ* 367 123388 (2024) **DOI:10.1016/j.apenergy.2024.123388**

[3] Yang, W., Kim, K.H., Lee, J. Upcycling of Decommissioned Wind Turbine Blades Through Pyrolysis. *J Clean Prod* 376 134292 (2022) **DOI:10.1016/j.jclepro.2022.134292**

[4] Global Offshore Wind Report 2024. Technical Report, from *https://gwec.net/global-offshore-wind-report-2024/*, accessed on 2024-06-01.

[5] Mishnaevsky Jr, L. Repair of Wind Turbine Blades: Review of Methods and Related Computational Mechanics Problems. *Renew Energ* 140 828-839 (2019) **DOI:10.1016/j.renene.2019.03.113**

[6] Savin, A., Iftimie, N., Steigmann, R., Rosu, D., Dobrescu, G.S., Grum, J.et al. Effective Methods for Structural Health Monitoring of Critical Zones of Scalable Wind Turbine Blades. *Stroj Vestn-J Mech E* 64 680-689 (2018) **DOI:10.5545/sv-jme.2017.5130**

[7] Fang, H., Feng, Y., Wei, X., Xiong, J. Wind Turbine Blade Damage Aerodynamic Profile Analysis and Its Repair Techniques. *Energ Rep* 9 1-10 (2023) **DOI:10.1016/j.egyr.2023.04.041**

[8] Cieslak, C., Shah, A., Clark, B., Childs, P. Wind-Turbine Inspection, Maintenance and Repair Robotic System. *ASME Turbo Expo: Power for Land, Sea, and Air* 87127 (2023) **DOI:10.1115/GT2023-101713**

[9] Sadeghian, R., Sareh, S. Multifunctional Arm for Telerobotic Wind Turbine Blade Repair. *International Conference on Robotics and Automation* 6883-6889 (2021) **DOI:10.1109/ICRA48506.2021.9560968**

[10] Ge J., Deng, Z., Li, W., Li, C. Research Progresses of Robot Grinding and Polishing Force Compliance Controls. *Chin Mech Eng* 32 18 2217-2230 (2021) **DOI:10.3969/j.issn.1004-132X.2021.18.011**

[11] Ke, X., Yu, Y., Li, K., Wang, T., Zhong, B., Wang, et al. Review on Robot-Assisted Polishing: Status and Future Trends. *Robot CIM-Int Manuf* 80 (2023) **DOI:10.1016/j.rcim.2022.102482**

[12] Guo, W., Yu, S., Tian, Y., Zhao, L., Cao, Z., Active Compliance Constant Force Control with Adaptive Variable Impedance for Robotic Grinding. *J Harbin Inst Tech*, 55 54-65 (2023) **DOI:10.11918/202212066**

[13] Lakshminarayanan, S., Kana, S., Mohan, D.M., Manyar, O.M., Then, D., Campolo, D. An Adaptive Framework for Robotic Polishing Based on Impedance Control. *Int J Adv Manuf Technol* 112 401-417 (2021) **DOI:10.1007/s00170-020-06270-1**

[14] Zhang, H., Li, L., Zhao, J., Zhao, J. The Hybrid Force/Position Anti-Disturbance Control Strategy for Robot Abrasive Belt Grinding of Aviation Blade Base on Fuzzy PID Control. *Int J Adv Manuf Technol* 114 3645-3656 (2021) **DOI:10.1007/s00170-021-07122-2**

[15] Zhang, T., WU, S., Cai, C. Constant force control method for robotic disk grinding based on floating platform. *J Shanghai Jiaotong Univ* 54 515-523 (2020) **DOI:10.16183/j.cnki.jsjtu.2020.05.009**

[16] Wei, Y., Xu, Q. Design of a New Passive End-Effector Based on Constant-Force Mechanism for Robotic Polishing. *Robot Comput-Integr Manuf* 74 102278 (2022) **DOI:10.1016/j.rcim.2021.102278**

[17] Zhang, J., Zhao, L., Li, L., Ma, F., Chen, G. Design of passive constant-force end-effector for robotic polishing of optical reflective mirrors. *Chin J Mech Eng* 35 141 (2022) **DOI:10.1186/s10033-022-00811-3**

[18] Chen, F., Zhao, H., Li, D., Chen, L., Tan, C., Ding, H. Contact force control and vibration suppression in robotic polishing with a smart end effector. *Robot Comput Integr Manuf* 57 391-403 (2019) **DOI:10.1016/j.rcim.2018.12.019**

[19] Xu, D., Lu, X., Xu, B. Design and Modeling of a Passive Magnetic Vibration Absorber for Robotic Polishing Process. *J Manuf Process* 95 204-216 (2023) **DOI:10.1016/j.jmapro.2023.03.074**

[20] Li, D., Yang, J., Zhao, H., Ding, H. Contact force plan and control of robotic grinding towards ensuring contour accuracy of curved surfaces. *Int J Mech Sci* 227 107449 (2022) **DOI:10.1016/j.ijmecsci.2022.107449**

[21] Mohammad, A.E.K., Hong, J., Wang, D. Design of a force-controlled end-effector with low-inertia effect for robotic polishing using macro-mini robot approach. *Robot Comp-Integr Manuf* 49 54-65 (2018) **DOI:10.1016/j.rcim.2017.05.011**

[22] Liang, S., Wei, X., Qi, P., Huang, S., Wang, L. Design of active constant output device based on cylinder. *Opt Precis Eng* 26 640-646 (2018). **DOI:10.3788/OPE.20182603.0640** (in Chinese)

[23] Huang, T., Sun, L., Wang, Z., Yu, X., Chen, G. Hybrid force/position control method for robotic polishing based on passive compliance structure. *Robot* 39 776-785, (2017) **DOI:10.13973/j.cnki.robot.2017.0776** (in Chinese)

[24] Genc, M.O. Cargo e-bike Robust Speed Control Using an MPC Battery Thermal Lumped Model Approach. *Stroj vestn-J Mech E* 70 381-391 (2024) **DOI:10.5545/sv-jme.2023.899**

[25] Gao, Z. On the Foundation of Active Disturbance Rejection Control. *Contr Theo Appl* 30 1498-1510 (2013) **DOI:10.7641/CTA.2013.31087** (in Chinese)

[26] Dong, K., Li, J., Lv, M., Li, X., Gu, W., Cheng, G. Active Disturbance Rejection Control Algorithm for the Driven Branch Chain of a Polishing Robot. *Stroj Vestn-J Mech E* 69 509-521 (2023) **DOI:10.5545/sv-jme.2023.680**

[27] Liu, F., Wang, L., Jia, X., Mi, J. Application of Linear/Nonlinear Active Disturbance Rejection Switching Control in Variable Load Pneumatic Loading System. *J Mech Eng* 54 225-232 (2018) **DOI:10.3901/JME.2018.12.225**

[28] Han, J. From PID to Active Disturbance Rejection Control. *IEEE Trans Ind Electron* 56 900-906 (2009) **DOI:10.1109/TIE.2008.2011621**

Data availability The data that underpin the results of this research are available for use by other researchers. Additionally, the corresponding author can provide additional raw data upon reasonable request.

Author contribution Xinrong Liu: supervision, project administration, methodology, writing – review & editing; Hao Li: methodology, formal analysis, validation, writing – original draft; Yu Fang: conceptualization, methodologa, writing – review & editing. Diqing Fan: formal analysis, data curation. All authors have contributed significantly to this work and thoroughly reviewed and approved the final version of the manuscript.

Zasnova in vrednotenje pasivne metode nadzora skladnosti robota za brušenje lopatic vetrnih turbin na morju

Povzetek Roboti, ki popravljajo lopatice vetrnih turbin na morju, so dovzetni za motnje različnih dejavnikov, kot je zunanji veter, zaradi česar lahko robot med postopkom brušenja poškoduje lopatice. Zato mora robot v neugodnem delovnem okolju ohranjati konstantno kontaktno silo brušenja. V tej študiji je bila za reševanje tega problema zasnovana naprava za nadzor konstantne sile, ki temelji na pnevmatskem sistemu. Za nadzor te naprave pa je bil predlagan krmilnik, ki temelji na izboljšanem algoritmu ADRC (Active Disturbance Rejection Control). Na podlagi analize mehanizma naprave za nadzor konstantne sile in glede na relativni red sistema je bil zasnovan ADRC algoritem drugega reda. Krmilnik uporablja sledilni diferencial (TD) za filtriranje vhodnega signala, razširjeni opazovalnik stanja (ESO) za oceno celotne motnje v sistemu in nelinearni zakon povratne kontrole napake stanja (NLSEF) za kompenzacijo. Da bi rešili težave z značilnostmi mrtve cone električnega proporcionalnega ventila, neznanimi motnjami med delovanjem na veliki nadmorski višini, spremembami kota nagiba med brušenjem, so bili v krmilnik vključeni algoritmi za kompenzacijo mrtve cone in kompenzacijo težnosti. Na koncu je bila zgrajena eksperimentalna platforma za izvajanje poskusov v različnih delovnih pogojih. Rezultati poskusov kažejo, da krmilnik v primerjavi s tradicionalnim proporcionalno-integralno-derivativnim (PID) algoritmom izboljša čas regulacije sistema za 59 %, pri čemer je prekoračitev blizu nič. V veliki meri sta se zmanjšali tudi absolutna vrednost največje napake in srednja kvadratna vrednost napake. Posledično ima krmilnik boljšo natančnost krmiljenja sile in zmogljivost dinamičnega sledenja, močno sposobnost zavračanja motenj in prilagodljivost ter zagotavlja teoretično podlago za praktično inženirsko uporabo.

Ključne besede izboljšani aktivni nadzor zavrnitve motenj, gravitacijska kompenzacija, kompenzacija mrtvega območja, lopatica vetrne turbine na morju, pnevmatski obremenilni sistem

Impact of Excitation Frequency and Fill Levels on Fuel Sloshing in Automotive Tanks

Rajamani Rajagounder ✉ – Jayakrishnan Nampoothiri

Department of Production Engineering, PSG College of Technology, India

✉ rajamani.vrr@gmail.com

Abstract   *Fuel sloshing in modern automotive fuel tanks is analyzed in this study to provide a better understanding of fuel system performance. The behaviour of sloshing waves was investigated under varying excitation frequencies and fuel fill levels using both experimental and numerical methods. A sinusoidal motion was applied to the fuel tank along its transverse axis, and the resulting wave profiles were captured using a digital camera setup. Numerical simulations were conducted using the volume of fluid (VOF) model and a user-defined function (UDF) in ANSYS Fluent to predict the sloshing wave profiles. The study reveals distinct wave patterns depending on the excitation frequency. Standing and traveling waves were observed at 0.5 Hz and 0.6 Hz, while multiple traveling waves with wave collisions occurred at 0.7 Hz. Additionally, increasing the fuel fill level (from 25 % to 60 % of tank height) significantly enhanced the damping of sloshing wave oscillations. Regression equations were developed to quantify the relationship between excitation frequency, fill level, and sloshing wave amplitude. These findings may contribute to the design of fuel tanks that mitigate sloshing effects and enhance overall vehicle performance.*

Keywords   *liquid sloshing, fuel tank, finite volume analysis, visualization, wave frequency*

Highlights
- *Visualized free-surface fuel motion using numerical and experimental methods*
- *Identified wave behaviour at 0.7 Hz with strong standing and traveling wave formation*
- *Found increased fill levels enhance damping and accelerate wave decay*
- *Developed regression models linking frequency and fill level to wave amplitude*

1 INTRODUCTION

Fuel sloshing in automotive tanks poses significant challenges, particularly in controlling wave behaviour under varying frequencies and fill levels [1]. Various studies have aimed to understand the dynamic sloshing phenomena and mitigate its effects using different modelling techniques, experimental methods, and tank modifications. One of the foundational approaches to studying sloshing was provided by Faltinsen [2], who developed a nonlinear numerical method for two-dimensional flow, offering crucial insights into the fluid motion inside a tank under excitation. Expanding further on this, Dongming and Pengzhi [3] employed a three-dimensional model to examine sloshing dynamics, illustrating the complexities introduced by additional spatial dimensions.

Recent advancements have focused on combining computational methods with experimental validation to enhance prediction accuracy. The volume of fluid (VOF) method, commonly used in numerical simulations, has been applied effectively to analyse sloshing behaviour under various conditions. Zhao et al. [4] utilized this approach to explore nonlinear sloshing in rectangular tanks under forced excitation, uncovering the development of standing and traveling waves at different frequencies. Similarly, Jin and Lin [5] analysed the viscous effects on sloshing, demonstrating the importance of accounting for fluid properties when modelling dynamic sloshing behaviour. Qiu et al. [6] and Liu et al. [7] used the VOF method to study liquid sloshing, finding that higher fill levels and first-order natural frequency intensify sloshing forces. Elahi et al. [8] and Topçuand Kılıç [9] also developed VOF-based numerical models for sloshing simulation.

Experimental approaches complement numerical methods by validating theoretical predictions. For instance, Rajamani et al. [10] conducted an experimental study to capture free surface wave profiles in a fuel tank subjected to uniform acceleration, and the resulting wave profiles were compared with numerical results. Furthermore, Babar et al. [11] explored the coupled Eulerian-Lagrangian (CEL) method for simulating multiphysics events in automobiles, bridging the gap between computational models and real-world applications.

The incorporation of baffles has emerged as an effective method to dampen sloshing. Frandsen [12] examined sloshing in tanks with an annular baffle, which showed significant suppression of wave amplitude. Similarly, Wang et al. [13] demonstrated that multiple rigid annular baffles in cylindrical tanks reduce sloshing effects by altering the flow dynamics and dissipating energy. Park et al. [14] conducted an experimental study on liquid sloshing in a rectangular tank with both rigid and flexible baffles, detailing the behaviour of free surfaces at different fill levels and excitation frequencies. Wang et al. [15] investigated the impact of different baffle configurations on liquid sloshing in a partially filled cylindrical tank mounted on a truck. The findings indicate that the introduction of baffles enhances the fundamental sloshing frequency and decreases the likelihood of resonance phenomena in tank vehicles. These findings have led to practical applications in automotive fuel tanks, whereby baffles and partitions are used to control the liquid motion and enhance vehicle stability. Moreover, parametric studies have revealed the influence of various factors, such as fill level, excitation frequency, and tank geometry, on sloshing behaviour. Gurusamy et al. [16] explored shallow water tanks' sloshing dynamics, focusing on the hydraulic jumps formed during wave interactions, providing insights into wave-breaking mechanisms under certain frequencies. Sanapala et al. [17] performed numerical simulations on baffled rectangular tanks, highlighting the relationship between baffle height and sloshing suppression.

Despite significant advancements in understanding fuel sloshing dynamics, challenges remain in accurately predicting sloshing

behaviour under varying operating conditions and improving mitigation techniques. Current models often overlook the interplay between multiple factors affecting sloshing, leading to suboptimal designs. Therefore, this study made an attempt on a comprehensive approach that combines experimental validation with numerical simulations to explore the effects of excitation frequency and fill levels on sloshing in automotive fuel tanks. By integrating innovative tank modifications and computational techniques, this research aims to enhance prediction accuracy and provide new insights for optimizing fuel tank designs. The combined use of numerical simulations and experimental methods has significantly advanced the understanding of fuel sloshing in automotive tanks. These studies not only help mitigate the risks associated with sloshing but also contribute to optimizing tank designs for improved vehicle safety and performance.

2 METHODS & MATERIALS

2.1 Numerical Simulation

This study uses the VOF method to simulate liquid sloshing, implemented in ANSYS FLUENT (V16.2). The governing equations for incompressible fluid motion in the tank are described by the continuity equation in Eq. (1) and the momentum equation in Eq. (2),

$$\nabla \cdot V = 0, \tag{1}$$

$$\rho \left(\frac{\partial V}{\partial t} + V \cdot \nabla V \right) = -\nabla P + \rho g + \mu \nabla^2 V. \tag{2}$$

An open channel flow boundary condition is applied, utilizing a first-order upwind scheme for discretizing convective terms. The geometric reconstruction scheme determines the cell values at the liquid-air interface, represented by volume fractions (λ), where '0' indicates air and '1' indicates liquid. The volume fraction equation is expressed as Eq. (3),

$$\frac{\partial \lambda}{\partial t} + \nabla \cdot (\lambda u) = 0. \tag{3}$$

The presence of air or liquid in each cell is calculated using Eq. (4),

$$\sum_{j=1}^{n} \lambda_j = 1, \tag{4}$$

where $n = 2$ for two phases fluid flow problems and λ_j is the volume fraction of jth phase.

The volume fraction equation is solved using explicit time formulation. In a two-phase flow problem, the density (ρ) of liquid in each cell is determined using Eq. (5),

$$\rho = \lambda_2 \rho_2 + (1 - \lambda_2) \rho_1. \tag{5}$$

The stability of the numerical solution is controlled by the time step (Δt) and element size (Δx) which is expressed in terms of Courant number (C) given in Eq. (6),

$$C = u \frac{\Delta t}{\Delta x}. \tag{6}$$

The C value is maintained at less than 1 to control the stability of the numerical solution. Also, to analyze the effects of random vibrations on the fuel tank, sinusoidal motion along the horizontal x-axis is applied, represented by Eq. (7),

$$u = X_0 \omega \cos \omega t. \tag{7}$$

In ANSYS Fluent software, a user defined function (UDF) with the macro DEFINE_CG_MOTION is used to set translation motion at the tank's centre of gravity. The quiescent liquid is assigned zero velocity and ambient pressure at the surface, while gravitational

acceleration is applied along a vertical axis. Implicit body force treatment enhances the solution convergence. Surface tension effects are neglected, and the tank wall is modelled as a rigid structure.

A grid independence study is conducted with three different mesh sizes. The total number of cells 90,561, 110,441, and 156,492 yielding free surface wave amplitudes of 9.43 mm, 10.27 mm, and 10.31 mm, respectively. Based on accuracy, computational time, and memory usage, numerical simulations are performed using 110,441 quadrilateral cells.
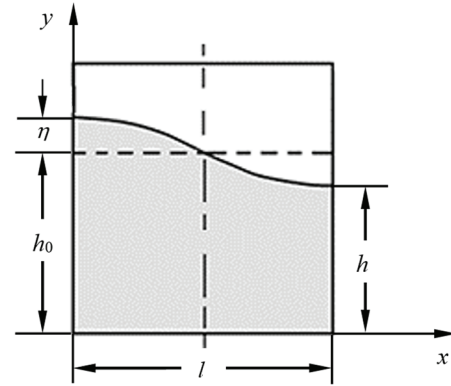
Fig. 1. Sloshing wave in a tank

Fig. 1 shows the sloshing wave in a tank and its amplitude. The natural frequency of the sloshing wave depends upon the fill level (h_0) and tank length (l). The motion of sloshing wave under gravity field can be expressed using Eq. (8) [18],

$$v = \frac{\partial \eta}{\partial t} + u \frac{\partial \eta}{\partial x}, \tag{8}$$

where $\partial \eta / \partial x$ represents the slope of the free surface.

The magnitude of free surface from mean liquid level 'η' can be calculated using linear analytical solution obtained by Faltinsen [2]. When the tank is subjected to sinusoidal motion, the magnitude of the free surface is given in Eq. (9). The amplitude of the sloshing waves obtained from numerical simulations and experimental studies is compared with the result of Eq. (9).

$$\eta = \frac{1}{g} \sum_{n=0}^{\infty} \sin \left\{ \frac{(2n+1)\pi}{l} x \right\} \cosh \left\{ \frac{(2n+1)\pi}{l} h_0 \right\}$$
$$\cdot \left[-A_n \omega_n \sin \omega_n t - C_n \omega \sin \omega t \right] - \frac{1}{g} A \omega x \sin \omega t. \tag{9}$$

where, $n = 0, 1, 2, 3, \ldots$.

$$\omega_n^2 = g \frac{(2n+1)\pi}{2l} \tan h \left\{ \frac{(2n+1)\pi}{2l} h_0 \right\},$$

$$C_n = \frac{\omega K_n}{\omega_n^2 - \omega^2}, \quad A_n = -C_n - \frac{K_n}{\omega}, \text{ and}$$

$$K_n = \frac{\omega A}{\cosh \left\{ \frac{(2n+1)\pi}{l} h_0 \right\}} \frac{4}{l} \left[\frac{l}{(2n+1)\pi} \right]^2 (-1)^n.$$

The fundamental frequency (f_n) of the sloshing waves in a partially filled tank is given in Eq. (10),

$$f_n = \frac{1}{2\pi} \sqrt{\frac{g\pi}{l} \tanh \left(\frac{\pi h_0}{l} \right)}. \tag{10}$$

With g = 9.81 m/s², tank length of 370 mm and fill level of 70 mm, the fundamental frequency of the wave is 1.06 Hz. At this

frequency, violent sloshing will occur and the sloshing wave motion becomes highly turbulent. To avoid this, the tank is excited below the first natural frequency of the sloshing wave.

2.2 Experimental Studies

The experimental setup consists of a reciprocating table with a slider-crank mechanism, a direct current (DC) motor, a transparent composite fuel tank, a speed control unit, and a digital camera, as illustrated in Fig. 2a. The computer aided design (CAD) model of the bottom portion of the tank is shown in Fig. 2b, while the spatial dimensions of the tank are detailed in Fig. 2c. Sinusoidal motion is applied using a slider crank with a crank radius of 25 mm, and the frequency is adjusted by varying the motor speed.

A transparent fuel tank is fabricated and the front portion of the tank is covered with an acrylic sheet for better visibility of the sloshing waves. Water mixed with a colouring agent serves as the working liquid. A Redlake's Motion Pro™ CMOS PCI camera with a maximum shutter speed of 10,000 fps (frames per seconds) records the sloshing waves at 60 fps. Captured images are converted to grayscale, and edge detection is employed to identify the liquid-air interface.

When using gasoline for experiments, the fuel tank must be sealed to prevent fuel vapor leakage. Therefore, water is utilized in this study. Kinematic and dynamic similarities in free surface flow are maintained using similitude relations based on Reynolds number (Re) and Froude number (Fr), as proposed by Abramson and Ransleben [19].
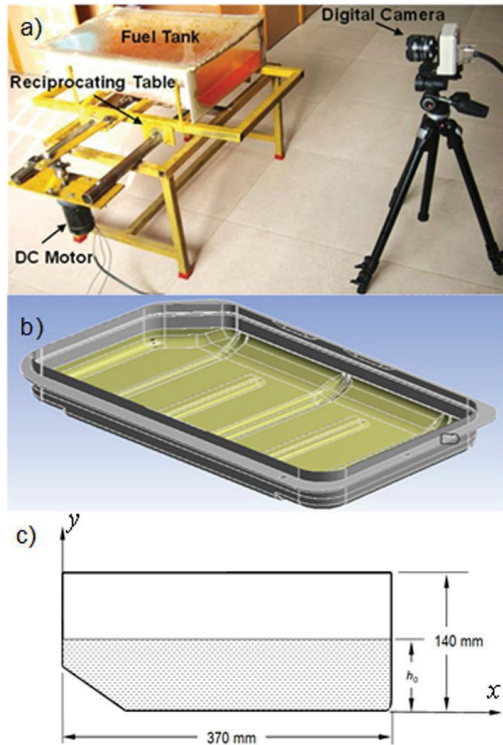
Fig. 2. a) Experimental setup, b) CAD model of a fuel tank, and c) spatial dimensions of a fuel tank

The similitude relation for free surface wave problem is given in Eq. (11)

$$\frac{Ft^2}{\rho l^4} = \phi\left(\frac{at^2}{l}, \frac{h}{l}, \frac{X_0}{l}, \frac{\rho l^2}{\mu t}\right). \tag{11}$$

From Eq. (11), the non-dimensional number for the amplitude of the sloshing wave (H^*) and time (T^*) can be expressed as Eqs. (12) and (13)

$$H^* = \frac{h}{l}, \tag{12}$$

$$T^* = t\sqrt{\frac{a}{l}} \quad \text{(or)} \quad T^* = \omega_n \cdot t. \tag{13}$$

In this study, the results obtained from numerical simulations and experimental studies are presented using the non-dimensional numbers H^* and T^*.

3 RESULTS AND DISCUSSION

The free surface motion of liquid in an automotive fuel tank is analysed for different excitation frequencies such as 0.5 Hz, 0.6 Hz and 0.7 Hz and fill levels (h_0/H) of 0.25, 0.33, 0.5 and 0.6. The formation of sloshing waves and the amplitude of the waves are predicted numerically and compared with the experimental results.

3.1 The Effect of Excitation Frequency on Sloshing Wave Motion

The formation of sloshing waves in a partially filled container depends on factors such as tank shape, liquid level, fluid properties, and excitation parameters [20]. This study investigates sloshing wave behaviour at various oscillation frequencies, specifically at 0.5 Hz, 0.6 Hz, and 0.7 Hz, comparing numerical results with experimental findings in a tank filled to 50 % of its height. Fig. 3a shows the initial position of the free surface of a liquid. At 0.5 Hz, Fig. 3 shows the evolution of sloshing waves, starting with a standing wave that transitions to a traveling wave (Figs. 3b and c), with numerical simulations closely aligning with experimental results (Figs. 3d to f). At 0.6 Hz, the initial standing wave (Figs. 4a and b) evolves into a traveling wave (Figs. 4c), with noticeable differences between numerical and experimental wave patterns emerging after 1.6 seconds (Figs. 4c and f), indicating a phase lag in oscillation magnitude (Fig. 6b).

At 0.7 Hz, Fig. 5 depicts the formation of a standing wave, which subsequently transforms into multiple traveling waves (Figs. 5a and b). The occurrence of two traveling waves colliding results in a superimposed wave (Figs. 5c and e), characteristic of bore wave patterns. These patterns are evident in the corresponding experimental results shown in Figs. 5g to h. The comparative analysis across frequencies highlights the complexities of wave dynamics in sloshing scenarios, emphasizing the relevance of numerical simulations in predicting wave behaviour.

The findings provide insights into sloshing wave dynamics across different oscillation frequencies. The transition from standing to traveling waves highlights the impact of frequency on wave propagation, with higher frequencies facilitating more dynamic interactions, such as collisions and superimpositions. The phase lag observed at 0.6 Hz indicates potential discrepancies between numerical simulations and experimental results, likely due to simplified model assumptions and the neglect of surface tension effects, which can significantly influence real-world wave behaviour. Nevertheless, the alignment of numerical and experimental results at lower frequencies suggests that the VOF approach effectively captures fundamental sloshing dynamics, establishing its utility in predicting sloshing behaviour in fuel tanks.

Fig. 6a compares the temporal evlolution of the non-dimensional amplitude of the free surface of liquid between numerical simulations and experimental studies, when the tank undergoes sinusoidal motion at 0.5 Hz. At this frequency, the maximum non-dimensional
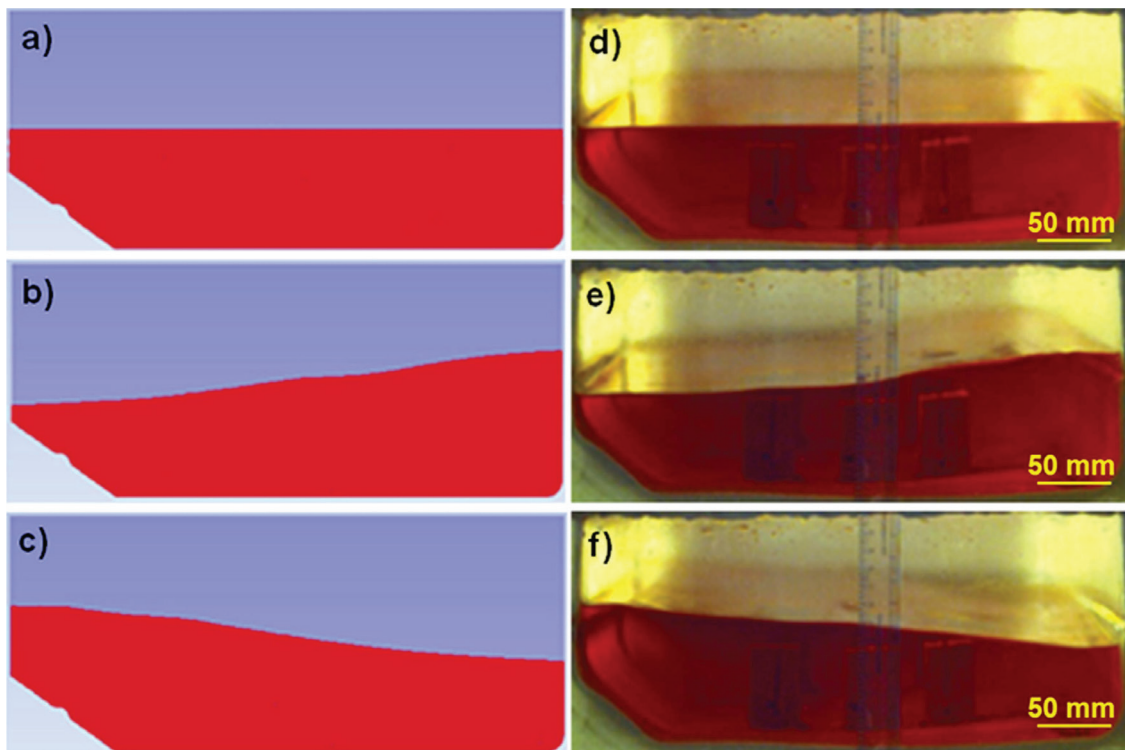
Fig. 3. Sloshing wave profiles at 0.5 Hz: numerical results; a) water level at t = 0 s, b) standing wave at t = 0.8 s, c) standing wave at t = 1.5 s; and experimental results: d) water level at t = 0 s, e) standing wave at t = 0.8 s, f) standing wave at t = 1.5 s
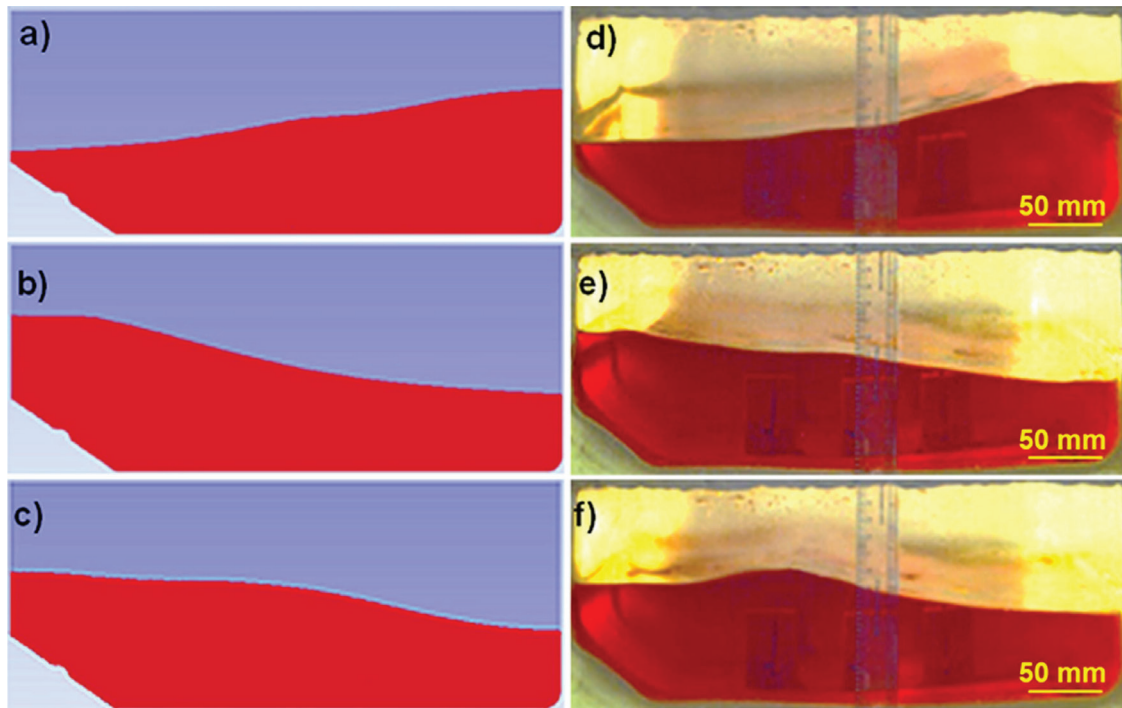
Fig. 4. Sloshing wave profiles at 0.6 Hz: numerical results; a) standing wave at t = 0.8 s, b) standing wave at t = 1.4 s, c) travelling wave at t = 1.6 s; and experimental results: d) standing wave at t = 0.8 s, e) standing wave at t = 1.4 s, and f) travelling wave at t = 1.6 s

amplitude of the sloshing wave (H^*) is 0.246 as showed by simulations and 0.233 determined from experiments, showing good agreement. However, the experimental results exhibit secondary wave crest-troughs that are absent in the numerical model.

Similarly, Fig. 6b presents the comparison at an oscillatory frequency of 0.6 Hz. The simulated maximum H^* values are 0.250,

while experimental value reach 0.246. Initially, the sloshing wave amplitudes align well, but subsequent cycles reveal additional crest-troughs in the experimental data, which are not predicted by the numerical simulations.

Fig. 6c illustrates the temporal evolution of H^* at 0.7 Hz. Here, the simulated maximum H^* values are 0.352 and 0.364 based on
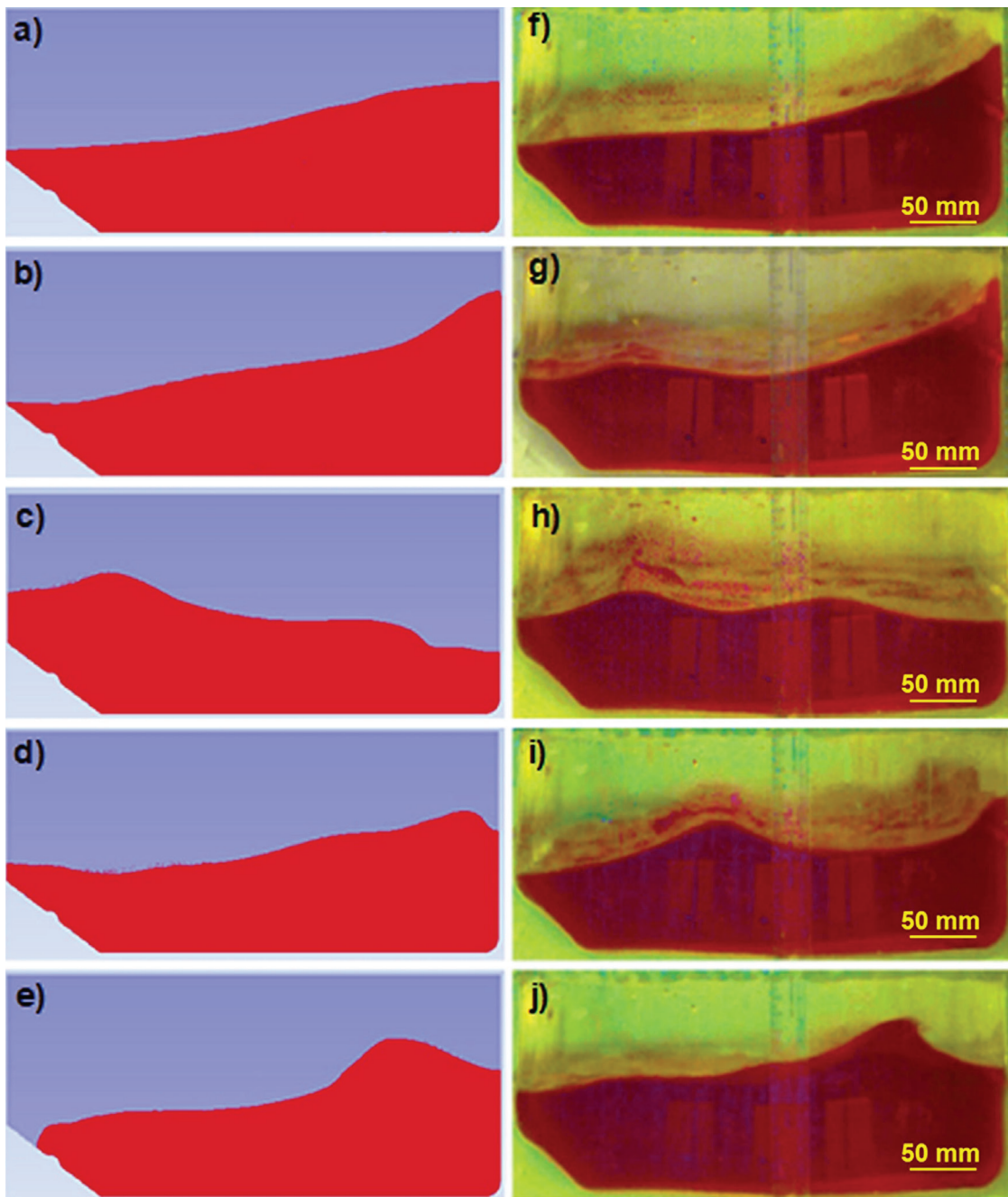
Fig. 5. Sloshing wave profiles at 0.7 Hz: numerical results; a) standing wave at t = 0.7 s, and traveling waves at b) t = 1.9 s, c) t = 2.5 s, d) t = 3.2 s, e) t = 3.6 s; and experimental results: f) standing wave at t = 0.7 s and traveling waves at g) t = 1.9 s, h) t = 2.5 s, i) t = 3.2 s, j) t = 3.6 s

experiments. A significant deviation in sloshing wave motion arises in the numerical results due to the formation and interaction of multiple traveling waves.

The maximum amplitude of sloshing waves (H^*) from numerical simulations and experimental studies is validated against the analytical solution provided by Faltinsen [2]. Fig. 7 depicts the relationship between the maximum non-dimensional amplitude (H^*) and the frequency ratio (ω/ω_n), showing an increase in amplitude with higher excitation frequencies. Regression equations derived from standard curve fitting techniques further illustrate this relationship, as represented in Fig. 7.

At 0.5 Hz and 0.6 Hz, the numerical and experimental results align closely with the analytical solution. However, at 0.7 Hz,

notable deviations between numerical and experimental findings are observed, highlighting limitations in the numerical model at higher frequencies. As the tank motion frequency approaches the natural frequency of the sloshing wave, the liquid's free surface experiences violent sloshing. Standing waves transition into traveling waves, leading to wave collisions that create turbulence. This turbulence results in deviations between the amplitudes of sloshing waves obtained from numerical and experimental analyzes compared to the analytical model.

3.2 The Effect of Fill Level on Amplitude of Sloshing Wave

The effect of fill levels on the amplitude of sloshing waves is analyzed using sinusoidal motion applied to the tank, as governed by

Eq. (7). An excitation amplitude of 25 mm and a frequency of 0.5 Hz are applied. The analysis considers various liquid levels: 25 %, 33 %, 50 %, and 60 % of the tank height. As the liquid level increases, the mass of the liquid absorbing the disturbances also increases, resulting in an increased fundamental frequency of the sloshing waves and a decrease in wave amplitude.
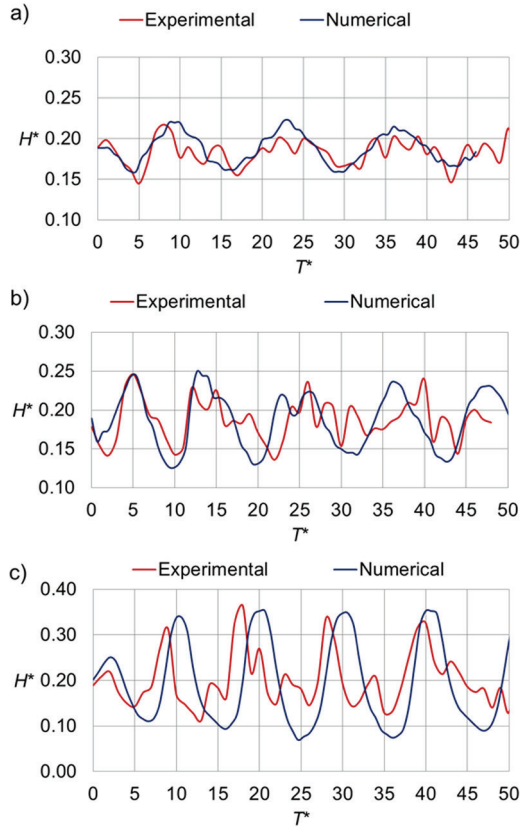
Fig. 6. Non-dimensional amplitude of sloshing wave for:
a) f = 0.5 Hz, b) f = 0.6 Hz, and c) f = 0.7 Hz
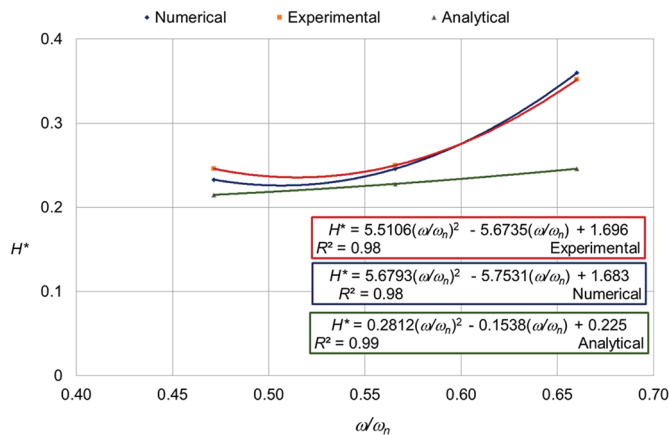
Fig. 7. Maximum amplitude of the sloshing wave versus frequency ratio

Fig. 8 compares the amplitude of sloshing wave motion at different liquid levels, highlighting changes in the wavelength of free surface oscillations as the liquid level increases. Fig. 9 illustrates the relationship between the non-dimensional amplitude of the sloshing wave (η/l) and the liquid level ratio (h_0/H). The study shows that the magnitude of the sloshing wave decreases with higher liquid levels. At a fill level of 50 %, experimental results deviate by a maximum of 18 % from numerical simulations. The formation of multiple

waves and turbulence in the liquid flow contributes to variations in numerical simulation results. A regression equation is formulated to estimate the amplitude of the sloshing wave at specified fill levels.
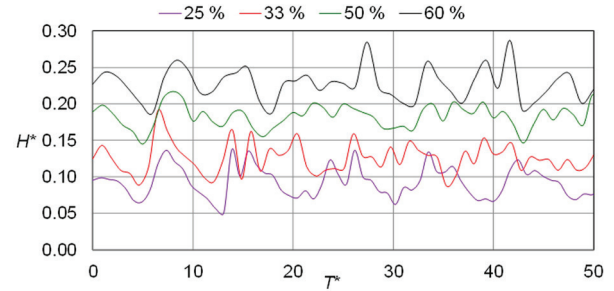
Fig. 8. Amplitude of the sloshing wave motion at the different fill levels

3.3 The Effect of Fill Level on the Damping of Sloshing Wave Oscillations

The damping factor of a sloshing wave in a closed container is influenced by the liquid's viscosity, tank size, and fill level.

This study examines the effect of fill level on the damping of free surface wave oscillations by applying an acceleration of 1.6 m/s² to the tank for 2 seconds, after which the tank is free from external excitation. The sloshing wave then oscillates under free vibration, and the decay rate of wave oscillations is recorded for fill levels of 25 %, 33 %, 50 %, and 60 % of the tank height. The amplitudes of the sloshing waves for these fill levels are presented in Fig. 10a.

The hydrodynamic damping of the free surface wave is calculated using the logarithmic decrement method adopted from Ibrahim [21]. The logarithmic decrement (δ) is determined using Eq. (14).

$$\delta = \frac{1}{n}\ln\left[\frac{x_r}{x_{n+r}}\right], \tag{14}$$

where x_r is the amplitude of the sloshing wave in any reference cycle and x_{n+r} is the amplitude of the sloshing wave after completing 'n' number of cycles.
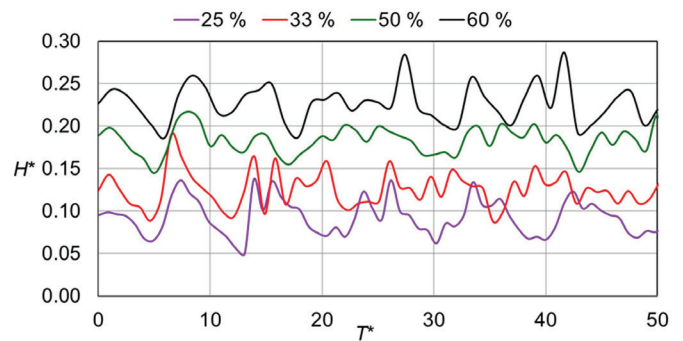
Fig. 9. Maximum amplitude of the sloshing wave at various fill levels

Fig. 10b illustrates the effect of fill level on the hydrodynamic damping of a sloshing wave. It is observed that damping increases with higher fill levels due to the increased liquid mass, which absorbs the kinetic energy of the sloshing waves. A regression equation is formulated to represent the relationship between the liquid fill level and changes in damping, minimizing sloshing effects.

The sloshing behaviour of fuel is analyzed by applying excitation motion along the transverse axis of the tank. Future work could extend this research by incorporating violent sloshing and combined excitation along both the longitudinal and transverse axes of the fuel tank. This regression equation can be used to predict the damping of

sloshing wave oscillations at fill levels within the range adopted in this study.

a)

b)

$$\delta = 0.3585(h_0/H)^2 - 0.1412(h_0/H) + 0.0316; \; R^2 = 0.9864$$
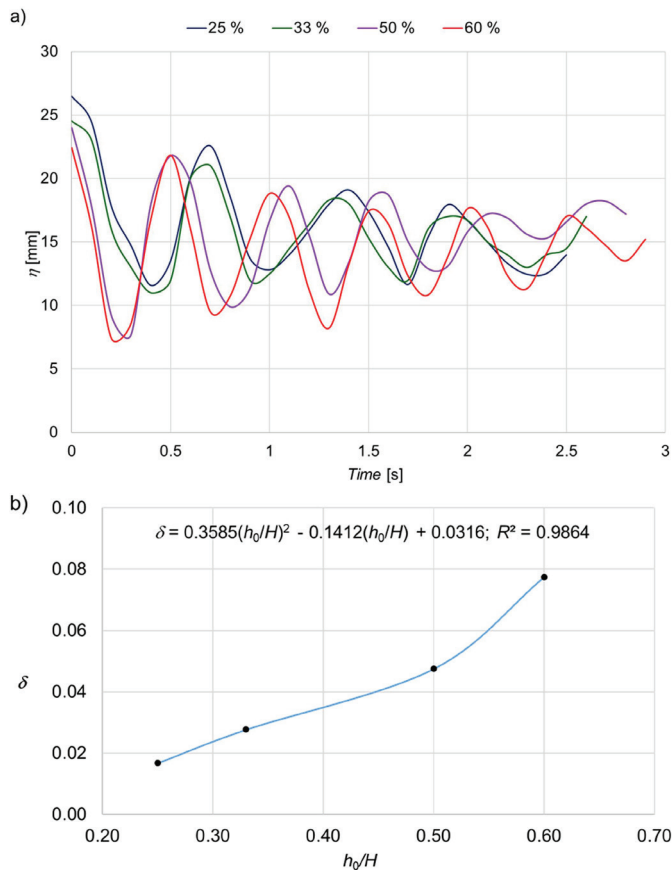
Fig. 10. a) Decay of the amplitude of the sloshing wave under free vibration, and b) damping of the sloshing wave oscillations

4 CONCLUSIONS

This study analyzes liquid sloshing in a fuel tank at various oscillation frequencies and fill levels through numerical simulations and experimental studies using the VOF approach. The key findings are as follows:

The applied oscillation frequency significantly affects the formation of sloshing waves. At frequencies of 0.5 Hz and 0.6 Hz, a standing wave forms and subsequently transitions into a traveling wave. At 0.7 Hz, the standing wave evolves into multiple traveling waves, leading to wave collisions that create turbulence in the liquid motion.

The effect of fill levels on the amplitude of sloshing waves is examined with tanks filled to 25 %, 33 %, 50 %, and 60 % of their height. As the fill level increases, the logarithmic decrement also increases, causing the oscillation of the free surface wave to decay more rapidly.

Regression equations are developed to represent the effects of tank motion frequency and fill levels on sloshing wave amplitude.

This study provides valuable insights for automotive engineers to visualize and understand free surface wave behaviour, aiding in the design of fuel tanks that minimize sloshing effects. Future research can expand on this work by exploring violent sloshing and combined excitations along both the longitudinal and transverse axes of the fuel tank.

Nomenclature

A velocity of the tank, [m s^{-1}]
a acceleration of the tank, [m s^{-2}]
C courant number, [-]
F force exerted by the liquid on tank wall, [N]
F_r Froude number, [-]
f_n natural frequency, [Hz]
g acceleration due to gravity, [m s^{-2}]
H tank height, [m]
H^* non-dimensional free surface elevation, [-]
h_0 fill level, [m]
h amplitude of free surface oscillations, [m]
l tank length, [m]
P fluid pressure, [N m^{-2}]
Re Reynolds number, [-]
T^* non dimensional number derived from time t [-]
t time, [s]
u velocity component along the x axis, [m s^{-1}]
V velocity of fluid, [m s^{-1}]
v velocity component along the y axis, [m s^{-1}]
X_0 displacement of the tank, [m]
x distance from origin, [m]
Δt time step, [s]
Δx grid length, [m]
λ volume fraction, [-]
η elevation of free surface from mean liquid level, [m]
μ dynamic viscosity of the fluid, [N s m^{-2}]
ρ density of the fluid, [kg m^{-3}]
ω excitation frequency, [rad s^{-1}]
ω_n natural angular frequency, [rad s^{-1}]

References

[1]   aus der Wiesche, S. Computational slosh dynamics: theory and industrial application. *Comput Mech* 30 374-387 (2003) **DOI:10.1007/s00466-003-0413-8**

[2]   Faltinsen, O.M. A numerical nonlinear method of sloshing in tanks with two-dimensional flow. *J Ship Res* 22 193-202 (1978) **DOI:10.5957/jsr.1978.22.3.193**

[3]   Liu, D., Lin, P. A numerical study of three-dimensional liquid sloshing in tanks. *J Comput Phys* 227 3921-3939 (2008) **DOI:10.1016/j.jcp.2007.12.006**

[4]   Zhao, D., Hu, Z., Chen, G., Lim, S., Wang, S. Nonlinear sloshing in rectangular tanks under forced excitation. *Int J Nav Arch Ocean* 10 545-565 (2018) **DOI:10.1016/j.ijnaoe.2017.10.005**

[5]   Jin, X., Lin, P. Viscous effects on liquid sloshing under external excitations. *Ocean Eng* 171 695-707 (2019) **DOI:10.1016/j.oceaneng.2018.10.024**

[6]   Qiu, Y., Bai, M., Liu, Y., Lei, G., Liu, Z. Effect of liquid filling level on sloshing hydrodynamic characteristic under the first natural frequency. *J Energy Storage* 55 105452 (2022) **DOI:10.1016/j.est.2022.105452**

[7]   Liu, Z., Yuan, K., Liu, Y., Andersson, M., Li, Y. Fluid sloshing hydrodynamics in a cryogenic fuel storage tank under different order natural frequencies. *J Energy Storage* 52 104830 (2022) **DOI:10.1016/j.est.2022.104830**

[8]   Elahi, R., Passandideh-Fard, M., Javanshir, A. Simulation of liquid sloshing in 2D containers using the volume of fluid method. *Ocean Eng* 96 226-244 (2015) **DOI:10.1016/j.oceaneng.2014.12.022**

[9]   Topçu, E.E., Kılıç, E. A numerical investigation of sloshing in a 3D prismatic tank with various baffle types, filling rates, input amplitudes and liquid materials. *Appl Sci* 13 2474 (2023) **DOI:10.3390/app13042474**

[10]   Rajamani, R., Guru Vignesh M., Prakasan K., A study of liquid sloshing in an automotive fuel tank under uniform acceleration. *Eng J* 20 71-85 (2016) **DOI:10.4186/ej.2016.20.1.71**

[11]   Babar, R.T., Pakalapati, V., Katkar, V. Application of CEL method for simulation of multiphysics events in automobiles. *SAE J Mater Manuf* 4 969-979 (2011) **DOI:10.4271/2011-01-0793**

[12]   Frandsen, J.B. Sloshing motions in excited tanks. *J Comput Phys* 196 53-87 (2004) **DOI:10.1016/j.jcp.2003.10.031**

[13]   Wang, J., Wang, C., Liu, J. Sloshing reduction in a pitching circular cylindrical container by multiple rigid annular baffles. *Ocean Eng* 171 241-249 (2019) **DOI:10.1016/j.oceaneng.2018.11.013**

[14] Park, T., Park, C.-J., Lee, J., Kim, Y. Experimental observation on violent sloshing flows inside rectangular tank with flexible baffles. *Appl Ocean Res* 154104307 (2025) **DOI:10.1016/j.apor.2024.104307**

[15] Wang, Q., Qi, W., Zheng, G., Xu, W., Yu, H. Liquid sloshing in a tank vehicle: A numerical and experimental investigation with baffle configurations. *Measurement* 234 114806 (2024) **DOI:10.1016/j.measurement.2024.114806**

[16] Gurusamy, S., Sanapala, V.S., Kumar, D., Patnaik, B.S.V. Sloshing dynamics of shallow water tanks: Modal characteristics of hydraulic jumps. *Journal Fluids Struct* 104 103322 (2021) **DOI:10.1016/j.jfluidstructs.2021.103322**

[17] Sanapala, V.S., Rajkumar, M., Velusamy, K., Patnaik, B.S.V. Numerical simulation of parametric liquid sloshing in a horizontally baffled rectangular container. *J Fluid Struct* 76 229-250 (2018) **DOI:10.1016/j.jfluidstructs.2017.10.001**

[18] Milne-Thomson, L.M. *Theoretical Hydrodynamics*. Macmillan Education, London (1968)

[19] Abramson, H.N., Martin, R., Ransleben, G.E. (1958). *Application of Similitude Theory to the Problem of Fuel Sloshing in Rigid Tanks*. Southwest Research Institute, San Antonio

[20] Chen, Y.G., Djidjeli, K., Price, W.G. Numerical simulation of liquid sloshing phenomena in partially filled containers. *Comput Fluids* 38 830-842, (2009) **DOI:10.1016/j.compfluid.2008.09.003**

[21] Ibrahim, R.A. (2005). *Liquid Sloshing Dynamics: Theory and Applications*. Cambridge University Press, Cambridge, **DOI:10.1017/CBO9780511536656**

Author contributions *Rajamani Rajagounder: conceptualization, formal analysis, investigation, methodology, resources and writing – original draft; Jayakrishnan Nampoothiri: writing – review & editing, data curation, validation and visualization.*

AI-Assisted writing *AI-based tools were employed solely to enhance the readability and grammatical accuracy of the manuscript.*

Vpliv vzbujalne frekvence in nivoja napolnjenosti na pljuskanje goriva v avtomobilskih rezervoarjih

Povzetek *Študija obravnava analizo procesa pljuskanja goriva v sodobnih avtomobilskih rezervoarjih z namenom boljšega razumevanja delovanja gorivnega sistema. Obnašanje valovanja pri pljuskanju je bilo obravnavano pri različnih vzbujalnih frekvencah in nivojih napolnjenosti rezervoarja, in sicer z eksperimentalnimi ter numeričnimi metodami. Rezervoar za gorivo je bil vzdolž prečne osi izpostavljen sinusnemu gibanju, profili valov pa so bili zajeti z digitalno kamero. Numerične simulacije so bile izvedene z uporabo aproksimacije proste površine (metoda VOF) in uporabniško definirane funkcije (UDF) v programu ANSYS Fluent. Študija je pokazala različne oblike valovanja glede na vzbujalno frekvenco. Pri frekvencah 0,5 Hz in 0,6 Hz so bili opaženi stoječi in potujoči valovi, pri 0,7 Hz pa več potujočih valov z medsebojnimi trki. Poleg tega je povečanje nivoja napolnjenosti (z 25 % na 60 % višine rezervoarja) bistveno izboljšalo dušenje oscilacij valov. Razvite so bile regresijske enačbe za kvantitativno opredelitev odnosa med vzbujalno frekvenco, nivojem napolnjenosti in amplitudo valov. Ti izsledki lahko prispevajo k načrtovanju rezervoarjev, ki zmanjšujejo učinke pljuskanja in izboljšajo delovanje vozila.*

Ključne besede *pljuskanje tekočine, rezervoar za gorivo, analiza končnih volumnov, vizualizacija, frekvenca valovanja*

The Effects of Oil Temperature and Oil Return Pressure on Oil Film Damping Characteristics of a High-Speed Solenoid Valve

Peng Liu ✉ – Qing Zhao – Shijian Peng – Wenwen Quan – Zhida Gao ✉
Changsha University of Science and Technology, College of Automotive and Mechanical Engineering, China
✉ liupeng@csust.edu.cn; 202103130116@stu.csust.edu.cn

Abstract   A high-speed solenoid valve (SV) is a critical executive component in common rail fuel injection systems, where its dynamic response significantly influences the control accuracy of fuel injection. Moreover, this response is particularly affected by the damping force (DF) of the oil film between the armature and the iron core. To investigate the effects of oil temperature and oil return pressure on the oil film damping characteristics of high-speed SV, a numerical simulation approach was employed. Computational fluid dynamics (CFD) models were constructed to analyze the influence of oil temperature and oil return pressure on both the DF of the oil film and its cavitation properties across varying operational air gaps. The results indicate that as the oil temperature increases, the DF of the oil film generally exhibits a decreasing trend during the suction and release processes of the high-speed SV. Additionally, increasing the initial and residual air gaps can mitigate the influence of temperature on the DF of the oil film, thereby reducing the incidence of cavitation. Notably, the oil return pressure does not affect the DF of the oil film during the suction process. However, during the release process, the DF of the oil film increases with the oil return pressure when the residual air gap is small. At medium residual air gaps, the DF initially increases with the oil return pressure before subsequently decreasing, and is accompanied by oscillations during cavitation collapse. For large residual air gaps, the impact of oil return pressure on the DF of the oil film becomes negligible.

Keywords   high-speed solenoid valve, oil temperature, oil return pressure, damping force of the oil film, cavitation

Highlights
- A CFD model is established to analyze the oil film damping characteristics of a high-speed SV.
- The impact of temperature and oil return pressure on the oil film damping characteristics is studied.
- The cavitation phenomenon during the release process of high-speed SV is analyzed.
- Enlarging the initial and residual air gaps helps mitigate temperature effects on the oil film's DF.

1 INTRODUCTION

The development of a diesel fuel injection system to ultra-high-pressure injection and flexible control direction of the injection amount, and the injection timing and injection rate, full electronic control of the fuel injection system has become an inevitable trend for achieving flexible control of the fuel injection process. A high pressure common rail system, as the latest generation of electronic fuel injection system, is one of the core technologies used to achieve energy saving and emission reduction of diesel engines now [1,2].

High-speed solenoid valve (SV) is a key executive component in high pressure common rail system. Gu et al. [3] built a one-dimensional model of the common-rail fuel injector based on AMESim software, and then reduced the total response time, injection pressure fluctuation and injection pressure drop of the injector by optimizing the solenoid valve preload, solenoid valve lift and other relevant parameters, thus greatly improving the comprehensive performance of the common-rail fuel injection system. Xu et al. [4] found that the energizing time of the solenoid valve affects the increasing speed and injection efficiency of the needle valve in the injector. If the energizing time of the solenoid valve is long enough, the injection speed can even be adjusted to reduce the injection volume gap between different pressure waves, which helps to improve the injection stability under large injection volume working conditions. Hung and Lim [5,6] found that spring stiffness, plunger mass, SV coil turns, and coil position have significant effects on the electromagnetic force and displacement of the plunger in the

injector, thus affecting the injection quality of the injector. Therefore, it is evident that the dynamic response characteristics of high-speed SV exert a significant influence on the control accuracy of the fuel injection system [7,8].

However, the armature of the high-speed SV operates in an oil environment. A thin damping oil film forms between the armature and the iron core. Whether it is the suction process of the high-speed SV (the armature gradually approaches the iron core) or the release process of the high-speed SV (the armature gradually moves away from the iron core), the armature will receive the damping force (DF) of oil film in the opposite direction of its movement, which hinders the movement speed of the armature itself, and then has an important impact on the dynamic response of the high-speed SV.

At present, scholars have conducted in-depth research on the oil film damping characteristics of high-speed SVs. Xia et al. [9,10] used the basic theory of parallel plate gap flow and laminar flow to simplify and analytically calculate the oil film damping flow problem of high-speed SVs, and explored the influence of the number and size of the damping holes on DF and pressure distribution for high-speed SVs with square and disk armatures. Resch and Scheidl [11] developed an advanced numerical computation model of the DF in the separation process of SVs, and analyzed the effects of fluid surface tension, cavitation, inlet pressure loss, and fluid viscosity on the accuracy of the DF calculation. Scheidl and Gradl [12] found that when two oil-filled plates are rapidly separated, if the pressure between the gaps is greater than the saturated vapor pressure of the oil, the oil film DF can be derived and solved by the Reynolds

equation. However, for very fast movements, such as the armature movement of a SV, cavitation is likely to occur on the armature surface. In this case, the Reynolds equation of single-phase flow cannot solve the DF of oil film. Scheidl and Gradl [13] proposed an approximate method for calculating the DF during the separation process of SVs according to the characteristics of the solution of the non-cavitating viscous flow problem, which can be applied to deal with the cavitating viscous flow problem. Nevertheless, this approach does not consider the influence of inlet pressure loss and fluid inertia on the DF of the oil film. Through numerical simulation, Zhao et al. [14] found that the opening of damping holes and straight grooves structure on the armature of high-speed SV can effectively reduce the DF oil film, and inhibit the occurrence of the cavitation phenomenon within a certain range. But the impact of opening damping holes and straight grooves on the electromagnetic force of high-speed SV was not taken into account. Opening damping holes and straight grooves leads to a reduction in the upper surface area of the armature and a decrease in the amount of magnetic flux passing through it, making the electromagnetic force decline, which in turn affects the dynamic response speed of the high-speed SV. Scheidl and Hu [15] and Scheidl et al. [16] found that the opening of cushioning grooves on the edge of the armature of the SV, as well as avoiding contact between the armature and the core, is conducive to the reduction of the DF oil film. However, the high-speed SV exhibits a rapid motion speed and a minimal initial air gap, which significantly constrains the role of the opening cushioning grooves at the armature edge. Zhang et al. [17] proposed a novel damping sleeve structure with holes that can be easily installed. This structure is designed to alter the pressure distribution on the spool surface and the oil jet angle, thereby reducing the DF of oil film and enhancing the opening speed of the valve.

In summary, existing studies on the analysis of oil film damping characteristics of high-speed SV primarily focus on two key areas: the calculation of the oil film DF of high-speed SV and the investigation into how structural parameters of the armature influence this force. It is important to note that the aforementioned studies are predicated on the assumption that the fuel properties within the armature chamber of the high-speed SV remain unaltered. However, in the practical application of common rail electric fuel injectors, the oil temperature in the armature cavity of the high-speed SV may change. This will lead to changes in the oil physical properties [18,19], and further affect the damping characteristics of the oil film. In addition, the oil return pressure in the armature cavity may also change the flow state and cavitation characteristics of the oil film, which in turn affects the damping characteristics.

In this study, a numerical simulation method was employed to investigate the effects of oil temperature and oil return pressure on the film damping characteristics during the suction and release phases of the high-speed SV in common rail fuel injectors. The aim is to provide a theoretical foundation for optimizing the design of high-speed SVs and enhancing their operational consistency control. The main contributions of this study can be summarized as follows:

1. Computational fluid dynamics (CFD) models are developed to analyze the oil film damping characteristics of the high-speed SV.
2. The influence of oil temperature and oil return pressure on the DF of the oil film of high-speed SV is revealed, along with an explanation of the underlying reasons.
3. The cavitation phenomenon on the armature surface during the release process of the high-speed SV is analyzed, revealing the influence of oil temperature and oil return pressure on the gas volume fraction.

2 METHODS AND MATERIALS

Figure 1 is a structural diagram of the high-speed SV, which is built into the common rail injector. Upon energizing the coil, the iron core exerts an electromagnetic force on the armature. When the electromagnetic force is greater than the spring preload force, the armature drives the control valve stem to move upward, that is, the suction process of the high-speed SV. At this time, the high-pressure oil channel is opened and the injector begins to spray oil. Once the coil is de-energized, the electromagnetic force disappears, and the armature moves downward to fully set under the action of the spring preload, that is, the release process of the high-speed SV. At this time, the high-pressure oil channel is closed and the injector stops spraying. As well, the distance between the armature and the iron core is very small, and the maximum distance is not more than 0.3 mm. However, other areas of the armature cavity have relatively large voids and can be regarded as areas with equal pressure [20]. Therefore, when using ANSYS Fluent to develop the CFD model for oil film damping characteristics, the computational domain mainly considers the oil between the armature and the iron core. As far as the good symmetry of the armature structure, to improve computational efficiency, a quarter of the computational domain for the CFD model (shown in Fig. 1) was built, in which the computational domain of the suction process and the release process only have gap differences. The motion velocity of the armature was obtained by differentiating the measured displacement curve of the high-speed SV [21], as shown in Fig. 2. Because the high-speed SV is integrated into the injector, directly measuring the DF of the oil film applied to the armature is challenging. To address this issue, this study referred to the fluid viscosity test during the SV armature separation process in reference [11] to guide the establishment of the CFD model. Resch and Scheidl [11] describe the use of a specific experimental rig to obtain the DF of the oil film between two parallel circular plates. The diameter of the test plate was 33 mm. The test fluid utilized was a mineral oil-based hydraulic fluid, with a nominal viscosity of 3.2×10^{-5} m²/s and an actual viscosity of 43.2 mPa·s at 25 °C and atmospheric pressure.
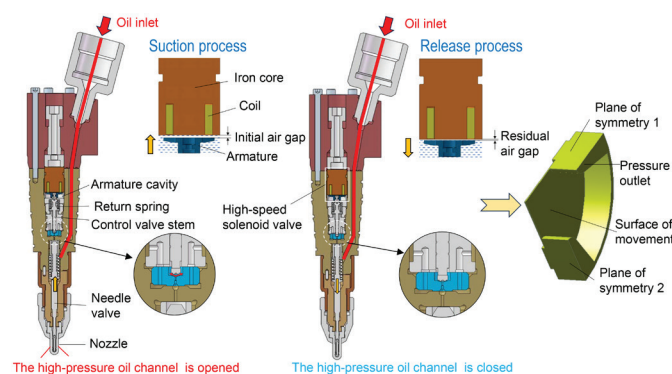

Fig. 1. High-speed solenoid valve (SV) for common rail injectors and its computational domain
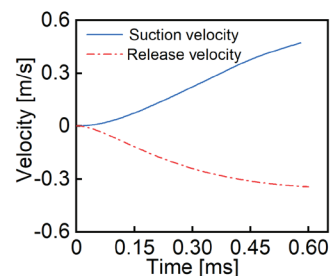

Fig. 2. Velocity profile of the armature during the suction and release processes
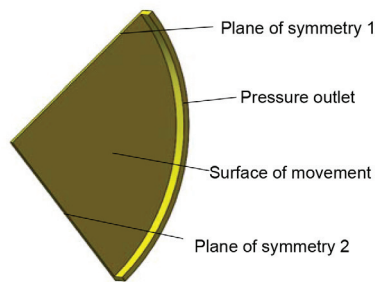
Fig. 3. Computational domain of oil film damping characteristics based on reference [11]
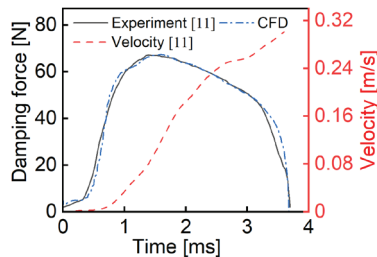
Fig. 4. Comparison of experimental result [11] and current CFD simulation result

Table 1. Setting of CFD models parameters

	Classification	Setting value
Main phase	As shown in Table 2	
Second phase	Viscosity [mPa·s]	1.8×10^{-3}
	Density [kg/m³]	0.029
Multiphase model	Mixture	
Turbulence model	SST-k-omega	
Cavitation model	Schnerr–Sauer	
	Bubble number density [m⁻³]	1×10^{11}
Wall boundary	No-slip surface conditions	
Dynamic mesh setup	Dynamic mesh method	Diffusion smoothing
	Diffusion function	Boundary distance
	Diffusion parameters	1.5
Speed of armature movement	As shown in Fig. 2	
Solving setup	Solution method	Pressure-velocity coupling scheme: simple
	Time step size [s]	2.5×10^{-6}
	Residual	1×10^{-5}

The computational domain was established for the analysis of oil film damping characteristics based on reference [11] as shown in Fig. 3. Also, Fig. 4 presents a comparison between the test results of the DF of the oil film from reference [11] and those obtained from CFD numerical analysis. As can be seen from Fig. 4, the results demonstrate

a high degree of consistency, with a correlation coefficient of 0.99. The CFD model for oil film damping characteristics, as presented in this study, differs from the above referenced model only in terms of the geometry of the computational domain and the properties of the oil. Consequently, the model for reference [11] can be referred to construct the CFD model in this study. According to the different gaps between the suction and release processes, six groups of CFD models were established. The parameters of these models are identical except for their mesh configurations. Tables 1 and 2 detail the specific settings of the model parameters. Table 3 shows mesh setup in models.

Table 2. Physical properties of oil [22]

Property	Value		
Oil temperature [°C]	20	40	60
Saturated vapor pressure [Pa]	1280	4595	17125
Dynamic viscosity [mPa·s]	3.7	3.0	2.2
Surface tension [mN/m]	27.19	25.97	24.75
Density [kg/m³]	833	812.31	803

3 RESULTS AND DISCUSSION

3.1 Effect of Oil Temperature on the Suction Process

Figure 5 illustrates the impact of oil temperature on the DF of the oil film during the suction process of the high-speed SV. It is observed that before 0.3 ms, the influence of different oil temperatures on the DF of the oil film is not obvious. However, as the armature gradually moves upward, that is, when it gradually moves closer to the iron core, the higher the oil temperature, the smaller the DF of the oil film. Moreover, by comparing Fig. 5a, b and c, it can be found that a smaller initial air gap in the high-speed SV results in a more pronounced effect of oil temperature on the DF of the oil film acting on the armature. At 0.58 ms, when the initial air gap is 0.2 mm, the DF of oil film at 20 °C is 199.25 N, which is 36.25 N greater than that at 60 °C. When the initial air gap is 0.25 mm, the DF of the oil film at 20 °C is 71.25 N, which is 10.69 N greater than that at 60 °C. When the initial air gap is 0.3 mm, the DF of the oil film at 20 °C is 39.17 N, which is 4.94 N greater than that at 60 °C.

This phenomenon can be attributed to the fact that with the increase of oil temperature, the surface pressure distribution is basically no different in the early movement of the armature. However, as the armature movement speeds up and the distance between the iron core and the armature decreases, the difference in surface pressure distribution gradually increases. Additionally, the surface pressure decreases with rising temperature (refer to Fig. 6). Moreover, with increasing temperature, the saturated vapor pressure of oil increases significantly, while its dynamic viscosity, surface tension, and density gradually decrease (as shown in Table 2). Through

Table 3. Mesh setup in CFD models

Classification	Suction process			Release process		
Initial/ Residual air gap [mm]	0.2	0.25	0.3	0.05	0.1	0.15
Mesh type	Tetrahedral mesh					
Body mesh [mm]	0.5			0.2		
Mesh of surface of movement [mm]	0.125			0.05		
Nodes numbers	26711	29622	32476	163029	167349	203010
Elements numbers	119435	136756	154348	730762	789185	1010515
Element quality (average)	0.82812	0.81745	0.82892	0.82037	0.82394	0.82992
Skewness (average)	0.24197	0.25725	0.24078	0.25242	0.24813	0.23855
Aspect ratio (average)	1.8775	1.9127	1.8726	1.9099	1.8913	1.8695
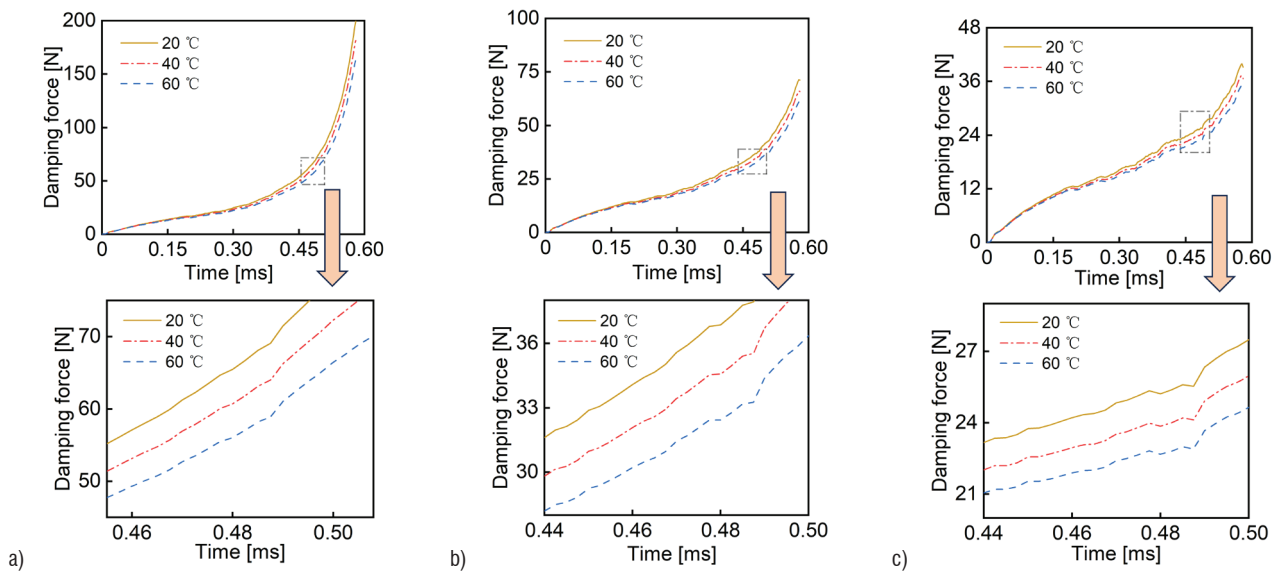
Fig. 5. Influence of temperature on the damping force (DF) of the oil film during the suction process at different initial gaps; a) 0.2 mm, b) 0.25 mm, and c) 0.3 mm

the single factor analysis of the relationship between oil physical properties and the DF of the oil film acting on the armature (as shown in Fig. 7), the authors found that the saturated vapor pressure and surface tension parameters have almost no effect on the DF of the oil film. However, as can be seen from Fig. 7b and d, the DF of the oil film acting on the armature decreases as the dynamic viscosity and density decrease. Moreover, this effect is more pronounced when the armature is close to the iron core. At 0.58 ms, the DF of the oil film at a dynamic viscosity of 2.2 mPa·s, which is 41.2 N smaller than that at 3.7 mPa·s; and the DF of oil film at a density of 803 kg/m³, which is 4.7 N smaller than that at 833 kg/m³. It is apparent that the dynamic viscosity has a more significant impact on the DF of the oil film. This is analogous to the conclusion that oil viscosity can exert a considerable influence on the DF of the oil film within the nozzle, as previously discussed in the literature [23]. Therefore, during the suction process, temperature mainly affects the damping characteristics of the oil film by influencing the dynamic viscosity and density of the oil.
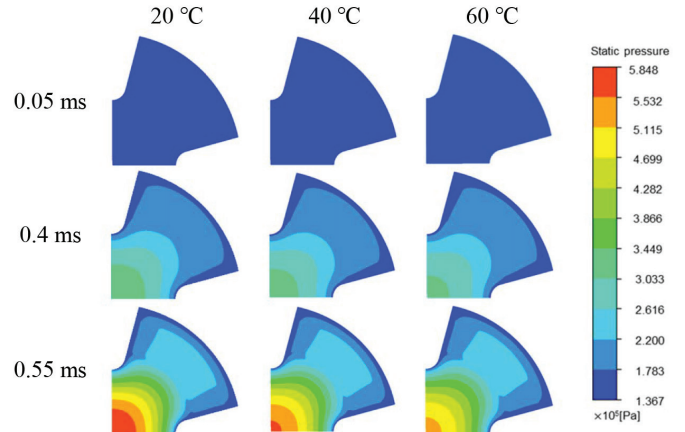
Fig. 6. Pressure distribution cloud at different temperatures for oil return pressure of 151,987.5 Pa and an initial air gap of 0.25 mm
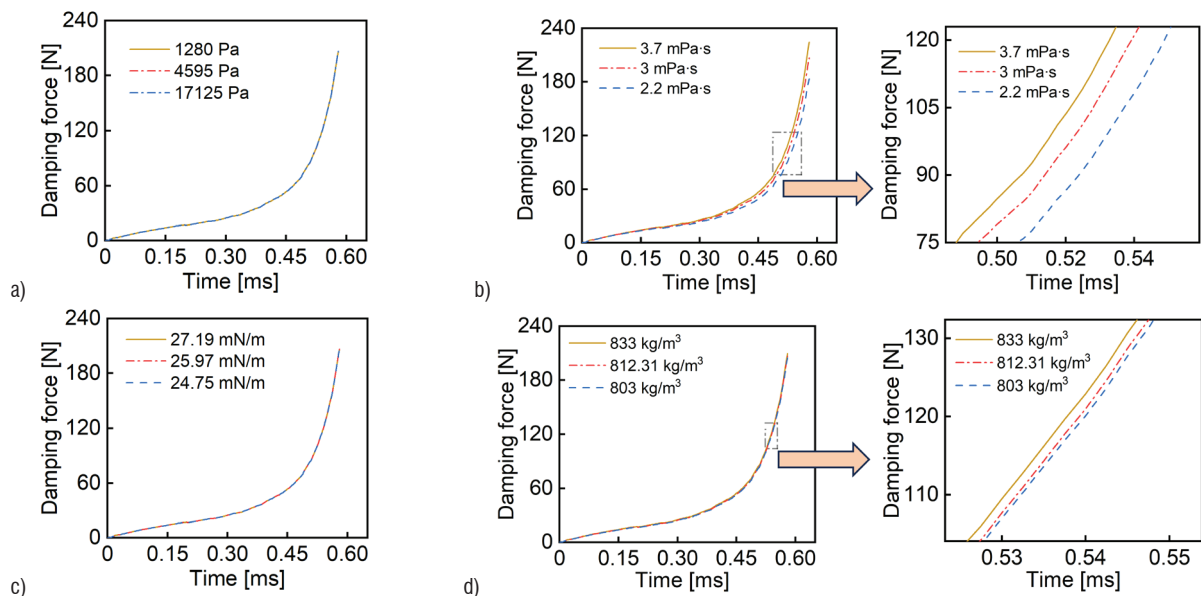
Fig. 7. Influence of oil physical parameters on the DF of the oil film during the suction process; a) saturated vapor pressure, b) dynamic viscosity, c) surface tension, and d) density
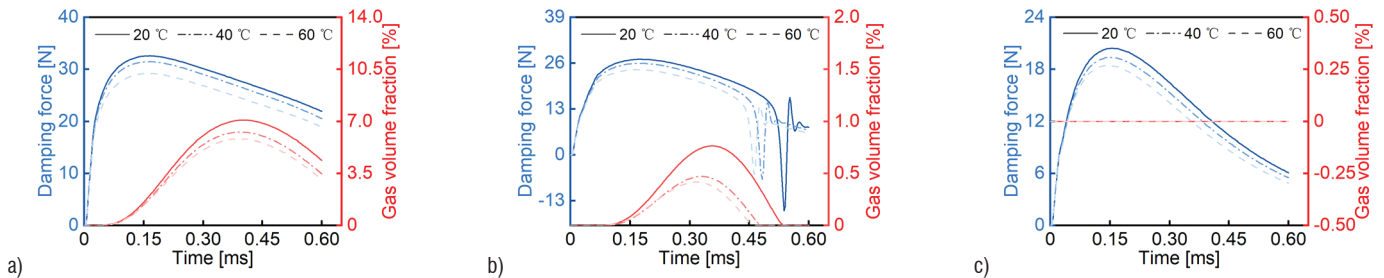
Fig. 8. Effect of temperature on the DF of the oil film and gas volume fraction during the release process at different residual gaps; a) 0.05 mm, b) 0.1 mm, and c) 0.15 mm

3.2 Effect of Oil Temperature on the Release Process

Figure 8 demonstrates the impact of oil temperature on the DF of the oil film and the gas volume fraction during the release process of the high-speed SV. As can be seen from Fig. 8, compared with the suction process (shown in Fig.5), the DF of the oil film on the armature during the release process is relatively small on the whole, and the maximum value of the DF of the oil film during the release process is 32.85 N. Also, as the oil temperature increases, the overall DF of the oil film during the release process gradually decreases, which is consistent with the influence law during the suction process. However, at the medium residual air gap (the small gap that still exists between the armature and the core after the SV is closed), the DF of the oil film appears to oscillate in the later stage of the armature movement. In addition, Fig. 8 also illustrates that at the small residual air gap, the gas volume fraction gradually decreases as the oil temperature increases. At 20 °C, 40 °C, and 60 °C, the maximum gas volume fraction was 7.08 %, 6.27 % and 5.81 %, respectively. After the armature stops moving, the gas volume fraction did not decrease to 0, that is, oil experienced cavitation, but no cavitation collapse phenomenon. At the medium residual air gap, with the increase of oil temperature, the change law of the gas volume fraction is similar to that of the small residual gap. At 20 °C, 40 °C and 60 °C, the gas volume fraction gradually increases from 0 % to 0.76 %, 0.46 % and 0.4 %, respectively, and gradually decreases to 0. Oil cavitation occurs and collapses. Notably, the moment when the DF of the oil film oscillates, it corresponds to the

point when the gas volume fraction drops to zero, and the larger the peak value of the gas volume fraction, the greater the oscillation amplitude of the DF of the oil film. Therefore, it can be inferred that the bubble collapse leads to the oscillation of the above DF of the oil film. In contrast, at the larger residual air gap, the gas volume fraction within the oil is always zero, and no cavitation phenomenon occurs.
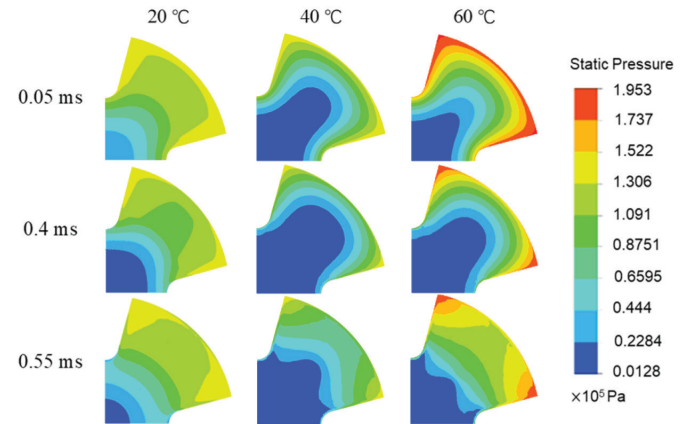
Fig. 9. Pressure cloud distribution at different temperatures for a pressure of 151987.5 Pa and a residual air gap of 0.1 mm

The above phenomena can be attributed to the fact that, as the oil temperature rises, the average pressure on the upper surface of
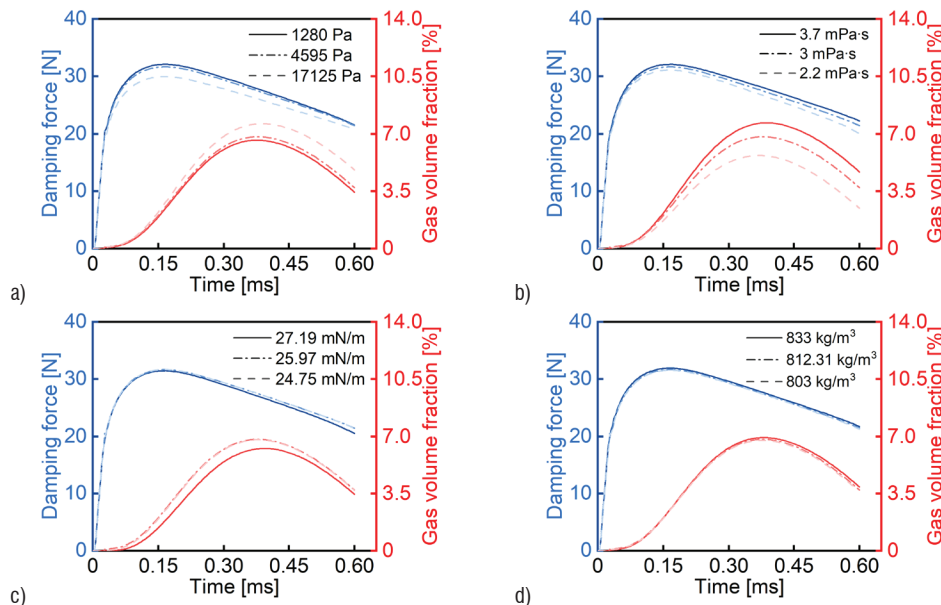
Fig. 10. Effect of oil physical parameters on the DF of the oil film and gas volume fraction during the release process at a residual air gap of 0.05 mm; a) saturated vapor pressure, b) dynamic viscosity, c) surface tension, d) density
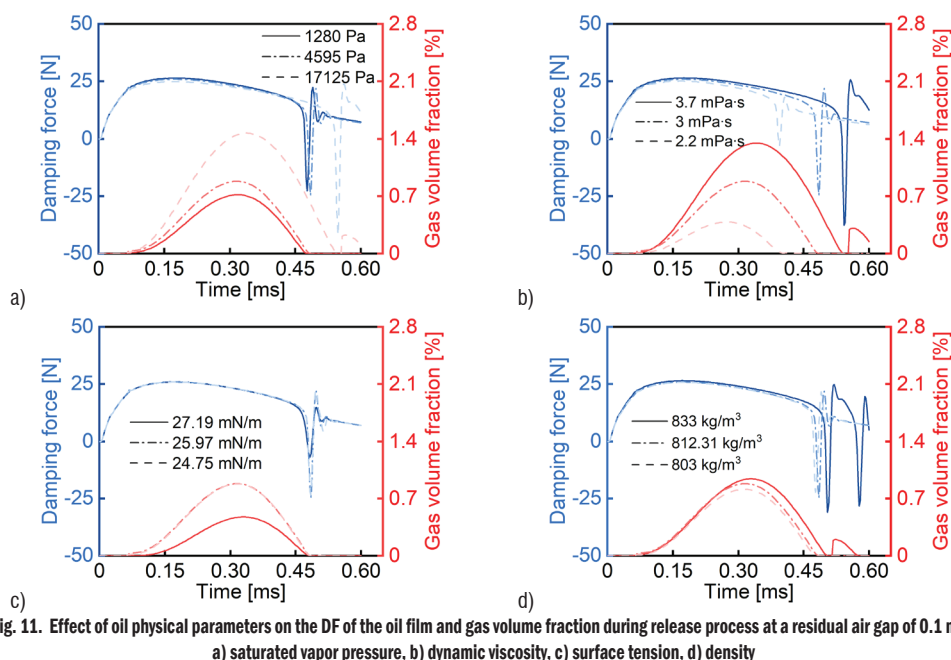
Fig. 11. Effect of oil physical parameters on the DF of the oil film and gas volume fraction during release process at a residual air gap of 0.1 mm;
a) saturated vapor pressure, b) dynamic viscosity, c) surface tension, d) density
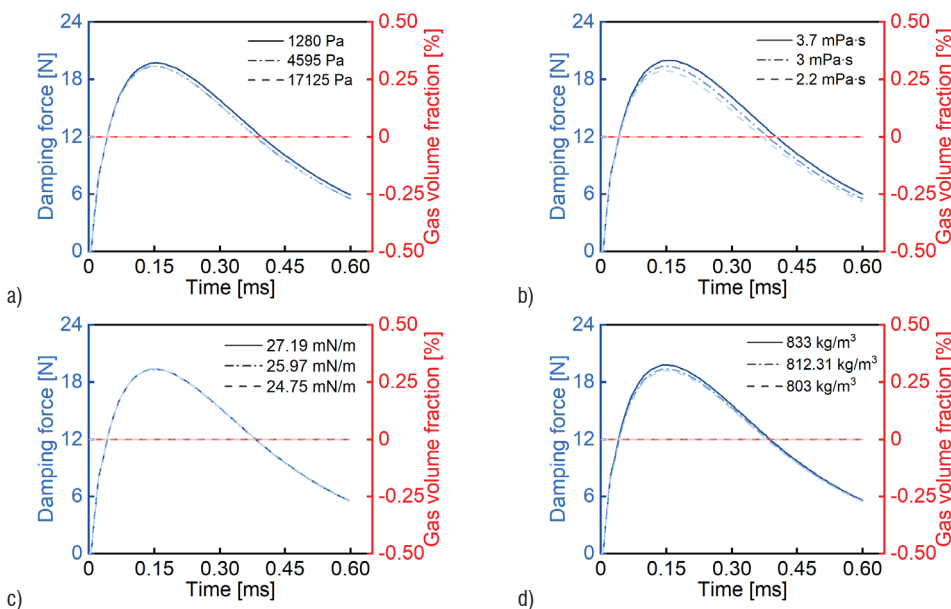
Fig.12. Effect of oil physical parameters on the DF of the oil film and gas volume fraction during release process at a residual air gap of 0.15 mm
a) saturated vapor pressure, b) dynamic viscosity, c) surface tension, d) density

the armature gradually increases (shown in Fig. 9) when there is no cavitation collapse in the oil. So that the pressure difference between the upper and the lower surface of the armature gradually decreases. Therefore, the DF of the oil film during the release process tends to decrease as a whole.

In order to further explore the essence of the influence of oil temperature on oil film damping characteristics, a single-factor analysis was conducted to elucidate the relationship between the physical properties of oil and the DF of the oil film, as well as the gas volume fraction within the oil during the release process of a high-speed SV, as depicted in Figs. 10-12. The results reveal that the surface tension and the density of the oil have less influence on the DF of the oil film and the gas volume fraction during the release process of the high-speed SV. The DF curves of oil film almost overlap under different surface tension at the medium and large residual air gap. At

the small residual air gap, the maximum difference between the DF of the oil film under the surface tension of 24.75 mN/m and 27.19 mN/m is only 0.88 N, and the maximum difference between the gas volume fraction is only 0.8 %. Similarly, at small and medium residual air gaps, the DF of the oil film curves at different densities almost overlap. At the large residual air gap, the difference between the DF of the oil film at a density of 833 kg/m^3 and 803 kg/m^3 is only 0.62 N at most, while the gas volume fraction curve also changes slightly, with a maximum difference of 0.31 %.

However, with the increase of saturated vapor pressure and the decrease of dynamic viscosity, the DF of the oil film acting on the armature decreases as a whole. Excluding oscillations due to cavitation collapse, the maximum difference between DF of oil film at saturated vapor pressure of 1280 Pa and 17125 Pa is 2.14 N, the maximum difference between the DF of oil film at the dynamic
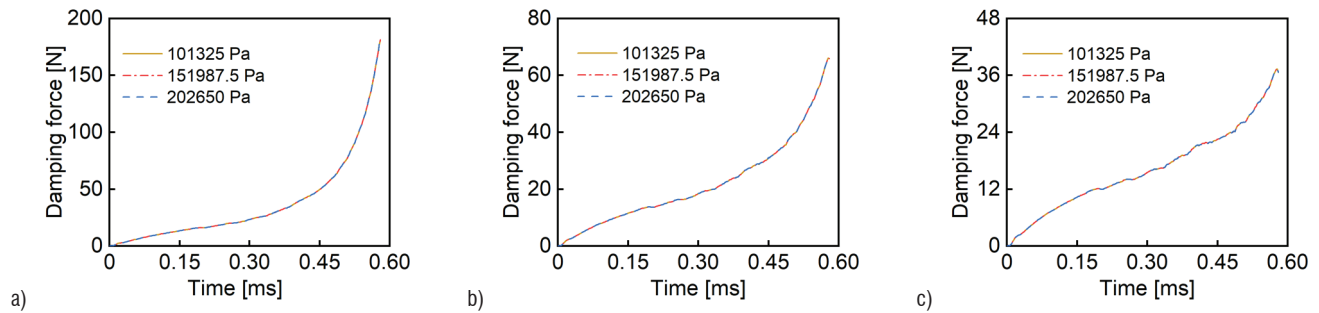
Fig. 13. Influence of oil return pressure on the DF of the oil film during the suction process at different initial air gaps; a) 0.2 mm, b) 0.25 mm, and c) 0.3 mm

viscosity of 3.7 mPa·s and the DF of the oil film at 2.2 mPa·s is 4.4 N. The saturated vapor pressure and dynamic viscosity of the oil also show the above pattern as the oil temperature increases. Therefore, as the oil temperature increases, the overall DF of the oil film acting on the armature also decreases gradually.

As can be seen from Figs. 10 and 11, the gas volume fraction gradually increases with an increase in the saturated vapor pressure and the dynamic viscosity, but the trend of the dynamic viscosity inversely correlates with temperature (shown in Table 2). However, it can be seen from Fig. 8 that the gas volume fraction decreases with increasing temperature at small and medium residual air gaps. This is because the effect of the dynamic viscosity on the oil cavitation is greater than that of the saturated vapor pressure at this time. At the small and medium residual air gaps, when the saturated vapor pressure of oil increases from 1280 Pa to 17125 Pa, the peak gas volume fraction increases by 1.37 % and 0.82 %, respectively. However, the viscosity decreases from 3.7 mPa·s to 2.2 mPa·s, the maximum gas volume fraction decreases by 2.23 % and 1.22 %, respectively.

In summary, during the release process, the temperature mainly changes the damping characteristics of the oil film by affecting the saturated vapor pressure and the dynamic viscosity of the oil.

3.3 Effect of Oil Return Pressure on the Suction Process

Figure 13 shows the influence of oil return pressure on the DF of the oil film during the suction process of the high-speed SV. As shown in Fig. 13, the oil return pressure has no influence on the DF during the suction process. As the armature progressively moves closer to the iron core during the suction process, the pressure on its upper surface incrementally rises, negating the possibility of cavitation. Therefore, it is not necessary to analyze the influence of oil return pressure on the gas volume fraction during the suction process. As can be seen from Fig. 14, during the suction process of the high-speed SV, the difference between the surface pressure of the armature and the oil return pressure does not change with the increase of the oil return

pressure. Therefore, the oil return pressure has no influence on the DF of the oil film during the suction process.

Fig. 14. Differential pressure cloud at different oil return pressures with a residual air gap of 0.1 mm during the suction process

3.4 Effect of Oil Return Pressure on the Release Process

Figure 15 demonstrates the impact of the oil return pressure on the DF of the oil film and the gas volume fraction within the oil during the release process of the high-speed SV. As shown in Fig. 15, when the residual air gap is small, the oil cavitation is observed, but the subsequent cavitation collapse does not occur. Also, the DF of the oil film gradually increases with the increase of oil return pressure. When the oil return pressure is 101,325 Pa, 151,987.5 Pa, and 202,650 Pa, the peak value of the DF of the oil film is 24.23 N, 31.48 N, and 37.75 N, respectively. Furthermore, the DF curve demonstrates a more rapid decline after reaching its peak with heightened oil return pressure. At the medium residual air gap, high oil return pressure effectively prevents the occurrence of oil cavitation, whereas medium and low pressures induce cavitation, with cavitation collapse occurring specifically medium oil return pressure. Under the circumstances, the DF of the oil film initially rises with increasing oil return pressure,
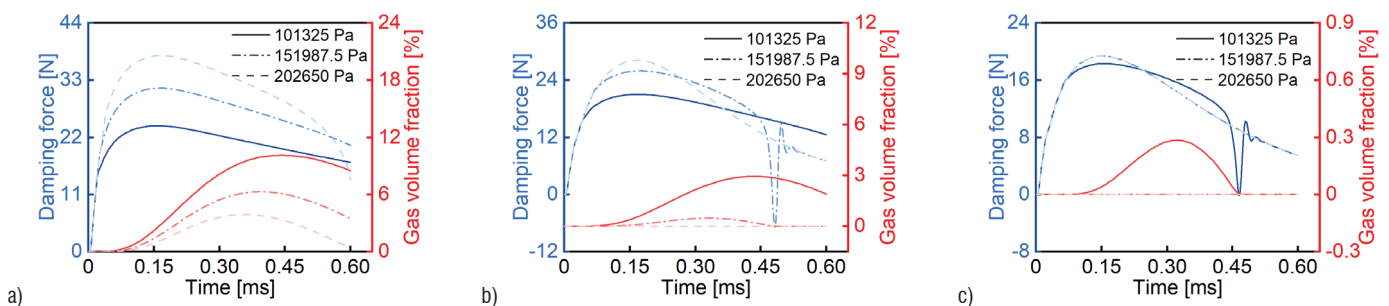

Fig. 15. Effect of oil return pressure on the DF of the oil film and gas volume fraction during the release process at different residual air gaps: a) 0.05 mm, b) 0.1 mm, and c) 0.15 mm

subsequently exhibiting a pattern of increase followed by decrease, with oscillations manifesting at the point of cavitation collapse. At the large residual air gap, oil cavitation and subsequent collapse occur only at low oil return pressure. The change law of the DF of the oil film is similar to that of the medium residual air gap, with the exception that the oil cavitation is absent at medium and high oil return pressures, rendering the oil return pressure inconsequential to the DF.

By comparing Fig. 15a, b, and c, it can be seen that under the same return oil pressure, when the residual air gap is larger, the DF of the oil film on the armature is smaller as a whole. When the oil return pressure is 101325 Pa, the peak values of DF of the oil film at small, middle, and large residual air gaps are 24.23 N, 21.02 N, and 18.29 N, respectively. When the return oil pressure is 151,987.5 Pa, the peak values of the DF of the oil film at low, middle, and high residual air gaps are 31.48 N, 25.94 N, and 19.36 N, respectively. When the return oil pressure is 202,650 Pa, the peak values of the DF of the oil film at small, middle, and large residual air gaps are 37.75 N, 28.17 N, and 19.37 N, respectively. Similarly, by comparing Fig. 15a, b, and c, it also can be noticed that for the same oil return pressure, the larger the residual air gap, the smaller the volume fraction of oil gas and the less likely the cavitation phenomenon is to occur.

The above behaviors can be explained by the fact that as the oil return pressure rises, when the fuel does not appear to collapse, the absolute difference between the upper surface pressure of the armature and the oil return pressure gradually increases (as shown in Fig. 16). Consequently, the pressure difference between the upper and lower surfaces of the armature gradually increases. Thus, the DF of the oil film overall rises with the ascent of the oil return pressure during the release process. Moreover, it is important to note that at a constant temperature, the saturated vapor pressure of the oil remains immutable; thus, a lower oil return pressure increases the likelihood of the cavitation occurring on the armature surface, consequently elevating the gas volume fraction. Therefore, appropriately increasing the oil return pressure can reduce the possibility of cavitation or cavitation collapse.
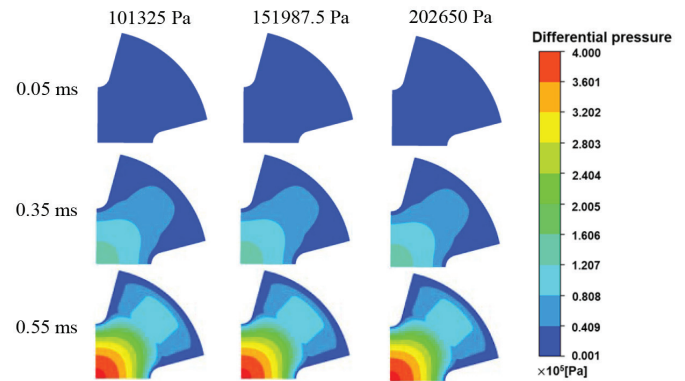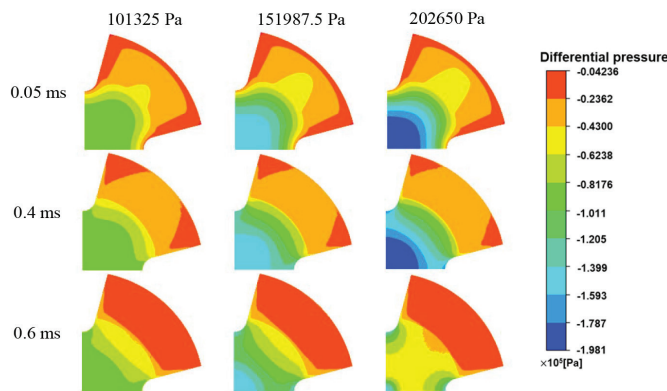

Fig. 16. Differential pressure cloud at different oil return pressures with a residual air gap of 0.05 mm during the release process

Furthermore, Fig. 17 illustrates that, under identical oil return pressure, a reduction in residual air gap results in a proportional increase in the absolute difference between the upper surface of the armature and the oil return pressure. Consequently, the DF of the oil film on the armature during the release process will also be amplified. This is similar to the law that the smaller the initial air gap, the greater the influence of the DF of the oil film during suction process. At the same time, a greater absolute pressure difference also means a lower pressure on the upper surface of the armature. Once the pressure on the upper surface of the armature falls below the saturated vapor

pressure of the oil, cavitation or even cavitation collapse will occur on the surface of armature, which will greatly affect the service life of the high-speed SV. Therefore, when designing the high-speed SV, the residual air gap is not easy to be too small.
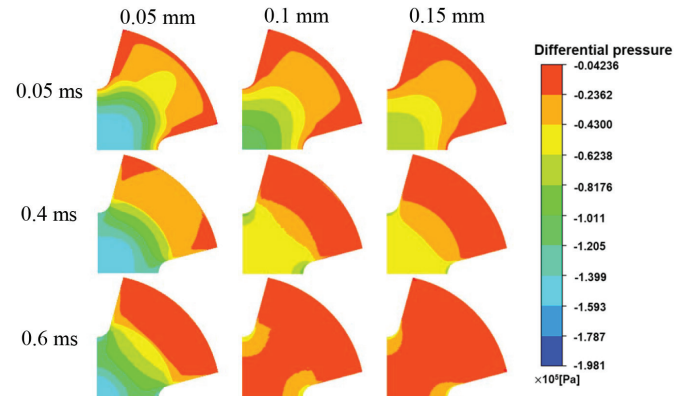
Fig. 17. Pressure difference cloud image under different residual air gaps when oil return pressure is 151987.5 Pa during the release process

4 CONCLUSIONS

The temperature greatly influences the DF of the oil film during both the suction process and the release process of the high-speed SV. Specifically, temperature changes the DF of the oil film during the suction process by affecting the dynamic viscosity and density of the oil, while temperature changes the DF of the oil film during the release process by affecting the saturated vapor pressure and dynamic viscosity of the oil. An increase in oil temperature results in a reduction the overall DF of the oil film in both processes of the high-speed SV. By enlarging the initial and residual air gaps, it is conducive to mitigate the impact of temperature on the DF of the oil film, thereby reducing the oil cavitation and improving the operational consistency and reliability of the high-speed SV.

The oil return pressure does not affect the DF of the oil film during the suction process of the high-speed SV. However, during the release process, at the small residual air gap, the DF of the oil film increases gradually with the oil return pressure, exhibiting a more rapidly descending curve beyond the peak value. At the medium residual air gap, the DF of the oil film shows a trend of increasing and then decreasing with the oil return pressure, and oscillations occur when the oil cavitation collapses. However, at the larger residual air gap, oil cavitation and collapse occur only under low oil return pressure, and the maximum gas volume fraction is only 0.3%. And at medium and high oil return pressures, cavitation does not occur, the DF of the oil film is consistent. Accordingly, when the residual air gap is large, the effect of the oil return pressure on the characteristics of the oil film is not significant.

In the context of the release process of high-speed SV, the increase of oil return pressure has the effect of reducing the possibility of cavitation on the armature surface. However, this increase also has the consequence of increasing the overall DF of the oil film, particularly when the residual air gap is small or medium. This represents a contradictory problem that is faced by high-speed SV in the working environment. To alleviate this contradiction, it is possible to expand the residual air gap in a way to reduce the impact of cavitation, while also reducing the DF of the oil film.

The design and optimization of novel damping characteristic structures on the armature for high-speed SVs should be prioritized in future research endeavors.

References

[1] Bai, Y., Lan, Q., Fan, L.Y., Yao, J., Kong, X.D., Yang, L., Wen, L.M. Pressure characteristics of the fuel system for two-stroke diesel engines under different operational modes. *Fuel*, 332, 126007 (2023) **DOI:10.1016/j.fuel.2022.126007**

[2] Bai, Y., Lan, Q., Fan, L.Y., Ma, X.Z., Liu, H. Investigation on the fuel injection stability of high-pressure common rail system for diesel engines. *Int J Engine Res* 22, 616-631 (2021) **DOI:10.1177/1468087419856981**

[3] Gu, Y., Fan, L., Lan, Q., Wei, Y., Zhou, J., Du, K. Multi-objective optimization of fuel injection performance of a common rail injector. *Int J Engine Res* 24, 3282-3296 (2023) **DOI:10.1016/j.applthermaleng.2024.123729**

[4] Xu, J., Fan, L., Chen, C., Lu, G., Tu, T. Study on fuel injection stability improvement in marine low-speed dual-fuel engines. *Appl Therm Eng* 253, 123729 (2024) **DOI:10.1016/j.applthermaleng.2024.123729**

[5] Hung, N.B., Lim, O. Development of a high-performance solenoid gas injector applied for compressed natural gas fueled engines. *Int J Automot Techn* 23, 567-576 (2022) **DOI:10.1007/s12239-022-0052-8**

[6] Hung, N.B., Lim, O. Improvement of electromagnetic force and dynamic response of a solenoid injector based on the effects of key parameters. *Int J Automot Techn* 20, 949-960 (2019) **DOI:10.1007/s12239-019-0089-5**

[7] Jeong, J., Kim, K., Jang, B., Park, G. Development of a fast-stabilized fuel injection system using a solenoid actuator. *J Mech Sci Technol* 37, 5207-5218 (2023) **DOI:10.1007/s12206-023-0923-6**

[8] Gowrishankar, S., Krishnasamy, A. Injection system modification and optimization for performance enhancement and emission reduction in a light-duty diesel engine fuelled by biodiesel-water emulsion *Fuel* 337, 127222 (2023) **DOI:10.1016/j.fuel.2022.127222**

[9] Xia, S.Z., Ouyang, M.Y., Zhou, M. Squeeze flow analysis of damping oil film in solenoid valve of electronic unit pump. *J Tsinghua Univ* 43, 693-697 (2003) **DOI:10.16511/j.cnki.qhdxxb.2003.05.031** (in Chinese)

[10] Xia, S.Z., Ouyang, M.Y., Zhou, M. Study on squeeze film damping of high speed and powerful solenoid valve. *Chin J Mech Eng* 39, 84-88 (2003) **DOI:10.3321/j.issn:0577-6686.2003.07.018** (in Chinese)

[11] Resch, M., Scheidl, R. A model for fluid stiction of quickly separating circular plates. *Proc Inst Mech Eng Part C J Mech Eng Sci* 228, 1540-1556 (2013) **DOI:10.1177/0954406213509613**

[12] Scheidl, R., Gradl, C. An oil stiction model for flat armature solenoid switching valves. *ASME/BATH Symposium on Fluid Power and Motion Control* V001T01A041 (2013) **DOI:10.1115/fpmc2013-4467**

[13] Scheidl, R., Gradl, C. An approximate computational method for the fluid stiction problem of two separating parallel plates with cavitation. *J Fluids Eng-T ASME* 138, 061301 (2016) **DOI:10.1115/1.4032299**

[14] Zhao, J.H., Zhao, S.N., Grekhov, L. Study on transient fuel hydrodynamic force characteristics of high-speed solenoid valve for common rail injector. *Int J Automot Techn* 21, 1257-1269 (2020) **DOI:10.1007/s12239-020-0119-3**

[15] Scheidl, R., Hu, Z.D. Fluid stiction with mechanical contact-a theoretical model. *Proceedings of the BATH/ASME Symposium on Fluid Power and Motion Control* V001T01A033 (2016) **DOI:10.1115/fpmc2016-1769**

[16] Scheidl, R., Gradl, C., Plöckinger, A. The cushioning groove for solenoid switching valves. *Int J Fluid Power Syst* 8, 76-81 (2014) **DOI:10.5739/jfpsij.8.76**

[17] Zhang, J.H., Wang, D, Xu, B., Gan, M.Y., Pan, M., Yang, H.Y. Experimental and numerical investigation of flow forces in a seat valve using a damping sleeve with orifices. *J Zhejiang Univ-Scien* A 19, 417-430 (2018) **DOI:10.1631/jzus.a1700164**

[18] Dernotte, J., Hespel, C., Foucher, F., Houillé, S, Mounaïm-Rousselle, C. Influence of physical fuel properties on the injection rate in a diesel injector. Fuel 96, 153-160 (2012) **DOI:10.1016/j.fuel.2011.11.073.7**

[19] Payri, R., Salvador, F.J., Gimeno, J., Brancho, G. The effect of temperature and pressure on thermo dynamic properties of diesel and biodiesel fuels. *Fuel* 90, 1172-1180 (2011) **DOI:10.1016/j.fuel.2010.11.015**

[20] Park, S.H., Yoon, H.K., Suh, S.H., Lee, C.S. Effect of the temperature variation on properties of biodiesel and bio science diesel-ethanol blends fuels. *Oil Gas Sci Technol* 63, 737-745 (2008) **DOI:10.2516/ogst:2008038**

[21] Liu, P., Zhang, R., Zhao, Q., Peng, S. Eddy effect and dynamic response of high-speed solenoid valve with composite iron core. *Materials* 16, 5823 (2023) **DOI:10.3390/ma16175823**

[22] Cao, T., He, Z., Si, Z., El-Seesy, A.I., Guan, W., Zhou, H., Wang, Q. Optical experimental study on cavitation development with different patterns in diesel injector nozzles at different fuel temperatures. *Exp Fluids* 61, 185 (2020) **DOI:10.1007/s00348-020-03006-5**

[23] Payri, R., Salvador, F.J., Carreres, M., De la Morena, J. Fuel temperature influence on the performance of a last generation common-rail diesel ballistic injector. Part II: 1D model development, validation and analysis. *Energ Convers Manage* 114, 376-391 (2016) **DOI:10.1016/j.enconman.2016.02.043**

Data availability *The data supporting the findings of this study are included in the article.*

Author contribution *Peng Liu: resources, funding acquisition, project administration, methodology, writing – review & editing; Qing Zhao: data curation, formal analysis, visualization, validation, writing – original draft; Shijian Peng: visualization, writing – review & editing; Wenwen Quan: data curation, writing – review & editing; Zhida Gao: conceptualization, methodology, writing – review & editing, resources.*

Vpliv temperature olja in povratnega tlaka olja na značilnosti dušenja oljnega filma elektromagnetnega ventila za visoke hitrosti

Povzetek *Elektromagnetni ventil visoke hitrosti je kritična komponenta v sistemih vbrizga goriva skupnim vodom kjer njegov dinamični odziv pomembno vpliva na natančnost krmiljenja vbrizga goriva. Poleg tega na ta odziv še posebej vpliva dušilna sila oljnega filma med armaturo in železnim jedrom. Za preučitev učinkov temperature olja in povratnega tlaka olja na značilnosti dušenja oljnega filma v elektormagnetnega ventila visoke hitrosti je bil uporabljen pristop numerične simulacije. Modeli računalniške dinamike tekočin so bili izdelani za analizo vpliva temperature olja in povratnega tlaka olja na dušilno silo oljnega filma in njegove kavitacijske lastnosti v različnih zračnih razmikih. Rezultati kažejo, da se s povečevanjem temperature olja dušilna sila oljnega filma na splošno zmanjšuje med procesi sesanja in izpuščanja pri elektromagnetnem ventilu visoke hitrosti. Poleg tega lahko s povečanjem začetne in preostale zračne reže ublažimo vpliv temperature na dušilno silo oljnega filma in s tem zmanjšamo pojavnost kavitacije. Pomembno je, da povratni tlak olja ne vpliva na dušilno silo oljnega filma med postopkom sesanja. Vendar pa se med postopkom sproščanja dušilna sila oljnega filma povečuje s tlakom vračanja olja, kadar je zaostala zračna reža majhna. Pri srednjih zaostalih zračnih režah se dušilna sila sprva povečuje s povratnim tlakom olja, nato pa se zmanjšuje in jo spremljajo nihanja med kavitacijskim kolapsom. Pri velikih preostalih zračnih režah je vpliv povratnega tlaka olja na DF oljnega filma zanemarljiv.*

Ključne besede *elektromagnetni ventil visoke hitrosti, temperatura olja, povratni tlak olja, dušilna sila oljnega filma, kavitacija*

Optimizing Support Patch Geometries in Adhesively Bonded Single Lap Joints: A Finite Element Analysis Approach

Ahmet Çalık ✉

Burdur Mehmet Akif Ersoy University, Department of Mechanical Engineering, Turkey
✉ acalik@mehmetakif.edu.tr

Abstract *In recent years, the preference for adhesive bonding over traditional methods like bolted or riveted connections has garnered the attention of researchers. This study employs finite element analysis to optimize the geometry and placement of support patches in adhesively bonded single lap joints, significantly reducing stress concentrations and enhancing joint strength. Initially, a comprehensive finite element analysis was conducted to numerically evaluate the influence of different support patch parameters and their positions on the strength of single lap joints (SLJs). To validate the finite element analyses (FEA), comparisons were made with existing studies in the literature and analytical solutions. The numerical results in this study reveal that the dimensions and placement of the support patch can potentially reduce the load and stress distribution in different regions of the adhesive joint, which could increase its strength.*

Keywords *Adhesive bonding, stress optimization, support patch geometry, finite element analysis.*

Highlights
▪ *Identified optimal support patch geometries to reduce stress in SLJs, improving durability and load distribution.*
▪ *Findings provide insights for stronger adhesive joints in aerospace, automotive, railway, and construction.*
▪ *3D finite element analysis shows how patch thickness, position, and length affect stress and joint performance.*

1 INTRODUCTION

Adhesive bonding, renowned for its high mechanical performance, is a widely preferred assembly technique in industries like automotive, aerospace, electronics, and construction [1-3]. Despite the extensive use of adhesive bonding in aerospace and automotive industries, stress concentration remains a critical challenge in single lap joints (SLJs). This issue significantly limits the joint's load-carrying capacity and durability, especially under dynamic or cyclic loading conditions. Its popularity arises from its ability to create strong, reliable joints in demanding applications [4]. Adhesive bonded joints are particularly effective when subjected to shear forces. SLJs are commonly used in adhesive bonding due to their straightforward geometry and easy application [5, 6]. Moreover, SLJs serve as an effective method in achieving structural integration and often exhibit high mechanical performance. This type of joint facilitates load transfer by leveraging the adhesive's shear properties. Therefore, SLJs are a preferred choice for many industrial applications, especially in the automotive and aerospace sectors [7].

The finite element method (FEM) has been extensively utilized to forecast the performance of joined structures. FEM provides numerous benefits, such as the ability to alter boundary conditions, modify the geometry of the structure, and analyze structures constructed from diverse materials. It also permits the assessment of how alterations in various parameters affect the behavior of bonded joints through intricate studies involving three-dimensional modeling. These models, coupled with effective failure criteria, are employed to scrutinize the distribution of stress in bonded joints and to anticipate potential failures. Research on adhesive bonding has primarily concentrated on the adhesive layer, which is identified as the vulnerable point in the assembly due to its mechanical characteristics [8]. While previous studies focus on adhesive properties or joint geometry, the combined influence of support patch parameters on

stress distribution and joint performance remains unexplored. This knowledge gap hinders the development of more robust and durable adhesive joint designs.

The SLJ is a frequently employed joint type in various industries because of its uncomplicated geometry. Nevertheless, when such joint is under tension, an eccentric load leads to a bending moment in its overlapping area. This generates peel stresses, which can lead to damage at the edges of the joint overlap region [9]. In adhesive-bonded joints, there are various approaches to reduce the significant stress concentration that affects the strength of the connection. On the other hand, the fundamental drawback of this joining technique is the persistent high-level stress concentration at the overlap edges, due to the slow transfer of loads in adhesively bonded joints and the rotation of adherends in the presence of asymmetric loads. There are various bonding combinations available, leading to different stress distributions and levels of strength. Nevertheless, the SLJ is the prevailing choice due to its straightforward manufacturing process. To avert premature failure of the SLJ, mitigating stress concentration along the adhesive edges is paramount. This paper addresses this gap by systematically analyzing the effects of support patch geometries on stress distribution using advanced 3-dimensional (3D) finite element (FE) modeling. The study evaluates how patch thickness, position, and length influence stress mitigation in SLJs, providing actionable insights for industrial applications. Assessing stress and strain distributions in these configurations is challenging due to the intricate geometry and varied material properties employed in this investigation. The generation of peel stresses at the visible edges of the overlap area is a pivotal factor influencing the mechanical robustness of adhesive connections. Mitigating these stresses, responsible for joint damage, enhances overall joint strength and, consequently, improves load-bearing capabilities. Various methods found in the literature have been employed to alleviate stresses at

both extremities of the bonding zone [10-13]. The alterations in the shape of SLJs represent a frequently employed strategy to mitigate stress distribution issues in adhesively bonded joints, a concept widely explored in existing literature. Adhesive fillets, as part of these geometric modifications, offer a practical means to diminish stress concentrations specifically at the edges of the joint overlap [14-18]. This study provides a detailed analysis of the effects of support patch geometry on stress distribution within adhesively bonded SLJs. While previous research has focused primarily on the adhesive layer and overall joint geometry, this work specifically addresses the combined effects of various support patch parameters.

Amaro et al.'s [10] study systematically explored the impact of inside and outside tapers (30°, 45°, 60°) on adhesive joints using optical and electrical methods. Numerical analyses identified taper geometries leading to higher adhesive compression. Experimental and numerical results concurred that reducing taper angles enhances joint strength, with outside tapers exhibiting superior tensile/shear strength. Despite similar mid-line shear-peel loads, the inside taper, inducing more compression and non-coincident peak stresses, emerged as the preferred configuration. These findings offer crucial insights for optimizing adhesive joint design.

Durmus and Akpinar's [19] study delves into adhesive bonding, a common method of joining materials, focusing on the SLJ type. The research addresses issues such as peel stress and damage in adhesively bonded joints, proposing the step-lap joint as a solution. By experimentally and numerically examining SLJ, one-step lap joint (OSLJ), and three-step lap joint (TSLJ) under tensile loading, the study highlights TSLJ's superior load-bearing capacity. Results reveal the significant impact of step length variation in TSLJ on joint failure loads. Experimental and numerical findings, employing the cohesive zone model, demonstrate good agreement. The study also determines the optimal length for the initial step in the TSLJ overlap area.

Marques and da Silva [20] study addresses aircraft damage, proposing adhesive-bonded patches as a repair method. Traditional techniques using screws or rivets create stress concentrations, leading to undetectable new cracks. To improve long-term behavior and reduce costs, the aeronautical industry explores patches with a taper, spew fillet, and dual adhesives. Experimental testing on aluminum alloy sheets shows advantages for brittle adhesives with a taper and dual adhesive for taperless configurations.

The influence of cohesive law shapes on the behavior of adhesively bonded patch repairs has been a focus of research. Fernandez-Canadas et al. [5], investigated the cohesive failure of the adhesive layer in single-lap joints under uniaxial tensile loads. In this study, a three-dimensional FE model was developed using Abaqus, comparing the effects of different cohesive law shapes, including linear, exponential, and trapezoidal, on the failure load of the joints. Their findings indicated that the trapezoidal law provided the best fit to experimental data due to its ability to capture the plastic flow of the adhesive, highlighting the importance of selecting an appropriate cohesive law shape based on the adhesive's behavior.

Andruet et al. [21] developed 2D and 3D adhesive elements for stress analysis in bonded joints, incorporating geometric nonlinearity to account for large displacements. Their model effectively reduces computational requirements while providing accurate predictions, as demonstrated in SLJs and crack patch geometries. This highlights the importance of advanced modeling techniques in adhesive joint design.

Demiral and Mamedov [22] examined the fatigue performance of adhesively bonded step-lap joints under tensile loads, finding that increasing the number of steps improved the joint's fatigue resistance. Paygozar et al. [23]'s study focuses on predicting failure

loads of adhesive double-strap joints through validated FE analyses. The dimensions of the patch significantly impact the failure load and stress distribution in various joint parts, potentially affecting joint performance. Results reveal similar performance between aluminum and composite straps, with the latter having an advantage when considering added weight to the system.

While the FEM has been extensively used to analyze the behavior and performance of adhesively bonded SLJs, this study introduces new insights into the optimization of support patch geometries. Unlike previous research, which has largely focused on the adhesive layer and overall joint geometry, the investigation specifically targets the nuanced effects of support patch parameters including thickness, position, length, and their combined influence on stress distribution and joint strength. This research analyzes a wide range of support patch configurations using a detailed parametric study. The novelty of the approach lies in the integration of multi-parameter variations to pinpoint the most influential factors contributing to the performance enhancement of adhesive bonded SLJs. The author employs advanced 3D FE analysis to capture the complex interplay between these variables, providing a more in-depth understanding of their impact on the mechanical behavior of the joint.

Furthermore, the study ventures beyond the typical analysis by comparing the numerical results with existing studies and analytical solutions like Volkersen [24] and Goland and Reissner [25], offering a validation perspective seldom taken in the literature. The resulting data set and findings are unique in their breadth and depth, delivering actionable insights for the design of more robust and efficient adhesive joints in industrial applications. By pushing the boundaries of current analytical methods and exploring the combined effects of various patch geometries, this study advances state-of-the-art in the FE analysis of adhesively bonded single lap joints (ABSLJs). The effect of the support patch on the outer part of the adherent layer of adhesively bonded SLJs on the stress distribution within the joint was investigated. A comprehensive FE analysis was conducted to numerically evaluate the influence of different support patch parameters and their positions on the strength of SLJs. The results showed that the dimensions and placement of the support patch have the potential to reduce the load and stress distribution in different regions of the adhesive joint, thereby potentially increasing its strength.

The findings contribute to closing the gap between theoretical research and practical, real-world applications, setting a precedent for future experimental validations and innovative design strategies in structural joint assemblies.

2 MATERIAL AND METHODS

The SLJ serves as a standard benchmark in adhesive comparisons, characterized by a non-uniform stress distribution along the adhesive thickness and lap length. Several factors intricately influence the shear and peel stresses within this joint assembly. The effectiveness of the joint is significantly impacted by adhesive application methods, surface preparation, physico-chemical properties of the adhesive, assembly dimensions, and adhesive thickness. The adhesively SLJ, renowned for its simplicity, finds extensive use with adherents composed of metallic or fiber composite materials. This joint type is a subject of frequent investigation to comprehend its strength and characteristics. Notably, the SLJ stands out for its uncomplicated design and ease of assembly, making it a cost-effective and widely employed configuration. In this study, adherence to the ASTM D1002 standard [25] for determining joint shear strength ensures consistency and reliability in the evaluation process.

2.1 SLJ Dimensions

The SLJ dimensions include a 0.18 mm adhesive thickness (t), 2 mm adherent thickness (k), 25 mm lap length, and 25 mm substrate width (w). The parametrically studied parameters, thickness of the support patch (u), the adhesive thickness bonding the support patch to the adherent (s), length of the support patch (d), and position of the support patch (e) are presented in Table 1. The position of the support piece, denoted as the distance between the adherent end (q) and the midpoint of the support piece, is shown in Figs. 1 and 2. The directions are indicated as longitudinal (x) and transverse (y), while the $z-$axis aligns with the substrate width direction.
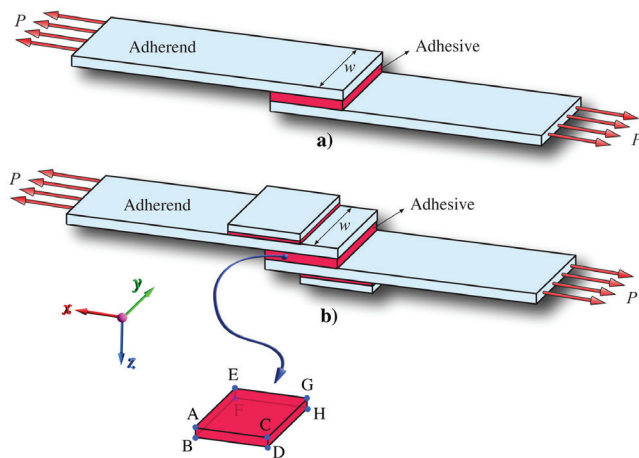

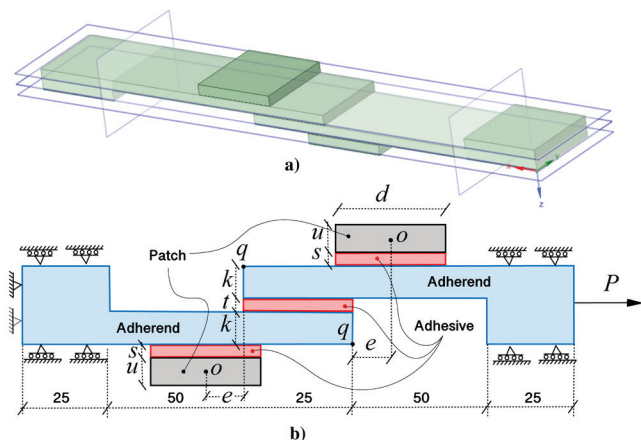
Fig. 1. 3D Support-patched SLJs

Fig. 2. Support-patched SLJs; a) ANSYS model, and b) geometry and boundary conditions

2.2 FE Analysis Setup and Loading Conditions for SLJ

In the FE analysis, the upper substrate of the adhesive joint was fixed at one end in a single bottom configuration, while the overlapping substrate was subjected to an axial force (F) at the opposite end. The transverse movement of the overlapping substrate was constrained, as indicated in Fig. 1. The end where the loading occurred retained the freedom to move along the x axis. Subsequent loading was applied to validate and predict the structural response for this specific analysis. Fig. 2 provides a visual representation of the loading conditions and constraints (boundary conditions, BC) essential for the analysis of the SLJ. This configuration allows for a comprehensive examination of the joint's behavior under applied loads, facilitating a thorough understanding of its structural performance.

In the FE analysis of the SLJs, careful consideration was given to the mesh configuration to optimize accuracy and computational efficiency. The model primarily utilized hexahedral mesh elements due to their suitability for capturing the complex stress gradients typical in adhesive joints. A convergence study was performed to determine the appropriate mesh density, particularly focusing on areas of high stress concentration where finer meshing was necessary. The advanced 3D FE analysis captures the complex interactions of support patch geometries. This methodology goes beyond existing 2D models, providing a more realistic simulation of the three-dimensional stress distribution in adhesive joints.

Table 1. The configuration of the SSLJ

Sp.	u [mm]	s [mm]	e [mm]	d [mm]	Joint type
1	-	-	-	-	SLJ
2	k	t	0	l	SSLJ
3	$k/2$	t	0	l	SSLJ-K2
4	$k/4$	t	0	l	SSLJ-K4
5	k	$t/2$	0	l	SSLJ-T2
6	k	$t/4$	0	l	SSLJ-T4
7	k	t	0	$l/2$	SSLJ-L2
8	k	t	$d/4$	$l/2$	SSLJ-D4-L2
9	k	t	$d/2$	$l/2$	SSLJ-D2-L2
10	k	t	$d/4$	l	SSLJ-D4
11	k	t	$d/2$	l	SSLJ-D2
12	k	t	0	$3l/2$	SSLJ-3L2
13	k	t	$d/4$	$3l/2$	SSLJ-D4-3L2
14	k	t	$d/2$	$3l/2$	SSLJ-D2-3L2
15	k	t	0	$2l$	SSLJ-2L
16	k	t	$d/4$	$2l$	SSLJ-D4-2L
17	k	t	$d/2$	$2l$	SSLJ-D2-2L

Surface interactions between the adhesive layer and the adherends were modeled using cohesive zone models (CZM) to simulate the potential delamination and failure modes realistically. This approach allows for the consideration of both the mechanical properties of the materials and the interface behavior under load. Tie constraints were applied where necessary to ensure that the movement between the adherends and the adhesive was realistically constrained, reflecting the physical bond. These constraints were essential in modeling the load transfer across the joint without slippage, which is critical for assessing the joint's integrity under stress.

2.3 Material Properties of Adhesive and Adherend

In this study, DP-460NS was utilized as the adhesive, with Aluminum 6061 serving as the adherend material in SLJs. DP-460NS is an epoxy adhesive manufactured by the company 3M, known for its chemical resistance and environmental durability [21]. It requires a mixing ratio of 2 parts resin to 1 part hardener, with a working time of approximately 20 to 30 minutes and full cure of about 24 hours at room temperature. It is suitable for bonding a variety of materials and is commonly used in aerospace, automotive, electronics, and general industrial applications. Aluminum 6061 is a popular alloy known for its excellent combination of strength, weldability, and corrosion resistance. It falls within the category of 6000 series aluminum alloys, a class distinguished by its predominant composition of aluminum, accompanied by the alloying elements magnesium and silicon [27]. The alloy's composition, characteristic of the broader series, imparts it with unique properties and versatile applications across various industries [23]. The material properties of the adherent and adhesive are presented in Table 2.

Table 2. Material Properties [28]

Material	Young's modulus [GPa]	Poisson ratio	Yield stress [MPa]	Tangent modulus [GPa]
Aluminum 6061	71	0.33	125	1.48
DP460-NS Adhesive	2.2	0.41	36	0.5

In this study, the adhesive layer was modeled using the CZM. CZM operates by utilizing the relationship between stresses and relative displacements and exhibits elastic behavior up to the cohesive strength (in tension, T_n; in shear, T_t) [28]. For analysis with CZM, it is essential to know the parameters $\sigma_{n\max}$, G_{IC}, $\tau_{t\max}$, and G_{IIC}, where $\sigma_{n\max}$ is is the maximum normal cohesive strength (32.6 MPa), G_{IC} is the mode I fracture energy (2.56 N/mm), $\tau_{t\max}$ is the maximum shear cohesive strength (28.5 MPa), and G_{IIC} is the mode II fracture energy (11.71 N/mm). The CZM parameters used in the analysis are provided in Table 3.

Table 3. CZM parameters of the adhesive [29]

Parameter	Value	Parameter	Value
$\sigma_{n\max}$ [MPa]	32.6	$\tau_{t\max}$ [MPa]	28.5
G_{IC} [N/mm]	2.56	G_{IIC} [N/mm]	11.71

2.4 Support Patch Geometry

Adhesive-bonded joint with support patch was analyzed using FEA with 21 different parameters to investigate its effect on the peel and shear stress distributions on the bonded joint adhesive surface. In order to compare the results, a classical SLJ analysis was also performed. To examine the influence of support patch thickness on the joint strength, three different values were considered. Additionally, three values of adhesive thickness (s) connecting the support patch were investigated. Furthermore, a 12-parameter analysis was conducted to study the effects of support patch length (d) and position (e). The results are presented below.

2.5 FE analysis of SLJ

Boundary conditions are critical for the accuracy of FE simulations. In this study, the boundary conditions were designed to replicate realistic service conditions of the SLJs. The ends of the adherends were constrained to mimic the fixed and free ends typically encountered in engineering applications, allowing for a detailed analysis of stress distributions under applied loads.

The model utilized hexahedral volume elements for their balance of accuracy in capturing stress gradients and efficiency in computation. Hexahedral elements, particularly well-suited for modeling regular geometries, provided a structured mesh conducive to capturing the mechanical behavior of the adhesive joint.

Mesh density is a pivotal factor in FE analysis, with a finer mesh typically leading to more accurate results. An iterative mesh refinement procedure was conducted to ascertain the optimal mesh density. Starting with a coarse mesh, the number of elements was progressively increased until the shear stress values at specific points of interest on the adhesive layer stabilized. This approach ensured that the mesh was sufficiently refined in the overlap and other regions of discontinuity, where stress gradients are the steepest, without unnecessarily increasing the computational load.

Fig. 3 depicts the meshing strategy utilized in the FE model. It highlights the refined mesh in the overlap area, reflecting the higher density of elements where the most significant stress variations are expected. The final mesh consisted of 662582 hexahedral elements and 2872700 nodes, providing the resolution required to accurately capture the essential stress characteristics of the SLJs.
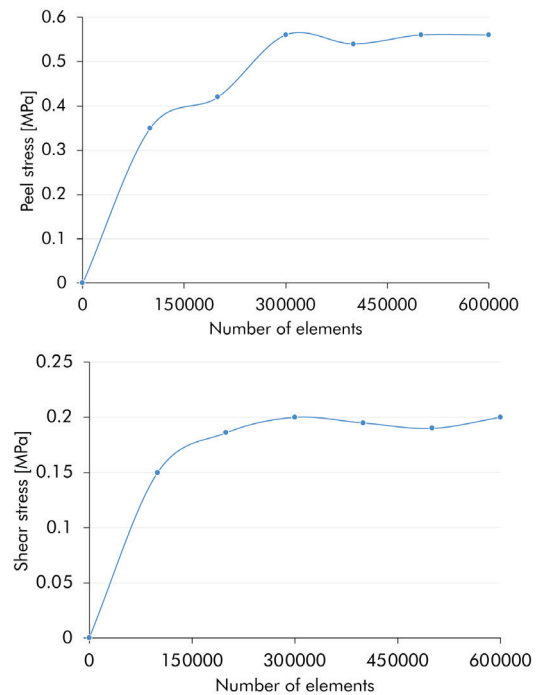
Fig. 3. FE mesh converge and the FE model of SLJ

2.6 Analytical Solutions

The Volkersen solution, which neglects the bending moment, is an analytical model used to analyze the adhesive shear stress distribution in a SLJ (Fig. 4). This model was developed by Volkersen in 1938 [24]. Also known as the "shear-lag model," it takes into account the differential shear of the adhesive in different regions. It is used to estimate the varying adhesive shear stress distribution along the bond line as in [30, 31].

When the substrates are of the same thickness, the shear stress reaches its maximum value. Therefore, it will be considered that the substrates have the same thickness. Furthermore, if the lap joint region also has equal length (l) and width (w), the equation simplifies as follows [31, 32]

$$\tau(x) = \sigma_{xz} = \frac{P\Psi}{2l^2}\left[\frac{\cosh[\Psi x]}{\sinh\left(\frac{\Psi L}{2}\right)}\right], \tag{1}$$

where

$$\Psi = \sqrt{\frac{2G_a}{Ekt}}. \tag{2}$$

Eq. (1) is applicable under the condition that the thicknesses of the two adherends are equal.
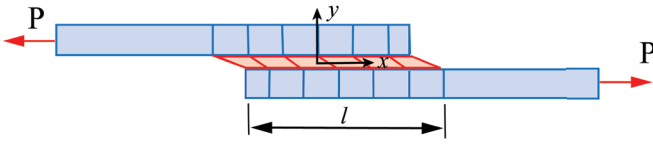
Fig. 4. Volkersen scheme for SLJ

The Goland and Reissner [25] analysis, which represents another analytical approach, is employed to assess the stress distribution in SLJs. This analysis assumes that the adhesive is elastic and that the adhesive layers are significantly stiffer. It takes into account the effects of rotation of the adherends, as shown in Fig. 5. Furthermore, the analysis considers the shear deformation of the adhesive layers [32]. The analysis provides equations that describe the adhesive shear stress distribution along the joint.

Fig. 5. Goland and Reissner scheme of SLJ

The formula for the distribution of adhesive shear stress τ according to Goland and Reissner [25] is given by the expression:
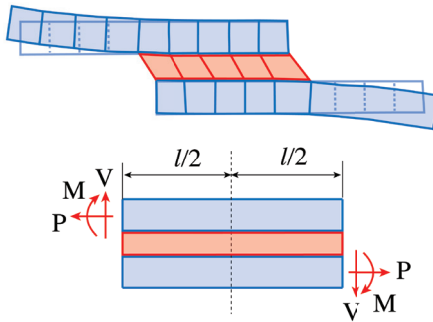
$$\tau = -\frac{1}{4}\frac{P}{l}\left\{\frac{\beta l}{2k}(1+3b)\frac{\cosh\left(\frac{\beta l}{2k}\frac{2x}{l}\right)}{\sinh\left(\frac{\beta l}{2k}\right)}+3(1-b)\right\}. \tag{3}$$

Parameter b corresponds to the bending moment factor, which is derived from [25] and cited in [32].

$$b = \frac{\cosh\left(u_2\frac{l}{2}\right)}{\cosh\left(u_2\frac{l}{2}\right)+2\sqrt{2}\sinh\left(u_2\frac{l}{2}\right)}, \tag{4}$$

where $u_2 = \sqrt{\frac{3(1-v^2)}{2}}\frac{1}{k}\sqrt{\frac{P}{kE}}$ and $\beta^2 = 8\frac{G_aE}{kt}$ is Poisson's ratio.

In the equations presented in this section, the variables are the following; E, elastic modulus [MPa], t, adhesive thickness [mm], k adherend thickness [mm], G_a shear modulus of adhesive [MPa], σ normal stress [MPa], τ, shear stress [MPa], P applied load [N], l overlap length [mm], Ψ parameter related to shear stress distribution [-], and b bending moment factor [-].

3 RESULTS AND DISCUSSIONS

3.1 Validation of the Current Numerical Study

Fig. 6 presents the adhesive shear stresses comparing the results from the current study with those from a numerical study by [7] and two analytical solutions [24, 25]. It validates the results of the study by using a SLJ with identical geometry and boundary conditions (support and loading) as those used in the referenced studies.

The comparison highlights significant differences between the 2D analytical solutions and the 3D FE analysis. The 2D models, while offering insights into shear and peel stress distributions, simplify the stress state by ignoring out-of-plane effects that are crucial for certain joint configurations. The 3D FE analysis incorporates these out-of-plane stresses, providing a more comprehensive understanding of the stress distributions across the adhesive joint. Notably, both shear and peel stresses were observed to be symmetric around the center of the joint length, reaching values significantly higher than those predicted by Volkersen 2D model. This discrepancy is mainly due to the 2D model's inability to effectively simulate the complex 3D stress state, particularly under multi-axial stress conditions.

Additionally, the Goland & Reissner model, although also 2D, includes considerations for the rotational stiffness of the adherends, offering a closer approximation to real-world conditions under certain loadings. This model displayed increased stress under specific conditions, likely influenced by moment effects not accounted for in simpler 2D models.
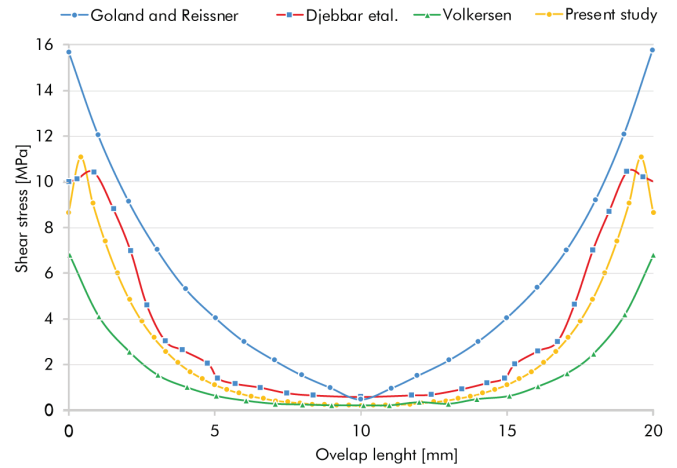
Fig. 6. Shear stress distribution from the finite element analysis of a SLJ, compared with analytical solutions

In conclusion, this comparative analysis emphasizes the critical role of 3D modeling for a more accurate representation of stress distributions in adhesive joints, especially in configurations where out-of-plane stresses are significant. However, 2D models still hold value for preliminary analyses in scenarios with minimal out-of-plane effects, due to their computational efficiency and simpler analytical approach. The choice between using 3D and 2D modeling should be guided by the specific requirements of the joint configuration. The results confirm that both the analytical and FE models provide coherent data that accurately predict joint behavior in SLJs, affirming the validity and reliability of the FE analysis.

3.2 Numerical Results

This section aims to investigate the effects of adhesive thickness, position, length, and thickness of reinforcement patches on the stress distributions of various SSLJs. To achieve this goal, a series of SLJs were simulated using the FE model in ANSYS software [33], incorporating various reinforcement patch configurations. These simulations encompass a range of SLJs with different parameter combinations, as detailed in Table 1. The obtained numerical results were analyzed to determine the optimized effects of varying adhesive thicknesses, positions, lengths, and thicknesses on the stress distributions of SLJs, aiming to identify the most suitable configuration.

Fig. 7 presents the peel stress distribution on the surface of a representative adhesive region. This distribution corresponds to the BDHF surface area depicted in Fig. 1. To facilitate a comparison of parametric analysis results, the stress distributions considered are along the 'overlap length' referred to as the BD line with the bonding region shown in Fig. 1. All two-dimensional graphs in this study are derived from stress distribution analyses along this BD line.

When adhesively bonded SLJs are subjected to bending loads, it is observed that the plates near the bonding area tend to bend outward. This bending notably increases the peel stresses within the adhesive region. In this study, the addition of a support patch to the bonded plate aims to reduce bending and, consequently, decrease peel stresses. The effects of the geometric dimensions and positioning of the support patch on the stress distribution will be thoroughly investigated.
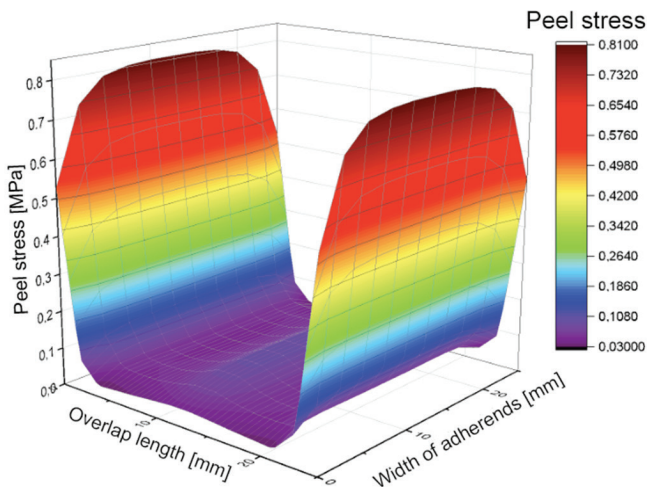
Fig. 7. 3D Stress distribution on the surface of the overlap region

3.3 Effect of Support Patch Thickness

To examine the influence of support patch thickness on the adhesive region, FE analysis was conducted for three different support patch thicknesses. The adhesive thickness used in the analysis was selected to be equal to the thickness of the support patches (i.e., denoted as $s=t$ in Fig. 2). Additionally, in the analysis, the center point (O) of the support patch and the points at the ends of the bonded plate (q) were aligned in the same vertical direction (i.e., set as $e=0$ in Fig. 2). Moreover, the patch length was chosen to be equal to the bonding length in the analysis (i.e., set as $d=l$ in Fig. 2).

For the purpose of comparing analysis results, changes in peel stress along the bonding length are presented graphically in Fig. 8a, while the shear stress results are illustrated in Fig. 9a.

Upon examination of Fig. 8a, it is observed that, at the edges of the adhesive region, there is a peel stress reduction of up to 70 % when compared to a SLJ with the same boundary conditions. This indicates significant alterations in the adhesive region.

In SSLJs, as the support patch thickness increases, peel stress values in the central regions of the adhesive area vary compared to SLJ. A decrease of 12 % for $u=k/4$, 25 % for $u=k/2$, and 40 % for $u=k$ is observed. However, an increase in support patch thickness has not caused a significant change in stress values at the edges.

Examining Fig. 9a, it can be seen how shear stress values change in the central regions of the adhesive area as the support patch thickness increases. A reduction of 11 % for $u=k/4$, 18 % for $u=k/2$, and 29 % for $u=k$ is recorded compared to SLJ. Peel and shear stress values in the middle sections of the bonded overlap region

decrease proportionally with an increase in support patch thickness. Additionally, the increase in support patch thickness has led to a more pronounced decrease in peel stress than observed for shear stress.

3.4 Effect of Support Patch Adhesive Thickness

To investigate the influence of adhesive thickness specific to the support patch on the bonding region of the main plates, FE analysis was conducted for three different adhesive thicknesses of the support patch. In the analysis, the thickness of the main plates bonded with adhesive and the thickness of the support patches were chosen to be equal (i.e., denoted as $u=k$ in Fig. 2). Additionally, in the analysis, the center point (O) of the support patch and the points at the ends of the bonded plate (q) were aligned in the same vertical direction (i.e., set as $e=0$ in Fig. 2). Moreover, the patch length was selected to be equal to the bonding length in the analysis (i.e., set as $d=l$ in Fig. 2).

For the purpose of comparing analysis results, changes in peel stress along the bonding length are presented graphically in Fig. 8b, while the shear stress results are illustrated in Fig. 9b.

In SSLJs, selecting the same thickness for the adhesive bonding the support patch (s) and the adhesive bonding the main plates (t) reduces peel stress at the edges of the bonding region by 71 % compared to SLJ. Choosing the patch adhesive thickness as half of t ($s=t/2$) or one-fourth of t ($s=t/4$) yields the same peel and shear stress results along the bonding length. Additionally, selecting the patch adhesive thickness equal to t reduces the maximum value of peel stress by 64 % compared to when s is half of t ($s=t/2$) or one-fourth of t ($s=t/4$), without causing any change in shear stress values. Selecting specific ratios for patch adhesive thicknesses in SSLJs significantly reduces peel stress without affecting shear stress values. These findings can provide guidance in the optimal selection of adhesive thicknesses in structural joint design.

3.5 Effect of Support Patch Position

To investigate the influence of support patch length (d) when the bonding length is two times smaller ($l=d/2$), analyses were conducted for different patch positions (e) of 0, $d/4$, and $d/2$. The results revealed that the lowest peel stress at the edges and center of the bonding region occurred at $e=0$, as observed in Figs. 8c and 9c. The peel stress value at the edges of the bonding region at $e=0$ is 68 % lower than at $e=d/4$ and 74 % lower than at $e=d/2$. It was also determined that the shear stress values were the same at all three positions.

For cases where the support patch length is equal to the bonding length ($d=l$), results for patch positions of 0, $d/4$, and $d/2$ showed that the lowest peel and shear stress values at the edges and center of the bonding region occurred at $e=0$, as observed in Figs. 8d and 9d. The peel stress value at the edges of the bonding region at $e=0$ is 63 % lower than at $e=d/4$ and 75 % lower than at $e=d/2$. Additionally, the shear stress value at the edges of the bonding region at $e=0$ is 60 % lower than at $e=d/4$ and $e=d/2$.

When the support patch length is 3/2 times the bonding length ($d=3l/2$), results for patch positions of 0, $d/4$, and $d/2$ showed that the highest peel stress at the edges of the bonding region occurred at $e=d/4$, as observed in Fig. 8e. Peel stress values at the edges of the bonding region at $e=0$ and $e=d/2$ positions are the same and 2 % lower than at $e=d/4$. Peel stress at the center of the bonding region at $e=0$ is 50 % lower than at $e=d/4$ and 40 % lower than at $e=d/2$, as observed in Fig. 8e. Additionally, shear stress values at the edges of the bonding region at $e=d/4$ and $e=d/2$ positions are the same and 12 % higher than at $e=0$. Shear stress values at the center of the bonding region at $e=0$ and $e=d/4$ positions are the same and 14 % higher than at $e=d/2$.
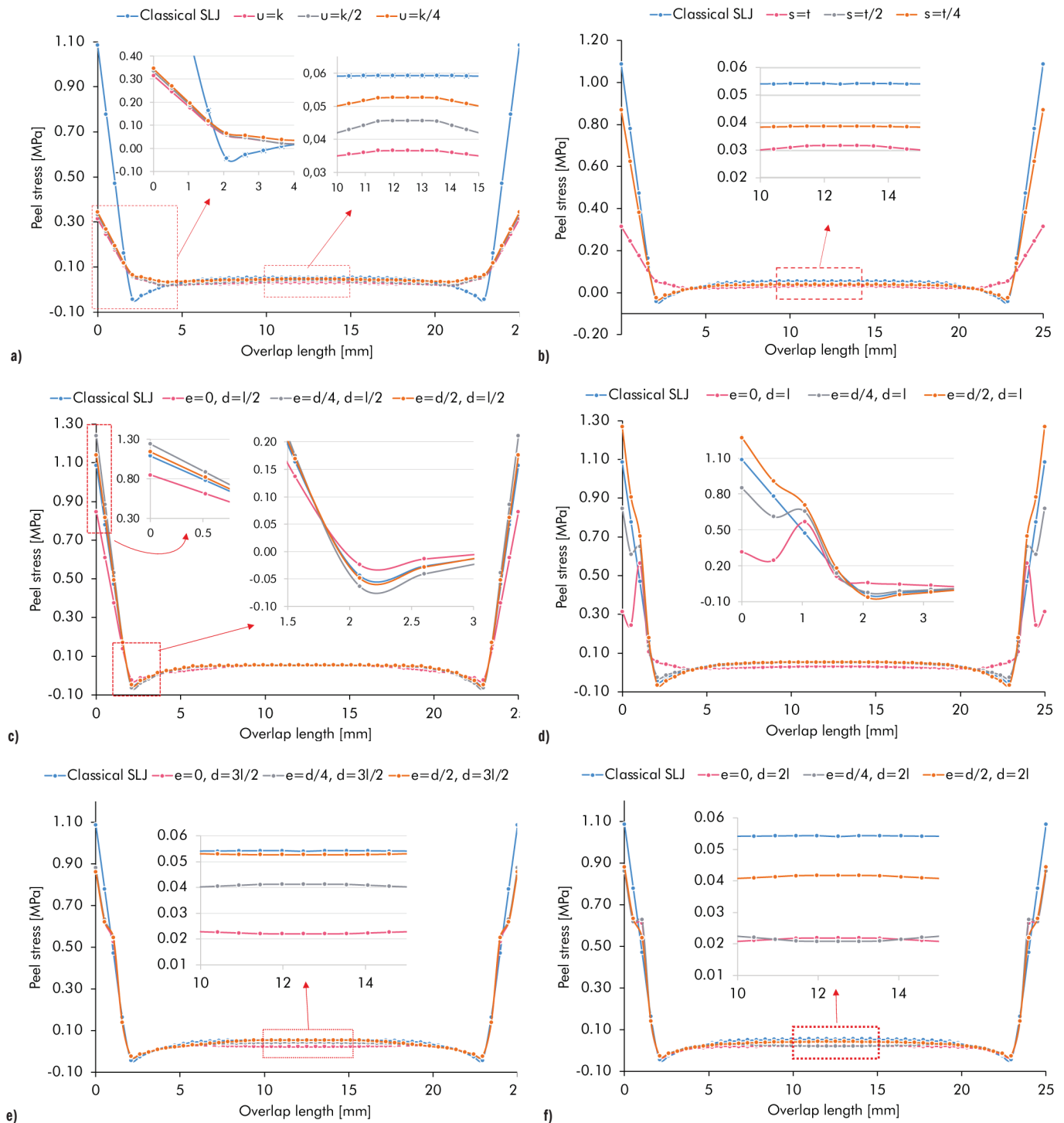
Fig. 8. Peel stress distribution along the length of the overlap zone

When the support patch length is twice the bonding length ($d=2l$), analyses for patch positions of 0, $d/4$, and $d/2$ showed that the highest peel stress at the edges and center of the bonding region occurred at $e=d/2$, as observed in Fig. 8f. Peel stress values at the edges and center of the bonding region at $e=0$ and $e=d/4$ positions are the same and 2 % lower than at $e=d/2$. For those cases the lowest shear stress at the edges and center of the bonding region occurred at $e=0$, as observed in Figs. 9e and f. The shear stress value at the edges of the bonding region at $e=0$ is 16 % lower than at $e=d/4$ and 30 % lower than at $e=d/2$. The shear stress values at the center of the bonding

region at $e=0$ is 7 % lower than at $e=d/4$ and 12 % lower than at $e=d/2$.

3.6 Effect of Support Patch Length

When the support patch is positioned at $e=0$, the author conducted analysis for different lengths of the support patch ($d=l/2$, l, $3l/2$, and $2l$). Notably, when the support patch length matches the adhesive length ($d=l$), the author observed the lowest peel stress at the edges of the bonded region (Figs. 8c, d, e, and f). In this scenario, the peel stress at the edges is 36 % lower compared to cases with $d=l/2$,
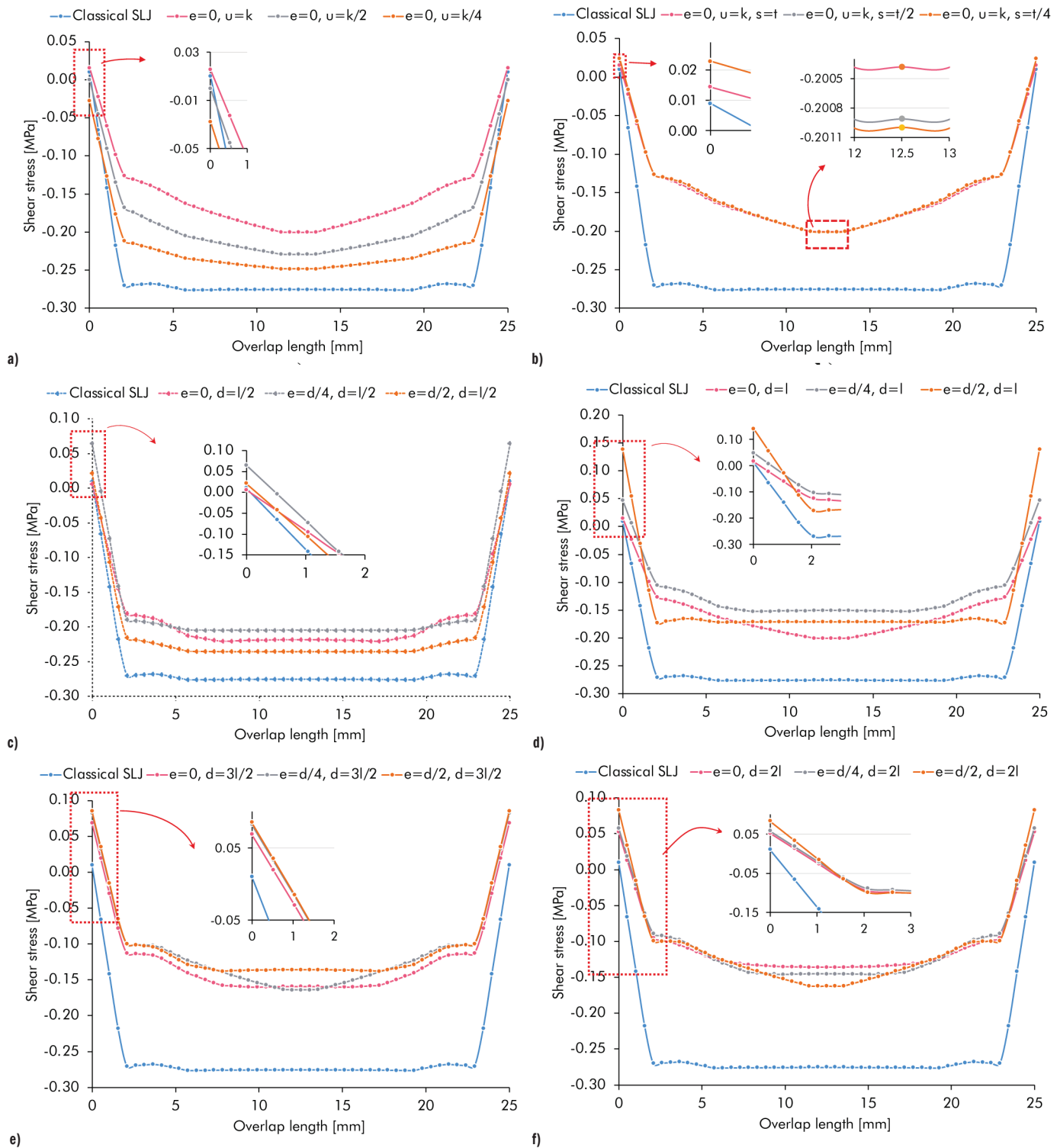
Fig. 9. Shear stress distribution along the length of the overlap zone

$d = 3l/2$, and $d = 2l$. Moreover, the peel and shear stresses reach their highest values at the midpoint when $d = l/2$. Specifically, when $d = l/2$, the peel stress at the midpoint is 66 % higher compared to $d = 1$, and 150 % higher compared to $d = 2l$ and $d = 2l$. Additionally, the shear stress at the midpoint is 10 % higher for $d = 2l$ compared to $d = l$, 37 % higher for $d = 3l/2$, and 57 % higher for $d = 2l$ (Figs. 8c, d, e, and f).

For $e = d/4$, analysis was performed for various lengths ($d = l/2$, l, $3l/2$, and $2l$). It was found that when the support patch length is

equal to the adhesive length ($d = l$), the lowest shear and peel stresses are observed at the edges of the bonded region (Figs. 8c, d, e, and f). In this scenario, the peel stress at the edges is 31 % lower for $d = l/2$, 3 % lower for $d = 3l/2$, and 1 % lower for $d = 2l$. Additionally, at the midpoint of the bonded region, the peel stress is lowest when $d = 2l$. Consequently, for $d = 2l$, the peel stress at the midpoint is 60 % lower than for $d = l/2$ and $d = l$, and 50 % lower than for $d = 3l/2$. Furthermore, the shear stress at the midpoint is 17 % lower for

$d=l/2$ and $2l$ compared to $d=3l/2$, and 37 % lower for $d=l/2$ and $2l$ compared to $d=3l/2$. The shear stress is lowest at the midpoint when $d=2l$ (Figs. 8c, d, e, and f).

For $e=d/2$, and when the support patch length is 3/2 times the adhesive length ($d=3l/2$), the lowest peel stress is observed at the edges of the bonded region (Figs. 8c, d, e, and f). Specifically, when $d=3l/2$, the peel stress at the edges is 25 % lower for $d=l/2$, 32 % lower for $d=l$, and 2 % lower for $d=2l$. Moreover, at the midpoint of the bonded region, the peel stress is lowest when $d=2l$. Consequently, for $d=2l$, the peel stress at the midpoint is 20 % lower than for $d=l/2$ and $d=l$, and 50 % lower than for $d=3l/2$. For support patch length $d=l/2$, the lowest shear stress is observed at the edges of the bonded region (Figs. 8c, d, e, and f). Specifically, when $d=l/2$, the shear stress at the edges is 85 % lower than for $d=l$, 80 % lower than for $d=3l/2$, and 80 % lower than for $d=2l$. Additionally, at the midpoint, the shear stress is lowest when $d=3l/2$. Consequently, for $d=3l/2$, the shear stress at the midpoint is 58 % lower than for $d=l/2$, 18 % lower than for $d=l$, and 12 % lower than for $d=3l/2$ (Figs. 8c, d, e, and f).

These results demonstrate that the length of the reinforcement patch significantly influences the stress values in the adhesive region and indicate that optimal results can be achieved at specific geometrical parameters.

3.7 The effect of Adhesive Material Properties on Optimal Support Patch Configurations

The optimal configuration of support patches is highly dependent on the mechanical properties of the adhesive material. A more flexible adhesive with lower stiffness and higher elongation capacity would result in a more uniform stress distribution across the bond line. In such a case, support patches with increased length and thickness might be required to counteract the increased deformation and potential stress concentration at the edges. Thicker adhesive layers might be beneficial in reducing peel stresses, thereby allowing a wider range of support patch positions to be effective. On the other hand, a brittle adhesive with higher stiffness and lower fracture toughness would be more sensitive to stress concentrations. In this scenario, it is crucial to design support patches that minimize sharp stress gradients. An optimal design could involve gradual tapering of the support patch edges and the inclusion of fillets to smoothly transfer loads across the adhesive region. Furthermore, smaller patch thicknesses and more centrally positioned patches might be preferred to avoid excessive stress localization at the interface. Recent study provides results about mechanical properties of pressure-sensitive adhesives and the effects of environmental factors, such as thermal shocks, on these properties [34]. It examines the interaction of adhesives with different materials and their resistance to environmental conditions. These insights suggest that while the general trends observed in this study hold, additional experimental and numerical validations are necessary to refine the selection of support patch geometries based on the specific adhesive type employed.

4 DISCUSSIONS

This research presents an in-depth analysis of the effects of support patch geometry on the stress distribution within adhesively bonded SLJs, advancing the understanding of joint behavior and optimization potential. The FE simulations provided a comprehensive evaluation of various patch parameters and their positions, with a particular focus on optimizing the support patch to mitigate stress concentrations, which are critical to the joint's integrity.

The FE results indicate that the dimensions and placement of support patches significantly affect load and stress distribution. For instance, increased support patch thickness (u) correlates with a marked reduction in both peel and shear stresses within the adhesive region, particularly along the joint's edges. Findings underscore the potential of support patches to enhance the mechanical performance of SLJs and, by extension, the reliability of structures that incorporate these joints. It is demonstrated that specific support patch configurations significantly reduce stress concentrations and improve load distribution in adhesive joints. Compared to previous studies, these results show lower stress levels and higher joint durability.

Interestingly, the study also reveals that while the adhesive thickness specific to the support patch significantly reduces peel stress, it has a negligible effect on shear stress. This observation is particularly relevant for structural joint design, where peel stress is a critical factor. It demonstrates the need for a targeted approach for adhesive thickness selection, one that aligns with the specific stress distribution requirements of the joint configuration.

The influence of support patch position (e) also proved to be significant, with optimal patch positioning leading to the lowest stress values at the edges and center of the bonding region. This aspect of the study offers the understanding of how patch positioning can be leveraged to further fine-tune the stress distribution within the joint.

Moreover, the relationship between the support patch length (d) and the bonding length (l) was highlighted as a key factor in determining the effectiveness of the support patch. The results from this study provide a benchmark for selecting appropriate patch lengths, indicating that a patch length equal to the bonding length offers the best performance in terms of stress reduction.

While FEA provides valuable insights into stress distribution, it has limitations in predicting real-world joint performance. Factors such as adhesive defects, environmental effects, and material nonlinearities are not fully captured. Experimental validation through mechanical testing is essential to refine numerical models and enhance their reliability for practical applications. For long-term structural reliability, the impact of environmental factors should be considered. Adhesive materials are known to be sensitive to temperature variations, humidity, and prolonged loading conditions. For instance, at elevated temperatures, some adhesives may experience a decrease in elastic modulus, while at lower temperatures, they may become more brittle, affecting bond strength. Additionally, moisture diffusion into the adhesive interface can weaken adhesion and cause degradation over time. Under sustained loading conditions, creep effects and fatigue behavior become significant concerns. Future studies should focus on experimental validation under temperature- and humidity-controlled environments to assess the durability of optimized patch configurations. Such investigations will enhance the reliability of adhesively bonded joints in long-term engineering applications.

5 CONCLUSIONS

This study investigates the effects of adhesive thickness, position, length, and reinforcement patch thickness on the peel and shear stress distributions in various SLJs. Utilizing the FE model in ANSYS R software, a series of SLJs with different reinforcement patch configurations were simulated. The obtained numerical results underwent detailed analysis to determine the optimized effects of varying adhesive thicknesses, positions, lengths, and thicknesses on the stress distributions of SLJs. The findings obtained are listed below:

- In SSLJs, the peel stress value in the middle part of the bonding region decreases proportionally with an increase in the support patch thickness, while the increase in support patch thickness has not caused a significant change in stress at the edge. Moreover, the

increase in support patch thickness results in a greater decrease in peel stress compared to the decrease in shear stress.

- In SLJs, the patch support has a negligible effect on the shear stress at the edges of the bonding region, while it is observed to reduce shear stress values in the middle section of the bonding region.
- Selecting specific ratios for patch adhesive thicknesses in SSLJs significantly reduces peel stress without affecting shear stress values.
- The analysis results indicate that the ratio of support patch length (d) to bonding length (l) has a determining effect on the patch position (e). Specifically, in the case of $d = l/2$, the lowest peel stress values are achieved at $e = 0$, while in the case of $d = 2l$, the highest peel stress values are observed at $e = d/2$.
- It is demonstrated that the optimal bonding performance is achieved when the support patch length is equal to the bonding length.

This study makes a significant contribution to the literature by optimizing support patch geometries in adhesively bonded SLJs. The findings have practical implications for designing more durable and long-lasting adhesive joints in industrial applications.

The FEA conducted in this study has comprehensively revealed the effects of support patches on stress distribution in adhesively bonded single lap joints. However, such numerical studies may be limited unless validated through real-world applications. Future studies should focus on experimentally verifying these numerical results to enhance their reliability. Conducting experiments in accordance with established standards and statistically analyzing the obtained stress data would significantly improve the accuracy and applicability of the findings. Such an approach would not only increase confidence in numerical analyses but also assist engineers in making more reliable design decisions for practical applications. Additionally, the impact of environmental factors, such as temperature variations, humidity, and long-term loading conditions, on the mechanical performance of the optimized patch configurations should be investigated in future research.

References

[1] Alves, D.L., Campilho, R.D.S.G., Moreira, R.D.F., Silva, F.J.G., da Silva, L.F.M. Experimental and Numerical Analysis of Hybrid Adhesively-Bonded Scarf Joints. *Int J Adhes Adhes* 83, 87-95 (2018) **DOI:10.1016/j.ijadhadh.2018.05.011**

[2] Araujo, H.A.M., Machado, J.J.M., Marques, E.S., da Silva, L.F.M. Dynamic Behaviour of Composite Adhesive Joints for the Automotive Industry. *Compos Struct* 171, 549-561 (2017) **DOI:10.1016/j.compstruct.2017.04.049**

[3] Banea, M.D., da Silva, L.F.M., Campilho, R.D.S.G. Principles of Adhesive Bonding. *Joining of Polymer-Metal and Polymer-Polymer Hybrid Structures: Principles and Applications*, p. 3-27 (2018) **DOI:10.1002/9781119429807.ch1**

[4] Gomes, L.A.R., Campilho, R.D.S.G., Valente, J.P.A., Queirós, M.J.R., Madani, K. Impact Loading Analysis of Double-Lap Composite Bonded Joints. *Int J Adhes Adhes* 128, 103547 (2024) **DOI:10.1016/j.ijadhadh.2023.103547**

[5] Fernandez-Canadas, L.M., Ivañez, I., Sanchez-Saez, S., Barbero, E.J. Effect of Adhesive Thickness and Overlap on the Behavior of Composite Single-Lap Joints. *Mech Adv Mater Struct* 28 1111-1120 (2019) **DOI:10.1080/15732479.2019.1573245**

[6] Ozer, H., Oz, O. The Use of the Exponential Drucker-Prager Material Model for Defining the Failure Loads of the Mono and Bi-Adhesive Joints. *Int J Adhes Adhes* 76, 17-29 (2017) **DOI:10.1016/j.ijadhadh.2016.12.006**

[7] Djebbar, N., Boutabout, B., Rachid, H.B., Ouadad, W. Effect of Spew Adhesive and Beveling Substrate Geometrical Shape on Stresses in a Bonded Single Lap Joint. *Eng Struct* 256, 114049 (2022) **DOI:10.1016/j.engstruct.2022.114049**

[8] Haddou, Y.M., Salem, M., Amiri, A., Amiri, R., Abid, S. Numerical Analysis and Optimization of Adhesively-Bonded Single Lap Joints by Adherend Notching Using a Full Factorial Design of Experiment. *Int J Adhes Adhes* 126 103482 (2023) **DOI:10.1016/j.ijadhadh.2023.103482**

[9] Demir, K., Bayramoglu, S., Akpinar, S. The Fracture Load Analysis of Different Support Patches in Adhesively Bonded Single-Lap Joints. *Theor Appl Fract Mech* 108 102653 (2020) **DOI:10.1016/j.tafmec.2020.102653**

[10] Amaro, A.M., Neto M.A., Loureiro A., Reis P.N.B. Taper's angle influence on the structural integrity of single-lap bonded joints. *Theor Appl Fract Mech* 96 231-246 (2018) **DOI:10.1016/j.tafmec.2018.06.005**

[11] Çalik, A. Effect of Adherend shape on stress concentration reduction of adhesively bonded single lap joint. *Eng Rev* 36 29-34 (2016)

[12] Afkar, A., Camari, M.N. Finite element analysis of mono- and bi-adhesively bonded functionally graded adherend. *J Fail Anal Prev* 14 253-258 (2014) **DOI:10.1007/s11668-014-9814-5**

[13] Marchione, F. Effect of hollow adherends on stress peak reduction in single-lap adhesive joints: FE and analytical analysis. *J Adhes Sci Technol* 98 656-676 (2021), **DOI:10.1080/00218464.2021.1995368**

[14] Bayramoglu, S., Demir, K., Akpinar, S. Investigation of internal step and metal part reinforcement on joint strength in the adhesively bonded joint: Experimental and numerical analysis. *Theor Appl Fract Mech* 108 102613 (2020) **DOI:10.1016/j.tafmec.2020.102613**

[15] Sancaktar, E., Nirantar, P. Increasing strength of single lap joints of metal adherends by taper minimization. *J Adhes Sci Technol* 17 655-675 (2003), **DOI:10.1163/156856103321340796**

[16] da Silva, L.F.M., Adams, R.D. Techniques to reduce the peel stresses in adhesive joints with composites. *Int J Adhes Adhes* 27 227-235 (2007) **DOI:10.1016/j.ijadhadh.2007.01.001**

[17] Kanani, A.Y., Hou, X., Ye, J. The influence of notching and mixed-adhesives at the bonding area on the strength and stress distribution of dissimilar single-lap joints. *Compos Struct* 241 112136 (2020) **DOI:10.1016/j.compstruct.2020.112136**

[18] Çalik, A., Yildirim, S. An investigation on the effect of parallel slot in Bi-adhesive single lap joints with spew fillet. *J Eng Res* 3 95-110 (2015)

[19] Durmus, M., Akpinar, S. The experimental and numerical analysis of the adhesively bonded three-step-lap joints with different step lengths. *Theor Appl Fract Mech* 105 102427 (2020) **DOI:10.1016/j.tafmec.2019.102427**

[20] Marques, E.A.S., da Silva, L.F.M. Joint strength optimization of adhesively bonded patches. *J Adhes* 84 915-934 (2008) **DOI:10.1080/00218460802427944**

[21] Andruet, R.H., Dillard, D.A., Holzer, S.M. Two- and three-dimensional geometrical nonlinear finite elements for analysis of adhesive joints. *Int J Adhes Adhes* 21 17-34 (2001) **DOI:10.1016/S0143-7496(00)00024-5**

[22] Demiral, M., Mamedov, A. Fatigue performance of a step-lap joint under tensile load: A numerical study. *Polymers* 15 1949 (2023) **DOI:10.3390/polym15081949**

[23] Paygozar, Banea, M.D.S., Sadigh, M.A.S., da Silva, L.F.M. Adhesively bonded aluminium double-strap joints: Effects of patch part on failure load. *J Braz Soc Mech Sci Eng* 42 (2020) **DOI:10.1007/s40430-019-2115-4**

[24] Volkersen, O. Rivet strength distribution in tensile-stressed rivet joints with constant cross-section. *Luftfahrtforschung* 15 41-47 (1938)

[25] Goland, M., Reissner, E. The stresses in cemented joints. *J Appl Mech* 11 A17-A27 (1944), **DOI:10.1115/1.4009336**

[26] ASTM D1002-10 Standard Test Method for Apparent Shear Strength of Single-Lap-Joint Adhesively Bonded Metal Specimens by Tension Loading (Metal-to-Metal) (2019) ASTM Int. **10.1520/D1002-10R19**

[27] Sharma, V.K., Kumar, V., Joshi, R.S. Investigation of rare earth particulate on tribological and mechanical properties of Al-6061 alloy composites for aerospace application. *J Mater Res Technol* 8 3504-3516 (2019) **DOI:10.1016/j.jmrt.2019.06.029**

[28] Khoramishad, H. Effects of mechanical and geometrical properties of adhesive and metal layers on low-velocity impact behavior of metal laminate structures. *J Adhes Sci Technol* 29 592-608 (2015) **DOI:10.1080/01694243.2014.999610**

[29] Bayramoglu, S., Akpinar, S., Calik, A. Numerical analysis of elasto-plastic adhesively single step lap joints using cohesive zone models with experimental verification. *J Mech Sci Technol* 35 641-649 (2021) **DOI:10.1007/s12206-021-0124-0**

[30] Crocombe, A.D., Ashcroft, I.A. Simple Lap Joint Geometry. *Modeling of Adhesively Bonded Joints*. Springer (2008) Berlin Heidelberg 3-23 **DOI:10.1007/978-3-540-79056-3_1**

[31] Ozer, H. Introductory chapter: Structural adhesive bonded joints. *Applied Adhesive Bonding Science and Technology* InTech (2018) **DOI:10.5772/intechopen.74229**

[32] Rodríguez, R.Q., Paiva, W.P., Sollero, P., Albuquerque, E.L., Rodrigues, M.B. Analytical and numerical tools for bonded joint analysis. *Mecánic Comput* 29 7557-7569 (2010)

[33] ANSYS Inc. Academic Research Mechanical Release R2 [Computer software], https://www.ansys.com, accessed on 2023-06-06

[34] Rudawska, A., Wahab, M.A. Mechanical properties of adhesive joints made with pressure-sensitive adhesives. *Stroj Vestn-J Mech E* 67 380-388 (2021) **DOI:10.5545/sv-jme.2021.7253**

Data availability *The datasets generated during and/or analyzed during the current study are available from the corresponding author on reasonable request.*

Author contribution *Ahmet Calik: conceptualization, investigation, visualization, writing-original draft, and writing-review and editing.*

Conflicts of interest *The author declares that he has no known competing financial interests or personal relationships that could have appeared to influence the work reported in this paper.*

Optimizacija geometrije podpornih ojačitev pri lepljenih enojnih prekrovnih spojih: Pristop z metodo končnih elementov

Povzetek *V zadnjih letih raziskovalci posvečajo vse več pozornosti uporabi lepljenih spojev v primerjavi s tradicionalnimi metodami, kot so vijačenje ali kovičenje. V tej študiji je uporabljena analiza s pomočjo metode končnih elementov za optimizacijo geometrije in namestitve podpornih ojačitev v lepljenih enojnih prekrovnih spojih, s čimer je možno občutno zmanjšati koncentracije napetosti in izboljšati trdnost spojev. Izvedena je obsežna numerična analiza z metodo končnih elementov, v kateri je preučen vpliv različnih parametrov podpornih ojačitev in njihove lege na trdnost enojnih prekrovnih spojev. Numerični rezultati so validirani s primerjavo z obstoječimi raziskavami iz literature ter analitičnimi rešitvami. Rezultati te raziskave so pokazali, da lahko ustrezna izbira dimenzij in položaja podpornih ojačitev učinkovito zmanjša obremenitve in izboljša porazdelitev napetosti v različnih območjih lepljenega spoja, kar bistveno poveča njegovo trdnost.*

Ključne besede *lepljeni spoji, optimizacija napetosti, geometrija podpornih ojačitev, metoda končnih elementov*

A Numerical Simulation and an Experimental Study on the Steady-State Levitation Characteristics of a Magnetic Ball Driven by External Electromagnets in a Fluid Tube: Applications to Micromachines in Human Blood Vessels

Zhanxiang Cui[1] – Yonghua Lu[1] ✉ – Yun Zhu[2] – Zezheng Wang[1] – Ziyuan Wang[1]

1 Nanjing University of Aeronautics and Astronautics, College of Mechanical and Electrical Engineering, China
2 Aero Engine Corporation of China, China
✉ nuaa_lyh@nuaa.edu.cn

Abstract   Research on micro-robots in the field of medicine has introduced innovative methods for treating various diseases. This study aims to expand the application of controllable micromechanical diagnoses and treatment within human blood vessels by designing a magnetic levitation ball system in a fluid-filled circular tube. The system enables a magnetic ball to be stably suspended along a specific path under the influence of an external magnetic field. Simulations of the system's electromagnetic field, flow field characteristics, and mechanical state were conducted by using finite element software. The study analyzed the effects of the ball's position, magnetic pole direction, driving current, and fluid flow rate on the forces acting on the magnetic ball. Joint simulations of the flow and magnetic fields were performed using the ANSYS Workbench platform, and a multi-objective optimization method was employed to determine the parameters for stable suspension. Experimental validation demonstrated the stable suspension of the magnetic ball in a fluid tube under an external magnetic field. The experiments revealed the relationships among the driving current, fluid flow rate, and the ball's stable suspension position, confirming the effectiveness of the simulation method and the feasibility of controlling object positions within fluid tubes.

Keywords   magnetic levitation, blood vessel, steady-state levitation, biomedical micromachines, multi-objective optimization

Highlights
- Proposed a magnetic drive control for micro-devices in fluid tubes, aiding vascular disease treatment.
- Identified factors affecting a magnetic ball's steady position in blood vessels via simulations and tests.
- Developed a simulation model and an optimization method for better control of the magnetic ball.

1 INTRODUCTION

In the medical field, interventional detection and procedures are essential for treating certain diseases, particularly cardiovascular blockages. Addressing the detrimental effects of cardiovascular disease is a significant concern within the global medical community. The integration of minimally invasive surgery and vascular robotics in patient treatment has increasingly become a mainstream research trend, showcasing considerable potential for practical application [1, 2]. In the traditional diagnosis and treatment of canaliculopathies, physicians often employ a guidewire mechanism to deliver microdevices to a targeted site. However, this method has several drawbacks, including limited controllability, inapplicability in narrow spaces, and a high risk of damaging the mucosa. Diagnostic and therapeutic devices based on micro-electro-mechanical systems (MEMS) represent a significant advancement for medical devices. Numerous innovations have been achieved in areas such as wireless endoscopes, micro-drug delivery systems, minimally invasive surgery, and in vivo detection. The application of these microdevices enables clinicians to conduct the diagnosis and treatment in a minimally invasive or non-invasive manner [3].

Researchers are exploring techniques for driving micromechanical devices within human body cavities. In biological tissues, micromachines are frequently powered by external magnetic fields,

electric fields, light energy, chemical energy, and bioenergy [4]. For instance, Cai et al. employed Helmholtz coils to generate external magnetic fields to drive microrobots through mucus tubes [1]. Similarly, Li et al. utilized an external magnetic field and bacteria to drive robots in blood vessels [5]. Fu et al. developed magnetically-driven microrobots powered by an oscillating tail [6].

The actuation of micro-robots using external magnetic fields is less harmful and more controllable within the human lumen [7]. Helmholtz and Maxwell coils are commonly used to generate external magnetic fields [8-10]. However, the coils need to completely encircle the target space, resulting in a very limited controllable range for the micro-robot. Hamal Marino et al. proposed an active magnetic levitation method to achieve controlled spiral motion of a micro-robot in viscous liquids [11]. Chi et al. invented a low-torque micro-robot designed for controllable motion within the human esophagus [12]. Furthermore, Li et al. developed a two-dimensional actuation technique for magnetic particles in confined spaces [13]. The magnetic levitation control technique enables precise motion control of micro-objects in small spaces [14, 15]. Due to the biologically harmless nature of magnetic fields, magnetic levitation can also be applied in the field of medicine for detection, analysis, and cell assembly [16].

Controllable micro-robots in human body cavities are usually equipped with helical structures [17], oscillating components [18],

and permanent magnets [19], powered by reactive forces with liquids. However, their traveling speed is slow, and they easily collide with the lumen wall, causing damage to body tissue. There is little research on the precise position control of micro-machines within the complex environment of human blood vessels. Numerical simulations are also commonly employed to study the motion characteristics of micro-robots within pipelines. For instance, Derbal et al. [20] investigated the effect of flow field parameters on the flow characteristics of magnetic fluids with nanoparticles. Meanwhile, Gkountas et al. [21] conducted simulations to analyze the impact of rotating magnetic field parameters on the forces and displacements of micro-robots in fluids, which has been applied to the structural design of micro-mechanics.

This paper presents a study on the development of external magnetic drive technology for micromachines operating within human blood vessels. In this system, permanent magnets serve as target objects, while a gradient magnetic field acts as the driving source, enabling the manipulation of controlled objects from a distance without physical contact. Specifically, a one-dimensional magnetic levitation ball system was designed and implemented within a fluid tube to investigate the effects of flow field and magnetic field parameters on the position control of suspended objects, as well as the influence of physical field characteristics. The Maxwell and Fluent finite element simulation platforms were utilized to perform numerical calculations on the distribution characteristics of the magnetic and flow fields, as well as the impact of physical parameters on the stress state of the suspended body. The workbench platform was employed to calculate the flow and magnetic fields of the suspended body, utilizing a multi-objective optimization method to determine the steady-state levitation parameters of the magnetic ball. Finally, a steady-state levitation experiment of the magnetically driven ball in a fluid tube was conducted and compared with the results from numerical simulations.

2 METHODS & MATERIALS

2.1 The Principle of a Magnetic Levitation Ball System Driven by an External Magnetic Field in a Fluid Tube

A magnetic levitation ball system is proposed to simulate the operational scenarios of micro-robotics within a fluid tube. The system, illustrated in Fig. 1, consists of a magnetic ball, a controller, a driving circuit module, a position measurement module, an electromagnetic driver, and a fluid tube. The magnetic ball is attracted by the magnetic force generated by the electromagnet. The controller manages the driving circuit to supply the appropriate current to the electromagnet, while the measurement circuit utilizes data from multiple position sensors to provide real-time position feedback of the magnetic ball to the controller. The magnetic ball can maintain a stable suspension state within the tube through the combined effects of blood flow and the attraction of the electromagnet.
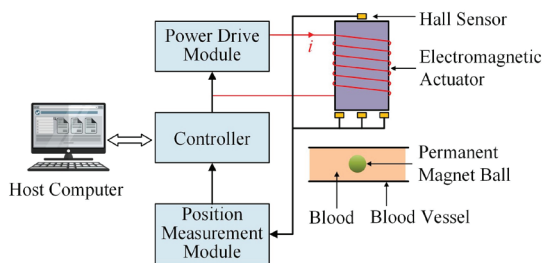

Fig. 1. Schematic diagram of the magnetic levitation ball system driven by an external magnetic field

As illustrated in Fig. 2, the structure of the electromagnet comprises a hollow cylindrical solenoid wound with multiple layers of enameled wire. The relevant parameters of the electromagnet are outlined in Table 1. Magnet design ensures that it can withstand high currents while providing sufficient suspension distance of the ball. The magnetic ball is a spherical permanent magnet made of NdFeB, with its adjacent hemispheres representing the north and south poles, respectively. The electromagnet can suspend magnetic balls with diameters ranging from 5 mm to 15 mm. Given the long-range position detection capabilities and minimal obstruction to the fluid, a magnetic ball with a diameter of 12.7 mm was selected. The mass of the ball m is 8.15 g, and the surface magnetic induction intensity B_s is 677.3 mT. The suspension distance range of the magnetic ball in air is [-15 mm, -38 mm] (from the lower end face of the electromagnet coil to the center of the magnetic ball). Fig. 3 shows a photo of the magnetic ball at the farthest suspension position.
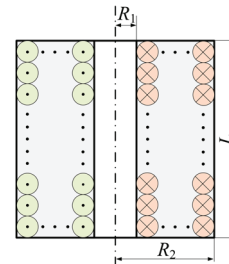

Fig. 2. Schematic diagram of the structure of the electromagnet

Table 1. Related parameters of electromagnet

Parameters	Symbol	Value
Number of coil turns	N	1489
Inner radius	R_1	8 mm
Outer radius	R_2	31.5 mm
Height	L	65 mm
Resistance	R_c	0.5 Ω
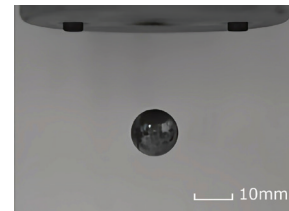
Fig. 3. The farthest suspension position of the magnetic ball in the air

2.2 Modeling

The electromagnetic and fluid resistance forces acting on a stably suspended ball in blood are challenging to establish through mathematical derivation. Therefore, the relationship between the electromagnetic field, fluid parameters, and the forces on the magnetic ball is determined using finite element simulation tools. By varying the driving current of the electromagnet, the electromagnetic force acting on the ball can be modified, resulting in different equilibrium states at various positions. Consequently, by controlling the driving current, the position of the magnetic ball within the blood vessel can be adjusted. A proportional–integral–derivative (PID) controller is used to achieve stable suspension of the magnetic ball. A Hall sensor is utilized to detect the position of the ball as feedback. Based on the difference between the current position and the target position, the controller adjusts the driving current of the electromagnet in real-time to maintain the ball's suspension at the desired position. When

the ball is adjusted and suspended in a fixed position, the driving current of the electromagnet remains constant, while the forces acting on the magnetic ball are balanced.

Fig. 4 illustrates the force analysis of the magnetic ball, where $\mathbf{F_m}$ represents the electromagnetic force, $\mathbf{F_d}$ denotes the fluid force, $\mathbf{G}$ signifies the gravitational force, and $\mathbf{F_u}$ indicates the buoyancy of the magnetic ball. $\mathbf{G}$ and $\mathbf{F_u}$ are always oriented vertically. With a constant blood flow rate, the magnetic ball can achieve the force balance at multiple positions. Fig. 4 depicts two positions of the magnetic ball: one near to the electromagnet and the other farther away. Assuming both positions are in a state of force balance, their force conditions and the required driving current will differ.
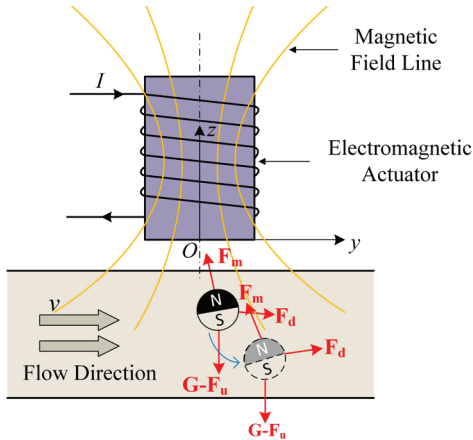

Fig. 4. Schematic diagram of the force analysis of the magnetic ball

Within blood vessels, the magnetic ball experiences fluid drag, buoyancy, and gravity. The electromagnet exerts an upward electromagnetic force on the ball. This force can be expressed as [22]:

$$\mathbf{F} = \mathbf{p}\nabla\mathbf{B} = \frac{3B_s}{2\mu_0}V_b\left(\frac{\partial\mathbf{B}}{\partial x}\mathbf{i} + \frac{\partial\mathbf{B}}{\partial z}\mathbf{k}\right), \quad (1)$$

where the magnetic dipole moment is denoted by $\mathbf{p}$, the magnetic permeability of air is denoted by μ_0, the surface magnetic induction of the magnetic ball is denoted by B_s, V_b represents the volume of the magnetic ball, $\mathbf{B}$ represents the magnetic flux density, $\mathbf{i}$ is a horizontal unit vector, and $\mathbf{k}$ is a vertical unit vector.

The upward buoyancy acting on the magnetic ball can be expressed as:

$$\mathbf{F_u} = \rho\mathbf{g}V_b. \quad (2)$$

In the bloodstream, a spherical object experiences two types of fluid resistance. One is the viscous resistance caused by friction, which can be expressed by Stokes' law as [23]:

$$f_1 = 6\pi\eta R v. \quad (3)$$

The other is the pressure difference resistance, which can be expressed as [24]:

$$f^2 = \frac{1}{2}\zeta A\rho v^2, \quad (4)$$

where ρ represents the density of blood, $\mathbf{g}$ is gravitational acceleration, η is the viscosity of blood, R is the the radius of the magnetic ball, v is the relative velocity of the ball to the blood, ζ is the resistance coefficient, and A is the projected area of the ball perpendicular to the direction of blood flow.

In the following sections, finite element simulation software is employed to calculate the electromagnetic and fluid forces acting on the ball. The parameters of the electromagnetic field and the flow

field are optimized to determine the conditions for force balance of the magnetic ball. Additionally, the appropriate drive current is selected for precise control of the target position.

2.3 Numerical Simulation Method of Electromagnetic Field

ANSYS Maxwell software is used to calculate the electromagnetic field by solving Maxwell's equations [25], as presented in Eq. (5). Three-dimensional modeling and simulation parameter settings are conducted. The electromagnetic model is shown in Fig. 5. The relative magnetic permeability of the magnetic ball is 1.1, and its coercive force is -808500 A/m. The model exhibits symmetry about the $x = 0$ plane. A rectangular coordinate system is established with original point O, located at the center of the lower end surface of the electromagnet. The center of mass of the ball lies on the $x = 0$ plane, with a position defined as $(0, y, z)$. Theoretically, the magnetic field generated by a hollow cylindrical solenoid is symmetric along the z-axis. The magnetic field of the magnetic ball at any position can be represented equivalently by that on the $x = 0$ plane. The angle between the N pole of the magnetic ball and the z-axis is defined as the magnetic pole orientation of the ball, denoted as θ. A negative value of θ indicates the counterclockwise direction.

$$\nabla\cdot\mathbf{B} = 0, \quad \nabla\times\mathbf{B} = \mu_0\mathbf{J}, \quad \nabla\times\mathbf{E} = -\frac{\partial\mathbf{B}}{\partial t}, \quad (5)$$

where ∇ is the gradient operator $\mathbf{B}$ is magnetic flux density, $\mathbf{E}$ is electric field intensity, and $\mathbf{J}$ is the current density.
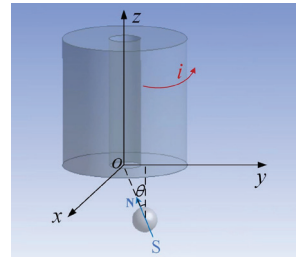

Fig. 5. Physical model of a magnetically levitated ball system

The model is calculated and simulated under various working conditions using a magnetostatic solver. The parameter values for electromagnetic field simulation are shown in Table 2. Each parameter is valued at uniform intervals within a specified range. The magnetic field generated by the hollow cylindrical electromagnet is centrally symmetrical. To reduce the computational load, only the position of the ball in the right half-plane of $x=0$ is considered. Therefore, the y-coordinate of the magnetic ball is set to a positive value. The north pole of the energized electromagnet faces in the $+z$ direction. According to the law of magnetic attraction, the magnetic ball's north pole will orient towards the electromagnet. Consequently, the range of magnetic pole orientation for the ball is set from –90° to 90°.

Table 2. Range of magnetic field simulation parameters

Parameters	Range	Parameters	Range
y	0 mm to 30 mm	Magnetic pole orientation	–90° to 90°
z	–45 mm to 0 mm	Drive current	0 A to 3 A

2.4 Influence of Driving Current and Position

The influence of the driving current of an electromagnet on the electromagnetic force of the ball is investigated. Two distinct positions of the ball, referred to as position 0 and position 1, are

selected for analysis. Position 0 is characterized by a position of [0 mm, 8 mm, -36 mm] and a magnetic pole orientation θ of 0°, while position 1 has a position of [0 mm, 15 mm, –26 mm] and θ of 0°. Fig. 6 illustrates the variation of the electromagnetic force and torque on the ball as the current gradually increases from 0 A to 3 A. It is observed that both the electromagnetic force and torque of the ball exhibit a linear relationship with the current. As the current increases, the electromagnetic force and torque also increase gradually, due to the closer proximity of position 1 to the electromagnet compared to position 0. Consequently, under the same current, the electromagnetic force and torque for position 1 are greater.
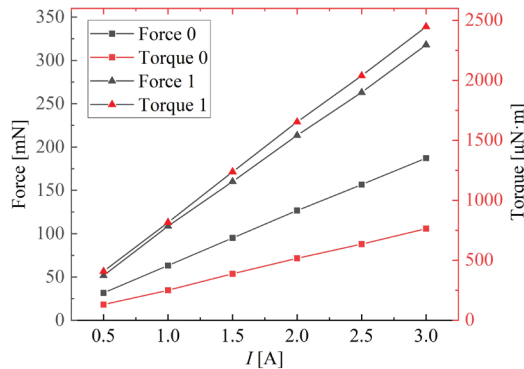

Fig. 6. Relationship between electromagnetic force, torque of the magnetic ball and the driving current of the electromagnet

As illustrated in Figs. 7a and c, the cloud diagram of the magnetic field distribution as the driving current of the magnetic ball at position 0 increases from 1 A to 2 A. The small black arrow indicates the direction of the magnetic pole of the magnetic ball. It is evident that the magnetic field surrounding the electromagnet and the magnetic ball exhibits a gradient distribution. As the current increases, the field strength near the electromagnet also increases.
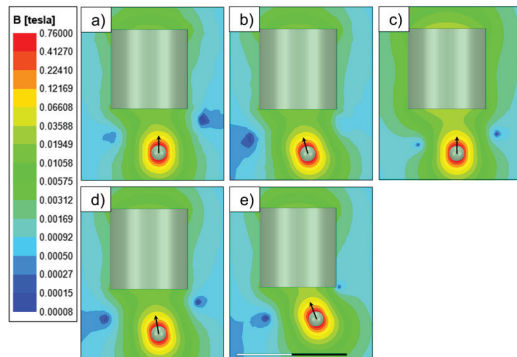

Fig. 7. Magnetic field cloud diagram of a magnetic ball and electromagnet in y-O-z plane where ball positions, magnetic pole orientation, and current are:
a) [0 mm, 8 mm, -36 mm], θ = 0, I = 1 A; b) [0 mm, 8 mm, -36 mm], θ = -20, I = 1 A;
c) [0 mm, 8 mm, -36 mm], θ = 0, I = 2 A; d) [0 mm, 8 mm, -36 mm], θ = -11, I = 1 A; and
e) [0 mm, 15 mm, -26 mm], θ = 0, I = 1 A

The influence of the magnetic pole orientation of the magnetic ball on the electromagnetic effect is studied. The specific position of the ball is designated as [0 mm, 8 mm, –36 mm], with a driving current of 1 A applied to the electromagnet. The magnetic pole orientation of the magnetic ball is gradually varied from –90° to 90°. Fig. 8 illustrates the relationship between the electromagnetic force, torque, and the magnetic pole orientation exerted on the magnetic ball. As the magnetic pole orientation shifts in the positive direction, the magnetic

ball undergoes clockwise rotation. Initially, the electromagnetic force of the magnetic ball increases, reaching a maximum value before subsequently decreasing. The torque of the magnetic ball is primarily directed along the x-axis, diminishing from the –x-axis direction to 0°, and then gradually increasing in the +x-axis direction. Clearly, the magnetic pole orientation of the ball significantly influences the electromagnetic force and torque. Fig. 7b depicts the contour map of the magnetic field distribution of the magnetic ball when the magnetic pole orientation θ is –20°. In comparison to θ of 0°, noticeable alterations are observed in the magnetic field distribution and the direction of the magnetic vector near the magnetic ball.
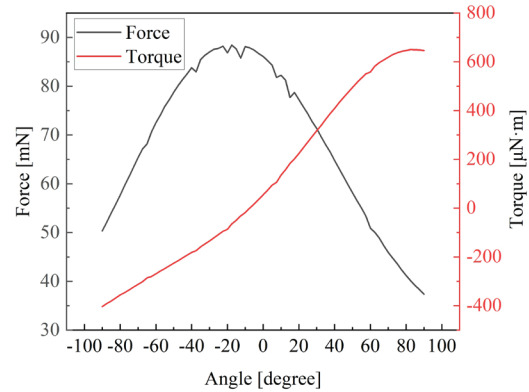
Fig. 8. Relationship between electromagnetic force and torque of the magnetic ball and magnetic pole orientation
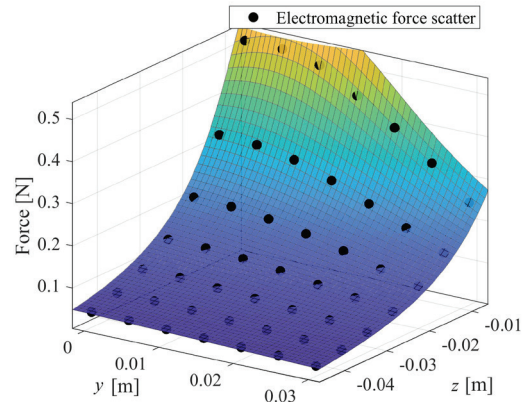
Fig. 9. Relationship between electromagnetic force and position of magnetic ball at different positions

The magnetic pole angle of the ball is calculated while the magnetic torque is zero. Fig 9 presents a scatter plot of the electromagnetic force on the magnetic ball at different positions, along with its fitted surface. Fig. 10 shows the calculated magnetic pole orientations at different positions when the electromagnet's driving current is 1 A and the torque of the ball is balanced. Fig. 7d shows the magnetic field distribution cloud diagram when the ball is located at the position [0 mm, 8 mm, –36 mm]. The calculated magnetic pole orientation is –11° as the ball's torque is balanced. Fig. 7e shows the magnetic field distribution cloud diagram when the ball is located at the position [0 mm, 15 mm, –26 mm]. The calculated magnetic pole orientation is –26° as the ball's torque is balanced. When fitting the electromagnetic force, the expression for the electromagnetic force in Eq. (1) becomes overly complex when expanded, so a simplified formula is typically used for approximation. According to literature [26], the electromagnetic force exerted on a permanent magnet

by an electromagnet is proportional to the current and inversely proportional to the square of the distance, and it can be expressed as

$$F_m = \frac{eI}{\left(a\delta^2 + b\delta + c\right)}, \tag{6}$$

where δ is the distance between the electromagnet and the permanent magnet. The distance between the electromagnet and the permanent magnet is related to both the y and z coordinates, and Eq. (1) can be rewritten as

$$F_m = \frac{eI}{\left(ay^2 + by + cz^2 + dyz + h\right)}, \tag{7}$$

where a, b, c, d, e, and h are constants. The values obtained from fitting results a = 2.25×10^{-5}, b = –0.705, c = 2.086, d = –1.093, e = 3.06×10^{-4}, and the goodness of fit is 0.996. The units of I, y and z are A, m and m within Eq. (7), respectively.

In Fig. 10, it can be seen that when the magnetic ball is subjected to the magnetic field of the electromagnet, the orientation of the magnetic poles is either zero or negative, tending toward the center of the electromagnet. When $y = 0$, meaning the ball is positioned along the axis of the electromagnet, the orientation of the magnetic poles aligns with the $+z$-axis direction. As the ball moves further away from the axis, the relative deviation angle of the magnetic pole orientation increases, resulting in a more rapid change in the magnetic pole orientation of the ball in the y-direction. As illustrated in Fig. 10, as the magnetic ball approaches the center of the lower end face of the electromagnet, the electromagnetic force intensifies. The rate of change of the electromagnetic force in the z-axis direction exceeds that in the y-axis direction. Consequently, the z-coordinate position of the magnetic ball significantly influences the electromagnetic force. Near the lower end face of the electromagnet, the field strength in the z-axis direction diminishes more rapidly than in the y-axis direction, resulting in a larger magnetic field gradient.
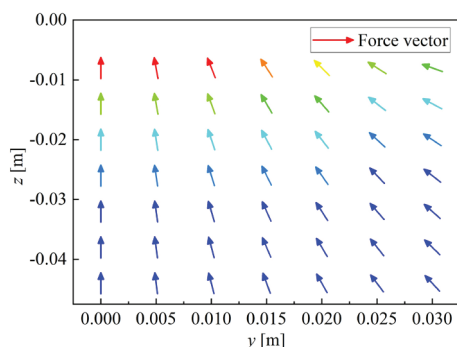

Fig. 10. Relationship between magnetic pole orientation and position of magnetic ball

3 RESULTS

3.1 Blood Flow Field Simulation Method

Simulations were conducted using Fluent software to analyze the blood flow environment surrounding the magnetic ball. Fig. 11 illustrates the fluid simulation model of the magnetic ball within a straight blood vessel. The blood fluid domain was cylindrical, with a diameter of 22 mm and a length of 100 mm. Blood flowed horizontally, and the magnetic ball was fully contained within the vessel. Point P represented the center of the magnetic ball, and the origin of the coordinate system is located at the center of the fluid domain's axis. The velocity inlet was set at the left end face of the fluid domain, while the right end face was designated as the zero-

pressure outlet. A standard k–ε epsilon model is used for turbulent modeling due to accuracy and stability. To simplify the model, blood was treated as a Newtonian fluid with a density of 1060 kg/m³ and a viscosity of 3.5×10^{-3} Pa·s due to the similarity between the blood and Newtonian fluid. The continuity equation and the Navier-Stokes equations were employed to describe characteristic variations of fluid, and the control equations were discretized and solved iteratively using the finite volume method. The coupling relationship between velocity and pressure was managed using the SIMPLE algorithm.
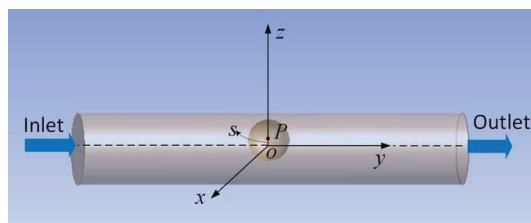

Fig. 11. Physical model of intravascular flow

The position of the ball in the vertical direction is considered an important influencing variable, which is represented by s relative to the origin O, as shown in Fig. 11. Positive values indicate that the position is located in the positive half of the z-axis. After parameterizing the vertical position s of the ball and the blood flow velocity v, finite element simulation calculations are conducted separately. Table 3 shows the range and interval of parameterization for both the vertical position of the magnetic ball and the blood flow velocity.

Table 3. The parameter range of blood flow field simulation

Parameter	Value	Parameter	Value
s	–4 mm to 4 mm	v	0.08 m/s to 0.24 m/s

3.2 The Effect of the Ball's Position and Blood Flow Velocity on Fluid Force

In the coordinate system depicted in Fig. 11, the position of the magnetic ball within the blood vessel can be characterized by its distance from the center of the vessel. Since the z-axis in the magnetic levitation ball system represents the direction of the magnetic force of the ball, the position change of the ball in the z-direction matters. Simulation results indicate that the maximum magnitude of the fluid force on the magnetic ball in the x-direction is on the order of 10^{-5} N, which can be considered negligible.

The fluid forces acting on the magnetic ball in the y- and z-directions are examined. The y-direction represents the direction of blood flow, while the z-direction indicates the vertical orientation. Fig. 12 illustrates the relationship between the force exerted on the magnetic ball in the direction of blood flow and the blood flow velocity. It is evident that when the vertical position of the ball remains constant, the fluid resistance acting on the ball in the direction of blood flow gradually increases as the blood flow velocity rises. When the blood flow velocity exceeds 0.16 m/s, a linear relationship emerges between fluid resistance and blood flow velocity. The fluid resistance curves for the vertical positions of the ball at 2 mm and –2 mm nearly overlap, as do the curves for the vertical positions of the ball at 4 mm and –4 mm. This indicates that the fluid resistance on the ball in the direction of blood flow depends on the distance s between the ball and the axis of the blood vessel. Fig. 13 presents the relationship between the force on the ball in the direction of blood flow and the vertical position. It can be observed that when the blood

flow velocity remains constant, the fluid resistance on the ball in the direction of blood flow increases as the s increases. At a high blood flow velocity of 0.24 m/s, the fluid resistance increases more rapidly as the s increases, with a maximum value of 7.7 mN.
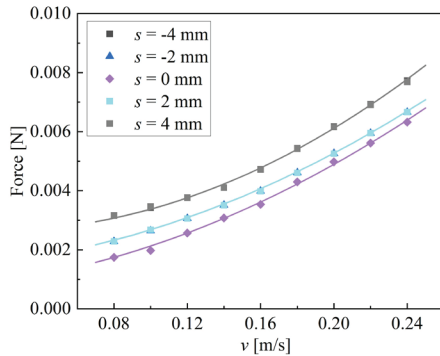

Fig. 12. The relationship between the fluid force exerted on the ball in the blood flow direction and the blood flow velocity
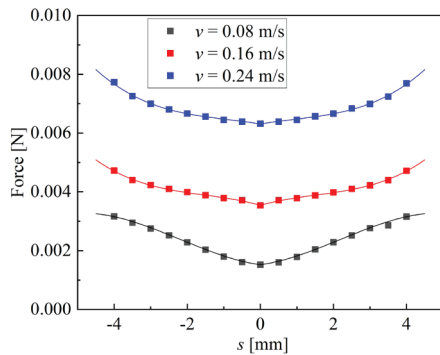

Fig. 13. The relationship between the fluid force on the ball in the direction of blood flow and its vertical position

The curves presented in Figs. 12 and 13 are the fitted curves for the fluid force scatter data. From Eqs. (3) and (4), it can be seen that the flow velocity affects the fluid force through both proportional and quadratic relationships. Then an empirical cubic equation is added to describe the influence of the vertical position s, so the expression for the fluid force is as follows:

$$F_d = \left(a'v^2 + b'v + c' \right)\left(d's^3 + e's^2 + g's + h' \right), \tag{8}$$

where the constants a', b', c', d', e', g', h' have values of: 10.03, 0.38, 0.208, 0.456, 10.07, 0.456, 0.0068, after fitting calculations with a goodness of 0.983. The units of v and s are m/s and mm within Eq. (8), respectively.

Fig. 14 depicts the relationship between the fluid force on the ball in the vertical direction and the vertical position. When the vertical position of the ball is at 0 mm and ±2 mm, the vertical force on the ball approaches zero. However, when the vertical position of the ball is at ±4 mm, the vertical force on the ball gradually increases as the blood flow velocity rises.

In Fig. 14, it is evident that as the distance of the ball's deviation from the axis of the blood vessel increases, the vertical fluid force also rises. When both the blood flow velocity and the vertical position of the ball are minimal, the vertical fluid force is correspondingly low, approaching zero. Conversely, when the blood flow velocity and vertical position are substantial, the vertical fluid force exerted on the ball becomes significant. When the ball deviates from the axis of the blood vessel by 4 mm, the vertical fluid force experiences a sudden increase, with the maximum force of 1.5 mN.
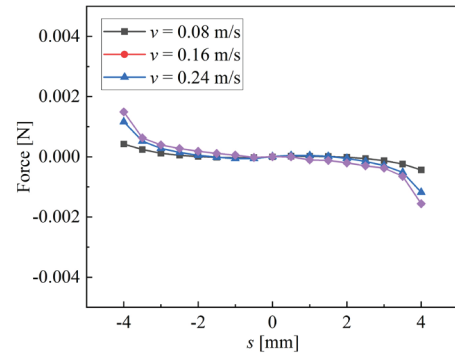
Fig. 14. The relationship between the fluid force exerted on the ball in the vertical direction and its vertical position

After calculations, the magnitude of the torque experienced by the magnetic ball in the blood vessel in the y-direction and z-direction is 10^{-8} N·m, and the magnitude of the torque experienced by the ball in the z-direction is 10^{-7} N·m. Therefore, they are not taken into account.

Fig. 15 illustrates the pressure cloud diagram of blood flow at varying velocities, with the ball positioned 2 mm above the axis of the blood vessel. Fig. 16 presents the shear stress distribution on the surface of the ball under the corresponding conditions. Fig. 17 depicts the corresponding blood velocity vector diagram. In Fig. 15, it is evident that when the ball is positioned above the axis of the blood vessel, a significant pressure differential exists between the fluid regions in front of and behind the ball. The pressure behind the ball is higher than that in front, resulting in a forward pressure gradient resistance. Furthermore, a notable pressure difference is observed on the upper and lower surfaces of the ball, causing the direction of the pressure gradient resistance to tilt slightly downward and exert a vertical downward force. Fig. 16 reveals that the shear stress on the rear surface of the ball exceeds that on the front surface, creating a forward viscous resistance. Consequently, the fluid resistance in the direction of blood flow comprises both pressure difference resistance and viscous resistance. In the vertical direction, the magnetic ball's resistance is primarily attributed to pressure difference resistance.

Fig. 17 shows that the inlet and outlet velocities of the blood vessel are essentially equivalent. However, in the region between the ball and the blood vessel wall, the flow velocities on either side differ. As the velocity of blood flow increases, both the pressure and flow velocity of the incoming fluid rise. Consequently, the differential pressure resistance and viscous resistance acting on the ball also increase significantly. Therefore, the fluid forces exerted by the ball in both the vertical and blood flow directions intensify as the blood inlet velocity increases.
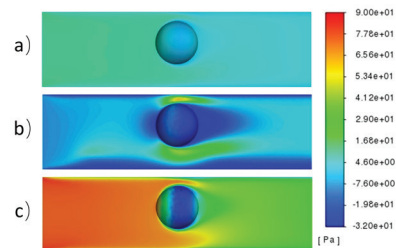
Fig. 15. Dynamic pressure cloud diagram in y-O-z plane of blood vessel under different blood flow velocity; a) v = 0.08 m/s, b) v = 0.16 m/s, and c) v = 0.24 m/s

Fig. 18 shows the pressure cloud diagram of the blood at various vertical positions of the ball when the blood flow velocity is 0.16 m/s. Fig. 19 shows the corresponding shear stress cloud diagram on the surface of the ball. Fig. 20 depicts the associated velocity vector

diagram of the blood. When the ball is positioned along the axis of the blood vessel, the flow field surrounding the ball is symmetric along this axis. The shear stress and pressure on the surface of the ball are greater on one side in the direction of the incoming flow, and they are symmetrically distributed on the upper and lower sides, as shown in Figs. 18c and 19c. The direction of the viscous drag and pressure difference resistance aligns with the direction of blood flow, resulting in a net vertical force of zero on the ball. However, when the ball deviates from the axis of the blood vessel, the shape of the blood flow around the ball becomes asymmetrical. Consequently, the blood flow velocity and pressure increase on the side where the space is narrower, altering the pressure distribution on the surface of the ball.
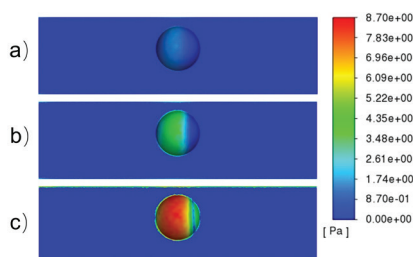

Fig. 16. Shear stress cloud diagram on the surface of the ball at different blood flow velocity
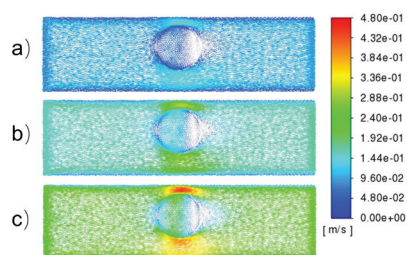

Fig. 17. Velocity vector cloud diagram at different blood flow velocity in the y-O-z plane of the vessel; v = 0.08 m/s, b) v = 0.16 m/s, and c) v = 0.24 m/s

When the vertical position of the ball is above the axis of the blood vessel, the pressure on the side of the ball adjacent to the vessel wall increases. The direction of the pressure difference resistance points toward the lower right, as indicated in Fig. 18d, while the direction of the viscous resistance acting on the ball points to the right, as shown in Fig. 19d. Consequently, the fluid force acting on the ball is directed toward the lower right, with the vertical component of the fluid force directed downward, resulting in a negative value for the force. Conversely, when the ball is positioned below the axis of the blood vessel, the vertical component of the fluid force is directed upward, yielding a positive value.
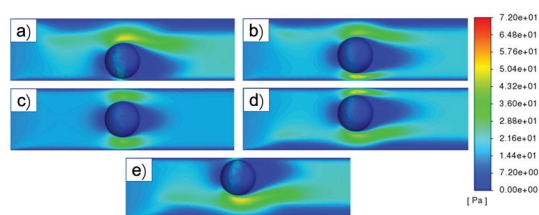

Fig. 18. Dynamic pressure cloud diagram in y-O-z plane of blood vessel; a) S = –4 mm, b) S = –2 mm, c) S = 0 mm, d) S = 2 mm, and e) S = 4 mm

As the vertical position of the ball increases relative to the axis of the blood vessel, the flow velocity near the upper surface of the ball also increases, resulting in a corresponding increase of shear force on that surface. Consequently, the vertical downward component

of shear stress increases. Furthermore, as the distance between the ball and the axis of the blood vessel increases, both the vertical and horizontal components of the pressure difference increase. When the distance between the ball and the axis of the blood vessel is small, the shear stress distribution on the surface of the ball remains relatively constant. As shown in Figs. 19a and b, when the ball is close to the vessel wall, the shear stress on the side adjacent to the wall significantly increases. This leads to an increase in the vertical component of viscous resistance acting on the ball. Therefore, as the position s increases, the horizontal fluid resistance of the ball markedly intensifies. The vertical fluid force exhibits a noticeable increase only as the position s has a substantial value.
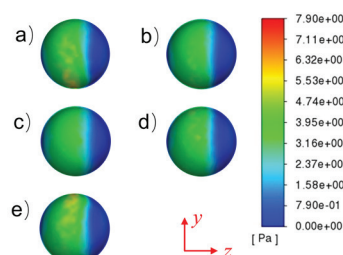

Fig. 19. Shear stress cloud diagram on the surface of the ball; a) S = –4 mm, b) S = –2 mm, c) S = 0 mm, d) S = 2 mm, and e) S = 4 mm
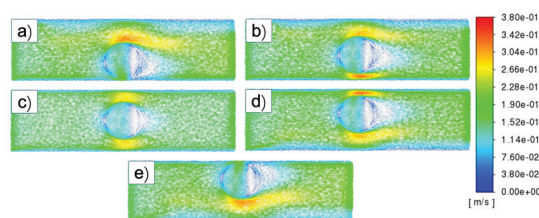
Fig. 20. Velocity vector cloud diagram of y-O-z plane of blood vessel and surface of ball; a) S = –4 mm, b) S = –2 mm, c) S = 0 mm, d) S = 2 mm, and e) S = 4 mm

Based on the fluid simulation results of the ball within the blood vessels, it can be observed that the ball experiences fluid forces in both the direction of blood flow and the vertical direction within the blood vessels. The fluid forces in the vertical direction are relatively smaller. The blood flow velocity and the position of the ball affect the distribution of the pressure field and velocity field of the blood, thereby influencing the magnitude and direction of the pressure difference resistance and viscous resistance of the ball. Both the blood flow velocity and the distance of the ball from the axis of the blood vessel contribute to an increase in the fluid forces acting on the ball.

3.3 Electromagnetic Field and Blood Flow Field Co-Simulation

Under the influence of appropriate electromagnetic field and blood flow field, magnetic balls can achieve force balance and remain suspended within blood vessels. The ANSYS Workbench platform integrates the Maxwell solver and the Fluent solver to simultaneously simulate both the electromagnetic field and the flow field. The resulting data is then transferred to the optimization module to calculate the steady-state physical parameters necessary for the levitation of the magnetic ball.

First, a three-dimensional model is created in Workbench based on the actual physical dimensions, as shown in Fig. 21. The origin of the coordinate system is positioned at the center of the lower surface of the electromagnet, with the direction of blood flow oriented along the $+y$ axis. The electromagnet is situated directly above the blood vessel, exerting an attractive force on the magnetic ball. The distance

between the bottom surface of the electromagnet and the axis of the fluid domain is 30 mm. The entire physical model is symmetric about the $x = 0$ plane. Theoretically, when the system reaches a steady state, the stable position of the ball will be located in the $x = 0$ plane. The position of the ball varies within the $x = 0$ plane and is denoted as $p_n(0, y_e, z_e)$. The magnetic pole direction of the ball θ, the driving current of the electromagnet I, and the blood flow velocity v are considered as the parameters to be optimized. The range of parameter optimization is equivalent to that specified Table 2 and Table 3. The total force and moment experienced by the ball in force equilibrium are zero, as shown in Eqs. (9) and (10). This condition is selected as the optimization objective, with a tolerance of 0.1 %,
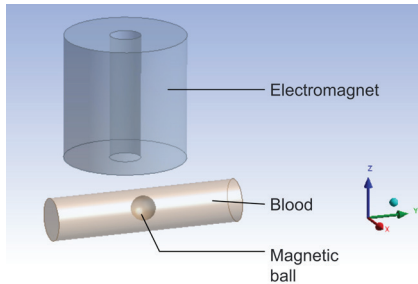

Fig. 21. Physical model of the co-simulation

$$F_e = 0 \Leftrightarrow \begin{cases} F_{mx} - F_{dx} = 0 \\ F_{my} - F_{dy} = 0, \\ F_{mz} - F_{dz} = 0 \end{cases} \tag{9}$$

$$T_e = 0 \Leftrightarrow \begin{cases} T_{mx} - T_{dx} = 0 \\ T_{my} - T_{dy} = 0, \\ T_{mz} - T_{dz} = 0 \end{cases} \tag{10}$$

where F_e is the resultant force on the ball, and F_{mx}, F_{my}, and F_{mz} are the components of the electromagnetic force in the x, y, and z directions, respectively. F_{dx}, F_{dy}, and F_{dz} are the fluid forces in the x, y, and z directions, respectively. T_e is the torque on the ball, and T_{mx}, T_{my}, and T_{my} are the components of the electromagnetic torque in the x, y, and z directions, respectively. T_{dx}, T_{dy}, and T_{dz} are the torque caused by fluid in the x, y, and z directions, respectively.

Multi-objective optimization is commonly used to design the parameters of mechanical structures [27]. In this study, the multi-objective genetic algorithm (MOGA) is employed to optimize the parameters of both the magnetic field and the flow field. Fig. 22 shows the flowchart of the MOGA optimization process. Initially, the variables are parameterized to generate the initial samples. Subsequently, the Maxwell and Fluent solvers are used to calculate the electromagnetic and fluid forces, which are then combined to determine the total forces and moments acting on the ball. The MOGA generates a new set of samples through hybridization and mutation to repeat the calculations. If the results meet the optimization objectives within the specified Pareto error, the calculation concludes, and the results are output. Otherwise, the generation of new samples continues for iterative calculations. The initial number of samples for optimization is set to 42, with 42 samples generated in each subsequent iteration.

The MOGA optimization process generated 287 design points and identified the three best candidate solutions. The parameters of these candidate solutions are presented in Table 4, with each result corresponding to a specific set of physical field parameters when the magnetic ball is in a state of steady equilibrium within the blood.
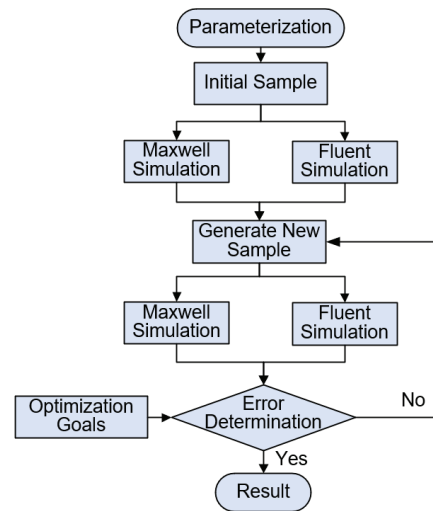
Fig. 22. Flow chart of MOGA optimization

Table 4. Results of MOGA optimization

Condition	Drive current [A]	Blood flow velocity [m/s]	Ball's position [mm]	N pole orientation of the ball [°]
A	0.5	0.14	(0, 1.53, −26.2)	7.7
B	0.75	0.09	(0, 0.50, −28.2)	2.6
C	1.2	0.18	(0, 2.37, −32.5)	5.1

4 DISCUSSION

An experiment was conducted to investigate the behavior of a magnetic ball's stable suspension within a fluid tube, and to validate the results of previous multi-objective optimization. As shown in Fig. 23, a mixture of water and glycerol (in a 2.3:1 mass ratio) was used as a substitute for blood, as it possesses similar density and viscosity characteristics. The fluid is propelled through the pipeline by a pump, with an adjustable flow rate. The magnetic levitation ball system consists of an electromagnet, a drive circuit, a controller, and a power supply. The magnetic ball is suspended within a fluid tube located beneath the electromagnet.
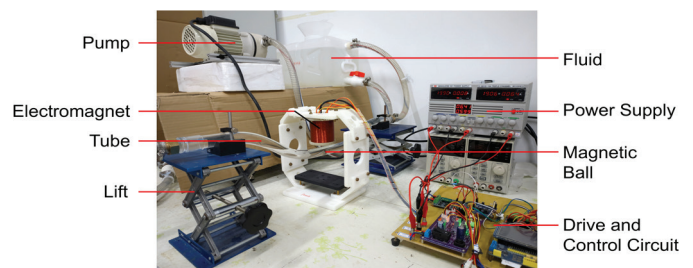
Fig. 23. Magnetic levitation experimental device

Fig. 24 presents photos of a magnetic ball in steady-state suspension within a fluid pipe at various flow velocities and different vertical positions. The green line indicates the central axis of the driver and the tube as a reference, while the red elliptical line outlines the ball. The '+' symbol marks the center of the ball. The sides of the ball appear elliptical due to refraction of light, which has been acounted. It can be seen that under the influence of the fluid, the suspension position of the ball deviates differently from the axis of the electromagnet. The driving current of the driver is adjusted to change the vertical levitation position of the ball within the fluid tube.
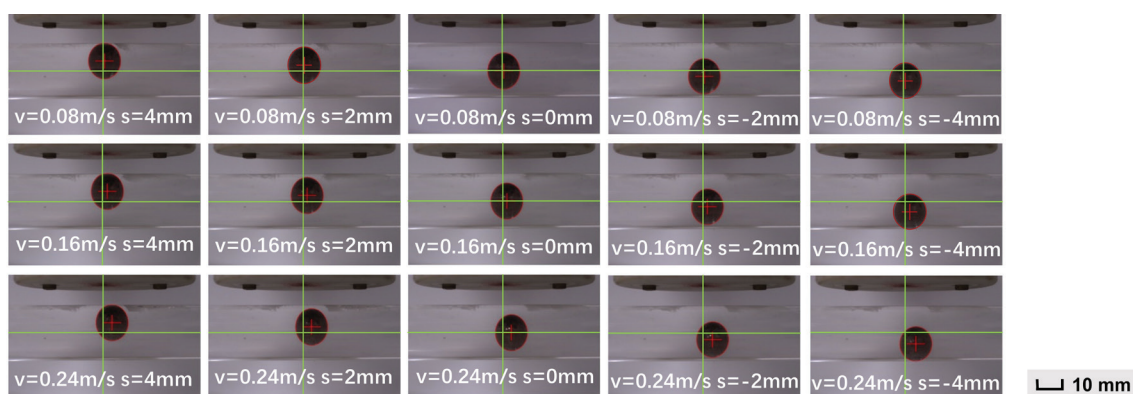
Fig. 24. Photos of a steady suspended ball in different conditions

Fig. 25 illustrates the relationship between the driving current of an electromagnet and the vertical position of a magnetic ball at various flow rates. This relationship is approximately linear; however, a sudden change of the driving current occurs when the ball reaches the extreme position near the tube wall ($s = \pm 4$ mm). As the driving current increases, the suspended position of the ball descends. According to the formula for the magnetic force of an electromagnet, the further the ball is from the electromagnet, the weaker the electromagnetic field becomes, necessitating a greater driving current to maintain force equilibrium. Additionally, at the same vertical position, the flow rate of the liquid has a minimal influence on the driving current required for suspension.

encounters horizontal fluid resistance, it must deviate from the z-axis to generate a horizontal component of electromagnetic force that counteracts the fluid resistance and maintains force equilibrium. Initially, the ball can be stably suspended at position p_1, where the resultant force is zero. An increase in fluid flow velocity results in heightened viscous and pressure drag a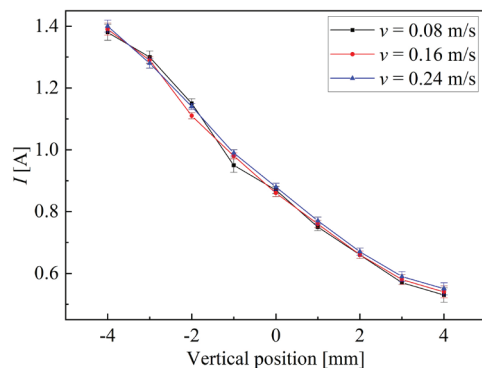cting on the ball, leading to an increase of $\mathbf{F_d}$. To maintain force equilibrium, $\mathbf{F_m}$ must increase and shift direction, which can be proved by the increase in current with the increase in flow rate, as shown in Fig. 25. Consequently, the ball shifts position from p_1 to p_2 or p_4, with a significant increase in horizontal offset.

Fig. 25. Relationship between the driving current of an electromagnet and the vertical position of the magnetic ball
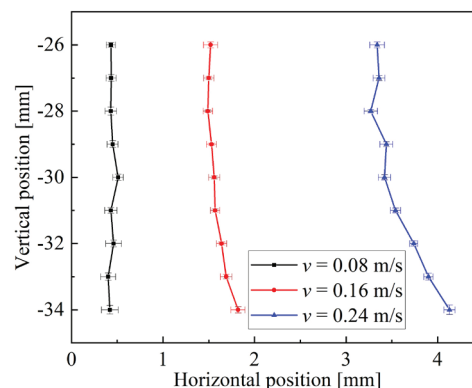
Fig. 26. The leviation trajectory of the magnetic ball within the fluid tube

Fig. 26 illustrates the steady-state suspension trajectories of the magnetic ball at three different flow velocities. As the flow velocity increases, the horizontal displacement of the ball also increases. It is evident that at higher fluid velocities, the horizontal displacement of the ball increases while the vertical position of the suspended ball decreases.

The experimental results indicate that both the driving current of the electromagnet and the fluid flow velocity influence the steady suspension position of the magnetic ball within the tube. The driving current is the primary parameter affecting the vertical position of the ball, while the fluid flow velocity predominantly influences the horizontal position. Fig. 27 illustrates the force analysis of the ball at four positions, where the ball achieves force equilibrium during steady suspension. The electromagnetic force $\mathbf{F_m}$ acting on the ball always points toward the central region of the electromagnet along the magnetic field lines, while the fluid resistance $\mathbf{F_d}$ primarily acts in the horizontal direction. The gravity $\mathbf{G}$ and buoyancy $\mathbf{F_u}$ in the horizontal direction remain constant. When the magnetic ball
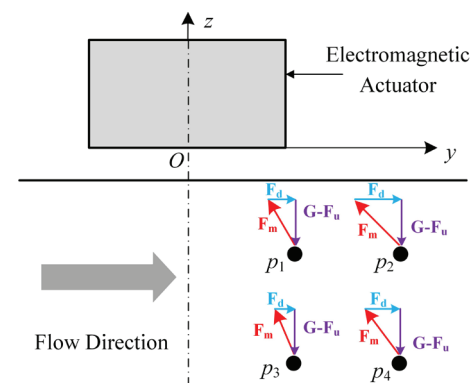

Fig. 27. Analysis of forces acting on a magnetic ball at various positions within a fluid tube

As seen in Fig. 8 and Fig. 12, the direction of the electromagnetic force rotates anticlockwise when the magnetic ball moves away from the electromagnet. The angle of deflection increases with an increase in horizontal position and decreases with a decrease in vertical

position. Additionally, the ball's fluid force $\mathbf{F_d}$ is greater when it is positioned further from the axis of the tube. As the vertical position s of the ball decreases, the magnetic ball must be deflected to the right and alter the direction of $\mathbf{F_m}$ for counteracting the increase in $\mathbf{F_d}$. The direction of the electromagnetic force then shifts to that shown at position p_4 while the ball reaches a new force equilibrium. Therefore, the horizontal offset distance increases as the position of the ball decreases, changing from p_1 to p_4.

The parameters of the three optimized results from Table 4 were applied in practical experiments to determine the actual suspended position of the ball. The comparison between the experimental results and the optimization results is presented in Table 5. In this study, the suspension of the magnetic ball occurs within a limited area, and the accuracy of the optimization results requires evaluation. To avoid the influence of the selection of the origin of the reference coordinate system on the error analysis, fiducial error [28] is used to evaluate the error between the simulation results and the experimental results, calculated as follows:

$$e = \frac{\Delta l}{\Delta d} \cdot 100 \text{ \%}, \tag{11}$$

where Δl represents the difference between the simulated value and the measured value, and Δd is the range of the magnetic ball's position. The range for the horizontal position is set to 30 mm, and the range for the vertical position is set to 45 mm.

The simulation error in condition C is greater than in the other conditions. This discrepancy is likely due to the large distance between the ball and the electromagnetic coil, resulting in a measurement accuracy of the linear Hall sensor. Overall, when the magnetically driven ball is stably suspended within the tube, the error between its position and the simulation results remains within 2 %, indicating that the simulation model is acceptable.

Table 5. Comparison between the experimental results and the optimization results

Condition	Simulation results [mm]	Experimental results [mm]	Y error [%]	Z error [%]
A	(0, 1.53, 3.8)	(0, 1.43, 3.1)	0.3	1.56
B	(0, 0.50, 1.8)	(0, 0.75, 1.2)	0.83	1.33
C	(0, 2.37, –2.5)	(0, 3.22, –1.7)	1.83	1.78

5 CONCLUSION

This study presents the design of a magnetic levitation ball system within a fluid tube, in which a magnetic ball is driven by an external magnetic field generated by an electromagnet. This system serves as a prototype for micro-mechanical diagnosis and therapy within the human circulatory system. Finite element numerical simulations of the electromagnetic field and blood flow are conducted to investigate the effects of blood flow velocity and the ball's position on fluid resistance, as well as the influence of position and angle on the magnetic force. Furthermore, a co-simulation of the flow field and magnetic field surrounding the magnetic ball is executed on the ANSYS Workbench platform. Based on the MOGA optimization, the physical field parameters for the steady-state levitation of the magnetic ball are calculated and verified through experiments. A comparison between the simulation and experimental results is presented. Finally, the characteristics of the steady-state suspended position of the magnetic ball are analyzed. The following conclusions can be drawn from this study:

1. An increase in the driving current or a decrease in the distance from the electromagnet results in a greater electromagnetic force of the magnetic ball. The gradient of the electromagnetic force along the axial direction of the electromagnet is observed to be greater than that along the radial direction. When the magnetic ball reaches a state of torque equilibrium under the influence of the electromagnet, its magnetic poles deviate and align toward the electromagnet.

2. The forces acting on the ball within the blood vessel are attributed to viscous resistance and pressure difference resistance. An increase in blood flow velocity and the distance of the ball from the axis of the blood vessel contribute to a rise in fluid resistance. The force exerted on the ball in the direction perpendicular to the blood flow is relatively small, while the fluid resistance in the direction of blood flow is significant.

3. The driving current of the electromagnet is the primary factor influencing the vertical position of the magnetic levitation ball, while the liquid flow velocity predominantly affects its horizontal position. At high blood flow rates, the horizontal position of the magnetic sphere is more significantly influenced by the driving current. As the driving current increases, the suspension height of the magnetic ball decreases, leading to a greater horizontal displacement.

4. An effective simulation model of a magnetically driven ball in a blood environment, along with a method for multi-objective optimization of parameters, is developed to determine the steady-state levitation parameters of the ball.

References

[1] Cai, Z., Fu, Q., Zhang, S., Guo, S., Guo, J., Zhang, X., Fan, C. Characteristic analysis of a magnetically actuated capsule microrobot in medical applications. *IEEE T Instrum Meas* 71, 4001511 (2021) **DOI:10.1109/TIM.2021.3130299**

[2] Schmidt, C.K., Medina-Sánchez, M., Edmondson, R.J., Schmidt, O.G. Engineering microrobots for targeted cancer therapies from a medical perspective. *Nat Commun* 11, 5618 (2020) **DOI:10.1038/s41467-020-19322-7**

[3] Zhang, D., Gorochowski, T.E., Marucci, L., Lee, H.T., Gil, B., Li, B., et al. Advanced medical micro-robotics for early diagnosis and therapeutic interventions. *Front Robot AI* 9, 1086043 (2023) **DOI:10.3389/frobt.2022.1086043**

[4] Elnaggar, A., Kang, S., Tian, M., Han, B., Keshavarz, M. State of the art in actuation of micro/nanorobots for biomedical applications. *Small Sci* 4, 2300211 (2024) **DOI:10.1002/smsc.202300211**

[5] Li, D., Choi, H., Cho, S., Jeong, S., Jin, Z., Lee, C., Ko, S. Y. et al. A hybrid actuated microrobot using an electromagnetic field and flagellated bacteria for tumor-targeting therapy. *Biotechnol Bioeng* 112, 1623-1631 (2015) **DOI:10.1002/bit.25555.**

[6] Fu, Q., Guo, S., Guo, J. Conceptual design of a novel magnetically actuated hybrid microrobot. *IEEE International Conference on Mechatronics and Automation,* 1001-1005 (2017) **DOI:10.1109/ICMA.2017.8015953**

[7] Zheng, L., Chen, L., Huang, H., Li, X., Zhang, L. An overview of magnetic micro-robot systems for biomedical applications. *Microsyst Technol* 22, 2371-2387 (2016) **DOI:10.1007/s00542-016-2948-6**

[8] Liang, N., Guo, J., Guo, S., Wei, X. Performance evaluation of the wireless micro robot in the fluid. *IEEE International Conference on Mechatronics and Automation,* 958-963 (2015) **DOI:10.1109/ICMA.2015.7237615**

[9] Larbi, M., Guechi, E.H., Maidi, A., Belharet, K. Observer-based control of a microrobot navigating within a 3D blood vessel along a trajectory delivered by a joystick device. *Machines* 11, 738 (2023) **DOI:10.3390/machines11070738**

[10] Qin, Y., Cai, Z., Han, J. Design and control of a magnetically-actuated anti-interference microrobot for targeted therapeutic delivery. *IEEE Robot Autom Let* 8, 5672-5679 (2023) **DOI:10.1109/LRA.2023.3295648**

[11] Marino, H., Bergeles, C., Nelson, B.J. Robust electromagnetic control of microrobots under force and localization uncertainties. *IEEE T Autom Sci Eng* 11, 310-316 (2013) **DOI:10.1109/TASE.2013.2265135**

[12] Chi, M., Zhang, J., Liu, R., Wang, Y., Nie, G., Qian, X. Coupled steering control of a low torsional torque capsule robot in the intestine. *Mechatronics* 77, 102596 (2021) **DOI:10.1016/j.mechatronics.2021.102596**

[13] Li, D., Niu, F., Li, J., Li, X., Sun, D. Gradient-enhanced electromagnetic actuation system with a new core shape design for microrobot manipulation. *IEEE T Ind Electron* 67, 4700-4710 (2019) **DOI:10.1109/TIE.2019.2928283**

[14] Liu, G., Lu, Y., Xu, J., Cui, Z., Yang, H. Magnetic levitation actuation and motion control system with active levitation mode based on force imbalance. *Appl Sci* 13, 740 (2023) **DOI:10.3390/app13020740**

[15] Estevez, P., Mulder, A., Munning Schmidt, R.M. 6-DoF miniature maglev positioning stage for application in haptic micro-manipulation. *Mechatronics* 22, 1015-1022 (2012) **DOI:10.1016/j.mechatronics.2012.08.002**

[16] Dabbagh, S.R., Alseed, M.M., Saadat, M., Sitti, M., Tasoglu, S. Biomedical applications of magnetic levitation. *Adv NanoBiomed R*, 2 2100103 (2022) **DOI:10.1002/anbr.202100103**

[17] Choi, K., Jang, G., Jeon, S., Nam, J. Capsule-type magnetic microrobot actuated by an external magnetic field for selective drug delivery in human blood vessels. *IEEE T Magn* 50, 1-4 (2014) **DOI:10.1109/TMAG.2014.2325055**

[18] Cha, K., Jeong, S., Choi, J., Qin, L., Li, J., Park, J. et al. Electromagnetic actuation methods for intravascular locomotive microrobot. *Annual International Conference of the IEEE Engineering in Medicine and Biology*, 1962-1965 (2010) **DOI:10.1109/IEMBS.2010.5627599**

[19] Qu, C., Pei, Y.-C., Xin, Q.-Y., Li, Z.-X., Xu, L. A reciprocating permanent magnetic actuator for driving magnetic micro robots in fluids. *P I Mech Eng C-J Mec* 235, 6451-6462 (2021) **DOI:10.1177/09544062211014547**

[20] Derbal, D., Bouzit, M., Mokhefi, A., Bouzit, F. Effect of the curvature angle in a conduit with an adiabatic cylinder over a backward facing step on the magnetohydrodynamic behaviour in the presence of a nanofluid. *Stroj Vestn-J Mech E* 69, 135-154 (2023) **DOI:10.5545/sv-jme.2022.239**

[21] Gkountas, A.A., Polychronopoulos, N.D., Sofiadis, G.N., Karvelas, E.G., Spyrou, L.A., Sarris, I.E. (2021). Simulation of magnetic nanoparticles crossing through a simplified blood-brain barrier model for Glioblastoma multiforme treatment. *Comput Meth Prog Bio* 212, 106477 **DOI:10.1016/j.cmpb.2021.106477**

[22] Ali, F., Sheikh, N.A., Khan, I., Saqib, M. (2017). Magnetic field effect on blood flow of Casson fluid in axisymmetric cylindrical tube: A fractional model. *J Magn Magn Mater* 423, 327-336 **DOI:10.1016/j.jmmm.2016.09.125**

[23] Belharet, K., Folio, D., Ferreira, A. Control of a magnetic microrobot navigating in microfluidic arterial bifurcations through pulsatile and viscous flow. *Proceedings of the 2012 IEEE/RSJ International Conference on Intelligent Robots and Systems*, 2559-2564 (2012) **DOI:10.1109/IROS.2012.6386030**

[24] Yesin, K.B., Vollmers, K., Nelson, B.J. Modeling and control of untethered biomicrorobots in a fluidic environment using electromagnetic fields. *Int J Robot Res* 25, 527-536 (2006) **DOI:10.1177/0278364906065389**

[25] Tillack, M.S., Morley, N.B. *Magnetohydrodynamics, Standard Handbook for Electrical Engineers*, McGraw Hill (1988) New York

[26] Choi, J.S., Baek, Y.S. A single dof magnetic levitation system using time delay control and reduced-order observer. *KSME Int J* 16, 1643-1651 (2002) **DOI:10.1007/BF03021666**

[27] Li, L., Wang, S. Experimental study and numerical analysis on windage power loss characteristics of aviation spiral bevel gear with oil injection lubrication. *Strojn Vestn-J Mech E* 69, 235-247, (2023) **DOI:10.5545/sv-jme.2023.558**

[28] Zhao, J., Cui, C., Zhang, P., Wang, K., Zhao, M. Parameter sensitivity analysis of the seismic response of a piled wharf structure. *Buildings*, 13349 (2023) **DOI:10.3390/buildings13020349**

Data availability *The data that support the findings of this study are available from the corresponding author upon reasonable request.*

Author contribution *Zhanxiang Cui: conceptualization, methodology, formal analysis, and writing – original draft; Yonghua Lu: writing – review & editing, Zezheng Wang: data curation and visualization; Ziyuan Wang: data curation and visualization; Yun Zhu: validation.*

Supplementary Information *The supplementary information includes the simulation results of the magnetic vector distribution of the magnetic ball and electromagnet, the calculation method of turbulence intensity in fluid simulation, the relationship between the fluid force of the magnetic ball and the blood flow velocity in fluid simulation, and the sensitivity analysis of parameters in MOGA optimization.*

Numerična in eksperimentalna študija stabilne levitacije magnetne krogle gnane z zunanjimi elektromagneti v cevki s tekočino: Uporaba v mikronapravah v človeških krvnih žilah

Povzetek *Raziskave na področju uporabe mikrorobotov v medicini uvajajo inovativne metode za zdravljenje različnih bolezni. Cilj te študije je razširiti uporabo nadzorovanih mikromehanskih diagnostičnih in terapevtskih pristopov znotraj človeških krvnih žil z zasnovo sistema magnetne levitacije krogle v cevki okroglega prereza, napolnjeni s tekočino. Sistem omogoča stabilno lebdenje magnetne krogle vzdolž določene poti pod vplivom zunanjega magnetnega polja. S pomočjo programske opreme so bile po metodi končnih elementov izvedene simulacije elektromagnetnega polja, tokovnega polja in mehanskega stanja sistema. Študija podaja analizo vpliva položaja krogle, usmerjenosti magnetnih polov, električnega toka in hitrosti toka tekočine na sile, ki delujejo na magnetno kroglo. Hkratna simulacija toka in magnetnega polja je bila izvedena na platformi ANSYS Workbench, pri čemer je bila uporabljena metoda večobjektne optimizacije za določitev parametrov, ki omogočajo stabilno levitacijo. Eksperimentalna potrditev je pokazala stabilno lebdenje magnetne krogle v tekočinski cevki pod vplivom zunanjega magnetnega polja. Eksperimentalni rezultati so potrdilo povezave med električnim tokom, hitrostjo toka tekočine in stabilnim položajem krogle, kar potrjuje natančnost simulacijske metode in izvedljivost nadzora položaja objektov v cevkah s tekočino.*

Ključne besede *magnetna levitacija, krvna žila, stabilna levitacija, biomedicinske naprave, večobjektna optimizacija*

Research on a Rapid Method for Obtaining the Matching Point of the Static Operating Pressure of a Supersonic Jet in a Wind Tunnel

Peng Liu ✉ – Jinglun Cai – Xuejing Shao – Hui Jin

Qingdao University of Technology, School of Mechanical and Automotive Engineering, China

✉ peng_liu@qut.edu.cn

Abstract   *In the wind tunnel test, mismatched operating pressures can cause the jet flow field to produce expansion waves, compression waves, and wave interference. The current wind tunnel pressure matching study requires continuous adjustment of the operating pressure at the inlet and outlet to obtain an ideal supersonic jet in an expanded state, and the pressure matching workload is substantial. This study presents a numerical simulation of the flow field of a supersonic wind tunnel under different outlet pressures based on the Reynolds-averaged Navier-Stokes (RANS) method. A method for quickly obtaining the static operating pressure matching point of a supersonic jet is proposed, which can quickly determine the matching operating pressure. When the Mach number of the monitoring point on the axis of the core area of the jet is within 5 % of the standard Mach number at the nozzle outlet, the jet in the wind tunnel test chamber is in an ideal expansion state, and the outlet pressure under this condition is the standard operating pressure for pressure matching. At the same time, the flow field structures under the conditions of over-expansion, ideal expansion, and under-expansion were compared, and it was shown that the key physical parameters in the core region of the supersonic jet field under the ideal expansion state obtained by this rapid matching method were stably distributed, which allowed the uniform region of the jet to exceed the limits of the diamond region and achieve uniform flow within the boundary of the supersonic jet.*

Keywords   *supersonic jet, pressure matching, expansion wave, compression wave*

Highlights
- *A fast method for obtaining back pressure matching points in supersonic wind tunnels is presented.*
- *Analyzed jet field structure and flow distribution in the core under non-matching parameters.*
- *Described shear layer development, vortex shedding, and large-scale vortex interactions.*

1 INTRODUCTION

A full understanding of the flow field characteristics of supersonic vehicles is of great significance for the research and development and performance optimization of supersonic vehicles. The quality of the wind tunnel test will have a significant impact on the design and concept verification of the aircraft, aerodynamic optimization, stability and control, flight characteristics simulation, noise testing, structural load analysis, and verification of simulation results.

In the supersonic wind tunnel test, the airflow is ejected from the nozzle outlet and directly impacts the low-speed gas in the test chamber without the constraint of solid wall boundaries. This strong impact and the collision of the jet with the object to be tested in the chamber change the state of the jet, forming a complex unsteady flow field in the confined space of the test chamber. In the shear layer of the supersonic jet, the vortex structures generated by the vortex shedding will continue to develop and evolve. These vortex structures interact with the rear collection device, and the pressure will change accordingly, showing strong pressure pulsations and making the instability of the flow field more obvious. For example, Liu et al. [1] studied the changes in the structure and turbulence characteristics of the boundary layer caused by the injection of the inner wall surface and the auxiliary injection of the scramjet engine through an experimental-based research method supplemented by numerical simulation. Sun et al. [2] studied the turbulent characteristics of the disturbed concave curvature boundary layer near the wall surface in a wind tunnel through numerical simulation.

Sabnis et al. [3] studied the interaction of the shock boundary layer in a supersonic wind tunnel with a nozzle geometry, explaining the importance of considering a uniform flow field in wind tunnel tests of shock-boundary-layer interaction. Sandham and Reynolds [4] studied three-dimensional transonic mixing-layer flows using direct numerical simulation (DNS). Vreman et al. [5] studied the effect of compressibility on the growth rate of the mixing layer using DNS. Flow characteristics such as Mach number, total and static pressure, total temperature and static temperature, as well as turbulent viscosity ratio distribution and heat flux density at the wind tunnel wall were investigated with the aim of improving the quality of the flow and expanding the scope of wind tunnel tests by Drozdov and Rtishcheva [6].

Lu et al. [7] conducted an experimental study on the interaction between shock waves and turbulent boundary layers in the Mach 3.4 supersonic low-noise wind tunnel. Lu et al. [8] also conducted an experimental study of the transition process of the 5° smooth straight cone boundary layer in the Mach 6 supersonic low-noise wind tunnel, and analyzed the instantaneous fine structure of the conical boundary layer under different attack angles and different unit Reynolds numbers. Egorov et al. [9] analyzed the influence of the amplitude of the incident Mach wave on the transition from laminar to turbulent flow in the supersonic boundary layer based on numerical simulation.

In the study of the design and flow field analysis of the supersonic wind tunnel, Junmou et al. [10] designed an integrated supersonic nozzle with a Mach 1.5 and 2 by using the non-viscous contour characteristic curve and correcting the overall curve of the boundary layer, which made the uniform area of the wind tunnel jet break through the limitation of the diamond-shaped area. Gounko and Kavun [11] used the Reynolds-averaged Navier-Stokes (RANS) equations and the SST k–ω turbulence model to study the unsteady

flow characteristics formed during the pulse start-up process of a supersonic wind tunnel with different diffusers. Kosinov et al. [12] experimentally studied the effect of a small angle of attack on the transition from laminar to turbulent flow in the supersonic boundary layer of a swept wing with a leading edge sweep angle of 72°.

Yu et al. [13] studied the starting characteristics of the wind tunnel in combination with the inlet model. The results show that a sudden increase in total pressure can generate a moving shock wave of sufficient strength to overcome the structure of the separation zone near the wind tunnel wall. Egorov et al. [14] used direct numerical simulation to simulate the roughness of the wind tunnel side wall in the boundary layer and then studied the effect of the incident Mach wave intensity on the laminar-turbulent transition (LTT). Bottini et al. [15] introduced the design of a Mach number supersonic wind tunnel for inducing boundary layer transition and analyzed the test intensity of free flow fluctuations. Wu et al. [16] performed RANS simulations on a supersonic wind tunnel with a perforated plate installed in a tandem nozzle, qualitatively analyzing the influence of the flow model on the synthetic flow field and the influence of the perforated plate on the flow quality in the test section.

Zhao et al. [17] analyzed the drag effect of hypersonic cones on free flow and found that hypersonic flow can reduce the skin friction between the main flow and the hypersonic jet, which is affected by the shear strength. Ermolaev et al. [18] studied the effect of small angles of attack on the transition from laminar to turbulent flow on swept wings at different Mach numbers using a T-325 wind tunnel. Milinović et al. [19] simulated supersonic and subsonic integral flight speed and rotational damping data based on wind tunnel tests and calculated aerodynamic coefficients. Lopez et al. [20] experimentally verified a simplified model of a wind turbine blade using aluminum beams of different geometries in a wind tunnel test, and studied the instability of nonlinear behavior caused by large deflections. Akbıyık et al. [21] analyzed the two- and three-dimensional flow structures and the induced flow effects generated by the plasma actuator in wind tunnel tests with a Reynolds number of 4.8×10^4.

Due to the influence of unsteady flow in the test chamber, it is difficult for the supersonic jet to achieve the ideal expansion state (pressure on both sides of the nozzle exit section is equal) as expected. When approaching the ideal expansion state, the supersonic jet will constantly change between under-expansion and over-expansion at the nozzle exit, and the core area of the jet will experience alternating shock waves and expansion waves, resulting in strong pressure fluctuations in the central flow field.

This study employs RANS and DNS methods to carry out steady and unsteady numerical simulations to study the back pressure matching relationship of the supersonic jet field in the test chamber. Under the conditions of the total pressure P_{in} at the inlet of the wind tunnel nozzle and the Mach number Ma_0 of the test chamber jet, the static pressure P_{out} at the outlet of the wind tunnel is adjusted the static pressure P_{out} at the wind tunnel outlet, the jet at the nozzle outlet is in an ideal expansion state, and a Mach number-height-uniform airflow is generated in the core region of the jet. Furthermore, the flow field characteristics of the supersonic jet in the limited space of the research test chamber were studied, and the development and instability of the shear layer of the supersonic jet, the interference of vortices and collectors, and the large-scale spatial vortex structure were characterized.

2 METHODS AND MATERIALS

2.1 Calculation Method Optimization

The fluid generated by the supersonic wind tunnel is turbulent, and it has the characteristics of diffusion, dissipation, randomness and vortex. The mainstream numerical simulation methods are divided into RANS, DNS, and large Eddy simulation (LES). RANS solves the uniform flow field and has a wealth of turbulence models for different types of flow. Its grid is Reynolds number independent and can better predict the flow trend of the flow field.

When calculating the steady-state flow field of a jet using the RANS method, there are usually five turbulence models to choose from, namely standard k–ε, RNG k–ε, realizable k–ε, standard k–ω and SST k–ω. Balabel et al. [22] used the above five turbulence models to numerically simulate the flow field of supersonic jets. The results show that the SST k–ω model performs best in the simulation of the flow field of supersonic jets, and the results of this model are basically consistent with the measured values. The SST k-ω model takes into account the influence of turbulent shear stress on the calculation results, and the turbulent viscosity formula is modified, which improves the calculation accuracy of the supersonic jet flow field.

To fully understand the development of the jet shear layer, instability, and vortex shedding in the wind tunnel test chamber under supersonic conditions, and to determine the flow characteristics of the supersonic jet field, this paper uses DNS to perform transient calculations of the supersonic jet flow field.

2.2 Numerical Simulation Model

The model of the wind tunnel test chamber is shown in Fig. 1. It is mainly composed of a Laval nozzle, a test chamber, a collector, and an outlet conduit [23]. The test chamber platform is equipped with a measuring probe to be tested in the wind tunnel test. After the gas is compressed and accelerated by the Laval nozzle, it forms a supersonic jet, which flows into the test chamber through the nozzle outlet and finally flows out through the collector connected to the outlet conduit.
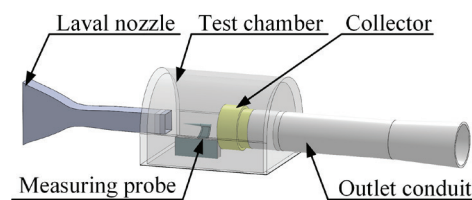

Fig. 1. Schematic diagram of the wind tunnel model

The flow field of the wind tunnel test model is shown in Fig. 2. The numerical calculation object is the total pressure $P_{in} = 180$ kPa at the nozzle inlet. By adjusting the static pressure P_{out} at the wind tunnel outlet, the Mach number at the nozzle outlet is Mach 1.5 and the nozzle outlet jet is in an ideal expansion state of supersonic flow. The nozzle outlet is a matrix with a side length of 2000 mm, and the axial computational domain length is 79500 mm. The inlet of the Laval nozzle is given as the pressure inlet boundary, the outlet of the wind tunnel is the pressure outlet, and the boundary conditions for the remaining surfaces are insulated non-slip walls.
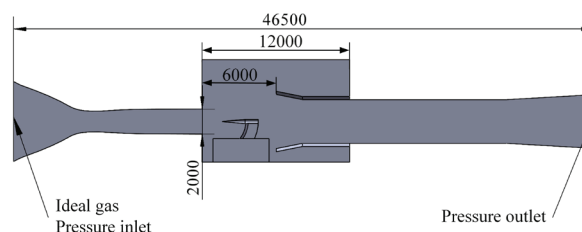

Fig. 2. Jet computational domain dimensions and boundary conditions
(central cross-section of the fluid domain) (in mm)

The section from the nozzle outlet to the test stylus is the core of the jet field in the test chamber. When achieving back pressure matching for a given jet Mach number, the Mach number at the nozzle outlet should be the main assessment object to ensure that the Mach number at the typical position on the centerline of the nozzle outlet jet is stable. Therefore, reasonable Mach number monitoring points should be set in the core area of the jet field to obtain the velocity distribution at typical locations. As shown in Fig. 3, the coordinates of the center point of the nozzle outlet section (0, 0, 0) are taken as the origin of coordinates. Five evenly distributed Mach number monitoring points P1 to P5 are set on the axis of the nozzle outlet in the core region of the jet field, of which monitoring point P1 is set at the origin of coordinates and monitoring point P5 is set at the tip of the probe. Table 1 demonstrates the specific coordinates of the five monitoring points.
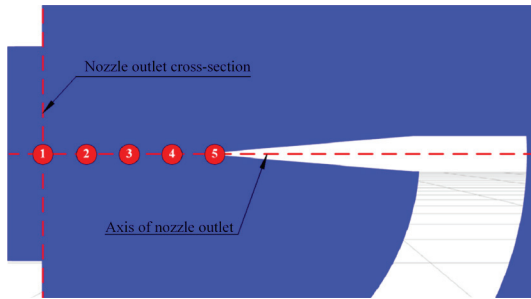

Fig. 3. Schematic diagram of the monitoring point on the axis of the nozzle outlet

Table 1. Coordinate data of the axis monitoring points

Point number	P1	P2	P3	P4	P5
X-coordinate [mm]	0	400	800	1200	1600
Y-coordinate [mm]	0	0	0	0	0
Z-coordinate [mm]	0	0	0	0	0

2.3 Back Pressure Matching Method

For the steady-state flow field simulation analysis of supersonic jets, the ideal expansion state of the jet at the nozzle outlet is required for pressure matching. A slight deviation in the back pressure can cause the jet state to deviate. Through a large number of back pressure matching simulation calculations, the Mach number distribution of the jet centerline from the nozzle outlet to the measuring probe satisfies the given supersonic Mach number, and summarizes the characteristics of the jet field structure and the distribution of flow parameters in the core region under typical non-matching parameters.

2.3.1 Numerical Simulation Parameter Optimization

The supersonic jet process is a compressible flow, and the ideal-gas model should be used for numerical simulation. The k–ω SST turbulence model is used to solve and turn on the energy equation. The density-based solver needs to be preprocessed to overcome the singularity of the system matrix in the low Mach number flow region. The pressure-based solver is good at capturing the physical characteristics of the jet flow field. For high-speed compressible flows, it is suitable to solve the energy and momentum equations by coupled method, which helps the numerical simulation to converge. The spatial discretization method for pressure is set to Second Order, which is suitable for compressible flow. Supersonic jets are often accompanied by the generation of shock waves. The default settings for other spatial discretization methods such as density and momentum are first-order upwind schemes. However, this format will smooth out the shock waves in compressible flows. Therefore,

the density, momentum, and other spatial discretization methods are changed to the quadratic upwind interpolation (QUICK) format to make the calculation results more accurate.

The numerical simulation monitors the residuals of each equation to estimate the convergence of the calculation. When the residual of the energy equation drops to 1×10^{-6} and the residuals of other equations such as the continuity equation and velocity equation drop to 1×10^{-3}, the numerical simulation program will converge by default. The residual calculation value is only a general method for roughly judging whether the calculation has converged. According to the law of conservation of mass, the mass flow rate values at the inlet and outlet of the nozzle should be the same. Therefore, the mass flow rate difference between the inlet boundary and the outlet boundary is monitored. When the residual of the monitored mass flow reaches 1×10^{-8}, it can be judged that the steady-state numerical simulation has reached a converged state.

2.3.2 Mesh Construction and Mesh-Independent Verification

The jet computational domain is discretized using a combination of hexahedral and polyhedral meshes, which ensures that the entire computational domain mesh is structured and effectively improves the mesh quality. To more accurately study and analyze the flow field in the core region of the supersonic jet in the wind tunnel, the mesh of the Laval nozzle as a whole and the core region of the jet from the nozzle outlet to the collector was densified; the boundary layer was added to the probe and the collector wall.

As shown in Fig. 4, when the fluid flow state is fully developed turbulence, the turbulent flow near the flat wall can be divided into three regions. At the near wall, the viscous force is dominant because the inertial force is small compared to the viscous force. The fluid velocity in this region varies linearly with the distance from the wall, exhibiting laminar flow. This region is the viscous sublayer. When the flow begins to transition to turbulence, the area away from the wall is called the buffer layer, and eventually, when the flow completely transitions to a turbulent state, it is called the turbulent core.
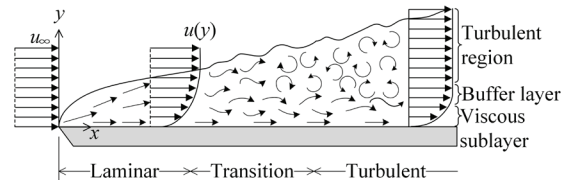

Fig. 4. Schematic diagram of fluid flow state

For the study of turbulent boundary layers, von Karman derived a logarithmic law based on the Prandtl mixing length theory using a dimensional analysis method, further subdivided the turbulent boundary layer into four regions: the viscous sublayer ($0<y^+<5$), the buffer layer ($5<y^+<30$), the log-law region ($y^+>30$), and the outer layer, as shown in Fig. 5. The boundary layer is usually defined by the two dimensionless physical quantities u^+ and y^+, which are defined as follows:

$$u^+ = \frac{u}{u^*}, \tag{1}$$

where u^+ represents the dimensionless velocity, u represents the fluid velocity in the boundary layer, and u^* is the friction velocity near the wall surface, which is defined as follows:

$$u^* = \sqrt{\frac{\tau_\omega}{\rho}}, \tag{2}$$

where τ_ω is the shear stress on the wall surface, y^+ represents the dimensionless distance to the wall, y represents the distance from a point in the boundary layer to the wall, and

v represents the kinematic viscosity of the fluid [m²/s]. Therefore, after determining y^+ at the first layer of the wall, the first layer spacing can be calculated.,

$$y^+ = \frac{u^* y}{v}. \tag{3}$$

For viscous bottom layers ($0 < y^+ < 5$), the viscous force is linearly related to the velocity gradient; for the fully turbulent layer, u^+ and y^+ are approximately logarithmically related, which is called the logarithmic law layer; for the buffer layer, the linear relationship curve and the logarithmic law curve intersect in the buffer layer, and the y^+ value corresponding to the intersection point is around 11.
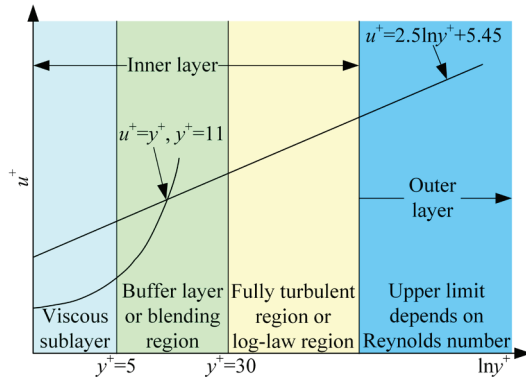

Fig. 5. Turbulent boundary layer region division

For the k–ω SST turbulence model used in this paper, the wall function is not used to solve the distribution of physical quantities in the viscous sublayer and buffer layer. Instead, the NS equation is discretized and solved throughout the basin, so the first layer of the boundary layer grid should be in the viscous sublayer. Taking $y^+ = 1$, the first mesh layer thickness is calculated to be 0.07 mm. The model includes a total of 18 million mesh cells, with a minimum cell size of 6 mm and a minimum orthogonal quality of 0.144.

The Mesh-independent verification is used to explore the impact of the number of mesh cells on the accuracy of the numerical simulation, so as to select an appropriate number of mesh cells to ensure the accuracy of the numerical simulation. Under the condition of ensuring that the computational domain model of the wind tunnel jet field is exactly the same, the mesh size of the entire nozzle and the shear layer in the test chamber (from the nozzle outlet to the collector area) is adjusted by adjusting the global size of the mesh. Three different mesh models with 16 million, 18 million and 20 million mesh elements are set up, and the minimum mesh element size is 6.5 mm, 6 mm and 5.5 mm, respectively. After meshing, the mesh quality is checked to ensure that a high-quality mesh model is output. The minimum orthogonal quality of the mesh is an important criterion for measuring the quality of the mesh. It represents the deviation of the shape of the representative element from the ideal orthogonal shape. In the case of adding a boundary layer to the fluid domain mesh, the minimum orthogonal quality should generally be greater than 0.1. Table 2 shows the results of the mesh quality check for the three types of jet field meshes described above.

Table 2. Mesh quality test results

Mesh cells in million	16	18	20
Minimum cell size [mm]	6.5	6	5.5
Minimum orthogonal mass	0.128	0.144	0.151

The results of the mesh quality test show that the meshes of the three sizes have high mesh quality. The steady-state flow field of

the supersonic jet is calculated under the same conditions, where the static pressure at the outlet P_{out} is set to 92 kPa. The comparison of the Mach number calculation results and the calculation error at the P1-P5 monitoring points are shown in Figs. 6-10.
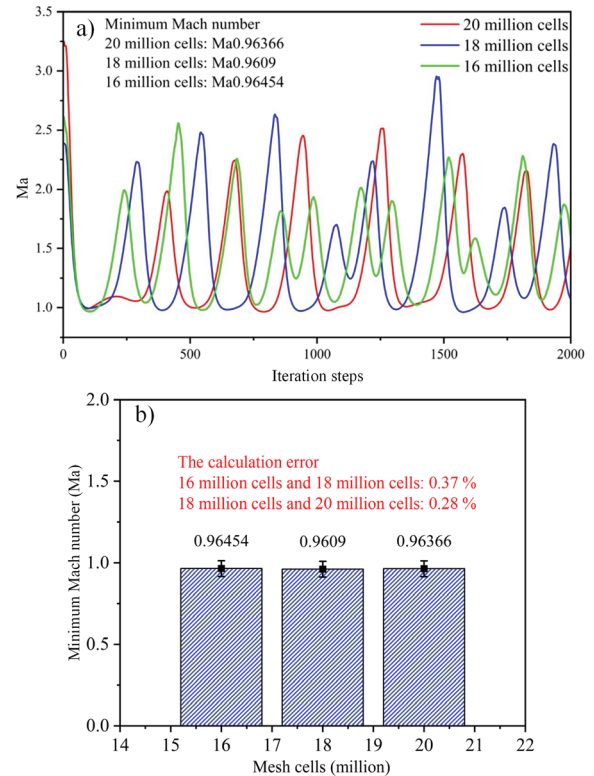

Fig. 6. P1 monitoring point independence verification;
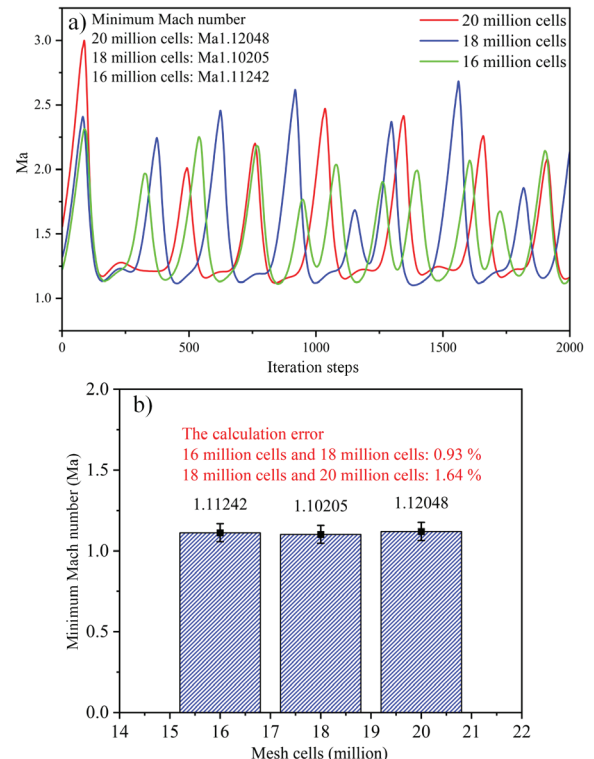a) minimum Mach number at P1, and b) calculation error at P1

Fig. 7. P2 monitoring point independence verification;
a) minimum Mach number at P2, and b) calculation error at P2
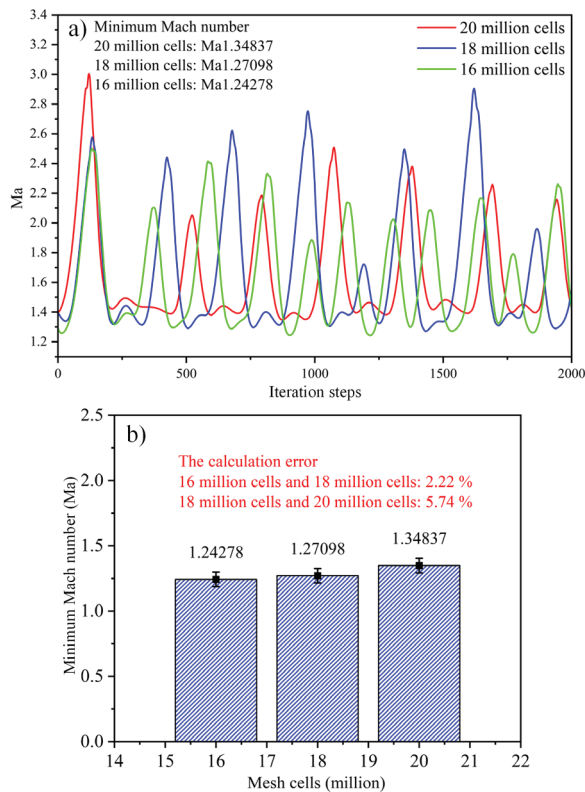
Process and Thermal Engineering

Fig. 8. P3 monitoring point independence verification;
a) minimum Mach number at P3, and b) calculation error at P3

Fig. 9. P4 monitoring point independence verification;
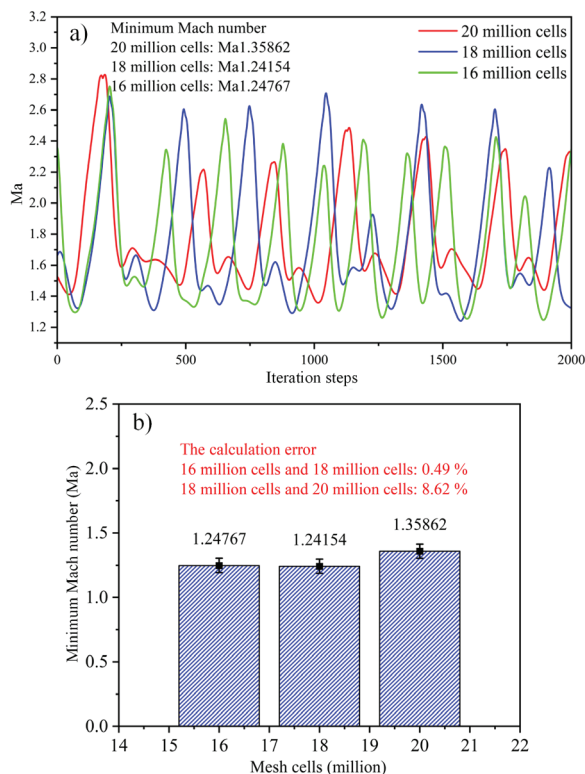a) minimum Mach number at P4, and b) calculation error at P4

From Figs. 6-10, it can be seen that for the five monitoring points (P1-P5) set in the core area of the jet from the nozzle outlet to the probe section, each point shows a regular fluctuation state. Taking the

minimum Mach number in the iteration of the axis monitoring points P1-P5 as the reference basis, the number of mesh cells increases from 16 million to 18 million, 20 million, and the minimum Mach number error values are all within 10 %. The impact of reducing the mesh size on the calculation results is negligible. The specific error values are shown in Table 3. The verification conditions for mesh independence are met, indicating that the calculation accuracy of 18 million mesh cells can meet the calculation requirements.
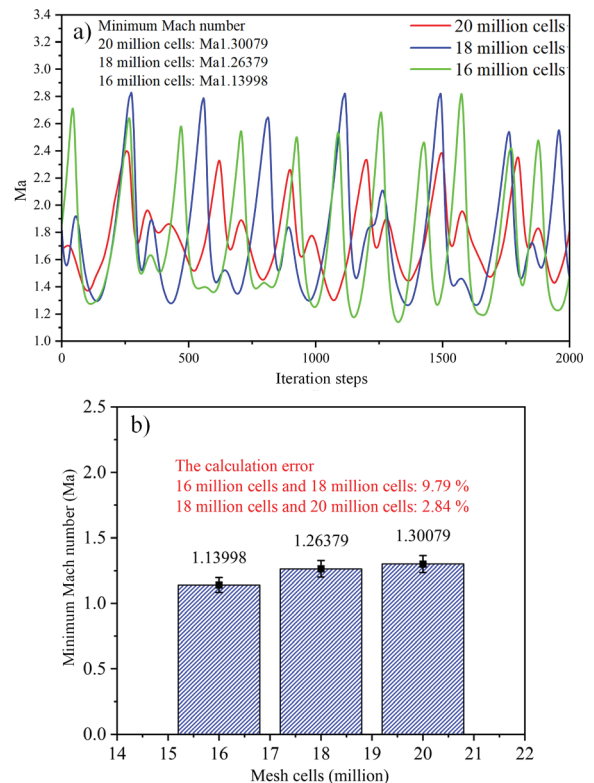

Fig. 10. P5 monitoring point independence verification;
a) minimum Mach number at P5, and b) calculation error at P5

Table 3. Mesh comparison error table

Point number	Mesh cells comparison	Error [%]
P1	16 and 18 million	0.37
	18 and 20 million	0.28
P2	16 and 18 million	0.93
	18 and 20 million	1.64
P3	16 and 18 million	2.22
	18 and 20 million	5.74
P4	16 and 18 million	0.49
	18 and 20 million	8.62
P5	16 and 18 million	9.79
	18 and 20 million	2.84

2.3.3 Propose a Back-Pressure Quick Matching Method

Propose back-pressure matching basis

The purpose of supersonic jet back pressure matching is to keep the total pressure P_{in} at the entrance of the wind tunnel constant at 180 kPa, and to adjust the static pressure P_{out} at the outlet of the wind tunnel so that the pressure at the outlet of the nozzle is consistent with the working environment pressure (atmospheric pressure). the
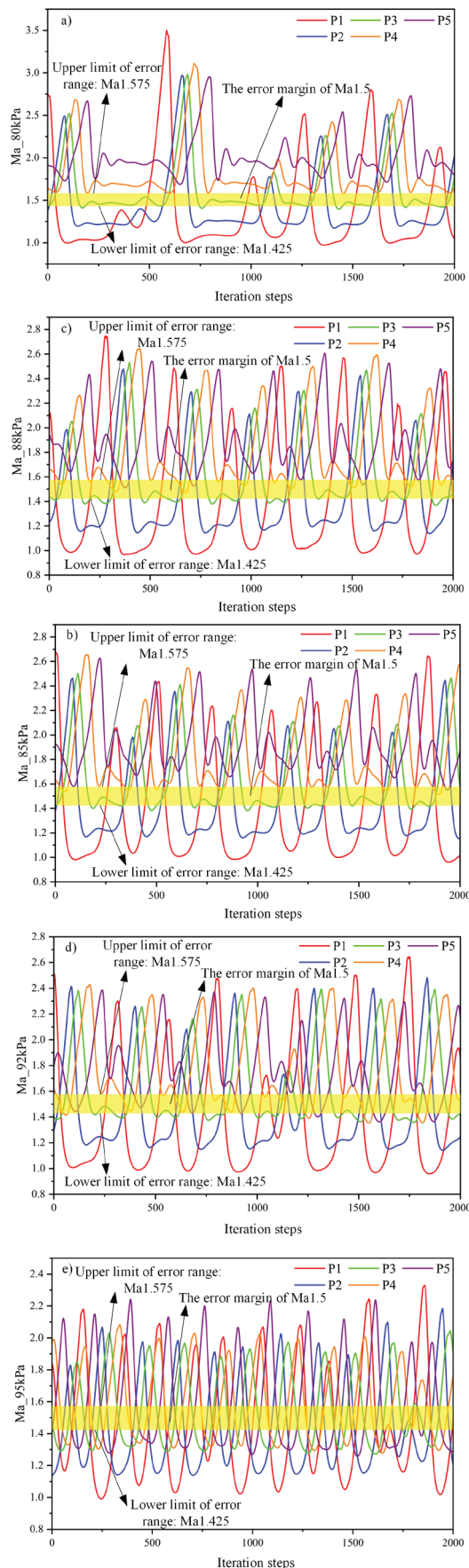
118 · SV-JME · VOL 71 · NO 3-4 · Y 2025

Fig. 11. Mach number at the axis monitoring point for different outlet pressures; a) P_{out} = 80 kPa, **b)** P_{out} = 85 kPa, **c)** P_{out} = 88 kPa, **d)** P_{out} = 92 kPa, **e)** P_{out} = 95 kPa

supersonic fluid ejected from the nozzle outlet is in an ideal expansion state, achieving a stable Mach number in the core area of the jet from the nozzle outlet to the probe section in the chamber. At this time, the static pressure at the wind tunnel outlet is the standard static pressure P_m for achieving wind tunnel jet back pressure matching.

Under ideal expansion conditions, a supersonic jet with a Mach 1.5 is ejected from the outlet of the Laval nozzle of this standard profile. The Mach number at the nozzle outlet is the main research object, and a steady-state numerical simulation is conducted on the 18 million cells. When the Mach number deviation at the typical position of the centerline of the nozzle jet does not exceed 5 %, the static pressure P_{out} at the outlet of the wind tunnel is the matching value of the back pressure P_m.

When the jet field simulation calculation converges, the number of iterations at convergence is recorded as S_0, which means that when the calculation is iterated to S_0, the residual values and mass flow rates have met the convergence conditions. Therefore, the solution results at any iteration step after S_0 can meet the actual flow field distribution under this working condition. Take the calculation result of the outlet pressure P_{out} of 92 kPa as an example Fig. 11a) shows the Mach number of the P1-P5 monitoring points after the S_0 and the change of the number of iterations. (2000 iterations are selected.) This means that the Mach number of the P1-P5 monitoring points at each iteration in the figure is the Mach number distribution of the actual jet field under the working condition. Fig. 11. shows the Mach number curves of the P1-P5 monitoring points after the convergence iteration step S_0 under the conditions of outlet pressures P_{out} of 80 kPa, 85 kPa, 88 kPa, and 95 kPa, respectively.

Rapid backpressure matching process

Step 1. Calculate and obtain the Mach number fluctuation curve of the measurement point that meets the error requirements. For example, the outlet speed of this type of Laval nozzle under standard ideal expansion conditions is Mach 1.5, so the curve of the monitoring point Mach number within 5 % of the calculated error (i.e. Mach 1.425 to 1.575) is selected.

Step 2. Since the Mach number changes at each monitoring point have obvious periodicity, in order to facilitate observation and statistics, the 500-step partial curve of the Mach number calculation process at each monitoring point under the above-mentioned P_{out} conditions is intercepted for study, and it should be ensured that the intercepted part contains the complete cycle of the Mach number change at the monitoring point, as shown in Figs. 12-16.
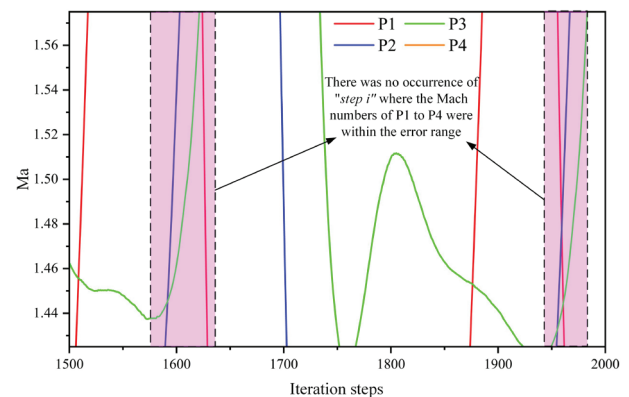

Fig. 12. Curve processing at an outlet pressure of 80 kPa

Step 3. Determine whether the Mach number fluctuation curve of a calculation step is within the error range. The P5 is at the tip of the measuring probe, and the flow field fluctuates greatly due to the influence of the measuring probe. The data analysis only takes
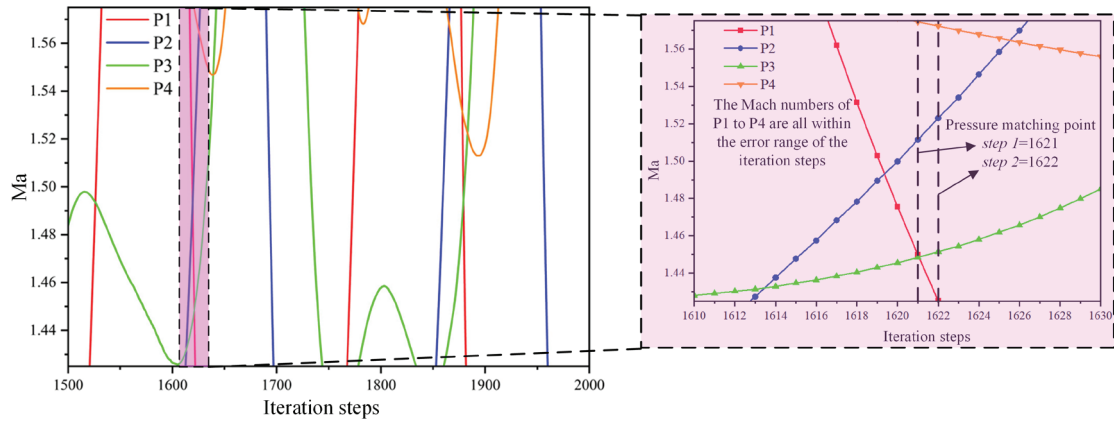
Fig. 13. Curve processing when back pressure matching is satisfied with an outlet pressure of 85 kPa
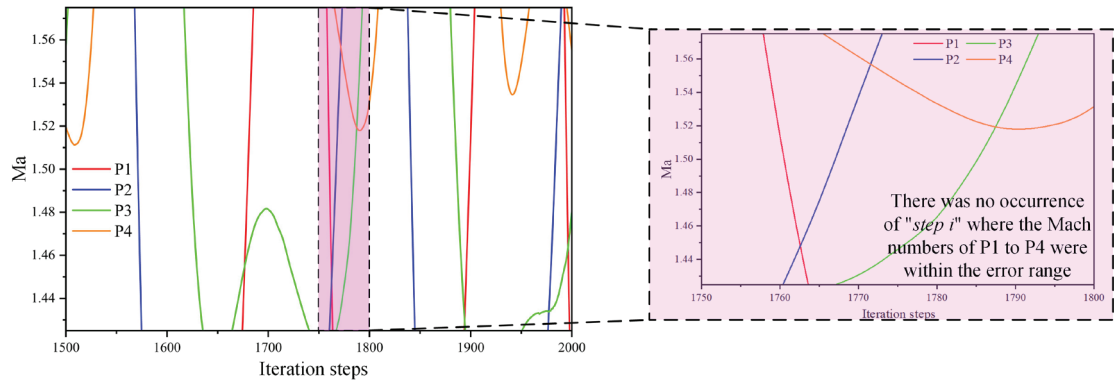

Fig. 14. Curve processing at an outlet pressure of 88 kPa

the key positions of the axial monitoring points P1-P4 as the basis for back pressure matching. When a certain iteration number step i exists in the intercepted partial curve, and the Mach number curve of the P1-P4 monitoring points at *step i* also exists in the Mach 1.425 to 1.575 curve, it means that the Mach number distribution on the centerline of the jet from the nozzle outlet to the probe at *step i* is uniform and within the error range of the standard Mach number of 1.5 when the back pressure is matched. The simulation results for this *step i* are the jet field distribution that satisfies the wind tunnel jet back pressure matching conditions. The set wind tunnel outlet pressure P_{out} is the solution P_m for matching the back pressure of the supersonic wind tunnel jet.

The specific processing results of the Mach number curves at the monitoring points with the outlet pressures P_{out} set to 80 kPa, 85 kPa, 88 kPa, 92 kPa, and 95 kPa are shown in the Figs. 12-16.

1. P_{out} = 80 kPa

As shown in Fig. 12, within the standard Mach number of 1.5 error range (Mach 1.425 to 1.575), there is no solution that satisfies the back pressure matching conditions at monitoring points P1-P4 during the calculation process, that is, there is no iteration step *step i* in the figure that makes the curves shown at P1-P4 all fall between Mach 1.425 to 1.575 at *step i*, thus not meeting the conditions for matching the back pressure of the wind tunnel jet.
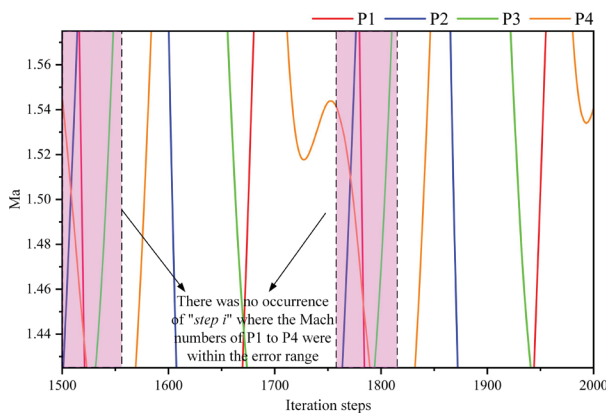

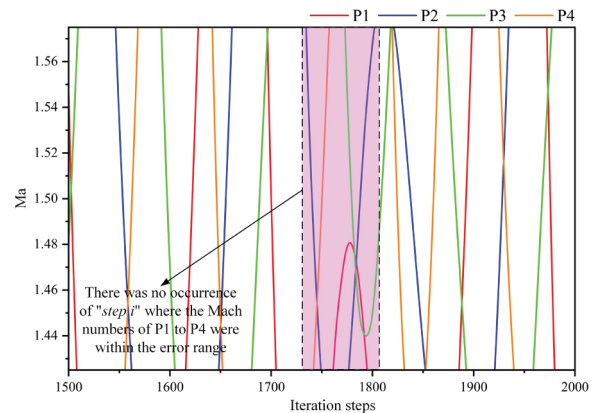Fig. 15. Curve processing at an outlet pressure of 92 kPa

Fig. 16. Curve processing at an outlet pressure of 95 kPa

2. P_{out} = 85 kPa

As shown in Fig. 13, when the outlet pressure P_{out} = 85 kPa, there are two solutions that satisfy the back pressure matching in the Mach number curve during the iteration process: step 1621 and step 1622. That is, *step 1* = 1621, *step 2* = 1622. When the iteration reaches *step 1* and *step 2*, the Mach numbers of the P1-P4 are all within the range of Mach 1.425-1.575. At this time, the velocity distribution of the core area of the jet from the nozzle outlet to the probe section is stable, achieving back pressure matching of the wind tunnel jet.
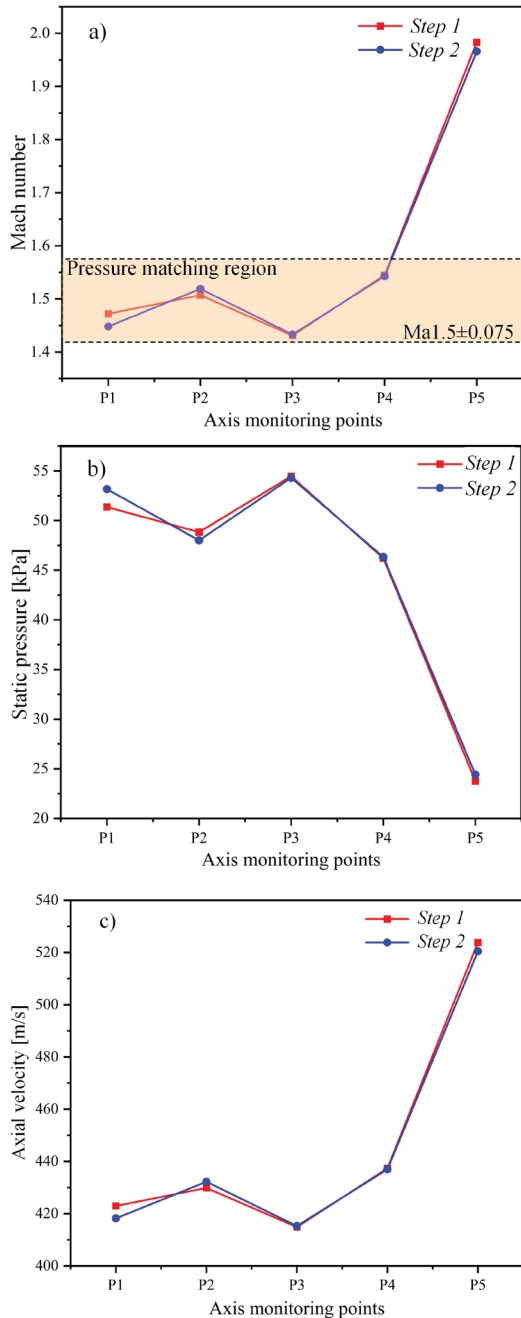

Fig. 17. Distribution of key physical parameters of the axis under back pressure matching conditions; a) Mach number distribution at monitoring points, b) static pressure distribution at monitoring points, and c) axial velocity distribution at monitoring

3. P_{out} = 88 kPa

As can be seen from Fig. 14, there is no solution for back pressure matching at an outlet pressure of 88 kPa, i.e. there is no iteration

number *step i* in the graph such that the curves shown by P1-P4 are simultaneously between Mach 1.425 and 1.575 at *step i*, thus not meeting the conditions for back pressure matching of the wind tunnel jet.

4. P_{out} = 92 kPa

As can be seen on Fig. 15, there is no solution for back pressure matching at an outlet pressure of 92 kPa.

5. P_{out} = 95 kPa

As can be seen on Fig. 16, no solution for back pressure matching is found for an outlet pressure of 95 kPa.

In summary, the ideal outlet pressure P_m = 85 kPa is achieved when the back pressure matching conditions of the wind tunnel are satisfied. At this time, the jet at the outlet of the nozzle is in an ideal expansion state, and the Mach number of the centerline of the jet in the cabin is stable at Mach 1.5.

Characteristics of the distribution of the axis of the nozzle jet at the back pressure matching point

Extract the data on the Mach numbers of monitoring points P1-P5 at step 1 and step 2 of the numerical simulation results under the operating condition of P_m = 85 kPa, as shown in Table 4.

Fig. 17a shows the Mach number distribution of monitoring points P1-P5 when back pressure matching is achieved. It is evident that the Mach number distribution on the centerline of the nozzle outlet jet fluctuates periodically within the Mach 1.5 error range, which can provide the supersonic jet at the desired expansion state of the nozzle outlet. The flow field near the tip of the P5 probe is highly turbulent, and the presence of the probe will greatly increase the Mach number, so it is not representative in the study. Figs. 17b and c show the static pressure and axial velocity distributions at monitoring points. It can be seen that the key physical parameters of the jet field from the outlet of the nozzle to the stylus are distributed stably, which further verifies the back pressure matching method described above.

Table 4. Mach number at monitoring points under back pressure matching condition

Point number	Mach number		Axial velocity [m/s]		Static pressure [kPa]	
	step 1	step 2	step 1	step 2	step 1	step 2
P1	1.472	1.448	422.975	418.239	51.37	53.17
P2	1.507	1.519	429.881	432.249	48.84	48.01
P3	1.431	1.433	414.885	415.279	54.47	54.31
P4	1.545	1.543	437.379	436.985	46.21	46.34
P5	1.983	1.966	523.805	520.451	23.77	24.43

Back pressure matching results and verification

The flow field analysis was performed using the steady-state simulation results of the wind tunnel jet field in *step 1*. Fig. 18 shows the Mach number, static pressure, and pathlines diagram of the core area of the jet (from the nozzle outlet to the collector inlet) in the central plane of the wind tunnel test chamber (Z = 0 mm) under the wind tunnel back pressure matching condition.

The numerical simulation results of the above back pressure matching working conditions can analyze and summarize the flow field characteristics of the ideal expansion state of the nozzle jet and the influence of the equipment in the test chamber, such as the probe, test bench, and collector, on the jet field. At this time, the static pressure at the nozzle outlet is equal to the static pressure in the test chamber, and the supersonic jet injected into the wind tunnel test chamber is in an ideal expansion state. As shown in the A1, B1, and C1 areas in Fig. 18, the core area of the jet from the nozzle outlet to the probe section, the supersonic jet in the ideal expansion state has a relatively uniform flow within the jet boundary, and the jet boundary is stable. At this time, there is no repeated phenomenon of accelerated

expansion and decelerated compression, which makes the range of the uniform jet zone break through the limitation of the rhombus zone in the traditional high-speed free jet wind tunnel during supersonic speed tests. The physical parameters such as the Mach number and static pressure in the core of the jet are uniform and stable. The jet trajectory is stable, and the supersonic jet flows steadily in the horizontal direction without significant airflow deviation, providing good simulation conditions for wind tunnel tests.
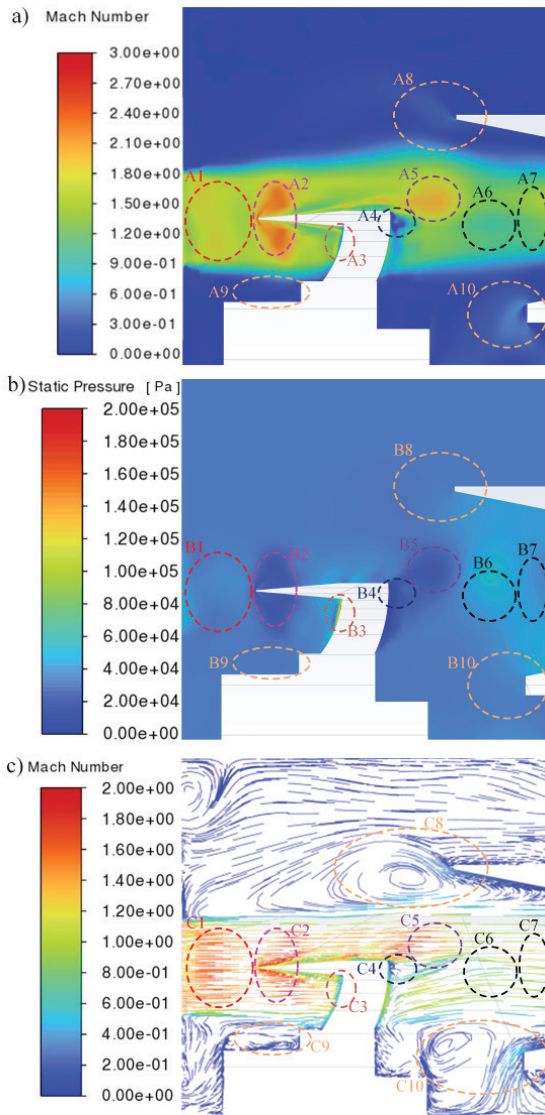

Fig. 18. Flow field at the center plane under back pressure matching conditions
(P_{out} = 85 kPa); a) Mach number contour, b) static pressure contour, c) pathlines diagram

There is a clear concentration of the velocity in the A2, B2, and C2 regions in Fig. 18. The reason is that after the uniform and stable supersonic jet is ejected from the nozzle into the test chamber under ideal expansion conditions, the jet flows through the probe and is blocked by the probe, as shown in the C2 region It is evident that the blocked supersonic jet will flow along the surface of the conical probe. Under the condition of constant flow rate, the cross-sectional area of the jet is reduced due to the influence of the probe, resulting in an increase in the flow velocity and a decrease in the pressure in this area, so that the tip of the probe has a higher Mach number.

Unlike the above-mentioned increase in flow velocity due to the decrease in the cross-sectional area of the basin at the tip of the probe, the jet Mach number at point A3 in Fig. 18 demonstrates a

very significant decrease. The reason for this is that the arc test stand of the probe device at this point has a larger gradient on the windward side than the conical probe mentioned above. Line flow situation shows that the jet flow to the arc test frame can not flow smoothly along the surface of the mechanism, but is hindered by the arc test frame, causing the flow to be blocked and slowed down, so the Mach number in the A3 area is reduced. The deceleration of the jet flow in this area causes the air flow to gather, causing the pressure to rise, as shown in the B3 area in Fig. 18.

After the jet flows through the test bench, the central area of the jet is blocked by the probe mechanism, and only a small amount of fluid passes through the area C4 in the pathlines diagram in Fig. 18c, resulting in a lower static pressure at point B4 compared to the surrounding static pressure, forming a low static pressure area as shown in Fig. 18b, and also resulting in a lower fluid velocity in this area, forming a low Mach number area A4 in the Mach number cloud diagram in Fig. 18a. When the jet passes completely through the test bench device, the fluid, which was previously decelerated, is briefly accelerated by the obstruction of the probe mechanism, as shown in the A5 area, producing a clearly high Mach number region. The increase in fluid is also reflected in the decrease in static pressure in the B5 area. At the same time, it can be seen from the pathlines diagram in the C6 area that after the supersonic jet flows through the probe mechanism, the blocked jet produces fluid separation in this area. The fluid flowing through the C6 area is less likely to form a low Mach number region at A6. As can be seen from the A7, B7, C7, the jet area that has undergone a brief separation will once again be integrated, and the physical parameters such as Mach number and static pressure will then be distributed stably, forming a uniform and stable jet again, which then flows through the collector and is ejected from the wind tunnel outlet conduit.

The flow structure in the wind tunnel test chamber of the open-mouth device is complex and has high unsteadiness, as shown in the C8, C9, and C10 areas in Fig. 18. The vortices formed by vortex shedding in the supersonic jet shear layer continue to develop, become unstable, and evolve, and interfere with the collector at the rear end, forming fluid disturbances that will exacerbate the instability of the flow field. These include the large-scale pseudo-order vortex structure in the jet shear layer shown in C8, the large-scale spatial vortex structure induced by the jet shear layer and the low-speed fluid in the suction test chamber shown in C10, and the separation vortex structure in the corner of the test chamber shown in C9. The mutual interference, fusion, and development of these spatial vortex structures increase the complexity of the flow field structure of the test chamber and exacerbate the pulsating characteristics of the flow field.

This study also studies the flow field characteristics in the plane on both sides of the backpressure matching (Z = 700 mm, Z = –700 mm). The center plane of the test chamber (Z = 0 mm) is set as *Plane 1*, and the plane at Z = 700 mm in the test chamber is set as *Plane 2* to analyze the influence of the measuring probe on the jet field. Fig. 19 demonstrates the Mach number, static pressure and pathlines diagram of the fluid domain in *Plane 1* and *Plane 2*.

Since there is no test bench device in the *Plane 2* to interfere with the supersonic jet, the Mach number and static pressure zone of the E1 and G1 jet core flow field shown in Fig. 19b are more uniform and stable. The I1 region jet is in an ideal expansion state, and the fluid pathlines is ejected horizontally from the nozzle outlet. Additionally, the Mach number jump region in the E2 region caused by the tip of the measuring probe is significantly reduced, and the Mach number in the E2 region is similar to the Mach number of the surrounding flow field, both remaining near the standard Mach 1.5 at the nozzle outlet. The static pressure in the G2 area and the flow field pathlines

in the I2 area in Fig. 19 can be compared with the flow fields in F2 and H2 in *Plane 1*. It is evident that the influence of the probe tip on the flow field is only in a small area near the tip, and the influence on the flow field in the outer area of the test bench is small. There is still a large range of Mach number mutation zones in the E3 region, indicating that the velocity concentration generated by the supersonic jet field flowing through the measuring probe in the outer region of the test bench still exists. The static pressure reduction region in the G3 region of the static pressure contour of *Plane 2* shown in Fig. 19d still exists, and the corresponding I3 region pathlines in the flow field pathlines diagram shown in Fig. 19f indicates that the jet fluid here has a significant acceleration process. This shows that the stepped shape of the test bench also has a more significant effect on the flow state of the jet field. After a short acceleration phase, the supersonic jet is re-integrated at the collector inlet. The flow field parameters are uniformly distributed in the E4, G4, and I4 areas of Fig. 19, and the jet field is again in a uniform and stable state, flowing through the collector and into the rear outlet conduit. It is worth noting that the separation of the flow field shown in Fig. 18 in the C4 region does not occur in the outer basin of the measuring probe, indicating that the separation of the flow field at the rear end of the measuring probe is caused by the blocking of the jet field by the measuring probe, and that this separation of the flow field only exists in the rear end of the measuring probe, and the effect on the flow field state of the core area of the jet is negligible. The spatial vortex structures shown in the E5 to E7, G5 to G7, and I5 to I7 regions of Fig. 19 still exist, indicating that the vortex structures generated by the shedding of the shear layer vortex of the supersonic jet have a significant impact on the flow field in the wind tunnel test chamber. The fluid disturbances caused by the collision of the spatial vortex structures with the collector and test bench device will make the unsteadiness of the flow structure in the wind tunnel test chamber more obvious.

This study summarizes and analyzes the characteristics of the jet field under typical non-matching parameters ($P_{out}=80$ kPa, $P_{out}=88$ kPa, $P_{out}=92$ kPa, $P_{out}=95$ kPa), and compares it with the standard jet field under the back pressure matching condition ($P_m=85$ kPa). Characteristics were compared, and the flow field structure characteristics and core flow parameter distribution laws under non-matched parameters were studied. The Mach number contours, static pressure contours, and flow field pathlines diagram under different outlet pressures are shown in Figs. 20 to 22.

As shown in Fig. 20 above, when the inlet pressure $P_{in} = 180$ kPa is constant and the outlet pressure is less than the outlet operating pressure of 85 kPa, the pressure at the nozzle outlet is greater than the ambient pressure in the test chamber, and the supersonic jet in the wind tunnel test chamber is in an under-expansion state; when the outlet pressure is greater than the 85 kPa, the pressure at the nozzle outlet is less than the ambient pressure in the test chamber, and the supersonic jet in the wind tunnel test chamber is in an over-expansion state. The fluid in the state of under-expansion or over-expansion can cause alternating expansion and compression waves and wave interference at the center of the jet.

As shown in Fig. 20a, when the outlet pressure is low, the large pressure difference can cause the supersonic jet injected into the test chamber to continue accelerating in the core area, resulting in an under-expansion region with a high Mach number in the J1 region. Due to wave interference, the Mach number distribution in the J1 region will be uneven. When the uneven supersonic jet hits the test bench device in the under-expansion state, it also produces a large flow field mutation at the tip of the probe. Additionally, the range of the Mach number mutation zone J2 at the tip of the probe is significantly larger than the corresponding K2 mutation zone under the back pressure matching condition. The flow field distribution

at the tip of the measuring probe is extremely uneven in the Mach number mutation zone, and a velocity concentration zone greater than Mach 3.0 is generated in the J4 zone. In addition, the supersonic jet in the J3 zone separates from the surface of the measuring probe, forming an unstable flow field with a large velocity gradient, which greatly reduces the flow field quality in the key flow field of the jet. This shows that the unstable under-expanded supersonic jet is more susceptible to the influence of the structure in the test chamber than the uniformly stable ideal expanded supersonic jet.
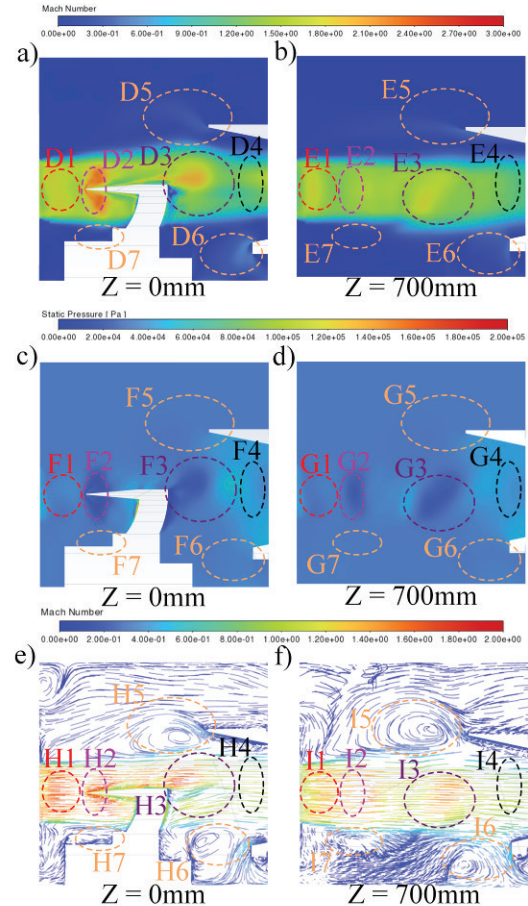

Fig. 19. Comparison of flow fields in different planes under back pressure matching conditions;
a) Mach number contour of Plane 1, b) Mach number contour of Plane 2,
c) static pressure contour of Plane 1, d) static pressure contour of Plane 2,
e) flow field pathlines diagram of Plane 1, f) flow field pathlines diagram of Plane 2

As shown in the structure of the supersonic jet field in the over-expansion state in Figs. 20c, d, and f, the Mach number in the core area will continue to decrease compared to the ideal expansion state. At the same time, the phenomenon of alternating expansion and compression waves in the supersonic jet flow field during over-expansion will become more pronounced, inducing stronger pressure pulsations at the back of the core area. As shown by the flow fields in the L1, M1, and N1 areas of the figure, as the back pressure increases, the boundary between the acceleration and deceleration regions in the core of the jet becomes more distinct, which exacerbates the uneven distribution of the physical parameters of the jet flow field. As shown in L2, M2, and N2 in Fig. 20, when a periodic expansion wave flows through the test rig device, the unstable jet field will generate a large-scale Mach number sudden change area at the stylus. Under $P_{out}=88$ kPa, a speed concentration caused by the instability of the jet shear layer appears in the L3 area.

Unlike the K4 region of the supersonic jet in the back pressure matching condition, which is re-integrated into a uniform and stable flow field, the flow field in the J6, L5, M4, and N4 regions in Fig. 20 shows that the fluid separation phenomenon still exists in the flow field at the rear end of the test chamber. The reason is that the flow field state of the under-expanded or over-expanded jet under back pressure mismatch is unstable, resulting in more drastic changes in the flow field structure after being disturbed by the test bench device, and then it is unable to re-rectify into a uniform and stable jet and spray into the collector.
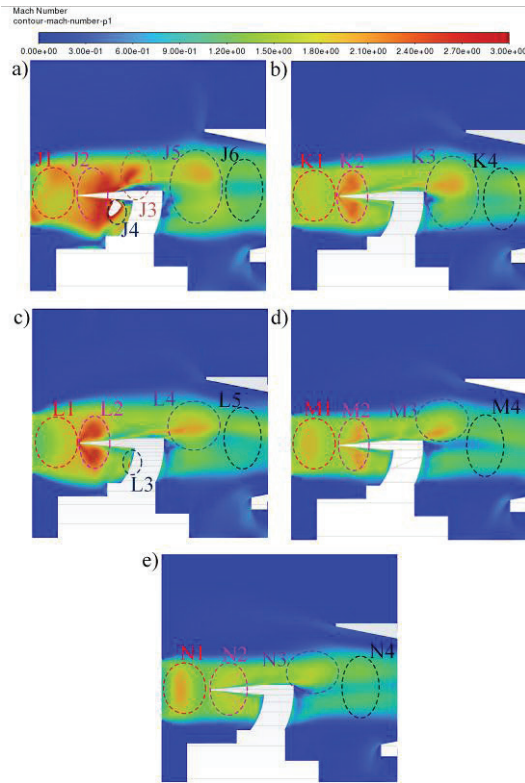

Fig. 20. Comparison of Mach number of different back pressure jet fields;
a) Mach number contour at P_{out} = 80 kPa, b) Mach number contour at P_{out} = 85 kPa,
c) Mach number contour at P_{out} = 88 kPa, d) Mach number contour at P_{out} = 92 kPa,
e) Mach number contour at Pout = 95 kPa

Fig. 21 shows the static pressure contours of the supersonic jet field at different outlet pressures of the wind tunnel. As shown in the O1 area in Fig. 21a, when the pressure at the outlet of the wind tunnel is low, the static pressure distribution in the core area of the jet is relatively chaotic, with obvious high static pressure areas, which will seriously affect the flow field quality of the supersonic jet. As shown in the Q1, R1, and S1 areas in the figure, when the pressure at the outlet of the wind tunnel is high, alternating high and low static pressure zones will appear in the core of the jet, and the greater the outlet pressure, the more obvious the boundary between the high and low static pressure zones. The expansion and compression waves that repeatedly appear are the main factors affecting the uniformity of the jet field. When an unstable jet under non-matching conditions collides with the stylus mechanism, a large low-static pressure area is formed at the tip of the stylus, as shown in the O2, Q2, R2, and S2 areas of the figure. It is worth noting that the jet field under various working conditions has obvious pressure concentration areas in the O3, P3, Q3, R3, and S3 regions, indicating that corners with large spatial gradients will affect the flow state of the fluid in a small area when they collide with supersonic jets.

After the supersonic jet passes through the test bench device under various working conditions, a significant low static pressure area appears in the O4, P4, Q4, R4, and S4 areas. This is because the supersonic jet undergoes a significant fluid acceleration process in this area, and the flow state of the jet field in the rear end area of the test bench changes significantly. Due to the interference of the test bench, the jet state becomes more unstable, which becomes the reason for the uneven static pressure distribution in the O5, Q5, R5, and S5 regions in the figure.
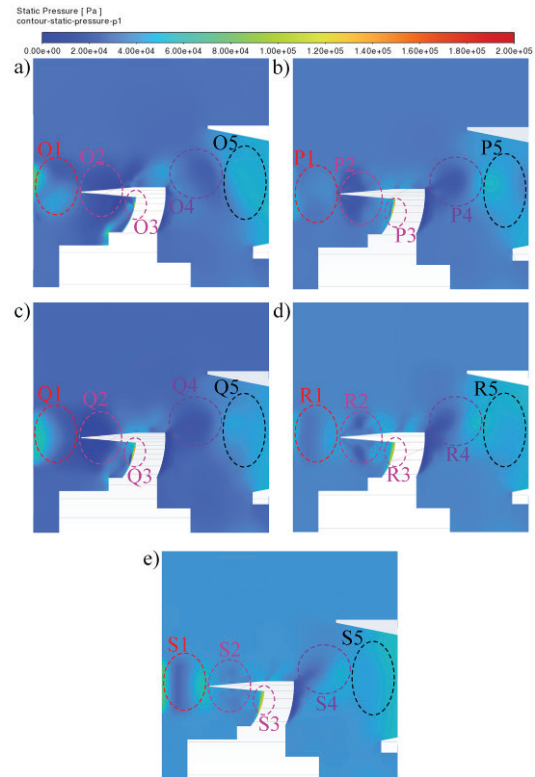

Fig. 21. Comparison of the static pressure of the jet field with different back pressures;
a) static pressure contour at P_{out} = 80 kPa, b) static pressure contour at P_{out} = 85 kPa,
c) static pressure contour at P_{out} = 88 kPa, d) static pressure contour at P_{out} = 92 kPa,
e) static pressure contour at P_{out} = 95 kPa

Fig. 22 shows the comparison of the flow field pathlines of the supersonic jet under different back pressures. For the flow in the core area U1 of the test chamber under the back pressure matching condition (P_{out} = 80 kPa), the fluid pathlines diagram are uniform and stable. There is no obvious disturbance in the field pathlines diagram in the core area, indicating that the supersonic jet is in an ideal expansion state. In a typical non-matching working condition, as shown in Fig. 22a, the jet in the under-expansion state has a significant expansion phenomenon in the core area T1 of the jet. The fluid pathlines of the shear layer of the jet gradually deviates from the axial direction and flows to both sides, indicating that the static pressure at the nozzle outlet under this working condition is greater than the ambient pressure in the test chamber. For the working conditions shown in Fig. 22 c, d, and e, the supersonic jet in the over-expansion state will alternate expansion and compression waves in the test chamber. The fluid traces in the core area of the jet shown by V1, W1, and X1 will repeatedly expand and compress, appearing to oscillate repeatedly near the axial direction. The shear layer of the supersonic jet in the non-matching working condition is extremely unstable. As shown in the figure, the jet traces in the V2, V3, W2, W3, X2, and X3 regions all show a flow field state in which the flow

expands outwardly relative to the axial direction and then continues to compress inwardly.

For the supersonic jet in the under-expansion state shown in Fig. 22a, the fluid traces show a flow field state in which the flow expands outward. As shown in the figure T4, U3, V4, W4, and X4, in the rear section of the test chamber, the jet in the U3 area with matched back pressure is rearranged after passing through the test bench, and the flow field traces are once again stable, and then spray horizontally along the axial direction into the outlet pipe.
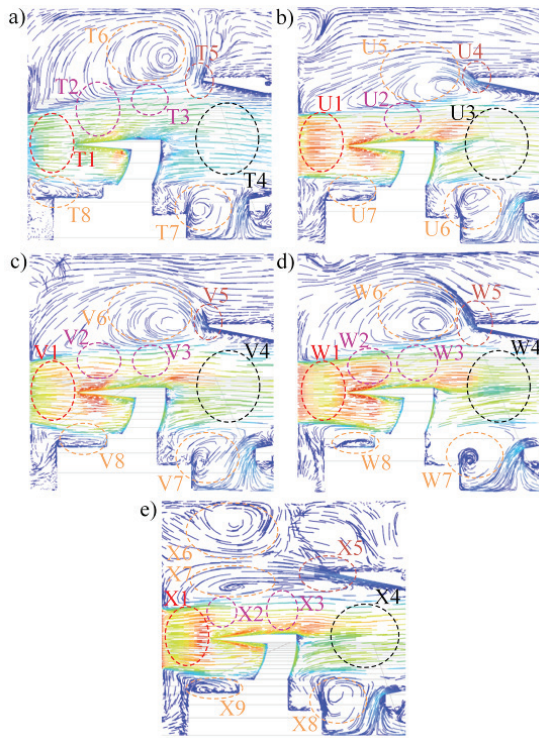

Fig. 22. Comparison of the jet field pathlines at different back pressures.
a) P_{out} = 80 kPa, b) P_{out} = 85 kPa, c) P_{out} = 88 kPa, d) P_{out} = 92 kPa, e) P_{out} = 95 kPa

As shown in the T5, U4, V5, W5, and X5 areas of Fig. 22, the jet shear layer and the collector interfere to produce obvious separation vortices in the test chamber. As the pressure at the outlet of the wind tunnel increases, the angle between the tangent line at the collector inlet and the axial direction of the separation vortex will gradually decrease. When the outlet pressure is too high, two large-scale space vortices appear in the X6 and X7 areas. The spatial vortex structure in the test chamber includes large-scale pseudo-ordered vortices in the jet shear layer, vortex structures generated by the jet shear layer being involved in the low-speed airflow in the test chamber, and the separation vortex structure in the spatial corners of the test bench and collector.

3 CONCLUSIONS

This study studies the conditions for generating an ideal expansion state jet in a supersonic wind tunnel with a standard Mach number of 1.5 at the nozzle outlet. A method for quickly obtaining the static operating pressure matching point of a supersonic jet is proposed, and the flow fields of an ideal expansion state jet and a supersonic jet under typical non-matching conditions are analyzed and compared. The research results show that:
1. When the Mach numbers of the monitoring points on the axis of the jet core are all within the Mach 1.5 error range of the standard

nozzle exit, the supersonic jet is in an ideal expansion state. The exit pressure P_{out} under this operating condition is the solution P_m for supersonic wind tunnel back pressure matching.
2. The static pressure at the outlet of the wind tunnel nozzle under the back pressure matching condition (P_{out} = 80 kPa) is equal to the ambient pressure in the test chamber, and the physical parameters of the supersonic jet field are uniformly and stably distributed, which makes the range of the uniform jet zone break through the limit of the diamond-shaped zone. The jet has a uniform flow within the jet boundary, which improves the quality of the wind tunnel test jet flow field.
3. When the back pressure of the wind tunnel does not match, the supersonic jet will vary between under-expansion and over-expansion at the nozzle outlet. The core of the jet will experience alternating shock waves and expansion waves, resulting in strong pressure fluctuations in the central flow field, which will reduce the quality of the wind tunnel test jet flow field.

References

[1] Liu, Y., Sun, M., Liang, C., Cai, Z., Wang, Y. Structures of near-wall wakes subjected to a sonic jet in a supersonic crossflow. *Acta Astronaut* 151 886-892 (2018) **DOI:10.1016/j.actaastro.2018.07.048**

[2] Sun, M., Sandham, N.D., Hu, Z. Turbulence structures and statistics of a supersonic turbulent boundary layer subjected to concave surface curvature. *J Fluid Mech* 865 60-99 (2019) **DOI:10.1017/jfm.2019.19**

[3] Sabnis, K., Galbraith, D.S., Babinsky, H., Benek, J.A. Nozzle geometry effects on supersonic wind tunnel studies of shock-boundary-layer interactions. *Exp Fluids* 63 191 (2022) **DOI:10.1007/s00348-022-03543-1**

[4] Sandham, N.D., Reynolds, W.C. Three-dimensional simulations of large eddies in the compressible mixing layer. *J Fluid Mech* 224 133-158 (1991) **DOI:10.1017/S0022112091001684**

[5] Vreman, A.W., Sandham, N.D., Luo, K. Compressible mixing layer growth rate and turbulence characteristics. *J Fluid Mech* 320 235-258 (1996) **DOI:10.1017/S0022112096007525**

[6] Drozdov, S.M., Rtishcheva, A.S. Numerical investigation of air flow in a supersonic wind tunnel. *J Phys Conf Ser* 891 012043 (2017) **DOI:10.1088/1742-6596/891/1/012043**

[7] Lu, X.G., Yi, S.H., He, L., Gang, D.D., Niu, H.B. Experimental study on unsteady characteristics of shock and turbulent boundary layer interactions. *Fluid Dyn* 55 566-577 (2020) **DOI:10.1134/S0015462820030088**

[8] Lu, X.G., Gang, D.D., Niu, H.B., Zheng, W.P., Yi, S.H. Experimental investigation of hypersonic boundary layer transition on a 5° smooth straight cone. *Fluid Dyn* 57 1054-1064 (2022) **DOI:10.1134/S0015462822601139**

[9] Egorov, I.V., Duong, N.H., Nguyen, N.C., Palchekovskaya, N.V. (2022) Numerical simulation of the influence of a Mach wave on the laminar-turbulent transition in a supersonic boundary layer. *Dokl Phys* 67 144-147 **DOI:10.1134/S1028335822050019**

[10] Shen, J., Dong, J., Li, R., Zhang, J., Chen, X., Qin, Y., Ma, H. Integrated supersonic wind tunnel nozzle. *Chinese J Aeronaut* 32 2422-2432 (2019) **DOI:10.1016/j.cja.2019.07.005**

[11] Gounko, Y.P., Kavun, I.N. Peculiarities of the flows forming in processes of an impulse starting of a supersonic wind tunnel with different diffusers. *Thermophys Aeromech+* 26 195-214 (2019) **DOI:10.1134/S0869864319020045**

[12] Kosinov, A.D., Kocharin, V.L., Liverko, A.V., Semenov, A.N., Semionov, N.V., Smorodsky, B.V., Yatskikh, A.A. Effect of small angles of attack on turbulence generation in supersonic boundary layers on swept wings. *Fluid Dyn* 58 371-380 (2023) **DOI:10.1134/S0015462823600165**

[13] Yu, K., Xu, J., Liu, S., Zhang, X. Starting characteristics and phenomenon of a supersonic wind tunnel coupled with inlet model. *AerospSciTechnol* 77 626-637 (2018) **DOI:10.1016/j.ast.2018.03.050**

[14] Egorov, I.V., Nguyen, N.K., Pal'chekovskaya, N.V. Numerical simulation of the interaction of a Mach wave and a boundary layer on a flat plate. *High Temp+* 61 689-696 (2023) **DOI:10.1134/S0018151X23050036**

[15] Bottini, H., Paniagua, G., Schreivogel, P., Sonda, A., de las Heras, S. Design and qualification of a supersonic wind tunnel for induced boundary layer transition research. *P I Mech Eng G-J Aer* 229 562-578 (2015) **DOI:10.1177/0954410014537612**

[16] Wu, J., Liu, X., Radespiel, R. RANS simulations of a tandem nozzle supersonic wind tunnel. *AerospSci Technol* 49 215-224 (2016) **DOI:10.1016/j.ast.2015.11.041**

[17] Zhao, X.H., Yi, S.H., Mi, Q., Hu, Y.F., Ding, H.L. Skin friction reduction of hypersonic body by supersonic layer. *Fluid Dyn* 57 686-696 (2022) **DOI:10.1134/S0015462822050123**

[18] Ermolaev, Y.G., Kosinov, A.D., Kocharin, V.L., Semenov, A.N., Semionov, N.V., Shipul', S.A., Yatskikh, A.A. Effect of small angles of attack on laminar-turbulent transition in the supersonic boundary layer on a swept wing with χ = 72°. *Fluid Dyn* 57 30-36 (2022) **DOI:10.1134/S0015462822010037**

[19] Milinovic, M., Jerković, D., Jeremić, O., Kovač, M. Experimental and simulation testing of flight spin stability for small caliber cannon projectile. *Stroj vestn - J Mech E* 58 394-402 (2012) **DOI:10.5545/sv-jme.2011.277**

[20] Lopez-Lopez, A., Robles-Ocampo, J.B., Sevilla-Camacho, P.Y., Lastres-Danguillecourt, O., Muniz, J., Perez-Sarinana, B.Y., de la Cruz, S. Dynamic instability of a wind turbine blade due to large deflections: An experimental validation. *Stroj vestn-J Mech E* 66 523-534 (2020) **DOI:10.5545/sv-jme.2020.6678**

[21] Akbıyık, H., Yavuz, H., Akansu, Y. (2018). A study on the plasma actuator electrode geometry configurations for improvement of the aerodynamic performance of an airfoil. *Stroj vestn-J Mech E* 64, 719-725 **DOI:10.5545/sv-jme.2017.5041**

[22] Balabel, A., Hegab, A.M., Nasr, M., El-Behery, S.M. Assessment of turbulence modeling for gas flow in two-dimensional convergent-divergent rocket nozzle. *Appl Math Model* 35 3408-3422 (2011) **DOI:10.1016/j.apm.2011.01.013**

[23] Luo, T.Y., Yin, J., Lin, X.D., Zu, X.Y., Xiong, B., Bai, B.Q., et al. *Method for obtaining supersonic jet static operation pressure matching point of jet wind tunnel.* China National Knowledge Infrastructure (CNKI) Patent No. 114184349B (2022)

Author Contribution *Peng Liu: writing - original draft, visualization, validation, methodology, investigation, resources; Jinglun Cai: writing - original draft, methodology, investigation, conceptualization, data curation; Xuejing Shao: validation, methodology, conceptualization; Hui Jin: validation, supervision, conceptualization.*

Raziskava hitre metode za določitev ujemajoče se točke statičnega obratovalnega tlaka nadzvočnega curka v vetrovniku

Povzetek *Pri preskusih v vetrovniku lahko neusklajeni obratovalni tlaki povzročijo, da se v toku curka pojavijo ekspanzijski valovi, kompresijski valovi in valovne interference. Trenutne raziskave usklajevanja tlakov v vetrovniku zahtevajo stalno prilagajanje obratovalnih tlakov na vstopu in izstopu, da se doseže idealno razširjeno stanje nadzvočnega curka, kar predstavlja veliko delovno obremenitev. V tej študiji predstavljamo numerično simulacijo toka v nadzvočnem vetrovniku pri različnih izstopnih tlakih na osnovi Reynoldsove metode povprečenih Navier-Stokesovih enačb (RANS). Predlagana je metoda za hitro določitev točke ujemanja statičnega obratovalnega tlaka nadzvočnega curka, s katero lahko hitro ugotovimo ustrezen obratovalni tlak. Kadar je Machovo število kontrolne točke na osi jedrnega območja curka znotraj 5 % standardnega Machovega števila na izstopu šobe, je curek v preskusni komori vetrovnika v stanju idealne ekspanzije. Izstopni tlak v teh razmerah predstavlja standardni obratovalni tlak. Hkrati smo primerjali strukture toka v pogojih prekomerne ekspanzije, idealne ekspanzije in premajhne ekspanzije. Pokazalo se je, da so ključni fizikalni parametri v jedrnem območju nadzvočnega curka v stanju idealne ekspanzije, pridobljene s to hitro metodo, stabilno porazdeljeni, kar omogoča, da enakomerno območje curka preseže meje rombastega območja in zagotovi enakomeren tok znotraj meja nadzvočnega curka.*

Ključne besede *nadzvočni curek, ujemanje tlaka, ekspanzijski val, kompresijski val*

Comparison and Optimization of Burnishing Parameters in Various Machining Conditions

Trung-Thanh Nguyen[1] – Minh-Thai Le[2] – Thai-Chung Nguyen[1] – Truong-An Nguyen[1] – Xuan-Ba Dang[3] – An-Le Van[4, ✉]

1 Le Quy Don Technical University, Faculty of Mechanical Engineering, Vietnam
2 Le Quy Don Technical University, Faculty of Special Equipment, Vietnam
3 Ho Chi Minh City University of Technology and Education, Vietnam
4 Nguyen Tat Thanh University, Faculty of Engineering and Technology, Vietnam

✉ lvan@ntt.edu.vn

Abstract   This study proposes a cryogenic diamond burnishing process and optimizes cooling parameters, including the distance to nozzle (N), nozzle diameter (D), and CO_2 flow rate (Q) to minimize the maximum roughness (R), energy consumption (E), and circularity (C). The Kriging and adaptive-network-based fuzzy inference system (ANFIS) methods were utilized to propose the response models. The CRITIC, non-dominated sorting genetic algorithm-II (NSGA-II), and MABAC were applied to calculate the weights, generate feasible solutions, and select the best optimal data. The result indicated that the optimal N, D, and Q were 15 mm, 9 mm, and 8 L/min, respectively. The reductions in the roughness, energy, and circularity were 15.5 %, 2.0 %, and 38.6 %, respectively. The roughness and energy models were primarily affected by Q, D, and N, respectively, while circularity model was influenced by the N, D, and Q, respectively. The proposed process could be used to machine different holes with minimizing environmental impacts. Lower roughness and circularity were achieved using the cryogenic diamond burnishing process. The Kriging-NSGA-II could be utilized to show non-linear data and produce the best results.

Keywords   cryogenic diamond burnishing; energy consumption; maximum roughness; circularity; Kriging model

Highlights
- *A cryogenic CO_2 diamond burnishing process is proposed and optimized.*
- *Minimizing the maximum surface roughness, energy, and circularity.*
- *The Kriging and ANFIS approaches are employed to develop the predictive models.*
- *The reductions in the R, E, and C were 15.5 %, 2.0 %, and 38.6 %, respectively.*

1 INTRODUCTION

Cryogenic cooling is an approach to cool workpieces and tools quickly and effectively in which refrigerants, such as liquid nitrogen or solid carbon dioxide, are used directly. This method has several advantages, including cost-effectiveness, faster cooling, improved tool life, better surface finish, and higher productivity. The cryogenic method has great potential to replace conventional cooling strategies in consideration of machinability.

The applications of cryogenic cooling on different burnishing operations have been extensively considered. Caudill et al. [1] presented that the roughness, hardness, and depth of the affected layer of the cryogenic burnished Ti-6Al-4V improved by 56.7 %, 64.2 %, and 25.2 %, respectively, compared to the dry condition. The temperature in the cryogenic burnishing operation of Co-Cr-Mo biomedical alloy was reduced by 50 %, while the depth of the affected layer was increased by 150 %, compared to the dry condition [2]. Yang et al. [3] emphasized that cryogenic cooling could be used to obtain a higher depth of the affected layer, increased micro-hardness, and fine grain size, compared to the base material. Huang et al. [4] presented those higher tangential forces and lower temperatures are observed from a cryogenic burnishing Al 7050-T7451. Tang et al. [5] indicated that the cryogenic conditions facilitated to produce the corrosion film on the subsurface layer of the Ti-6Al-4V. Similarly, a low roughness and nanocrystalline layer on the burnished Ti-6Al-4V titanium alloy was produced with the aid of cryogenic burnishing [6]. A set of experiments was conducted to reduce the roughness and improve the hardness of the burnished 17-4 PH stainless steel [7]. The authors stated that the roughness of 0.03 μm and hardness

of 413 HV could be generated at the optimal solution. The optimal burnishing force, feed, and speed of the machined 17-4 PH stainless steel were selected using the desirability approach [8]. The outcomes presented that a roughness of 0.20 μm and a hardness of 397.48 HV were achieved. Rotella et al. [9] presented that the wear resistance of the burnished Ti6Al4V titanium alloy was enhanced by 86.2 % with the aid of cryogenic cooling and coated tools. The regression models of the roughness, hardness, wear rate, and the depth of the affected layer were developed for the cryogenic burnishing Ti-6Al-4V alloy [10]. The small errors between models and experiments indicated that the developed models were adequate. Sachin et al. [11] presented that the roughness was reduced when higher values of speed, feed, and force were employed. Caudill et al. [12] presented that cryogenic cooling increased the yield strength and produced nanostructured layer of the burnished Ti-6Al-4V. Huang et al. [13] emphasized that the surface hardness of the cryogenic burnished Al 7050-T7451 could be increased by 29.8 %. Maximov et al. [14] presented that the roughness of the burnished stainless steel could be changed from 0.041 to 0.049 μm using a cryogenic condition. Van and Nguyen stated that roughness and energy of the cold air-based burnishing process were reduced by 34.1 % and 1.5 %, respectively, while the power factor and Vickers hardness improved by 13.2 % and 9.5 %, at the selected solution [15]. Maximov stated that the fatigue strength of the cryogenic-burnished SS304 was improved by 36.4 %, compared to the untreated specimen [16].

However, an internal diamond burnishing process using the liquid CO_2 has not been developed and optimized. The impacts of the liquid CO2, including the distance to the nozzle, nozzle diameter, and flow rate on the roughness, energy, and hole circularity have not

been investigated. Finally, a multi-response optimization has not been performed to reduce energy as well as roughness and improve circularity.

The following section presents the optimization strategy. After that, the experimental setup and results are explained. Lastly, some conclusions are made.

2 METHODS AND MATERIALS

2.1 Optimizing Framework

In this study, the roughness (R) is calculated as:

$$R = \frac{\sum_{i=1}^{3} Sz_i}{3}, \tag{1}$$

where Sz_i is the maximum height of the scale limited surface roughness. The energy consumption (E) is calculated as:

$$E = P_m \times t_m, \tag{2}$$

where P_m and t_m denote the burnishing power and burnishing duration, respectively. The circularity (C) is calculated as:

$$C = \frac{\sum_{i=1}^{3} CC_i}{3}, \tag{3}$$

where CC_i is the circularity of the burnished hole.

The parameters and their levels, including the distance to the nozzle, nozzle diameter, and CO_2 flow rate are shown in Table 1. The flow rate is selected using the properties of the valve and CO_2 storage equipment. The distance to nozzle and nozzle diameter are referenced from related publications and experts in the brunishing field.

The optimizing procedure for the burnishing process is illustrated in Fig. 1. In this work, the advantages of various methods (Kriging, ANFIS, CRITIC, NSGA-II, and MABAC) were combined to propose the optimization approach.

Step 1: Executing 27 trials using the full factorial method [17-20].
Step 2: The CRITIC is used to compute the weights of the responses [21]. The response (f_{ij}) is normalized as:

$$f_{ij} = \frac{x_{ij} - x_{worst}}{x_{best} - x_{worst}}, \tag{4}$$

where x_{best} and x_{worst} are the best and worst values of each response, respectively. The standard deviation (s_j) is calculated as:

$$s_j = \sqrt{\frac{(\sum_{i=1}^{m} f_{ij} - x_m)^2}{m-1}}. \tag{5}$$

The conflict (I_j) among criteria is calculated as:

$$I_j = \sum_{k=1}^{m} (1 - r_{jk}), \tag{6}$$

where r_{jk} is the correlation coefficient between the vectors x_j and x_k. The quantity (C_j) is calculated as:

$$C_j = s_j \sum_{k=1}^{m} (1 - r_{jk}). \tag{7}$$

The computed (ω_i) is calculated as:

$$\omega_i = \frac{C_j}{\sum_{k=1}^{n} C_j}. \tag{8}$$

Step 3: The Kriging approach is used to construct the predictive models of the responses [22-25]. The Kriging model is expressed as:

$$f(x) = f^T(x)\beta + r^T(x)R^{-1}(Y - F\beta), \tag{9}$$

where β denotes the least-squares estimate, and Y presents the true responses at the sample. The log-likelihood of the model parameters is expressed as:

$$\ln\left(u', \widehat{\sigma}^2, \theta\right) = -\frac{n}{2}\ln(2\pi) - \frac{n}{2}\ln\left(\widehat{\sigma}^2\right) - \frac{1}{2}\ln(|R|)$$
$$-\frac{1}{2\widehat{\sigma}^2}(Y - F\beta)' R^{-1}(Y - F\beta). \tag{10}$$

The σ^2 is estimated as:

$$\widehat{\sigma}^2 = \frac{1}{n}(Y - F\widehat{\beta})^T R^{-1}(Y - F\widehat{\beta}). \tag{11}$$

Step 4: The R, E, and C models are proposed using the ANFIS approach [26-29].
Layer I: The outputs of R, E, and C responses are expressed as:

$$R(x) = \mu_E A_1 x(R), \tag{12}$$

$$E(y) = \mu_T A_2 y(E), \tag{13}$$

$$C(z) = \mu_D A_3 z(C), \tag{14}$$

where A_i is the connected label of each response.
Layer II: The fixed function is expressed as:

$$L_2, x = \mu_E A_1 x(R) \times \mu_T A_2 y(E) \times \mu_D A_3 z(C). \tag{15}$$

Layer III: The firing strength is expressed as:

$$L_3, x = \overline{w_i} = \frac{w_i}{\sum_{i=1}^{n} w_i}, \tag{16}$$

Layer IV: The output is expressed as:

$$L_4, x = \overline{w_i} f_i(x) = \overline{w_i}(g_i x + h_i x + k_i), \tag{17}$$

where g_i, h_i, and k_i are the consequent parameters, respectively.

Layer V: The fixed node is expressed as:

$$L_5, x = \sum_i \overline{w_i} f_i. \tag{18}$$

Step 5: The selection of the optimality using the NSGA-II and MABAC. The operating principle of the NSGA-II is expressed as [30-33]. An initial population P_0 of size N is randomly generated at the start of the procedure.

The non-domination ranks and crowding distance are used to evaluate each individual. The crowding distance among individuals is computed as:

$$d_j = \sum_{m=1}^{M} \frac{f_m^{\max j+1} - f_m^{\min j-1}}{f_m^{\max} - f_m^{\min}}, \tag{19}$$

where f_m is the mth objective function. The parent-offspring generation is produced in the crossover operation. The arithmetic crossover function is expressed as:

$$S_i = 0.5(1 + \gamma)P_i + 0.5(1 - \gamma)P_{i+1}, \tag{20}$$

where S and P are the off spring and parent, respectively, and γ is a crossover coefficient. The mutation operation is used to produce the individual diversity and expressed as:

$$S = \begin{cases} S + (2r)^{1/n_m + 1} - 1, & \text{if } r \le 0.5 \\ S + 1 - (2 - 2r)^{1/n_m + 1} & \text{else} \end{cases}. \tag{21}$$

The MABAC is expressed as [34]. The weighted response (v_{ij}) is calculated as:

$$v_{ij} = \omega_j (n_{ij} + 1), \tag{22}$$

where n_{ij} is the normalized response. The approximation area (g_i is calculated as:

$$g_i = (\prod_{j=1}^{m} v_{ij})^{1/m}. \tag{23}$$

The alternative distance (d_{ij}) is calculated as:

$$d_{ij} = v_{ij} - g_i. \tag{24}$$

The performance index (P_i) is calculated as:

$$P_i = \sum_{j=1}^{n} d_{ij}.\qquad(25)$$

The best solution is selected with the highest P_i.

Table 1. Process parameters of the burnishing operation

Parameters	Levels
Distance to the nozzle, N [mm]	15-25-35
Nozzle diameter, D [mm]	6-8-10
CO2 flow rate, Q [L/min]	4-8-12

2.1 Experimental Facilities

The experiments are performed with the aid of a NC lathe (Fig. 2). The EN24 steel is applied to produce the high-strength shafts, punches, dies, bushings, rings, and gears. The workpiece with a length of 64 mm, an internal diameter of 44 mm, and an external diameter of 58 mm is used. The pre-machined surface is generated using the drilling and turning operations. The roughness and circularity of the initial surface are 14.034 μm and 50.63 μm, respectively.
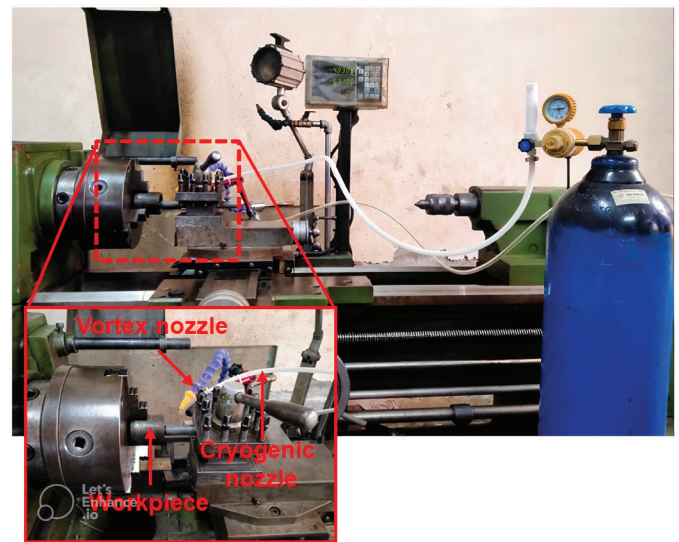

Fig. 2. Experimental burnishing

Fig. 1. Optimization approach

The roughness, power, and circularity are measured using the ZeGage Pro-3D, Kyoritsu 6315, and ZEISS CONTURA CMM, respectively. The roughness is measured in three different points of the burnished surface. The power is captured from ten peak values of the obtained data. The circularity is measured at 8 positions at various circular cross-sections, and the average value is then determined (Fig. 3c). The experimental outcomes at various burnishing conditions are presented in Fig. 3.

3 RESULTS AND DISCUSSIONS

3.1 Comparing Responses in Various Conditions

The experimental data are shown in Table 2. To prove the effectiveness of the proposed process, a set of experiments is conducted in dry, wet, and cryogenic conditions. The comparative results for the roughness are shown in Fig. 4. Quantitatively, the cryogenic CO_2 reduces the roughness from 28.82 % to 34.42 %, compared to the dry environment. Similarly, the cryogenic CO_2
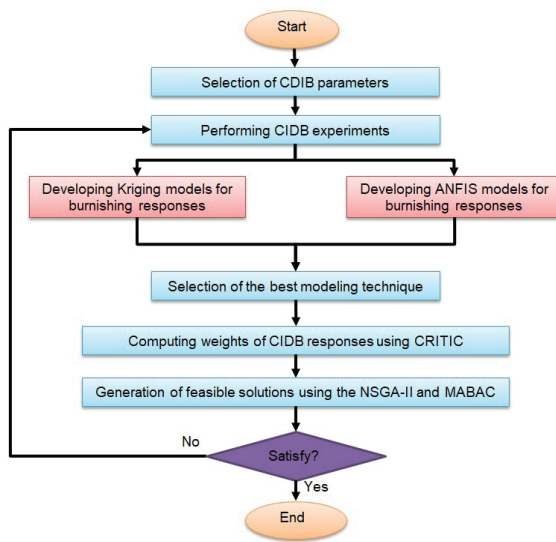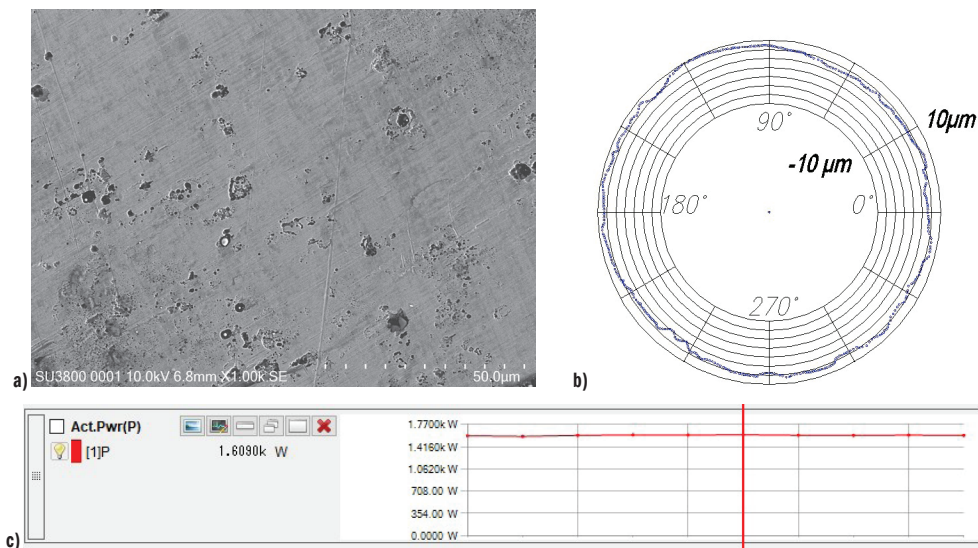

Fig. 3. Example results of the burnishing process at the experimental No. 6; SEM image, b) circularity, and c) power consumed

reduces the roughness from 13.03 % to 17.11 %, compared to the wet environment. Greater roughness occurs under dry conditions due to inadequate heat dissipation from the workpiece surface. The liquid CO_2 effectively removes the temperature and friction at the interfaces due to thin-film lubrication, resulting in low roughness.

Table 2. Experimental results

No.	N [mm]	D [mm]	Q [L/min]	R [µm]	E [kJ]	C [µm]
			Experimental data for developing models			
1	15	6	4	4.226	60.14	19.46
2	25	6	4	4.508	64.72	22.31
3	35	6	4	5.031	67.52	27.67
4	15	6	8	3.725	65.87	14.73
5	25	6	8	3.992	69.97	17.25
6	35	6	8	4.497	72.26	22.28
7	15	6	12	3.549	70.04	12.89
8	25	6	12	3.797	73.61	15.07
9	35	6	12	4.286	75.42	19.76
10	15	8	4	3.873	65.14	13.51
11	25	8	4	4.181	69.37	16.77
12	35	8	4	4.731	71.79	22.54
13	15	8	8	3.151	70.66	9.31
14	25	8	8	3.442	74.42	12.22
15	35	8	8	3.974	76.34	17.66
16	15	8	12	2.754	74.58	7.97
17	25	8	12	3.028	77.83	10.55
18	35	8	12	3.543	79.28	15.65
19	15	10	4	3.746	69.51	10.26
20	25	10	4	4.079	73.38	13.93
21	35	10	4	4.654	75.45	20.11
22	15	10	8	2.803	74.82	6.55
23	25	10	8	3.119	78.26	9.89
24	35	10	8	3.677	79.78	15.74
25	15	10	12	2.185	78.52	5.73
26	25	10	12	2.484	81.41	8.73
27	35	10	12	3.025	82.51	14.24
			Experimental data for testing models			
28	20	7	5	3.953	66.64	15.93
29	20	9	7	3.251	73.68	9.62
30	18	7	9	3.365	70.83	11.54
31	22	9	10	2.836	77.43	8.51
32	26	7	11	3.469	75.32	13.07
33	30	9	5	4.108	74.12	16.32
34	32	7	10	3.828	75.73	16.36
35	16	9	9	2.811	74.35	7.24
36	34	9	11	3.297	80.36	14.12
37	24	7	8	3.649	71.95	14.01

The comparative results for the circularity are shown in Fig. 5. Quantitatively, cryogenic CO_2 reduces the circularity from 29.47 % to 32.17 %, compared to the dry environment. Similarly, cryogenic CO_2 reduces the circularity from 16.11 % to 19.18 %, compared to the wet environment. The liquid CO_2 enhances the cooling efficiency, leading to even deformation of the burnished hole; thus the circularity reduces.

3.2 The Selection of a Better Modelling Technique

The comparisons between the actual and predcitve data of the Kriging and ANFIS models are shown in Tables 3 and 4, respectively. For the

Kriging model, the errors of the roughness, energy, and circularity lie from –0.63 % to 0.39 %, –0.72 % to 0.42 %, and –1.10 % to 0.78 % respectively. For the ANFIS model, the errors of the roughness, energy, and circularity lie from –3.30 % to 2.36 %, –1.61 % to 4.45 %, and –5.78 % to 5.43 %, respectively. As compared to the models produced by the ANFIS approach, the predictive data generated by the Kriging method have a stronger association with the experimental data.
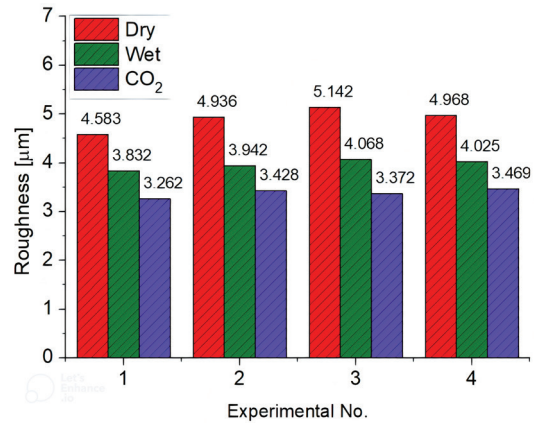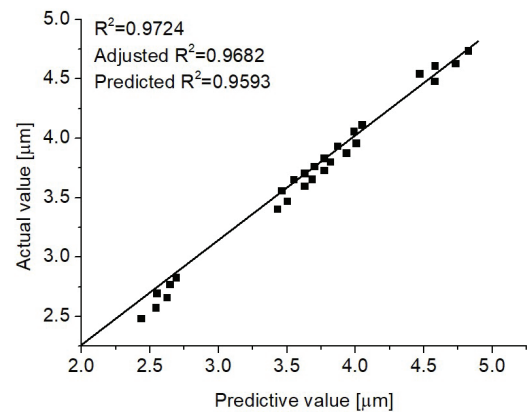

Fig. 4. Comparative roughness

Fig. 5. Comparative circularity

Fig. 6 presents the consistent data of the burnishing responses; thus the developed Kriging models are adequate.

3.3 ANOVA Analysis for Burnishing Responses

The computed ANOVA results for the roughness, energy, and circularity are presented in Tables 5-7, respectively. The F-values of the roughness, energy, and circularity models are 27.42, 61.59, and 26.80, respectively, indicating their significance. For the roughness model, the Q has the highest contributions (21.35 %), followed by the D (20.76 %) and N (16.96 %), respectively. The contributions of the ND, NQ, and DQ are 6.43 %, 7.52 %, and 4.67 %, respectively. The contributions of the N^2, D^2, and Q^2 are 7.04 %, 7.62 %, and 7.65 %, respectively. For the energy model, the contributions of the N, D, and Q are 19.92 %, 28.87 %, and 29.28 %, respectively. The contributions of the ND, NQ, and DQ are 2.52 %, 3.42 %, and 1.92 %, respectively. The contributions of the N^2, D^2, and Q^2 are 6.323 %, 2.21 %, and 5.63 %, respectively. For the circularity model, the contributions of the N, D, and Q are 25.69 %, 22.61 %, and 19.11 %, respectively. The contributions of the ND, NQ, and DQ are 2.51 %, 2.07 %, and 3.13 %, respectively. The contributions of the N^2, D^2, and Q^2 are 7.71 %, 8.28 %, and 8.85 %, respectively.

Table 3. Testing results for developed Kriging models

No.	R [μm]			E [kJ]			C [μm]		
	Exp.	Kri.	Er. [%]	Exp.	Kri.	Er. [%]	Exp.	Kri.	Er. [%]
28	3.953	3.967	–0.35	66.64	66.52	0.18	15.93	15.82	0.69
29	3.251	3.267	–0.49	73.68	73.52	0.22	9.62	9.71	–0.94
30	3.365	3.354	0.33	70.83	70.53	0.42	11.54	11.45	0.78
31	2.836	2.854	–0.63	77.43	77.86	–0.56	8.51	8.58	–0.82
32	3.469	3.456	0.37	75.32	75.02	0.40	13.07	13.14	–0.54
33	4.108	4.113	–0.12	74.12	74.65	–0.72	16.32	16.25	0.43
34	3.828	3.842	–0.37	75.73	75.92	–0.25	16.36	16.48	–0.73
35	2.811	2.824	–0.46	74.35	74.56	–0.28	7.24	7.32	–1.10
36	3.297	3.284	0.39	80.36	80.48	–0.15	14.12	14.18	–0.42
37	3.649	3.662	–0.36	71.95	71.76	0.26	14.01	14.09	–0.57

Table 4. Testing results for ANFIS models

No.	R [μm]			E [kJ]			C [μm]		
	Exp.	Kri.	Er. [%]	Exp.	Kri.	Er. [%]	Exp.	Kri.	Er. [%]
28	3.953	3.842	2.81	66.64	65.23	2.12	15.93	16.85	–5.78
29	3.251	3.362	–3.41	73.68	74.02	–0.46	9.62	9.84	–2.29
30	3.365	3.402	–1.10	70.83	69.32	2.13	11.54	11.96	–3.64
31	2.836	2.964	–4.51	77.43	78.64	–1.56	8.51	8.96	–5.29
32	3.469	3.365	3.30	75.32	74.25	1.42	13.07	12.36	5.43
33	4.108	4.196	–2.14	74.12	73.21	1.23	16.32	16.94	–3.80
34	3.828	3.901	–1.91	75.73	72.36	4.45	16.36	15.86	3.06
35	2.811	2.765	1.64	74.35	75.03	–0.91	7.24	7.56	–4.42
36	3.297	3.152	4.40	80.36	81.65	–1.61	14.12	14.63	–3.61
37	3.649	3.552	2.66	71.95	72.86	–1.26	14.01	13.56	3.21

Table 5. ANOVA results for the roughness model

So	SS	MS	F value	p-value
Model	5.8247	0.6472	27.42	<0.0001
N	12.8611	12.8611	544.96	<0.0001
D	15.7427	15.7427	667.06	<0.0001
Q	16.1901	16.1901	686.02	<0.0001
ND	4.8760	4.8760	206.61	<0.0001
NQ	5.7025	5.7025	241.63	<0.0001
DQ	3.5413	3.5413	150.06	0.0006
N^2	5.3386	5.3386	226.21	<0.0001
D^2	5.7784	5.7784	244.85	<0.0001
Q^2	5.8011	5.8011	245.81	<0.0001
Res.	0.1653	0.0236		
Cor.	5.99			
$R^2 = 0.9724$; Adjusted $R^2 = 0.9682$; Predicted $R^2 = 0.9593$				

Table 6. ANOVA results for the energy model

So	SS	MS	F value	p-value
Model	19509.10	1393.51	49.50505051	<0.0001
N	321.51	35.72	61.59	<0.0001
D	70.00	70.00	120.69	<0.0001
Q	101.45	101.45	174.92	<0.0001
ND	102.89	102.89	177.40	<0.0001
NQ	8.86	8.86	15.27	0.0011
DQ	12.02	12.02	20.72	0.0006
N^2	6.75	6.75	11.63	0.0015
D^2	21.89	21.89	37.75	0.0003
Q^2	7.77	7.77	13.39	0.0009
Res.	4.07	0.58		
Cor.	325.58			
$R^2 = 0.9875$; Adjusted $R^2 = 0.9802$; Predicted $R^2 = 0.9786$				

3.4 The Impacts of Cooling Parameters on the Roughness, Energy, and Circularity

The main impacts of process parameters on the roughness are shown in Fig. 7. A higher N increases the friction at the burnishing area due to lower cooling effects; thus a higher roughness is produced. A higher D increases the cooling efficiency at the interfaces. The friction and temperature decrease; results in a lower roughness. As depicted in an increased Q leads to a higher CO_2 intensity, leading to reductions in friction and temperature; thus this reduces the roughness.
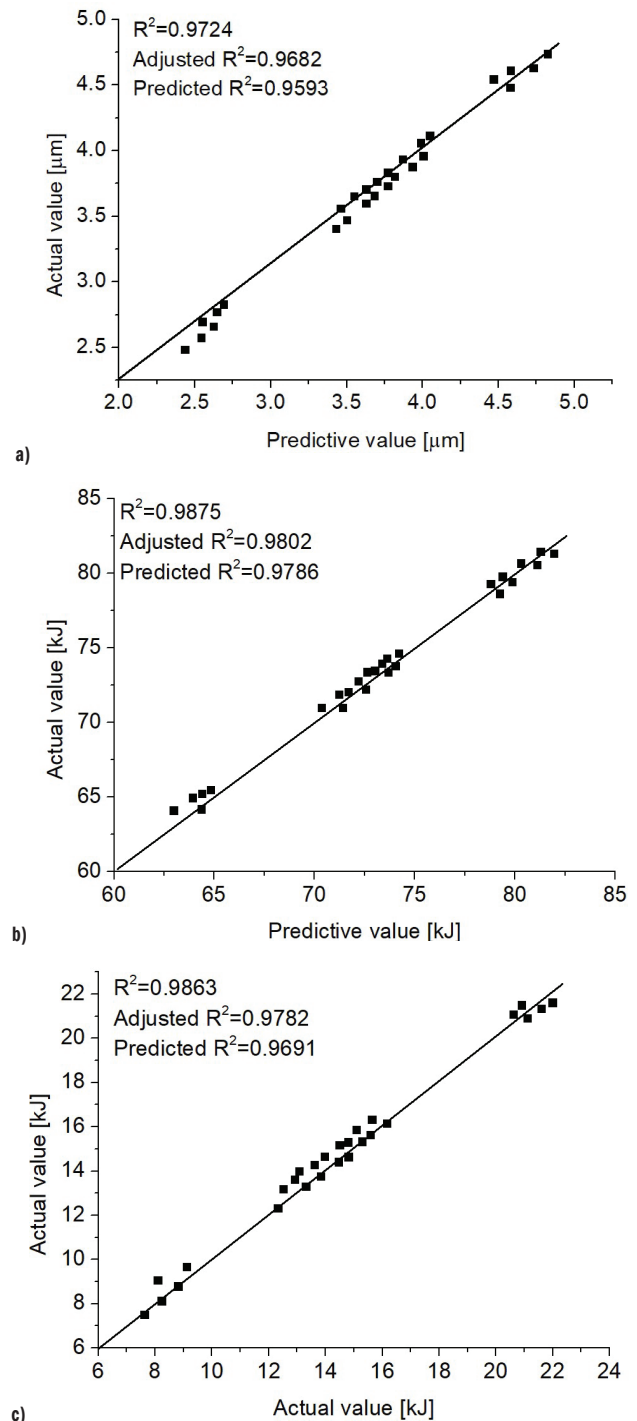

Fig. 6. Comparisons between the predictive and actual values; a) roughness model, b) energy model, and c) circularity model

The main impacts of parameters on the energy are shown in Fig. 8. A higher N causes higher friction at the machining region; thus a higher energy is required to overcome a greater load. A higher D increases the amount of the CO_2 and the workpiece hardness increases; thus a higher energy is required. An increased Q leads to a higher CO_2 intensity, leading to higher workpiece hardness; thus a higher energy is used to overcome a greater resistance.

The main impacts of parameters on the circularity are shown in Fig. 9. A higher N increases friction at the interface, resulting in hard compression of material; thus the circularity increases. A higher D increases cooling efficiency due to higher liquid CO_2

quantity. The friction decreases, leading to even deformation of the material compression; thus the circularity reduces. An increased Q leads to a higher CO_2 intensity, leading to reductions in friction at the burnishing region. The material compression evenly is produced; thus the circularity reduces.

3.5 The Impacts of Cooling Parameters on the Microstructure

The microstructure of the burnished specimen under various parameters is presented in Fig. 10. When the N increases from 15 mm to 35 mm, the Vickers hardness and the depth reduce from
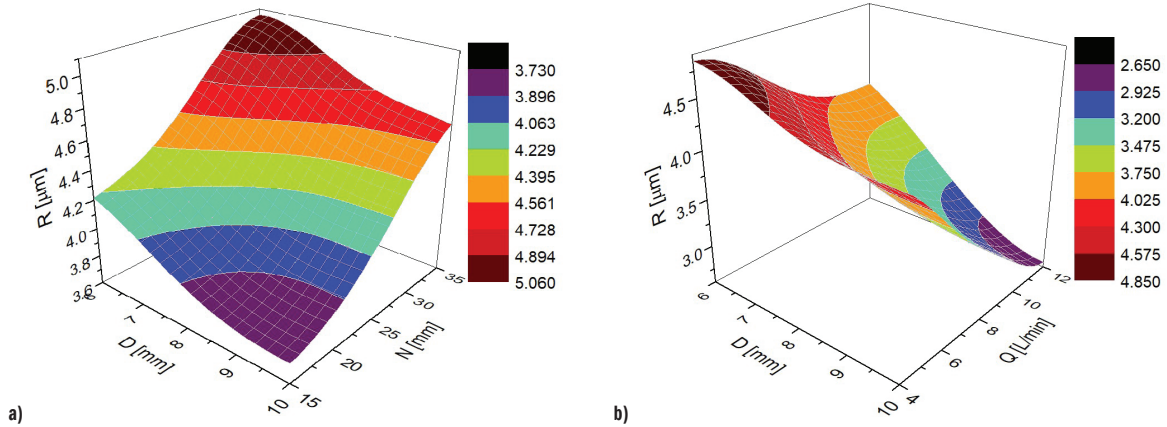
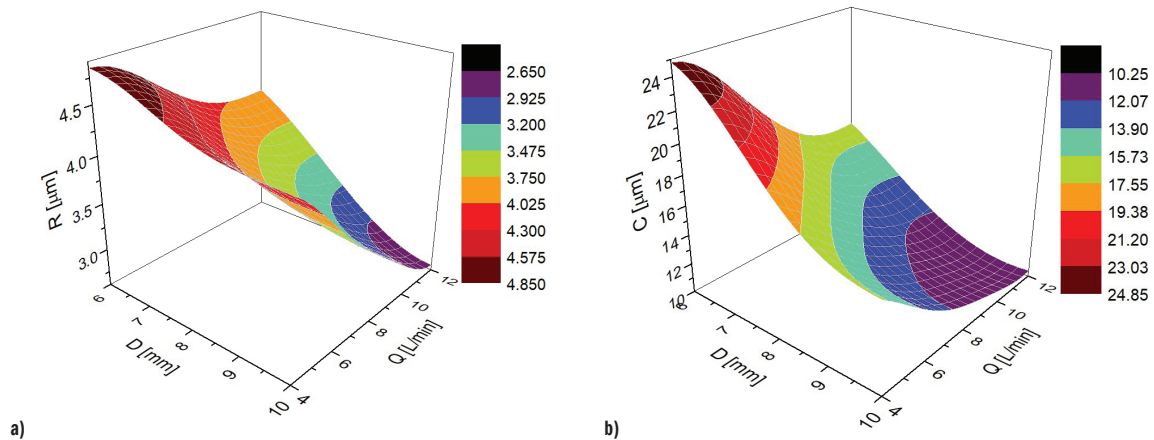**Fig. 7.** Kriging plots for the roughness model; a) R vs. N and D, and b) R vs. Q and D

Fig. 8. Kriging plots for the energy model; a) E vs. N and D, and b) E vs. Q and D
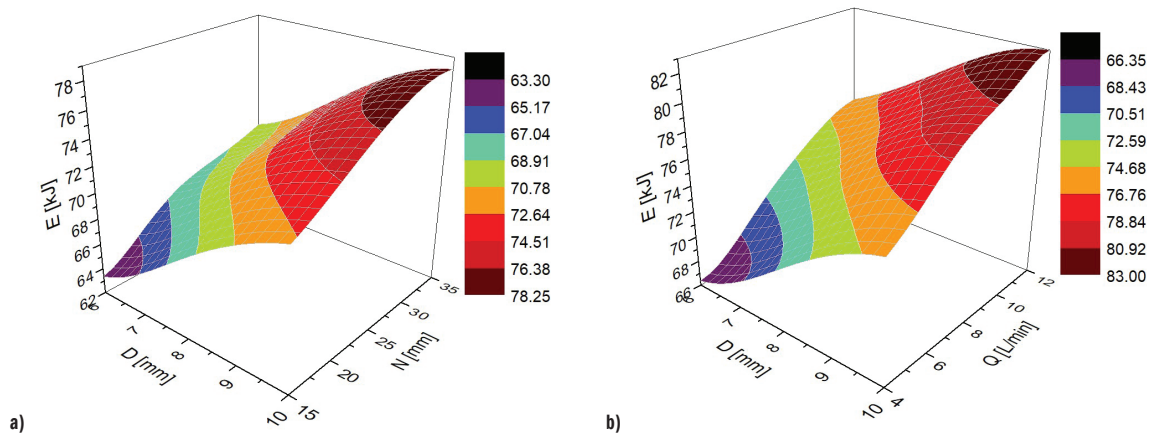

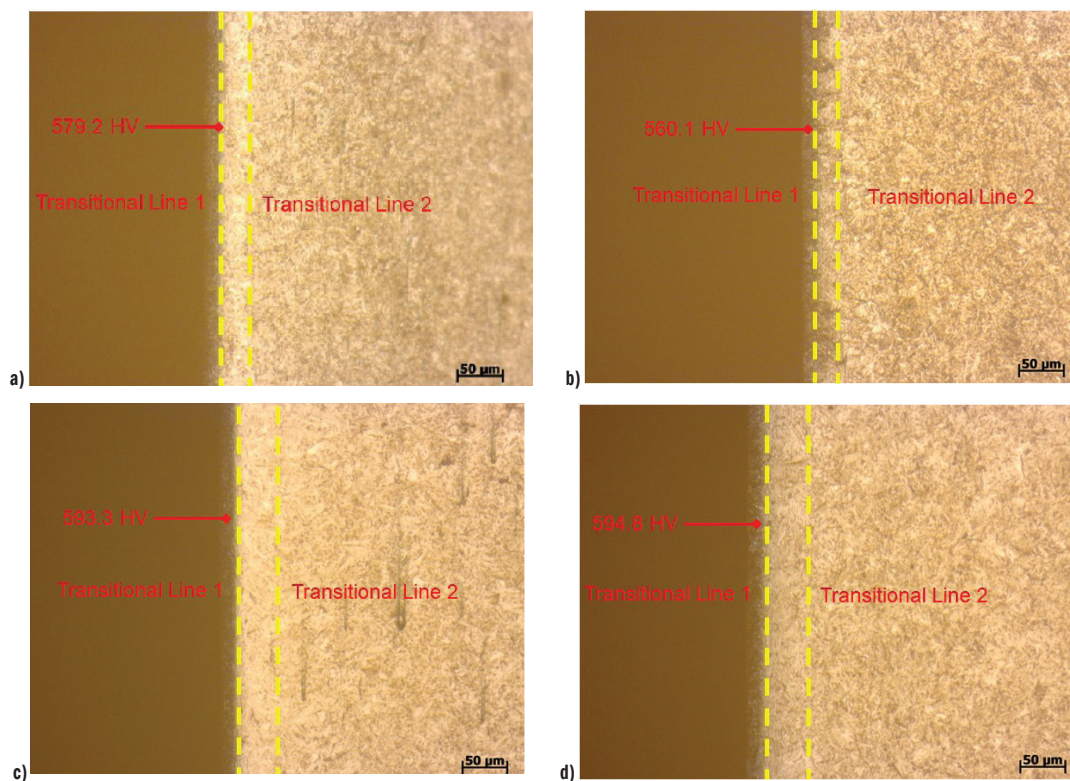**Fig. 9.** Kriging plots for the circularity model; a) C vs. N and D, and b) C versus Q and D

Fig. 10. The impacts of the cooling parameters on the microstructure; a) N = 15 mm, D = 6 mm, Q = 8 L/min, b) N = 35 mm, D = 6 mm, Q = 8 L/min, c) N = 15 mm, D = 10 mm, Q = 8 L/min, and d) N = 15 mm, D = 6 mm, Q = 12 L/min
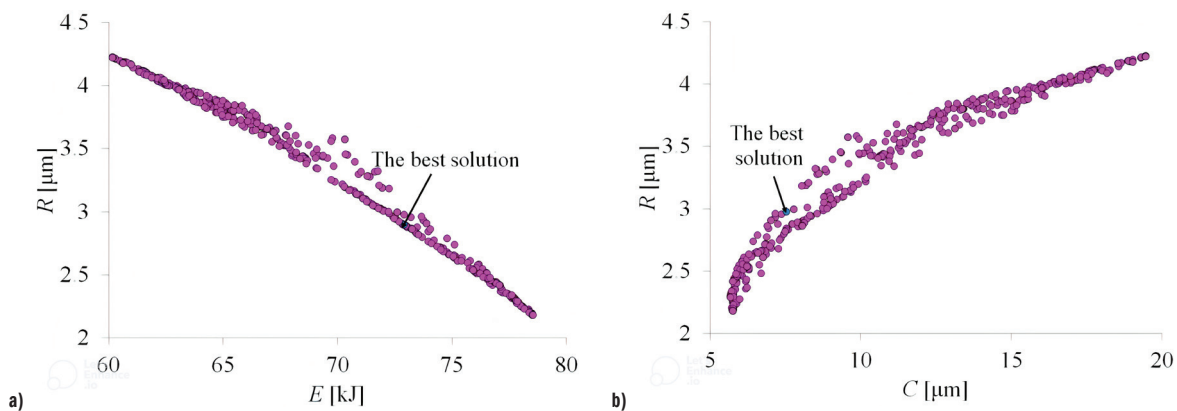

Fig. 11. Pareto fronts generated by NSGA- II; a) roughness and energy, and b) roughness and circularity

579.2 HV to 560.1 HV and 126 μm to 102 μm, respectively (Fig. 10a and b). A lower N between the nozzle and workpiece enhances cooling efficiency, leading to a reduction in friction. The material compression is easily performed; thus higher hardness and depth are obtained. A higher N reduces cooling impact, lowering Vickers hardness and depth values.

When D increases from 6 mm to 10 mm, the Vickers hardness and the depth enhance from 579.2 HV to 593.3 HV and 126 μm to 158 μm, respectively (Figs. 10a and c). An increased D improves cooling efficiency at the interfaces; thus higher values of the Vickers hardness and depth are obtained.

When the Q increases from 8 L/min to 12 L/min, the Vickers hardness and depth reduce from 579.2 HV to 594.8 HV and 126 μm to 168 μm, respectively (Figs. 10a and d). A higher amount of liquid CO_2 reduces the friction at the interfaces; thus material compression is easily performed. A higher degree of plastic deformation is obtained, leading to higher Vickers hardness and depth.

Table 7. ANOVA results for the circularity model

So	SS	MS	F value	p-value
Model	349.51	38.83	26.80	< 0.0001
N	42.90	42.90	62.17	< 0.0001
D	37.75	37.75	54.72	< 0.0001
Q	31.91	31.91	46.25	< 0.0001
ND	4.19	4.19	6.07	0.0006
NQ	3.46	3.46	5.01	0.0007
DQ	5.23	5.23	7.57	0.0005
N^2	12.87	12.87	18.66	0.0002
D^2	13.83	13.83	20.04	0.0001
Q^2	14.78	14.78	21.42	< 0.0001
Res.	4.85	0.69		
Cor.	354.36			
R^2 = 0.9863; Adjusted R^2 = 0.9782; Predicted R^2 = 0.9691				

3.6 Optimal Outcomes Produced by the NSGA-II

The weight values of the roughness, energy, and circularity are 0.38, 0.26, and 0.36, respectively. Fig. 11 shows the contradictory trends of the burnishing responses. As a result, the optimal N, D, and Q are 15 mm, 9 mm, and 8 L/min, respectively. At the selected solution, the roughness, energy, and circularity are reduced by 15.5 %, 2.0 %, and 38.6 %, respectively (Table 8).

It can be stated that the cryogenic internal diamond burnishing process generated a smooth surface without any morphological irregularities. The reductions in the roughness and circularity are 79.2 % and 85.2 %, respectively, compared to the pre-burnished surface (Table 9).

Table 8. Optimization results produced by by the Kriging models-NSGA II

Method	Optimization parameters			Responses			P_i
	N [mm]	D [mm]	Q [L/min]	R [µm]	E [kJ]	V [µm]	
Initial results	25	8	8	3.464	74.42	12.22	
Optimal results	15	9	8	2.926	72.91	7.50	0.7246
Reductions [%]				15.5	2.0	38.6	

Table 9. Comparisons between the initial and optimized surfaces

Method	R [µm]	C [µm]
Initial surface	14.034	50.63
Optimal surface	2.926	7.50
Reductions [%]	79.2	85.2

4 CONCLUSIONS

In the current study, the improvements in the roughness, energy, and circularity of the diamond burnishing process were obtained using optimal N, D, and Q. The Kriging and ANFIS methods were employed to develop the response models, while the CRITIC method was applied to estimate the weights. The NSGA-II and MABAC were used to generate an optimal solution. Based on the obtained results, the following conclusions have been drawn:

1. A set of trials were executed to find the accuracy of the proposed correlations. Compared to the ANFIS, the Kriging technique provided a lower error average and a better capacity to forecast the response.
2. A lower N could be used to minimize the roughness, energy, and circularity. Higher D and Q could be applied to reduce roughness and circularity. In contrast, minimal energy was achieved using the lower D and Q.
3. For the roughness and energy models, Q had the highest contribution, followed by D and N, respectively. For the circularity model, N had the highest contribution, followed by D and Q, respectively.
4. The optimal N, D, and Q were 15 mm, 9 mm, and 8 L/min, respectively. The reductions in the roughness, energy, and circularity were 15.5 %, 2.0 %, and 38.6 %, respectively.
5. The roughness, energy consumed, and circularity of the burnished hole produced by the cryogenic CO_2 are lower than the dry one.
6. The developed process and burnishing device could be utilized for various machining internal holes with different diameters.
7. The Kriging model could be used to present complicated data when deal with the diamond burnishing operation, as compared to the ANFIS.

The impacts of the cooling parameters on the surface hardness and tribological factors will be explored in future works.

References

[1] Caudill, J., Huang, B., Arvin, C., Schoop, J., Meyer, K., Jawahir, I.S. Enhancing the surface integrity of Ti-6Al-4V alloy through cryogenic burnishing. *Procedia CIRP* 13, 243-248 (2014) **DOI:10.1016/j.procir.2014.04.042**

[2] Yang, S., Dillon, O.W. Jr., Puleo, D.A., Jawahir, I.S. Effect of cryogenic burnishing on surface integrity modifications of Co-Cr-Mo biomedical alloy. *J Biomed Mater Res B* 101, 139-152 (2013) **DOI:10.1002/jbm.b.32827**

[3] Yang, S., Umbrello, D., Dillon, O.W. Jr., Puleo, D., Jawahir, I.S. Cryogenic cooling effect on surface and subsurface microstructural modifications in burnishing of Co-Cr-Mo biomaterial. *J Mater Process Tech* 217 211-221 (2015) **DOI:10.1016/j.jmatprotec.2014.11.004**

[4] Huang, B., Kaynak, Y., Sun, Y., Jawahir, I.S. Surface layer modification by cryogenic burnishing of Al 7050-T7451 alloy and validation with FEM-based burnishing model. *Procedia CIRP* 31 1-6 (2015) **DOI:10.1016/j.procir.2015.03.097**

[5] Tang, J., Luo, H., Qi, Y., Xu, P., Ma, S., Zhang, Z. et al. The effect of cryogenic burnishing on the formation mechanism of corrosion product film of Ti-6Al-4V titanium alloy in 0.9% NaCl solution. *Surf Coat Tech* 345 123-131 (2018) **DOI:10.1016/j.surfcoat.2018.03.102**

[6] Tang, J., Luo, H.Y., Zhang, Y.B. Enhancing the surface integrity and corrosion resistance of Ti-6Al-4V titanium alloy through cryogenic burnishing. *Int J Adv Manuf Tech* 88, 2785-2793 (2017) **DOI:10.1007/s00170-016-9000-y**

[7] Sachin, B., Narendranath, S., Chakradhar, D. Enhancement of surface integrity by cryogenic diamond burnishing toward the improved functional performance of the components. *J Braz Soc Mech Sci* 41, 396 (2019) **DOI:10.1007/s40430-019-1918-1**

[8] Sachin, B., Narendranath, S., Chakradhar, D. Application of desirability approach to optimize the control factors in cryogenic diamond burnishing. *Arab J Sci Eng* 45, 1305-1317 (2019) **DOI:10.1007/s13369-019-04326-3**

[9] Rotella, G., Rinaldi, S., Filice, L. Roller burnishing of Ti6Al4V under different cooling/lubrication conditions and tool design: Effects on surface integrity. *Int J Adv Manuf Tech* 106, 431-440 (2020) **DOI:10.1007/s00170-019-04631-z**

[10] Rotella, G., Caruso, S., Del Prete, A., Filice, L. Prediction of surface integrity parameters in roller burnishing of Ti6Al4V. *Metals-Basel* 10 1671 (2020) **DOI:10.3390/met10121671**

[11] Sachin, B., Charitha, M.R., Naik, G., Puneet, N.P. Influence of slide burnishing process on the surface characteristics of precipitation hardenable steel. *SN Appl Sc* 3 223 (2021) **DOI:10.1007/s42452-021-04260-w**

[12] Caudill, J., Schoop, J., Jawahir, I.S. Correlation of surface integrity with processing parameters and advanced interface cooling/lubrication in burnishing of Ti-6Al-4V alloy. *Adv Mater Process Tech* 5 53-66 (2019) **DOI:10.1080/2374068X.2018.1511215**

[13] Huang, B., Kaynak, Y., Sun, Y., Khraisheh, M.K., Jawahir, I.S. Surface layer modification by cryogenic burnishing of Al 7050-T7451 alloy with near ultra-fine grained structure. *J Manuf Sci E-T ASME* 144 031002 (2022) **DOI:10.1016/j.procir.2015.03.097**

[14] Maximov, J., Duncheva, G., Anchev, A., Dunchev, V., Anastasov, K., Argirov, Y. Sustainable diamond burnishing of Chromium-Nickel austenitic stainless steels: Effects on Surface Integrity and Fatigue Limit. *Appl Sci-Basel* 14, 9031 (2024) **DOI:10.3390/app14199031**

[15] Van, A.L., Nguyen, T.T. Machine learning-based optimization of diamond burnishing parameters in terms of energy efficiency and quality indexes. *Arab JSci Eng* (2024) **DOI:10.1007/s13369-024-09449-w**

[16] Maximov, J., Duncheva, G., Anchev, A., Dunchev, V., Argirov, Y. Improvement in fatigue strength of Chromium-Nickel austenitic stainless steels via diamond burnishing and subsequent low-temperature gas nitriding. *Appl Sci-Basel* 14, 1020 (2024) **DOI:10.3390/app14031020**

[17] Gao, J., Wu, Y., Shen, T. On-line statistical combustion phase optimization and control of SI gasoline engines. *Appl Therm Eng* 112, 1396-1407 (2017) **DOI:10.1016/j.applthermaleng.2016.10.183**

[18] Kılavuz, F., Goren Kiral, B. Design optimization of mechanical valves in dishwashers based on the minimization of pressure losses. *Strojn vest-J Mech E* 70 194-208 (2024) **DOI:10.5545/sv-jme.2023.768**

[19] Deang, Y., Qui, L, Shao, Y., Yao, Y. Process modeling and optimization of anaerobic co-digestion of peanut hulls and swine manure using response surface methodology. *Energ Fuel* 33 11021-11033 (2019) **DOI:10.1021/acs.energyfuels.9b02381**

[20] Zhao, L. C, He, Y., Deng, X., Xia, X. H., Liang, J., Yang, G. L.; Li, W., Wang, H. Ultrasound-assisted extraction of syringin from the bark of ilex rotunda thumb using response surface methodology. *Int J Mol Sci* 13 7607-7616 (2012) **DOI: 0.3390/ijms13067607**

[21] Diakoulaki, D., Mavrotas, G., Papayannakis, L. Determining objective weights in multiple criteria problems: The critic method. *Comput Oper Res* 22 763-770 (1995) **DOI:10.1016/0305-0548(94)00059-H**

[22] Sathiya, P., Panneerselvam, K., Soundararajan, R. Optimal design for laser beam butt welding process parameter using artificial neural networks and genetic algorithm for super austenitic stainless steel. *Opt Laser Technol* 44, 1905-1914 (2012) **DOI:10.1016/j.optlastec.2012.01.025**

[23] Feng, Y., Shi, X.J., Lu, X.Q., Sun, W., Liu, K.P., Fei, Y.F:. Predictions of friction and wear in ball bearings based on a 3D point contact mixed EHL model. *Surf Coat Technol* 502 131939 **DOI:10.1016/j.surfcoat.2025.131939**

[24] Zheng, L., Zhu, Y., Zhou, Y. Meta-transfer learning-based method for multi-fault analysis and assessment in power system. *Appl Intell* 54 12112-12127 (2024). **DOI:10.1007/s10489-024-05772-9**

[25] Zhu, Y., Zhou, Y., Yan, L., Li, Z., Xin, H., Wei, W. Scaling graph neural networks for large-scale power systems analysis: Empirical laws for emergent abilities. *IEEE Trans Power Syst* 39 7445-7448 (2024) **DOI:10.1109/TPWRS.2024.3437651**

[26] Gao, D., Liu, S., Gao, Y., Li, P., Zhang : H., Wang, M A comprehensive adaptive interpretable Takagi-Sugeno-Kang fuzzy classifier for fatigue driving detection. *IEEE T Fuzzy Syst* 33 108-119 (2025) **DOI:10.1109/TFUZZ.2024.3399400**

[27] Rodić, D., Gostimirović, M., Sekulić, M., Savković, B., & Aleksić, A. Fuzzy logic approach to predict surface roughness in powder mixed electric discharge machining of Titanium Alloy. *Stroj Vestn-J Mech E* 69 376-387 (2023) **DOI:10.5545/sv-jme.2023.561**

[28] Esmaeili, M., Osanloo, M., Rashidinejad, F., Bazzazi, A.A., Taji, M. Multiple regression, ANN and ANFIS models for prediction of backbreak in the open pit blasting. *Eng Comput* 30 549-558 (2014) **DOI:10.1007/s00366-012-0298-2**

[29] Chen, J., Wang, Y., Zhang, Y., Lu, Y., Shu, Q., Hu, Y. Extrinsic-and-intrinsic reward-based multi-agent reinforcement learning for multi-UAV cooperative target encirclement. *IEEE T Intell Transp* (2024) **DOI:10.1109/TITS.2024.3524562**

[30] Tabari, M.M.R., Soltani, J. Multi-objective optimal model for conjunctive use management using SGAs and NSGA-II models. *Water Resour Manag* 27 37-53 (2013) **DOI:10.1007/s11269-012-0153-7**

[31] Miler, D., Birt, D., Hoić, M. Multi-objective optimization of the chebyshev lambda mechanism. *Stroj Vestn-J Mech E* 68 725-734 (2023) **DOI:10.5545/sv-jme.2022.349**

[32] Yao, Y., Sheng, H., Luo, Y., He, M., Li, X., Zhang, H., He, W., An, L. Optimization of anaerobic co-digestion of Solidago canadensis L. biomass and cattle slurry. *Energy* 78 122-127 (2014) **DOI:10.1016/j.energy.2014.09.013**

[33] Gao, J., Liu, A., Yang, J., Zhao, S., Liu, J. Optimization of outer-rotor flux-switching permanent magnet motor using response surface method. *Stroj Vestn-J Mech E* 70 543-553 (2024) **DOI:10.5545/sv-jme.2023.859**

[34] Pamučar, D., Ćirović, G. The selection of transport and handling resources in logistics centers using multi-attributive border approximation area comparison (MABAC). *Expert Syst Appl* 42 3016-3028 (2015) **DOI:10.1016/j.eswa.2014.11.057**

Authors Contributions *Trung-Thanh Nguyen: conceptualization, methodology, validation, writing – original draft, writing – review & editing; Minh-Thai Le: conceptualization, methodology, validation, writing – original draft, writing – review & editing; Thai-Chung Nguyen: conceptualization, methodology, validation, writing – original draft, writing – review & editing; Truong-An Nguyen: conceptualization, methodology, validation, writing – original draft, writing – review & editing; Xuan-Ba Dang: conceptualization, methodology, validation, writing – original draft, writing – review & editing; An-Le Van: conceptualization, methodology, validation, writing – original draft, writing – review & editing. All authors have read and agreed to the published version of the manuscript.*

Primerjava in optimizacija parametrov glajenja pri različnih pogojih obdelave

Povzetek *Ta raziskava predlaga postopek kriogenega diamantnega glajenja in optimizira parametre hlajenja, kot so razdalja do šobe (N), premer šobe (D) in pretok CO_2 (Q), z namenom minimiziranja maksimalne hrapavosti (R), rabe energije (E) in krožnosti (C). Za izdelavo odzivnih modelov sta bili uporabljeni metodi Kriging in ANFIS (adaptive-network-based fuzzy inference system). Za izračun uteži, generiranje izvedljivih rešitev in izbiro optimalnih podatkov pa so bile uporabljene metode CRITIC, nedominirana sortirna genetska optimizacija NSGA-II in metoda MABAC. Rezultati so pokazali, da optimalne vrednosti parametrov N, D in Q znašajo 15 mm, 9 mm oziroma 8 L/min. Zmanjšanje hrapavosti, energije in krožnosti je bilo 15,5 %, 2,0 % oziroma 38,6 %. Na modela hrapavosti in energije so najbolj vplivali parametri Q, D in N, medtem ko je bil na model krožnosti vpliv parametrov N, D in Q. Predlagan postopek se lahko uporablja za obdelavo različnih lukenj ob zmanjšanem vplivu na okolje. Z uporabo kriogenega diamantnega glajenja smo dosegli manjšo hrapavost in krožnost. Kriging-NSGA-II se je izkazal kot učinkovit za prikaz nelinearnih podatkov in doseganje najboljših rezultatov.*

Ključne besede *kriogeno diamantno glajenje, raba energije, maksimalna hrapavost, krožnost, Kriging model*

Research on the Cutting Performance of Self-Lubricating Tools with Microtexture of the Front and Back Surfaces

Yan Zhang ✉ – Haodong Sun – Qi Li – Kaiming Sun – Yuanjing Mou – Shihong Zhang

Changchun University, School of Mechanical and Vehicle Engineering, China

✉ 220101010@ccu.edu.cn

A novel hexagonal microtexture is proposed to enhance the cutting performance of polycrystalline cubic boron nitride (PCBN) tools. Three-dimensional models of both conventional and microtextured tools are developed, and the turning process is simulated using AdvantEdge finite element software. The effects of cutting force, temperature, and stress on tool performance are investigated. Additionally, microtextured turning tools are fabricated for orthogonal experiments to analyze the effects of different texture positions on cutting performance. When the tools with microstructures on both the rake and flank faces (T4) are used in conjunction with solid lubricants, the cutting force is reduced by 3 % to 7 %. Furthermore, implementation of microtextures decreases the friction coefficient, improves the surface quality of the workpiece, and enhance the tool's wear resistance. Therefore, tools featuring microstructures on both the rake and flank faces, combined with solid lubricants, effectively enhance cutting performance.

Keywords *hexagonal microtexture, PCBN tools, turning, finite element simulation, solid lubricant integration*

Highlights
- *A novel hexagonal microtexture structure is proposed.*
- *Microtextures are applied to both the rake and flank faces of the cutting tool.*
- *The cutting performance of microtextured tools at various locations is verified using finite element simulation.*
- *Cutting performance is analyzed through the synergy of microtextured tools and solid lubricants using orthogonal experiments.*

1 INTRODUCTION

Polycrystalline cubic boron nitride (PCBN) is an advanced cutting material that surpasses conventional cubic boron nitride in several key aspects. It exhibits exceptional thermal stability, chemical inertness, and outstanding hardness. Due to these properties, PCBN is widely employed in machining applications for cutting various materials, including bearing steels, high-speed steels, hardened ferrous alloys, superalloys, and wear-resistant cast irons. To enhance machining efficiency, researchers have extensively explored strategies to reduce cutting forces and improve workpiece quality using PCBN tools, yielding valuable scientific insights [1,2].

Microtexturing reduces the tool-chip contact length, thereby minimizing wear and extending tool life [3]. Furthermore, optimizing texturing parameters has been shown to mitigate adverse cutting phenomena, further enhancing machining performance [4]. Patel et al. [5] demonstrated that the micro-grooved texture of carbide inserts significantly affects cutting forces and tool wear during the turning of Ti-6Al-4V titanium alloy. Pan et al. [6] established that microtextured PCBN tools enhance surface quality and wear resistance in the machining of bearing steel GCr15. Rajurkar and Chinchanikar [7] reported that pit-texture tools achieve superior surface finishes and reduce cutting forces when machining Inconel 718. Li et al. [8] revealed that a microporous texture with an 80 μm diameter exhibits exceptional wear resistance. Feng et al. [9] and Liu et al. [10] determined that well-structured microtextures effectively reduce cutting forces and temperatures. Wang et al. [11] identified abrasive and adhesive wear as the primary wear mechanisms in PCBN tools.

Kumar et al. [12] investigated TiSiVN self-lubricating coatings on Al_2O_3–SiC ceramic tools for the dry cutting of Ti6Al4V alloy. Their findings indicated that the coating effectively reduced friction, wear, surface roughness, and cutting temperatures. Xing et al. [13] utilized additive manufacturing to develop self-lubricating coatings, where MoS_2 particles formed a lubricating film that significantly decreased friction and wear. Struzikiewicz [14] determined that feed rate and depth of cut were the primary factors influencing cutting forces when employing Prime Turning with high-pressure cooling. Korpysa et al. [15] demonstrated that both tool coating and machining parameters had a substantial impact on surface quality when using TiB2- and TiAlN-coated carbide end mills. Additionally, coated tools have been shown to enhance tool life and improve surface finish [16-18].

Previous studies have primarily concentrated on the development of surface topographies, such as dimples and grooves, on the rake face of cutting tools, often in combination with self-lubricating coatings. However, there is a significant gap in evaluating the cutting performance of self-lubricating tools that feature microtextures on both the rake and flank faces, particularly when these textures are integrated with solid lubricants. To address this, the present research proposes a novel approach of fabricating hexagonal microtextures on both the rake and flank surfaces of PCBN tools through laser processing, followed by the incorporation of solid lubricants within these microtextures. Finite element analysis and cutting experiments are performed on bearing steel to assess the synergistic effects of microtexturing and solid lubricants on cutting force, surface roughness, and tool wear. The findings provide essential insights into the design and fabrication of tool surface textures to enhance machining performance.

2 METHODS & MATERIALS

2.1 Origin of Bionic Microtexture Structures

Maladen et al. [19] demonstrated that the sandfish lizard possesses the remarkable ability to navigate desert environments in a manner

similar to swimming. Furthermore, the lizard's skin exhibits exceptional abrasion resistance and low-friction properties against sand, outperforming even steel. While the epidermal scales of the sandfish lizard appear smooth at the macroscopic level, they reveal a complex, non-smooth microstructure under closer inspection. These specialized non-smooth epidermal scales have evolved as adaptations to the harsh conditions of the sandfish lizard's habitat, enabling it to thrive over extended periods. This study analyzes the configuration of the sandfish lizard's surface structures, focusing on the extraction of the hexagonal microtexture, as depicted in Fig. 1.
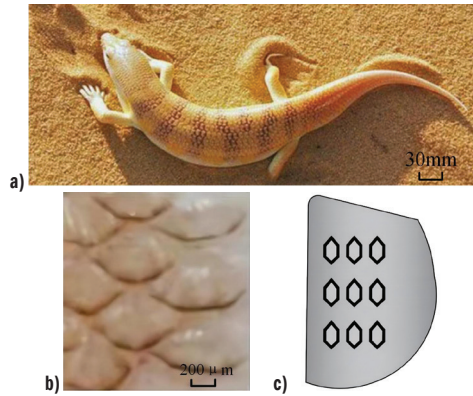
Fig. 1. Source of bionic microtexture structures; a) sandfish lizard; b) epidermal structure; and c) tool microstructure morphology

2.2 Mechanism of Action of Self-Lubricating Cutting Tools

Ge et al. [20] investigated the application of laser-cut micro-groove textures with varying widths on cutting tool surfaces to enhance the penetration of cutting fluids and improve lubrication at the tool-chip interface. As illustrated in Figs. 2 and 3, the friction surfaces of conventional cutting tools typically come into direct contact, resulting in a dry friction state that exacerbates wear at the contact points.
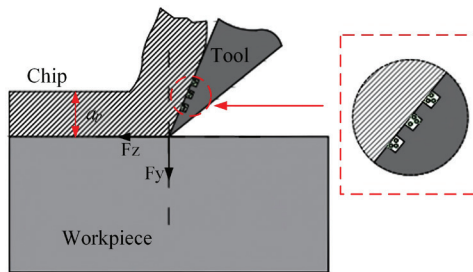
Fig. 2. Mechanism of surface microstructure action

In contrast, the introduction of microtextured structures facilitates the entry of chips into the grooves, thereby alleviating secondary cutting forces and promoting the expulsion of solid lubricants. As
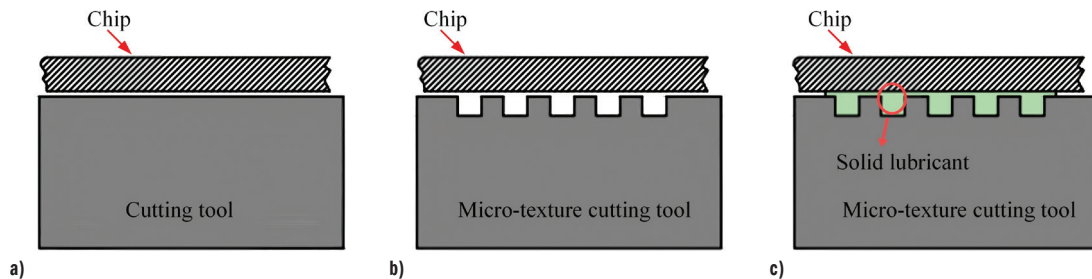
the machining process progresses, this solid lubricant undergoes transformation due to increased temperature and pressure, leading to the formation of a lubricant film that adheres to the insert surface. This mechanism significantly improves lubrication conditions on the tool surface, effectively reducing both friction and wear.

2.3 Establishment of the Cutting Force Model

Fig. 4 presents a simplified model of the microtexturing tool-cutting process. According to metal cutting theory [21], the three-dimensional cutting forces during turning are represented by Eqs. (1) to (4).

$$F_x = a_w L \tau_c \left(\cos \gamma_0 - \frac{\sin \gamma_0}{\tan \beta} \right) \cos(\phi_a + \phi_b), \tag{1}$$

$$F_y = a_w L \tau_c \left(\cos \gamma_0 - \frac{\sin \gamma_0}{\tan \beta} \right) \sin(\phi_a + \phi_b), \tag{2}$$

$$F_z = a_w L \tau_c \left(\sin \gamma_0 + \frac{\sin \gamma_0}{\tan \beta} \right), \tag{3}$$

$$F = \sqrt{F_x^2 + F_y^2 + F_z^2}. \tag{4}$$

where γ_0 is the tool forward tilt angle, ϕ_a is the deflection angle, β is the friction angle, ϕ_b is the chip flow angle, τ_c is the friction shear strength, L is the tool-chip contact length, and a_w is the cutting width.

The actual contact length between the tool and the chip varies as a result of machining the microtexture in the region near the tip and cutting edge of the tool's front face:

$$L' = L - nL_0, \tag{5}$$

where L' is the actual tool-chip contact length, n is the number of textured single edges in the tool-chip contact area, and L_0 is the width of textured single edges in the tool-chip contact area. The actual cutting component forces are represented by Eqs. (6) to (9).

$$F'_x = a_w L' \tau_c \left(\cos \gamma_0 - \frac{\sin \gamma_0}{\tan \beta} \right) \cos(\phi_a + \phi_b), \tag{6}$$

$$F'_y = a_w L' \tau_c \left(\cos \gamma_0 - \frac{\sin \gamma_0}{\tan \beta} \right) \sin(\phi_a + \phi_b), \tag{7}$$

$$F'_z = a_w L' \tau_c \left(\sin \gamma_0 + \frac{\sin \gamma_0}{\tan \beta} \right), \tag{8}$$

$$F' = \sqrt{F'^2_x + F'^2_y + F'^2_z}. \tag{9}$$

Theoretical analysis and derivations presented above clearly demonstrate that the microtextured tool reduces the contact area between the insert and the tool, thereby minimizing cutting forces. Based on these findings, microtextured tools were fabricated, simulated, and experimentally tested in this study.
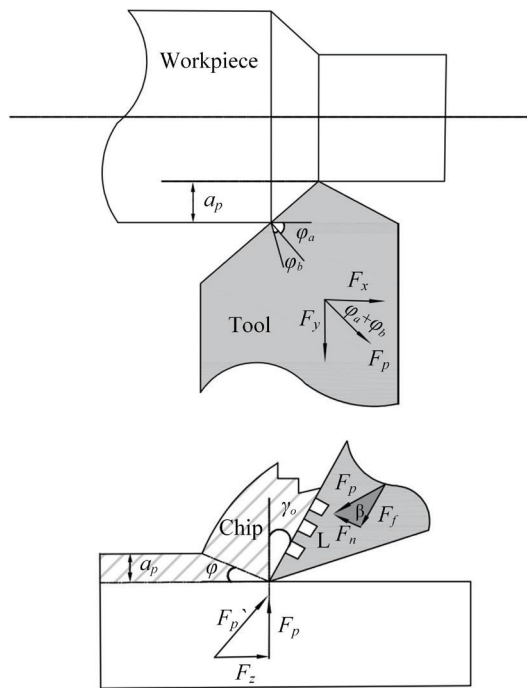

Fig. 3. Mechanism of action of self-lubricating cutting tools, a) traditional tool; b) microtextured tool, and c) self-lubricating tool

Fig. 4. Simplified model of turning

2.4 Simulation and Analysis of Cutting Performance of Microtexture Tools

2.4.1 Three-Dimensional Modeling of Microtextured Tools

To investigate the influence of various texture placements on cutting performance, microtextures were fabricated on both the front and rear cutting surfaces of the PCBN tool. The tool specifications were as

follows: length and width of 12.73 mm, thickness of 4.76 mm, and a tilt angle of 80°. The texture dimensions included a width of 30 μm, a pitch of 100 μm, and a depth of 30 μm. The workpiece was modeled as a cylindrical component with a diameter of 30 mm and a length of 10 mm. Fig. 5 illustrates the tool dimensions and the three-dimensional model.

2.4.2 Finite Element Simulation Test of Microtextured Tools

In this study, simulation tests were conducted using AdvantEdge finite element software. Table 1 presents the mechanical performance parameters of the PCBN tool, as determined through finite element analysis. The workpiece material employed in the experiments is GCr15 steel, with a hardness rating of 65 HRC. The cutting simulation model, as shown in Fig. 7, utilizes the Lagrangian self-division method for meshing, with a maximum grid size of 0.1 mm and a minimum grid size of 0.02 mm. The simulation procedure, including the turning model, is depicted in Figs. 6 and 7.

Table 1. Mechanical property parameters of PCBN tool for finite element analysis

Young's modulus [GPa]	Thermal conductivity [W/(m·K)]	Poisson's ratio	Density [g/cm³]	Specific heat capacity [J/(kg·K)]
690	120	0.2	3.8	700
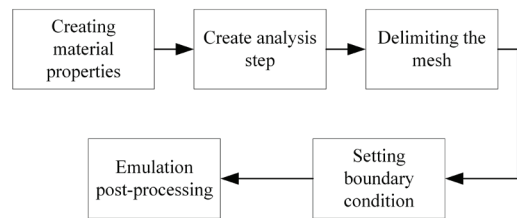
Fig. 6. Cutting simulation process
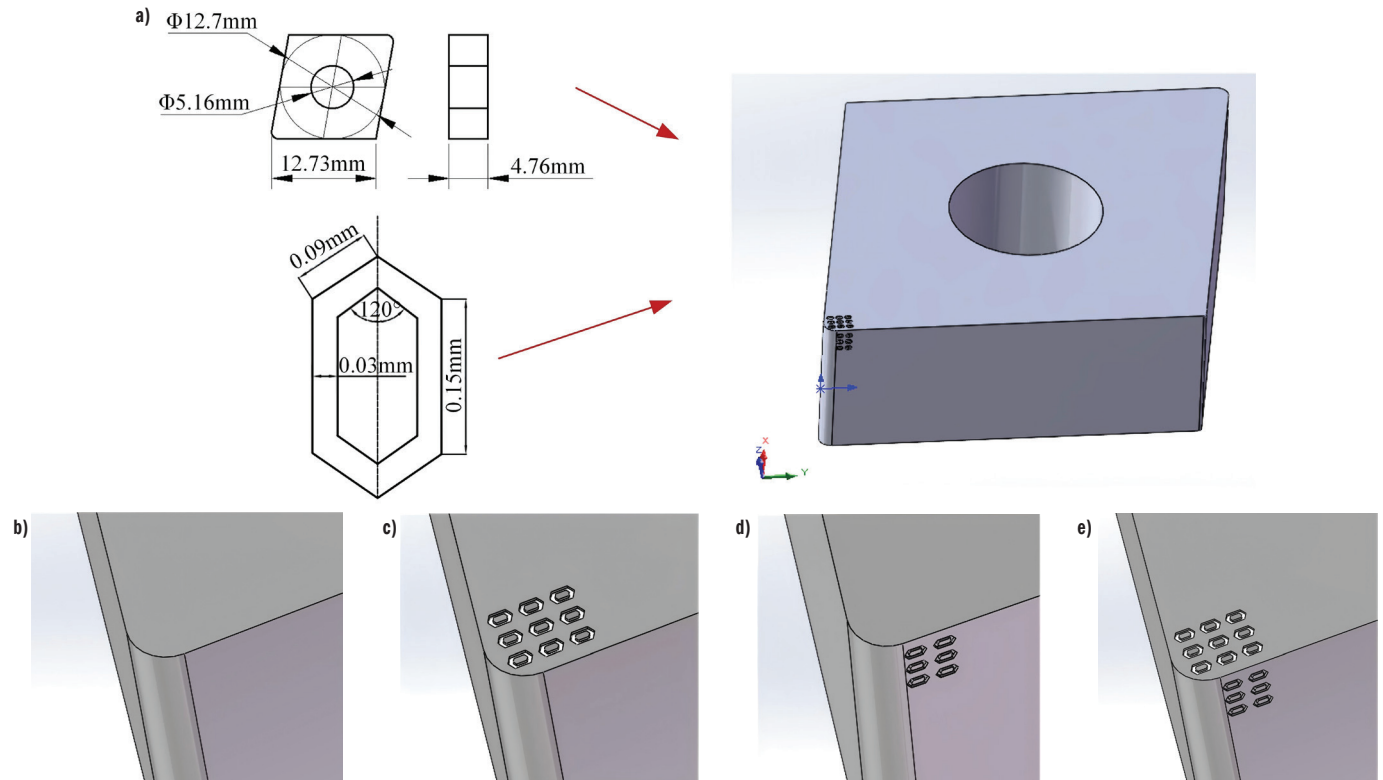
Fig. 5. CNGA120408 tool dimensions and 3D model; a) CNGA120408 tool size; b) T1 tool; c) T2 tool; d) T3 tool; and e) T4 tool
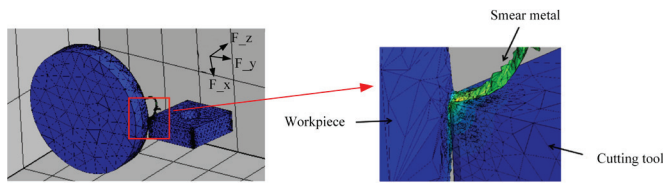
Fig. 7. Simulation flow and cutting model

The mechanical behavior observed during the cutting process was characterized using the Johnson-Cook (J-C) model, which accounts for nonlinear strain hardening and strain rate sensitivity, as expressed in Eq. (10). The parameters relevant to the J-C model for GCr15-bearing steel are provided in Table 2.

Table 2. Parameters of the J-C constitutive equation for GCr15 bearing steel [22]

A [GPa]	B [GPa]	C	m	n
1.67	0.283	0.018	0.88	0.41

$$\bar{\sigma} = [A + B(\bar{\varepsilon})^n]\left(1 + C\ln\left(\frac{\dot{\varepsilon}}{\dot{\varepsilon}_0}\right)\right)\left[1 - \frac{T - T_r}{T_m - T_r}\right]^m. \qquad (10)$$

where $\bar{\sigma}$ is the material flow stress; A, B, C, m, and n are material constants; $\bar{\varepsilon}$ is the equivalent plastic strain; $\dot{\varepsilon}$ is the plastic strain rate; $\dot{\varepsilon}_0$ is the effective plastic strain rate for quasi-static tests; T is the material temperature; T_r is the reference temperature; and T_m is the melting temperature of the material.

To investigate the effect of texture position on the cutting process, finite element simulations were conducted using T2, T3, and T4 microtextured tools, in addition to the T1 conventional tool. The experimental design is outlined in Table 3.

Table 3. Cutting test program

Group number	Spindle speed V [r/min]	Feed rate f [mm/r]	Back to eat knife a_p [mm]
1	800	0.1	0.1
2	1000	0.15	0.15
3	1250	0.2	0.2

2.4.3 Analysis of Simulation Test Results

During the turning process, the feeding motion of the turning tool generates turning forces, including tangential, radial, and vertical forces. Simultaneously, the high-speed rotation of the workpiece generates substantial heat, which is primarily concentrated at the cutting edge. To evaluate these effects, a finite element analysis was conducted to determine the three components for each group of turning tools. The combined forces were calculated according to Eqs. (4) and (9). Furthermore, the temperature and stress distribution at the tool tip were also analyzed. As illustrated in Fig. 8 to 10, the simulation results reveal that the turning forces, temperature distribution, and stress state exhibit continuous variations depending on the positional configuration of the microtexture structures. First, the microtexture stores chips generated during turning, reducing chip-tool tip contact and tool wear, thereby reducing the turning force. Second, the micro groove enhances heat dissipation by providing additional space, facilitating heat release and reducing the turning temperature.

Influence of front and back face microtexture on cutting forces. Fig. 8 illustrates the cutting force simulation curves for each tool. At a spindle speed of 800 rpm, the average cutting force

is reduced by 16.87 % for tool T4, and by 14.6 % and 5.62 % for tools T2 and T3, respectively, compared to the conventional tool. The reduction in cutting forces can be attributed to the microtextures, which, as indicated by the theoretical analysis, reduce the contact area between the tool and the workpiece, thereby decreasing the cutting force. Among the three sets of simulation results, tool T4 demonstrates the best performance.
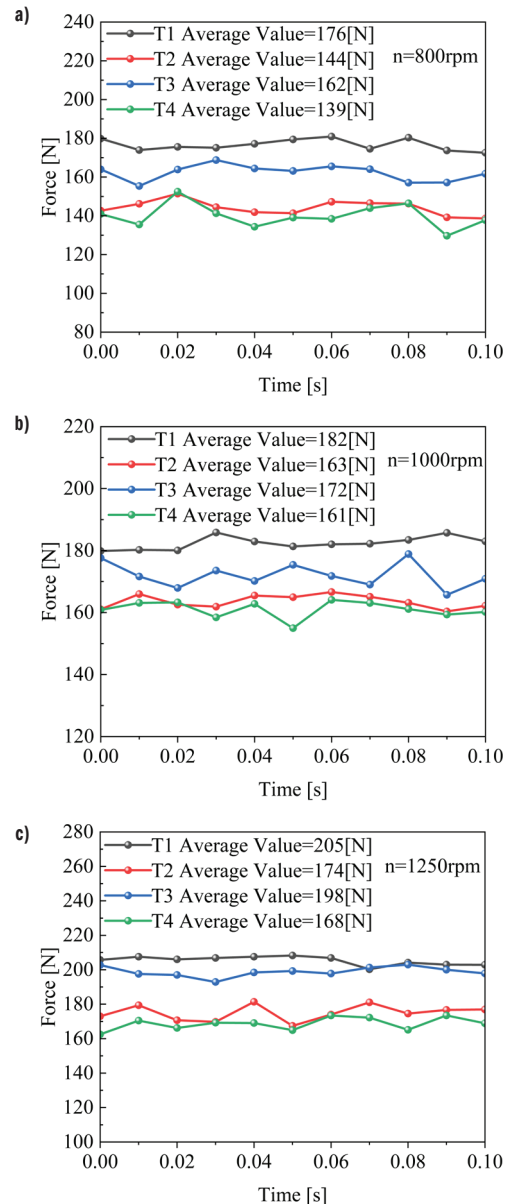

Fig. 8. Cutting forces at different speeds for four tools; a) 800rpm; b) 1000rpm; and c) 1250 rpm

Influence of microtexture on cutting temperature at the front and rear faces. As depicted in Fig. 9, the temperature at the tool tip is observed to be the highest. The thermal energy generated during the cutting process can be attributed to two primary sources: firstly, frictional heat generated by the interaction between the tool, chip, and workpiece, and secondly, the energy consumed in the deformation of the bearing steel. Under identical cutting conditions, biomimetic microtextured tools demonstrate a significantly improved heat dissipation capability compared to conventional tools. This improvement is primarily attributed to additional micro features, which reduce cutting forces by minimizing direct contact between

the tool and the workpiece material. Additionally, the microtexture increases the available surface area for heat dissipation, leading to a subsequent reduction in cutting temperature.

Influence of front and back face microtexture on cutting stresses. The extrusion contact between the workpiece and the cutting edge, which induces elastic-plastic deformation and chipping damage, results in a notable increase in stresses within the cutting zone. Fig. 10 illustrates the distribution of equivalent stress across the surfaces of various tools during the cutting process. The stress attenuation rates for tools T2, T3, and T4 are 10.23 %, 7.45 %, and 15.66 %, respectively, compared to conventional tools. When cutting with tool T1, the average equivalent stress values range between 900 MPa and 1000 MPa, while those for tool T4 are reduced to the range of 800 MPa to 900 MPa. The stresses decrease progressively, with maximum stress concentrations primarily localized in the tip region. Notably, tool T4 demonstrates an 11.1 % reduction in equivalent stress, along with a substantial improvement in the internal stress distribution, when compared to the conventional tool T1.

Finite element simulations conducted on the microtextured tool demonstrated significantly improved performance compared to conventional tools in several key metrics, including cutting forces, stress distribution, and cutting temperature. These results provide a strong basis for the subsequent turning tests and validate the underlying theoretical framework.
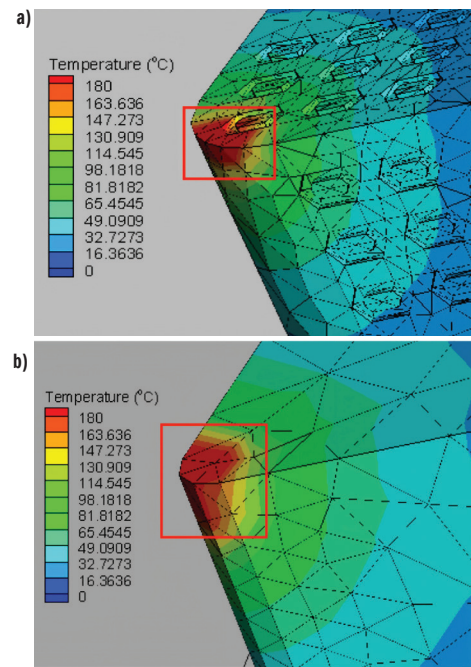
Fig. 9. Tip temperature distribution of tools; a) T4 tool; and b) T1 Tool
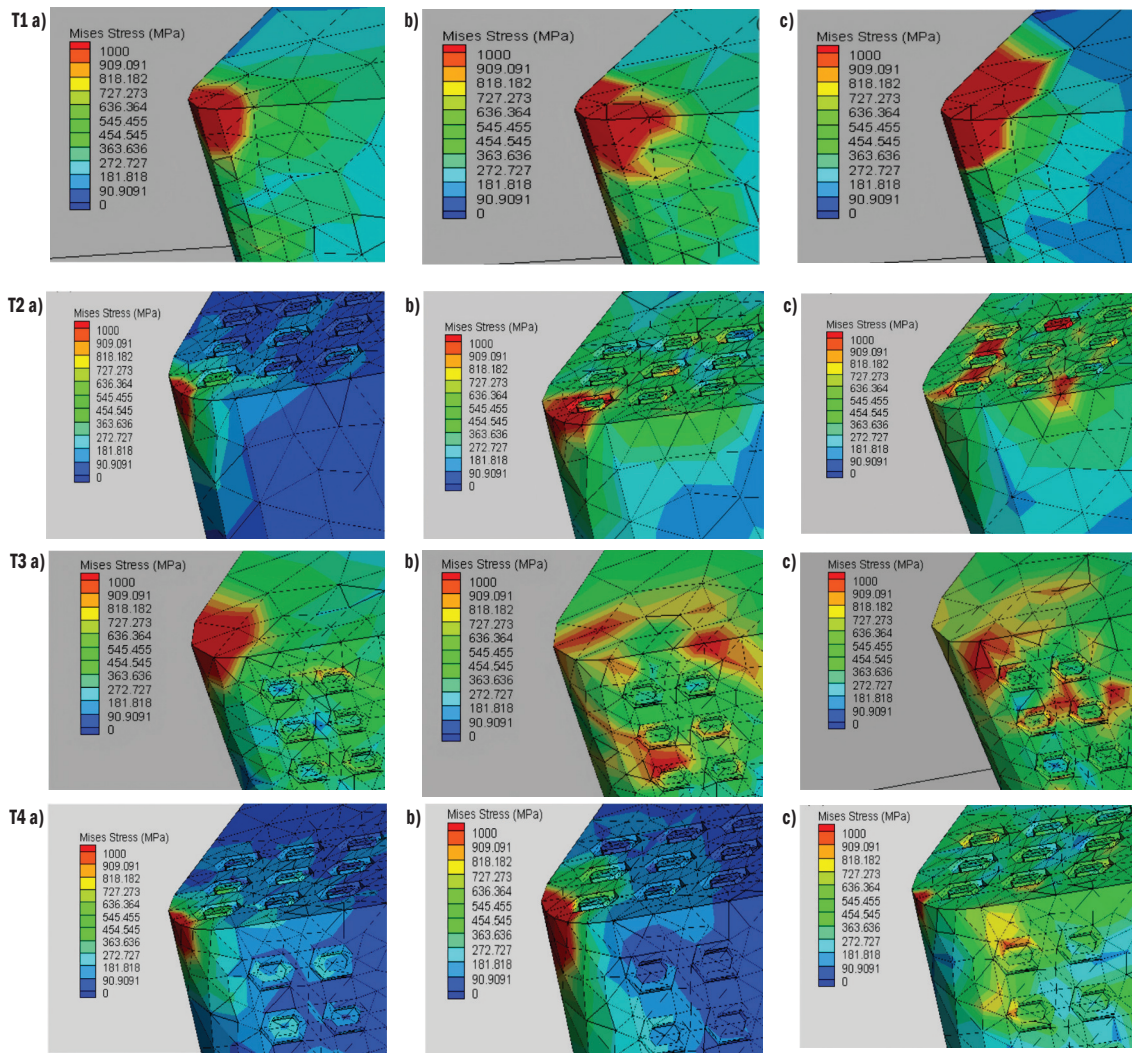
Fig. 10. Stress distribution diagrams of four types of cutting tools over time; a) 0.001s; b) 0.002s; and c) 0.003s

2.5 Experimental Analysis Of Cutting Performance of Microtextured Tools

2.5.1 Microtexture and Solid Lubricant Preparation for Front and Rear Tool Surfaces

In recent years, microtexture machining technology has emerged as a prominent area of research within surface engineering. This technology primarily focuses on creating micro- or nano-scale structures on material surfaces to enhance the cutting performance of tools. Among various methods, laser processing has gained recognition for its high precision, controllability, broad applicability, and environmental sustainability, making it a crucial technique in modern manufacturing. In this study, a ZT-Y-50W YAG laser, provided by Beijing Zhentian Laser Co., Ltd., China, was utilized to fabricate microtextures on the tool surface. Laser processing parameters: spot diameter 0.03 mm, processing speed 60 mm/s, frequency 60 KHz, power 50%, focal length 245 mm, wavelength 1064 nm, number of processes 50. The fabricated hexagonal microtexture featured an edge length of 15 μm, with grooves measuring 30 μm in both depth and width and a spacing of 30 μm between adjacent structures. The surface morphology of the microtexture was analyzed using a Leica DVM2500 super-depth-of-field microscope, as depicted in Fig. 11. Furthermore, Fig. 12 presents the depth profile from the texture edge to the center of the groove, confirming that the groove depth reached 30 μm, in accordance with the established design specifications.

To enhance the cutting performance of microtextured PCBN tools, a solid lubricant composed of molybdenum disulfide (MoS_2) was synthesized by mixing 5000 to 8000 mesh MoS_2 with analytical reagent-grade arsenic trioxide powder in a 1:1 ratio. This solid lubricant was subsequently integrated into the microtextured regions to develop self-lubricating cutting tools. The influence of the lubrication state on the resulting surface quality was then systematically analyzed.

2.5.2 Microtexture Cutting Test for Front and Rear Tool Surfaces

The experiments were performed using a CA6140A machine tool. The cutting tests employed PCBN tools of the CNMG120408 type. The workpiece was composed of GCr15-bearing steel with a diameter of 50 mm and a length of 300 mm. Three-dimensional cutting forces were measured using the DynoWare 2825A-02 force measurement

software and calculated in accordance with Eq. (1). To validate the reliability of the theoretical and simulation results, an orthogonal cutting experimental matrix was designed, as detailed in Table 4.

The static working point fluctuates when the cutter operates within the idle cutting zone, primarily due to temperature variations and an unstable power supply voltage. These fluctuations result in a nonzero cutting force, leading to the zero-drift phenomenon, which introduces variability in the test data. As illustrated in Fig. 13, to mitigate errors associated with zero drift, the average cutting force within the cutting stability interval (sampling interval) was selected as the measurement value. The sampling frequency for the test interval was set at 3000 Hz.

Table 4. Experimental matrix

Group number	Spindle speed V [r/min]	Feed rate f [mm/r]	Back to eat knife a_p [mm]
1	800	0.1	0.1
2	800	0.15	0.2
3	800	0.2	0.15
4	1000	0.1	0.2
5	1000	0.15	0.15
6	1000	0.2	0.1
7	1250	0.1	0.15
8	1250	0.2	0.1
9	1250	0.2	0.2

3 RESULTS AND DISCUSSION

3.1 Effect of Lubricated Tools on Cutting Forces

The radial, axial, and tangential forces were measured using a force gauge, and the total cutting forces were obtained by summing these three directional components. Fig. 14 presents the cutting forces measured during turning experiments under the conditions outlined in Table 3. The results indicate that, compared to the T1 tool, the average cutting forces decreased by 19.8 % for the T4 tool, 16.7 % for the T2 tool, and 11.2 % for the T3 tool, indicating a beneficial effect from the microtextured structure combined with the solid lubricant.
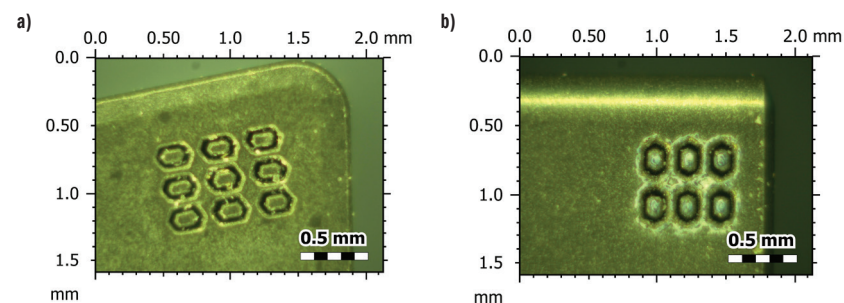

Fig. 11. Micro-structure morphology of the tool; a) front face of cutting tool; and b) back face of cutting tool
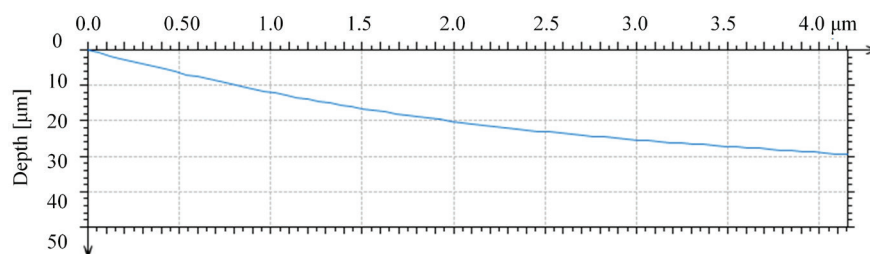

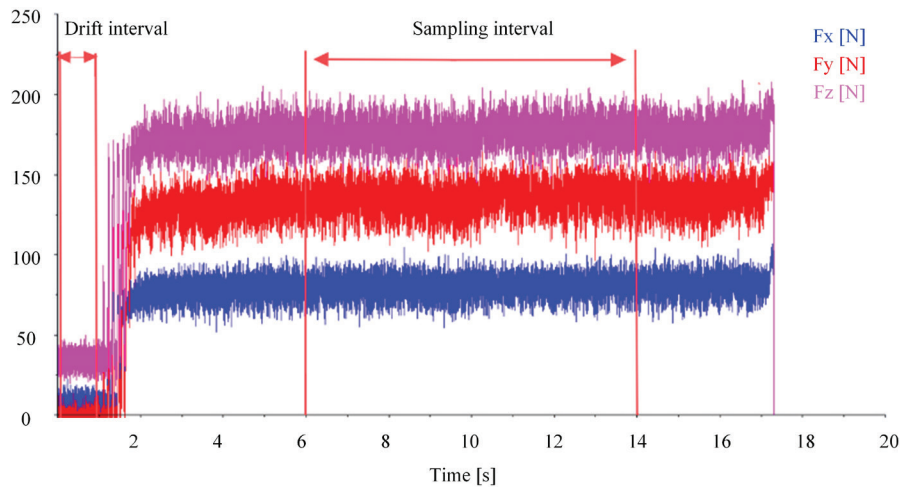Fig. 12. Micro-structure depth profile

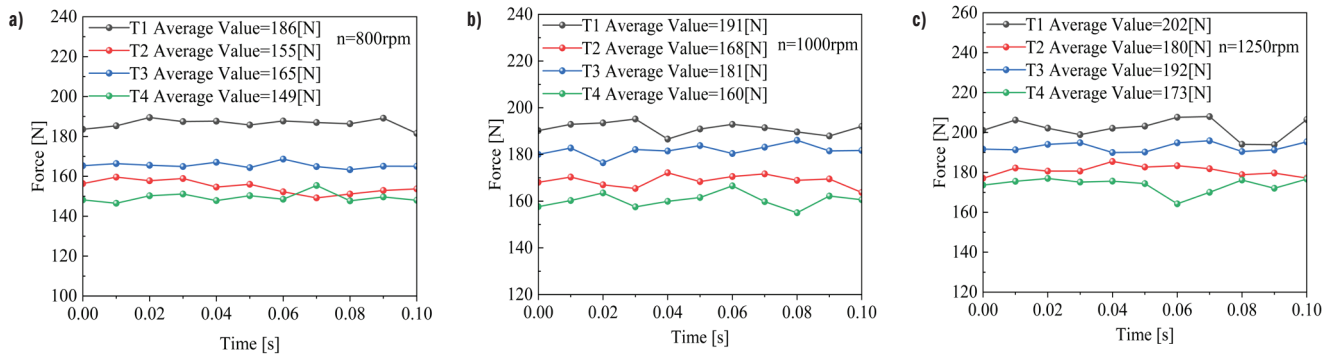Fig. 13. Distribution of cutting force measurement interval

Fig. 14. Cutting forces at different spindle speeds; a) 800 rpm; b) 1000 rpm; and c) 1250 rpm
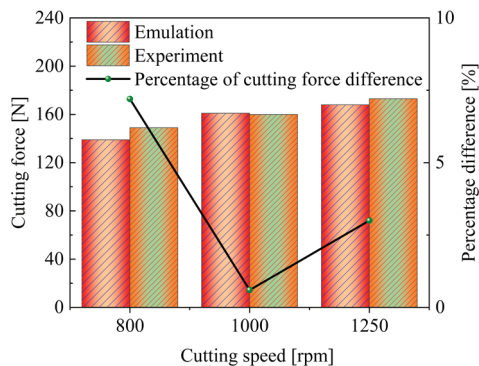

Fig. 15. Comparison of cutting force experiments values and simulation values
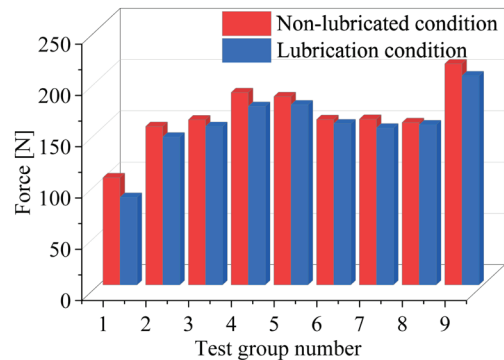

Fig. 16. Comparison of cutting force before and after lubrication

Fig. 15 compares the experimentally measured turning forces of the T4 tool with the simulation data. The error between experimental and simulated data ranged from 1 % to 7 %, which is within an acceptable error range. Additionally, the experimental results of each group demonstrated values slightly higher than the simulation results. This difference arose because the simulation analysis assumes absolutely ideal conditions. However, experimental outcomes in actual processing typically experience influences from factors such as machine tool vibration or environmental temperature changes, leading to an increase in turning force. Furthermore, Fig. 16 compares the cutting forces between the lubricated and non-lubricated conditions for T4 tools, revealing an average reduction of 6.41 %. This result highlights the beneficial synergistic effect of microtexture and solid lubricant on the cutting process.

3.2 Influence of Lubricated Tools on Surface Roughness

Fig. 17a presents a comparative analysis of the surface roughness of bearing steel machined using conventional (T1) and microtextured tools (T2, T3, T4). The T4 tool achieved a surface roughness of 1.51, corresponding to a 37.6 % reduction relative to T1. Surface roughness reductions of 30.6 % and 23.9 % were observed for T2 and T3 respectively. These findings indicate that microtextured tools significantly enhance surface finish, with T4 demonstrating the most pronounced improvement. Fig. 17b further compares test groups 1, 6, and 8, revealing surface roughness reductions of 13.5 %, 6.04 %, and 6.9 % respectively, in comparison to dry cutting. However, minor surface defects, such as pits and scratches, are observed, primarily resulting from tool adhesion deformation. Fig. 18 illustrates the surface morphology of the machined workpiece. The extrusion of
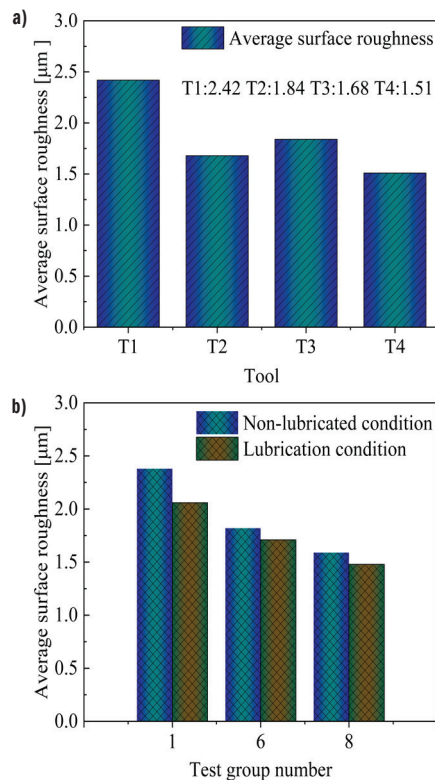
Fig. 17. Comparison of surface roughness; a) surface roughness of workpieces machined using four different cutting tools; and b) surface roughness comparison before and after lubrication
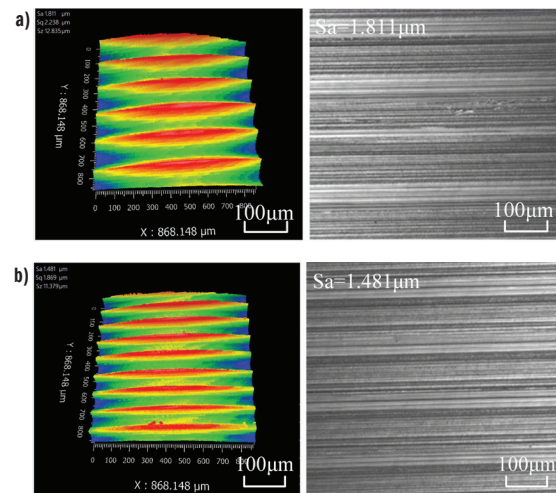
Fig. 18. Comparison of surface morphology before and after lubrication; a) 3D surface topography and profile of the workpiece in dry cutting; and b) 3D surface topography and profile of the workpiece under lubricated conditions

lubricant facilitates the formation of a lubricating film on the contact surface, which enhances wear resistance and improves surface smoothness.

Fig. 18 shows the surface morphology of the workpiece before and after lubrication, where Sa is the area-based arithmetic mean height. The results indicate a reduction in surface roughness following lubrication, along with enhanced wear resistance and improved surface smoothness.
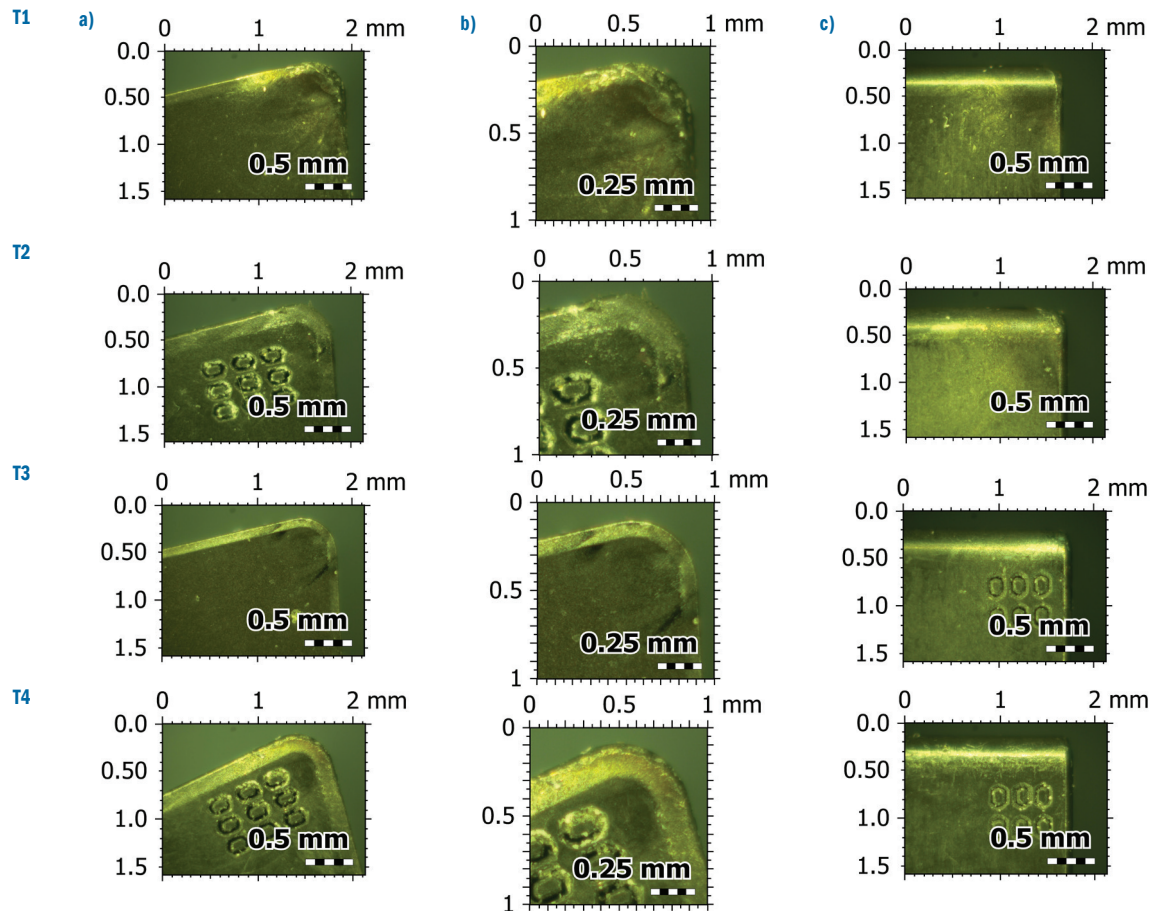
Fig. 19. SEM tool wear patterns of four types of cutting tools; a) front surface; b) local magnification; and c) side surface (all units in mm)

3.3 Influence of Lubricated Tools on Tool Wear

As shown in Fig. 16b, after excluding the maximum and minimum cutting forces, group 2 in the orthogonal test exhibits lower cutting forces. The corresponding tool wear under these conditions (v = 800 rpm, f = 0.15 mm/r, a_p = 0.2 mm) is depicted in Fig. 19, whereby r represents the number of revolutions per minute of the lathe spindle. For the conventional tool (T1), material tearing occurs, resulting in pits, scratches, and fracture marks on the tool surface. During continuous machining, the temperature at the tool-chip interface increases, leading to tip sintering and accelerated wear. The T3 tool undergoes mechanical plowing, where rough chip peaks embed into the tool surface under elevated temperatures, causing material displacement and sliding. In contrast, the microtexture structures of T2 and T4 promote efficient chip flow or partial embedding during extrusion, thereby reducing surface wear. The rear surface exhibits less wear compared to the front surface. Severe pit wear, scratching, and sintering are observed in T1, whereas T2, T3, and T4 display significantly reduced wear. The microtexture present on both tool surfaces effectively reduces friction. According to ISO 1993:3685 [23], Fig. 20 presents the tool flank wear after the turning tests, where VB is the wear width of the rear face. The measured wear widths before and after lubrication were 0.085 mm, 0.081 mm, 0.068 mm, and 0.062 mm respectively. Lubrication resulted in a 20 % to 24 % reduction in tool wear, demonstrating the effectiveness of solid lubricants in mitigating wear and prolonging tool life.
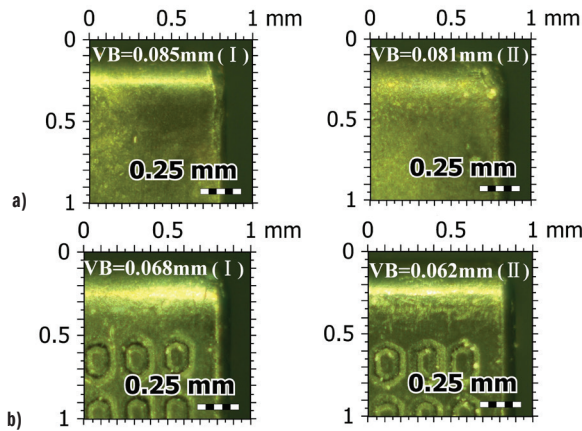

Fig. 20. Tool wear before and after lubrication; a) non-lubricated condition; and b) lubrication condition (all units in mm)

3.4 Influence of Lubricated Tools on Chip Formation

To facilitate clearer observation of the chip pattern, a larger feed rate and depth of cut were selected. Cutting tests were conducted under the conditions of V = 800 rpm, f = 0.2 mm/r, and a_p = 0.5 mm. The chip width and the average chip thickness were measured, along with the standard deviation for ten chip segments across four tool types. As illustrated in Fig. 21, conventional tools generate higher cutting forces, leading to severe deformation of the cutting layer and significant burr formation. Chips produced by conventional tools exhibit smaller curl radii and are less prone to breaking. During turning, curled chips were observed scratching the workpiece surface, adversely affecting machining accuracy. In contrast, under continuous cutting conditions, the microtextured tools effectively facilitate chip breaking. Fig. 22 shows that the actual chip thicknesses obtained from T1, T2, T3, and T4 exceeds theoretical values, with relative deviations of 14 %, 8 %, 11.5 %, and 7 %, respectively. This discrepancy arises due to plastic deformation along the shear line and friction compression in the secondary deformation zone, leading to chip accumulation. However, the microtextured tools mitigate chip

accumulation, producing chips with thicknesses closer to theoretical predictions.
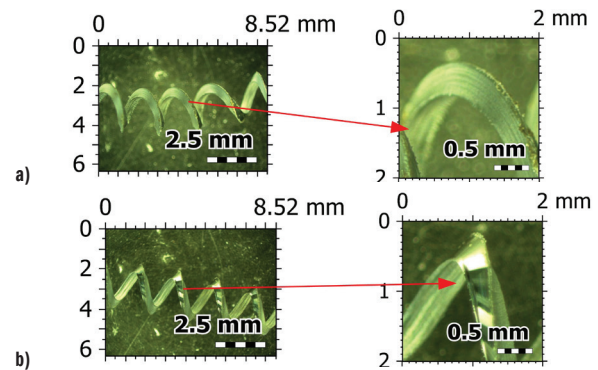

Fig. 21. Cutting chip morphology; shape; a) chip profile of the T1 tool under non-lubricated conditions; and b) chip profile of the T4 tool under lubricated conditions (all units in mm)
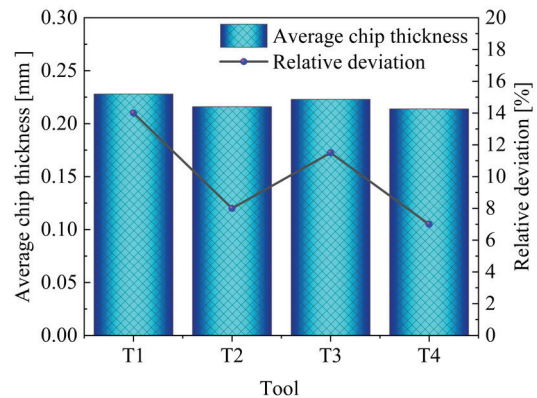

Fig. 22. Chip thickness and relative deviation for the four tool types

During the cutting process, the three distinct patterns of tool surface microtextures investigated in this study enhanced surface wettability. This improvement facilitated greater penetration of cutting fluid into the tool-chip interface, thereby establishing effective cooling and lubrication channels. The enhanced lubrication and heat dissipation within the cutting zone reduced frictional resistance between the tool and chip, resulting in diminished three-dimensional cutting forces and decreased tool wear. Additionally, the improved wettability promoted the removal of minute chips during tool-chip sliding friction, minimizing chip adhesion on the machined surface. Consequently, fewer surface defects, such as pits and scratches, were observed, resulting in improved surface integrity. Among the tools evaluated, the front and rear microtextured tools exhibited the highest wettability, providing superior cooling and lubrication, which contributed to the most substantial improvement in cutting performance.

4 CONCLUSION

To improve the cutting performance of turning tools, a novel PCBN microtextured composite tool has been proposed. The feasibility of the tool structure has been validated through turning tests. The following conclusions have been drawn:

1. Experimental and simulation data for the T4 tool have been compared, revealing an error in the range from 1 % to 7 %. This confirms the model's reliability and applicability for predicting cutting forces under specific conditions.
2. Under dry cutting conditions, the T4 tool demonstrated an average reduction of 19.8 % in cutting force compared to the T1

tool, indicating its superior cutting performance. The addition of solid lubricant further reduced the cutting forces of the T4 tool by an average of 6.41 %. These results underscore the significant improvement in cutting performance achieved through the combined effect of surface texturing and solid lubricants.

3. The T4 tool reduced workpiece surface roughness by 37.6 % compared to the T1 tool, while T3 and T2 achieved reductions of 30.6 % and 23.9 %, respectively. At a feed rate of $f = 0.15$ mm/r and depth of cut $a_p = 0.2$ mm, post-lubrication wear widths were 5.23 μm for T1 and 3.86 μm for T4, indicating wear reductions of 18.1 % and 19.5 % respectively. These results highlight the synergistic effect of solid lubricants and microstructures in improving surface quality and reducing tool wear.

4. The chip thickness for both T1 and T4 tools exceeded theoretical values due to compression and friction in the second deformation zone, leading to increased material accumulation. However, the T4 tool produced thinner chips than the T1 tool, as its surface microstructure facilitated chip fragmentation and reduced accumulation thickness.

Further research on microtextures with varying parameters and sizes, coupled with optimized cutting conditions and tool-workpiece material compatibility, could further enhance tool performance.

References

[1] Ding, X., Liew, W.Y.H., Liu, X.D. Evaluation of machining performance of MMC with PCBN and PCD tools. *Wear* 259 1225-1234 (2005) **DOI:10.1016/j.wear.2005.02.094**

[2] Persson, H., Filip Lenrick, Franca, L., Ståhl, J.E., Bushlya, V. Wear mechanisms of PcBN tools when machining AISI 316L. *Ceram Int* 47 31894-31906 (2021) **DOI:10.1016/j.ceramint.2021.08.075**

[3] Fan, L., Deng, Z., Gao, X., He, Y. Cutting performance of micro-textured PCBN tool. *Adv Mater Res-Switz* 4 023004 (2021) **DOI:10.1063/10.0004372**

[4] Kishawy, H.A., Salem, A., Hegab, H., Hosseini, A., Balazinski, M. Micro-textured cutting tools: Phenomenological analysis and design recommendations. *CIRP Ann* 70 (2021) **DOI:10.1016/j.cirp.2021.04.081**

[5] Patel, K., Kaftanoğlu, B., Özel, T. (2019). Micro textured cutting tool effects on cutting forces, volumetric wear and adhesion in dry turning of titanium alloy. Int J Mech Manuf Syst 12 180 **DOI:10.1504/ijmms.2019.103482**.

[6] Pan, C., Li, Q., Hu, K., Jiao, Y. Song. Y. (2018). Study on surface roughness of gcr15 machined by micro-texture PCBN tools. *Machines* 6 42 **DOI:10.3390/machines6030042**

[7] Rajurkar, A., Chinchanikar, S. Experimental investigation on laser-processed micro-dimple and micro-channel textured tools during turning of Inconel 718 alloy. *J Mater Eng Perform* 31 4068-4083 (2022) **DOI:10.1007/s11665-021-06493-7**

[8] Li, Q., Pan, C., Jiao, Y., Hu, K. Investigation on cutting performance of micro-textured cutting tools. *Micromachines* 10 352 (2019) **DOI:10.3390/mi10060352**

[9] Feng, Y., Zhang J., Wang, L., Zhang, W., Tian, Y., Kong, X. Fabrication techniques and cutting performance of micro-textured self-lubricating ceramic cutting tools by in-situ forming of Al2O3-TiC. *Int J Refract Met H* 68 121-129 (2017). **DOI:10.1016/j.ijrmhm.2017.07.007**

[10] Dai, L., Zheng, J, Dong., D., Sun, S, Liu, G.Effect of insert micro-texture types on the cutting force and temperature under various cooling conditions. *Int J Mechatr Manuf Syst* 14228-239 (2022) **DOI:10.1504/ijmms.2021.121240**

[11] Wang, H., Meng, D., Wu, Z., Kang, J., She, D., Qin, W., Yue, W. Tribological behavior of polycrystalline cubic boron nitride sliding against WC-Co cemented carbide in vacuum conditions. *J Mater Eng Perform* 33 1975-1984 (2024) **DOI:10.1007/s11665-023-08119-6**

[12] Kumar, C.S., Urbikain, G., De Lucio, P.F., Lopez de Lacalle, L.N., Pérez-Salinas, P., Gangopadhyay, S., and Fernandes, F. Investigating the self-lubricating properties of novel TiSiVN coating during dry turning of Ti6Al4V alloy. *Wear* 532-533 205095-205095 (2023) **DOI:10.1016/j.wear.2023.205095**

[13] Xing, Y., Luo, C., Zhu, M., Zhao, Y., Ehmann, K., Wu, Z., Liu, L. Assessment of self-lubricating coated cutting tools fabricated by laser additive manufacturing technology for friction-reduction. *J Mater Process Tech* 318 118010 (2023) **DOI:10.1016/j.jmatprotec.2023.118010**

[14] Struzikiewicz, G. Investigation of the titanium alloy turning process with Prime A tools under high-pressure cooling conditions. *Stroj Vestn-J Mech E* 70 70-79 (2024) **DOI:10.5545/sv-jme.2023.718**

[15] Korpysa, J., Kuczmaszewski, J., Zagórski, I. Surface quality of AZ91D magnesium alloy after precision milling with coated tools. *Strojn Vestn-J Mech E* 69 497-508 (2023) **DOI:10.5545/sv-jme.2023.651**

[16] Tamang, S.K., Chandrasekaran, M., Palanikumar, K., Arunachalam, R.M. Machining performance optimisation of MQL-assisted turning of Inconel-825 superalloy using GA for industrial applications. *Int J Mach Mach Mater* 21 43-65 (2019) **DOI:10.1504/ijmmm.2019.098066**

[17] Ginting, A., Nouari, M., Bencheikh, I., Increasing productivity in hard turning of steels using CVD-coated carbide. *Int J Mach Mach Mater* 22 309-330 (2020) **DOI:10.1504/ijmmm.2020.107060**

[18] Wang, Z., Wang, Y., Lv, D., Yu, X. Gao, Y. Performance and wear mechanisms of coated PCBN tools in high-speed turning superalloy GH4202. *Int J Adv Manuf Tech* 127 5083-5097 (2023) **DOI:10.1007/s00170-023-11803-5**

[19] Maladen, R.D., Ding, Y., Li, C., Goldman, D.I. Undulatory swimming in sand: Subsurface locomotion of the sandfish lizard. *Science*, 325 314-318 (2009). **DOI:10.1126/science.1172490**

[20] Ge, D., Deng, J., Duan, R., Liu, Y., Li, X.,Yue, H. Effect of micro-textures on cutting fluid lubrication of cemented carbide tools. *Int J Adv Manuf Tech* 103 3887-3899 (2019) **DOI:10.1007/s00170-019-03763-6**

[21] Gupta, M.K., Korkmaz, M.E., Sarıkaya, M., Krolczyk, G.M., Günay, M., Wojciechowski, S. Cutting forces and temperature measurements in cryogenic assisted turning of AA2024-T351 alloy: An experimentally validated simulation approach. *Measurement* 188110594 (2022) **DOI:10.1016/j.measurement.2021.110594**

[22] Zhao, Z., Xie, X., Tang, G., Padhiar, M.A., Xiao, J., Liang, Z. Study on the effect of the strengthen grinding process surface coverage on the micro-morphology, micro-hardness, roughness, and residue stress of GCr15 bearing steels. *J Manuf Process* 99 362-372 (2023) **DOI:10.1016/j.jmapro.2023.05.041**

[23] ISO 3685: 1993 (E). *Tool-life testing with single point tools* (1993)

Author contribution *Yan Zhang: conceptualization, formal analysis, writing – review & editing; Haodong Sun: writing – original draft, writing – review & editing, validation; Qi Li: validation, project administration; Yuanjing Mou: data curation; Kaiming Sun: data curation; Shihong Zhang: validation, supervision.*

Raziskava rezalne učinkovitosti samomazivnih orodij z mikrotesturo sprednje in zadnje rezalne površine

Povzetek *Študija obravnava implementacijo nove šestkotne mikrosture za izboljšanje rezalne učinkovitosti orodij iz polikristalnega kubičnega borovega nitrida (PCBN). Razviti so tridimenzionalni modeli običajnih orodij in orodij z mikrotesturo, postopek struženja pa je simuliran s programsko opremo za končne elemente AdvantEdge. Preučeni so vplivi rezalne sile, temperature in napetosti na zmogljivost orodja. Rezultati kažejo, da se pri uporabi orodij z mikrostrukturami na sprednji in zadnji rezalni površini v kombinaciji s trdnimi mazivi rezalna sila zmanjša za 3 % do 7 %. Poleg tega se zmanjša koeficient trenja, izboljša se kakovost površine obdelovanca in poveča se odpornost površine orodja proti obrabi. Posledično orodja z mikrostrukturami v kombinaciji s trdnimi mazivi učinkovito izboljšajo rezalno zmogljivost.*

Ključne besede *šestkotna mikrostruktura, orodja PCBN, struženje, simulacija končnih elementov, integracija trdnih maziv*

Retraction notice

Retraction notice to "Improvement of the Dimensional Accuracy of a Ti-6Al-4V Ripple Disc During Electric Hot Incremental Sheet Forming" SV-JME 70(2024)1-2, p. 20-26

Zhengfang Li[1] – Xudong Di[2] – Zhengyuan Gao[3] ✉ – Zhiguo An3 – Ling Chen[4] – Yuhang Zhang[1] – Shihong Lu[5]

1 Kunming University, School of Mechanical and Electrical Engineering, China
2 Jianghuai Automobile Group Co., Ltd., Passenger Car Research Institute of Technology Center, China
3 Chongqing Jiaotong University, School of Mechanotronics and Vehicle Engineering, China
4 Kunming University, Office of Science and Technology, China
5 Nanjing University of Aeronautics and Astronautics, College of Mechanical & Electrical Engineering, China

✉ zhengyuangao@cqjtu.edu.cn

This article has been retracted. Please see COPE policy on Article Retraction (https://publicationethics.org/guidance/guideline/retraction-guidelines).

This article has been retracted at the request of the Authors. Following concerns raised by the authors, an investigation of this paper was undertaken by the editors. The authors provided the reasons for a retraction request: "In this paper, the figures of the paper have been published in a thesis of Xudong Di entitled "Investigation on Incremental Forming Process of Titanium Alloy Corrugated Disk Using Current Assisted" by Nanjing University of Aeronautics and Astronautics, The Graduate School, College of Mechanical and Electrical Engineering, and the evidence of significant deficiencies is shown in Figs. 1-4. Therefore, the paper published has significant deficiencies. To maintain academic integrity, all authors agree to retract the paper."

International conference on
Additive Manufacturing and Post-Processing

7. - 9. 9. 2025 - Portorož, Slovenia

This conference will deliver discussions about the **challenges**, **opportunities**, and **state-of-the-art** on **additive manufacturing technologies** and **post-processing.**

ICAMPP 2025

Academic and industry participants invited to join!

- Plenary lectures
- Distinguished invited lectures
- Technical sessions
- Panel discussions
- Networking sessions

Supported by the Horizon EU project

SEAMAC
STRENGTHENING THE EXCELLENCE OF ADDITIVE MANUFACTURING CAPABILITIES

Funded by the European Union

NO REGISTARTION FEE! Number of participants limited to 100!

ICAMPP 2025

JOIN NOW

www.icampp.si

TU BERGAKADEMIE FREIBERG

TUBAF
Die Ressourcenuniversität.
Seit 1765.

FS
UNIVERSITY OF LJUBLJANA | Faculty of Mechanical Engineering

TECHNION
Israel Institute of Technology

Contents

since 1955

https://www.sv-jme.eu/